

# Time-Domain and Harmonic Balance Turbulent Navier-Stokes Analysis of Wind Turbine Aerodynamics using a Fully Coupled Low- Speed Preconditioned Multigrid Solver

By  
**Minghan Yan**

---

Thesis submitted for the degree of Doctor of Philosophy  
at Lancaster University

Engineering Department  
Lancaster University  
Bailrigg, LA1 4YW, Lancaster, United Kingdom

**Submitted**  
**November 2015**

# *Abstract*

The research work reported in this thesis stems from the development of an accurate and computationally efficient Reynolds-Averaged Navier-Stokes (RANS) research code, with a particular emphasis on the steady and unsteady aerodynamics analysis of complex low speed turbulent flows. Such turbulent flow problems include horizontal axis wind turbine (HAWT) and vertical axis wind turbine (VAWT) operating at design and off-design conditions. On the algorithmic side, the main contribution of this research is the successful development of a rigorous novel approach to low-speed preconditioning (LSP) for the multigrid fully coupled integration of the steady, time-domain and harmonic balance RANS equations coupled to the two-equation shear stress transport (SST) turbulence model. The design of the LSP implementation is such that each part of the code affected by LSP can be validated individually against the baseline solver by suitably specifying one numerical input parameter of the LSP-enhanced code. The thesis has investigated several important issues on modelling and numerical aspects which are seldom thoroughly analysed in the computational fluid dynamics problems of the type presented herein. The first and most important modelling issue is the necessity of applying the low speed preconditioning to both RANS and SST equations and maintaining the turbulent kinetic energy in the definition of the total energy, which, to the best knowledge of author, has never been seen in any published literature so far. Based on the results obtained in the analysis of the vertical axis wind turbine application, we have demonstrated that by preconditioning the SST turbulence equations, one can significantly improve the convergence rate; and keeping the turbulence kinetic energy in the total energy has a great positive effect on the solution accuracy. The other modelling issue to be analysed is the sensitivity of the flow solution to the farfield boundary conditions, particularly for low speed problems. The analyses reported in the thesis highlight that with a small size of the computational domain, the preconditioned farfield boundary conditions are crucial to improve the solution accuracy. As for the numerical aspects, we analyse the impact of using the relative velocity to build the preconditioning parameter on the flow solutions of an unsteady moving-grid problem. The presented results demonstrate that taking into account the grid motion in building the preconditioning parameter can achieve a noticeable enhancement of the solution accuracy. On the other hand, the nonlinear frequency-domain harmonic balance approach is a fairly new technology to solve the unsteady RANS equations,

which yields significant reduction of the run-time required to achieve periodic flows with respect to the conventional time-domain approach. And the implementation of the LSP approach into the turbulent harmonic balance RANS and SST formulations is another main novelty presented herein, which is also the first published research work on this aspect.

The newly developed low speed turbulent flow predictive capabilities are comprehensively validated in a wide range of tests varying from subsonic flow with slight compressibility to user-defined extremely low speed incompressible flows. The solutions of our research code with LSP technology are compared with experiment data, theoretical solutions and numerical solutions of the state-of-the-art CFD research code and commercial package. The main computational results of this research consist of the analyses of HAWT and VAWT applications. The first one is a comparative analysis of 30% and 93.5% blade sections of a VESTAS multi-megawatt HAWT working in various regimes. The steady, time-domain and frequency-domain results obtained with the LSP solver are used to analyse in great detail the steady and unsteady aerodynamic characteristics in those regimes. The main motivation is to highlight the predictive capabilities and the numerical robustness of the LSP-enhanced turbulent steady, time-domain and frequency domain flow solvers for realistic complex and even more challenging problems, to quantify the effects of flow compressibility on the steady and yawed wind-induced unsteady aerodynamics in the tip region of a 82-m HAWT blade in rated operating condition, and to assess the computational benefits achieved by using the harmonic balance method rather than the conventional time-domain method. The second application is the comparative aerodynamic analyses of the NREL 5MW HAWT working in the inviscid steady flow condition. The main motivation of this analysis is to further demonstrate the predictive capabilities of the LSP solver to simulate the three-dimensional wind turbine flows. The last application is the time-domain turbulent flow analysis of the VAWT to the aim of demonstrating the accuracy enhancement of the LSP solver for this particular problem, the necessity of applying the full preconditioning strategy, the important effect of the turbulent kinetic energy on the solution accuracy and the proper implementation of the preconditioning parameter required for an accurate numerical solution to an unsteady moving grid low-speed problem.

**Keywords:** low speed preconditioning, compressible Reynolds-Average Navier-Stokes equations, shear stress transport turbulence model, fully coupled multigrid integration, harmonic balance formulation, horizontal axis wind turbines.

# *Acknowledgements*

I would like to express my sincere gratitude to my supervisor Dr M. Sergio Campobasso, for his four year's great support and guidance throughout my entire PhD time, both to my research and personal life. He is a brilliant researcher with abundant knowledge in CFD area, and his strict attitude and passion towards academic research always inspire and encourage me to conquer any challenge and obstacle arising in my study. Although he is quite busy with the research and teaching, he still manages to arrange a regular meeting to discuss my work and helps me solve the issue with his amazing idea. I would also like to acknowledge my colleague Jernej Drofelnik and Fabio Gigante for providing me with the computational meshes of the three-dimensional NREL wind turbine application and the 30% blade section of the VESTAS horizontal axis wind turbine. I would also like to acknowledge my examiners Professor Xi Jiang and Dr Manosh Paul (University of Glasgow) for reading my thesis and providing greatly beneficial advice to improve the quality of my work.

My warmest and deepest sense of gratitude goes to my parents and my girlfriend Nan Wang, who always offer me the endless love, support, encouragement and advice during the whole period of my PhD. Last but not the least, I would like to take this thesis as a gift for my grandparents, and wish they have a forever happy life in the heaven.

# *Declarations*

Part of the work presented in this thesis has been already published in the following articles:

**M. S. Campobasso, A. Piskopakis, M. Yan**, “Analysis of an Oscillating Wing in a Power-Extraction Regime Based on the Compressible Reynolds-Averaged Navier-Stokes Equations and the  $K - \omega$  SST Turbulence Model,” in *ASME Turbo Expo*, San Antonio, Texas, USA, 2013. [DOI:10.1115/GT2013-94531](https://doi.org/10.1115/GT2013-94531)

**M. S. Campobasso, M. Yan, J. Drofelnik, A. Piskopakis, M. Caboni**, “Compressible Reynolds-Average Navier-Stokes Analysis of Wind Turbine Turbulent Flows using a Fully-Coupled Low-Speed Preconditioned Multigrid Solver,” in *ASME Turbo Expo*, Dusseldorf, Germany, 2014. [DOI:10.1115/GT2014-25562](https://doi.org/10.1115/GT2014-25562)

I declare that this thesis is my own work and it has not been submitted for any other degree at the Lancaster University or any other institution.

Minghan Yan

Lancaster, November 2015

# Contents

<b>Abstract</b> .....	2
<b>Acknowledgements</b> .....	4
<b>Declarations</b> .....	5
<b>Contents</b> .....	6
<b>Nomenclature</b> .....	9
<b>Chapter 1 Introduction</b> .....	14
<b>1.1 Computational fluid dynamics</b> .....	14
<b>1.2 Incompressible, low-speed, and multi-speed flows</b> .....	19
<b>1.3 Low speed preconditioning</b> .....	21
<b>1.4 Frequency-domain computational fluid dynamics</b> .....	25
<b>1.5 Motivation, objectives and overview</b> .....	26
<b>Chapter 2 Governing Equations</b> .....	31
<b>2.1 Differential conservative form of the time-dependent Navier-Stokes equations</b> .....	32
<b>2.2 Differential conservative form of the URANS and Menter’s Shear Stress Transport (SST) turbulence model equations</b> .....	33
<b>2.3 Integral form of the URANS and Shear Stress Transport (SST) turbulence model equations</b> .....	39
<b>2.4 Arbitrary Lagrangian/Eulerian Integral form of the URANS and Shear Stress Transport (SST) turbulence model equations</b> .....	41
<b>2.5 Harmonic balance form of URANS and Shear Stress Transport (SST) turbulence model equations</b> .....	42
<b>2.6 Quasi-linear form of URANS and Shear Stress Transport (SST) turbulence model equations</b> .....	45
<b>Chapter 3 Solution of the RANS Equations</b> .....	46
<b>3.1 Space discretisation</b> .....	46
<b>3.1.1 moving grid problems</b> .....	49
<b>3.2 Numerical integration</b> .....	50
<b>3.2.1 strongly coupled integration</b> .....	51
<b>3.2.2 steady problems</b> .....	52
<b>3.2.3 time-dependent problems</b> .....	54
<b>3.2.4 harmonic balance problems</b> .....	55
<b>3.3 Farfield boundary conditions</b> .....	58

3.3.1	BCs based on multi-dimensional compatibility equations .....	59
3.3.2	BCs based on one-dimensional Riemann invariants .....	62
<b>Chapter 4</b>	<b>Low Speed Preconditioning .....</b>	<b>64</b>
4.1	Low-speed preconditioner .....	64
4.2	LSP in Implicit and explicit CFD .....	72
4.3	Preconditioning parameter analysis .....	78
<b>Chapter 5</b>	<b>Preconditioning of Fully Coupled RANS and SST Equations .....</b>	<b>83</b>
5.1	Governing equations (2D) .....	83
5.2	Artificial dissipation .....	85
5.2.1	construction of numerical dissipation .....	87
5.3	Farfield BCs (2D) .....	88
5.3.1	mathematical model .....	89
5.3.2	validation .....	90
5.4	Numerical integration .....	95
5.4.1	time-dependent problems .....	95
5.4.2	harmonic balance problems .....	95
5.5	Preconditioning parameter for moving grid problem .....	96
<b>Chapter 6</b>	<b>Validation .....</b>	<b>98</b>
6.1	Steady turbulent flat plate boundary layer .....	99
6.2	2D Backward facing step .....	104
6.3	2D NASA wall-mounted hump .....	111
6.4	2D Convex Curvature Boundary Layer .....	118
6.5	2D Nakayama Model-A aerofoil case .....	125
6.6	NACA4412 aerofoil case .....	132
6.7	Summary .....	140
<b>Chapter 7</b>	<b>Results .....</b>	<b>141</b>
7.1	Horizontal axis wind turbine aerodynamics (2D) .....	142
7.1.1	yawed wind modelling .....	144
7.1.2	simulation set-up .....	148
7.1.3	steady flow analysis .....	150
7.1.4	yawed wind analysis with time-domain approach .....	154
7.1.5	yawed wind analysis with frequency-domain approach .....	160
7.2	Horizontal axis wind turbine aerodynamics (3D) .....	167
7.3	Vertical axis wind turbine aerodynamics (2D) .....	175

7.4	Summary .....	184
<b>Chapter 8 Conclusion .....</b>		<b>185</b>
8.1	Summary and concluding remarks .....	185
8.1.1	algorithmic conclusions .....	185
8.1.2	fluid dynamics conclusions .....	187
8.2	Future work .....	189
<b>Appendices .....</b>		<b>190</b>
A	Space discretisation (standard form) .....	190
B	Space discretisation (preconditioned form) .....	193
C	Space discretisation (simplified preconditioned form) .....	203
(C.1)	simplified form No. 1 .....	203
(C.2)	simplified form No. 2 .....	205
D	Similarity transformation .....	208
E	Non-dimensionalisation .....	208
F	Compact differential form of the URANS and SST equations .....	211
<b>Bibliography .....</b>		<b>214</b>

# Nomenclature

$\alpha_k$	Runge-Kutta stage coefficient
$c$	Speed of sound, aerofoil chord
$c'$	Artificial speed of sound
$c_v$	Specific heat at constant volume
$c_p$	Specific heat at constant pressure
$C_t$	Blade torque coefficient
$C_p$	Static pressure coefficient
$C_f$	Skin friction coefficient
$C_l$	Lift coefficient
$C_d$	Drag coefficient
$C_m$	Momentum coefficient
$C_y$	Vertical force coefficient
$C_x$	Horizontal force coefficient
$d$	Distance to the wall
$D_k$	Destruction of $k$
$D_\omega$	Destruction of $\omega$
$e$	Internal energy per unit mass
$E$	Total energy per unit mass
$E_c$	$x$ -components of $\hat{\Phi}_c$
$E_d$	$x$ -components of $\hat{\Phi}_d$

$F_c$	$y$ -components of $\widehat{\Phi}_c$
$F_d$	$y$ -components of $\widehat{\Phi}_d$
$F_x$	Horizontal component of the force per unit blade length
$F_y$	Axial component of the force per unit blade length
$f_{mg}$	Multigrid forcing function
$h$	Mesh width, static enthalpy per unit mass
$H$	Total enthalpy per unit mass
$k$	Turbulent kinetic energy
$K$	Condition number
$\kappa$	Thermal conductivity
$L_{IRS}$	Implicit residual smoothing operator
$\Delta l_r$	Root mean square of the cell residuals
$M$	Jacobian transformation matrix
$M_\infty$	Freestream Mach number
$\mathbf{n}$	Unit vector
$N_H$	Number of complex harmonics
$p$	Static pressure
$p_b$	Pressure at the farfield boundary
$p_i$	Pressure extrapolated from the inner cells
$p_\infty$	Pressure specified at infinity
$P_c$	Preconditioning matrix with respect to conservative flow variables
$Pr$	Prandtl number

$Pr_T$	Turbulent Prandtl number
$P_d$	Production term
$P_k$	Production of $K$
$P_\omega$	Production of $\omega$
$\mathbf{q}$	Heat flux vector
$q_{i(j)}$	Cartesian components of the heat flux vector $\mathbf{q}$
$\mathbf{q}_T$	Turbulent heat flux vector
$\mathbf{q}_{T(j)}$	Cartesian components of the turbulent heat flux vector $\mathbf{q}_T$
$\hat{Q}$	Array of unknowns
$Re$	Reynolds number
$R$	Rotor radius
$\hat{R}$	Cell residuals
$S$	Total entropy, surface
$dS$	Surface element
$\mathbf{S}$	Strain rate tensor, turbulent source terms
$S_{ij}$	Cartesian components of Strain rate tensor $\mathbf{S}$
$t$	Time
$T$	Static temperature, blade torque
$\hat{U}$	Conservative flow variables
$U_{nb}$	Normal velocity at the farfield boundary
$U_{ni}$	Normal velocity extrapolated from the inner cells
$U_{n\infty}$	Normal velocity specified at infinity

$U_{ref}$	Reference velocity
$\hat{V}$	Primitive flow variables
$u_\infty$	Free-stream velocity
$\mathbf{u}$	Velocity vector
$u_{i(j)}$	Cartesian components of the flow velocity vector $\mathbf{u}$
$u_\tau$	Friction velocity vector
$u^+$	Nondimensionalised velocity component parallel to the wall
$v_b$	Velocity vector of the boundary
$V$	Volume
$dV$	Volume element
$V_p$	Preconditioned velocity
$W$	Characteristic variables
$W_x$	Axial component of the freestream velocity
$W_\theta$	Circumferential component of the freestream velocity
$y^+$	Nondimensionalised wall distance
$\epsilon$	Preconditioning cutoff parameter
$\beta^*$	Turbulent coefficient
$\beta$	Turbulent coefficient, preconditioning parameter
$\gamma$	Ratio of specific heat, turbulent coefficient
$\gamma^*$	Turbulent coefficient
$\gamma_p$	Blade twisted angle <sup>9*</sup>
$\Gamma_p$	Preconditioning matrix with respect to primitive variables

$\delta_{ij}$	Kronecker Delta Function
$\delta$	Yaw angle
$\lambda$	Eigenvalues, reduce frequency
$\mu$	Molecular dynamic viscosity
$\mu_T$	Eddy viscosity
$\nu_T$	Kinematic eddy viscosity
$\rho$	Density
$\rho_p$	Partial derivative of density with respect to pressure
$\rho_T$	Partial derivative of density with respect to temperature
$\rho_p'$	Modified partial derivative of density with respect to pressure
$\sigma_k$	Turbulent coefficient
$\sigma_\omega$	Turbulent coefficient
$\tau$	Molecular stress tensor
$\tau^R$	Reynolds stress tensor
$\Delta\tau$	Local pseudo-time-step
$\hat{\Phi}_c$	Generalized convective flux vectors
$\hat{\Phi}_d$	Generalized diffusive flux vectors
$\Phi_\infty$	Angle of attack perceived by the blade
$\omega$	Specific dissipation rate, excitation frequency
$\Omega$	Modulus of vorticity

# *Chapter 1*

## **Introduction**

### **1.1 Computational fluid dynamics**

With the development of the semiconductor industry, a rapid advancement has been achieved in terms of the modern computing technology in the recent decades, which has allowed engineers to reduce the time spent on accurately analysing and solving complex fluid dynamics problems. Thanks to the growing computing power and new revolutionary powerful computing devices such as General Purpose Graphics Processing Units (GPU) (Owens et al., 2008), large numbers of designs of significantly improved quality have thus been made in various areas of engineering research and development, such as automotive or aerospace industry. Moreover, it has also led to numerous innovations on complex design problems which have been previously hindered by the lack of satisfactory resolution for a long time. Therefore, on the basis of the new hardware technology, many new advanced aerodynamic and aeroelastics analysis methods have come into reality, and have been applied extensively to modern cutting-edge engineering tasks.

One representative approach to carry out the above said analyses refers to the area of high-fidelity computational aerodynamics and computational aeroelasticity both based on Computational Fluid Dynamics (CFD). The use of high-fidelity CFD is of crucial importance to multiple areas, including mechanical, aeronautical, marine and civil engineering. Important aspects about CFD are the fundamental theory on which it is based, which provides the foundations of the conservation laws of fluid mechanics. With CFD the numerical solution of the governing equations is obtained at the discrete points of a computational grid obtained by discretising the physical domain of interest (Blazek, 2005, Kundu and Cohen, 2008, Hirsch, 2007). As a consequence, many newly-developed numerical methods or solvers of commercial or research codes, have been implemented for the purpose of solving both academic and industrial problems, and have gained great success in terms of both accuracy and computational efficiency. In the recent years the great development of CFD and the

growth of its modelling capabilities have significantly benefited the analysis and design of aircraft components (Nielsen and Anderson, 1999) or rotorcraft components (Cathy et al., 2013) or the whole body, wind turbine rotors (Zahle et al., 2014), hydraulic machines (Xiao et al., 2013) and gas turbine rotors (Walther and Nadarajah, 2012) and automobile shapes (Ahmed and Chacko, 2012). In the past few decades, the increasing popularity of CFD has helped industry to greatly reduce product development budgets by replacing expensive experimental campaigns with much cheaper CFD simulations. However, it should be also noted that experimental testing still plays a critical role and is considered as the only reliable source of solution in certain applications characterised by very high complexity of the flow physics. For this reason, experimental testing has another essential function, namely that of validating new CFD methods and modelling capabilities. Despite the fact that the final stage of complex products development such as aircraft and aircraft engines is still based on the very expensive experiments, the important function of CFD in the product development process is also undeniable, and gives birth to more innovative and imaginative design to be tested.

In general, using the CFD approach requires running a computer code to solve numerically the physical conservation laws governing the fluid problem at hand. Various fluid flow models of widely varying complexity have been developed and implemented in different codes, ranging from the steady incompressible inviscid irrotational potential flow model to the time-dependent compressible Navier-Stokes (NS) viscous model (Ferziger and Perić, 2002), which can be solved (numerically in general, and analytically only in special cases) by considering a Laplacian operator, and solved with a system of parabolic partial differential equations (with respect to time-dependent variables) respectively. Unfortunately, providing the most comprehensive description of fluid flow physics, the Navier-Stokes flow model cannot be solved analytically in the majority of flow problems of interest, and this has prompted the development of novel numerical approaches to solve engineering flow problems by means of Navier-Stokes CFD codes.

Historically, the name of Navier-Stokes equations denoted only the conservation law of the linear momentum of the fluid flow under consideration; currently, however, the name is used to refer to the whole system of conservation laws, namely the conservation of mass, the conservation of linear momentum (which is a vectorial equation with 2 or 3 components depending on the problem dimensionality), and the conservation of energy. For problems involving the flow past stationary or moving objects (e.g. wings, blades, aircraft or ships),

they are mostly turbulent, and always stochastic and chaotic, which results in the occurrence of eddies of widely different length- and time-scales.

An extremely high temporal and spatial resolution is often linked to directly solving the Navier-Stokes equations for high Reynolds number turbulent flow problems, because of the wide range of temporal and spatial scales in such flows. The approach whereby the Navier-Stokes equations are solved ‘directly’, modelling all temporal and spatial scales of turbulent eddies is called Direct Numerical Simulation (DNS) (Cook and Riley, 1996). However, DNS is seldom used in industrial engineering problems due to the lack of sufficiently large computational resources, and is used in academic research mainly to investigate fundamental aspects of the physics of turbulence making use of simple three-dimensional simulation set-ups. Consequently, several computationally less expensive alternatives have been developed which enable the solution of complex turbulent flow problems with the Navier-Stokes equations while by reducing the computational burden with respect to the DNS approach. Such alternative approaches rely on approximations level of the turbulent flow features. The use of models to simulate the turbulent characteristics of the flow rather than the NS equations to resolve directly all physical characteristics of turbulent flows, significantly reduce the computational burden, enabling the NS model to be used on a wide scale for research and development tasks both in the industry and the Academia.

The most popular approach to approximating the effects of turbulence relies on the use of the so-called Reynolds-Averaged Navier-Stokes (RANS) equations, in which a time averaging scheme is applied to the NS equations on the time-scales of turbulence. Although the 3 partial differential equations (PDEs) of the RANS system are almost identical to their original forms, they differ from the NS equations for the presence of additional unknown terms resulting from the time-averaging, and taking into account the effects of turbulence in a mean sense. The occurrence of new unknowns in the RANS system requires the introduction of new equations, since the number of PDEs and unknowns must be equal (closure problem). Thus, one has to choose a specific turbulence model (Wilcox, 1994). A large number of turbulence models exist, and they can be classified according to different criteria. One of such criteria is the number of equations the turbulence model is made up of. For example, there exist semi-empirical models with a single algebraic equation, like the Baldwin-Lomax model (Baldwin and Lomax, 1978); one-equation models, such as the Spalart-Allmaras model (Spalart and Allmaras, 1994); two equation models, such as the  $K - \varepsilon$  (Jones and Launder, 1973) and the

$k-\omega$  (Wilcox, 1988) models, or even seven-equation models, such as the Reynolds stress model (Launder et al., 1975, Dreeben and Pope, 1997).

In essence, the main differences between the NS and RANS equations lie in the definition of the flow variables: the flow variables of the former flow model represent the instantaneous values of the time-dependent fluctuating turbulent flow, whereas the variables of the latter flow model represent time-averaged values of the turbulent fluctuating flow field. In the RANS model, the averages of the flow fluctuations appear explicitly only in the additional unknown terms introduced by the equation averaging, and such terms are modelled by means of the selected turbulence model. The advantage of the Reynolds averaging approach is that the temporal and spatial refinement of the computational grids required to analyse realistic engineering problems is much smaller than for DNS. This is because the RANS approach does not require the resolution of all the small and medium temporal and spatial scales of turbulence, but only the large ones associated with the characteristic length of the object surrounded by the flow of interest (e.g. wing or blade chord) and a characteristic time depending on the mean flow velocity (e.g. the time taken by a flow particle to travel a chord length).

The modelling fidelity of RANS approach is generally lower than that achieved by DNS, which is a consequence of the partly empirical nature of turbulence models for the system closure: some of the coefficients of turbulence models are based on a limited amount of experimental data, and turbulence models often end up being used for turbulent problems quite different from those used to define their constants. Nevertheless, the fidelity of the RANS model is found to be adequate when solving a surprisingly wide range of flow problems, in which a low to medium degree of separation near solid wall boundaries characterises the flow field. Even when the evolution of wakes and shed vorticity is not sufficiently well resolved by the RANS approach (the degree to which this occurs, however, also depends on the complexity of the adopted turbulence model), the force acting on the body of interest, which are often the main output of engineering interest, are well resolved.

It should be noted that in addition to the DNS and RANS approaches to account for the effects of turbulence, there are other approaches featuring a fidelity level between that of RANS and DNS. The best known one of such models is called Large Eddy Simulation (LES) (Piomelli, 1998), and is conceptually similar to the RANS approach. The major difference between the RANS and LES models is their specific approach to deal with the turbulence

scales. The RANS approach models the mean effects of turbulence only on the large scales associated with the typical dimension of the engineering geometry being analysed and times depending on such characteristic length and the mean flow speed; LES, unlike RANS, computes directly the larger scales of turbulence, but, like RANS, uses turbulence modelling to account for the effects of turbulence on the smallest spatial and temporal scales not resolved by the computational grid. For these reasons, LES often provides better resolution than RANS of the temporal and spatial evolution of wakes and shed vorticity in the middle- and farfield regions, where the LES model is indeed expected to outperform the RANS model; for cases in which low, moderate and sometimes fairly high levels of separation occur, however, LES and RANS are often found to give comparable accuracy for predicting the forces acting on aerodynamic bodies such as aircraft wings and wind turbine blades (Johansen et al., 2002). However, in case of high-Reynolds number wall-bound problems, a relatively high grid refinement is required to ensure an accurate LES, and this leads to similar limitations as those incurred by DNS, which can be used only in the very few cases in which very large supercomputers are available. This is also, though often to a slightly lower extent, the main drawback of the hybrid RANS/LES approach known as Detached Eddy Simulations (DES) (Spalart et al., 1997, Nikitin et al., 2000, Bechmann and Sorensen, 2010) and Delayed Detached Eddy Simulation (DDES) (IM and Zha, 2011, Spalart et al., 2006).

In DES, the RANS and LES models are applied in a mixed fashion in the whole computational domain. In this method, the region close to solid walls is simulated with RANS and the flow in the rest of the domain is simulated with LES. As a consequence, substantially coarser grids than in a fully LES approach are required in the wall proximity which help reducing the computational cost of the DES technology with respect to that of LES, although the cost remains significantly higher than that of the RANS model. Nevertheless, it is undeniable that the DES approach constitutes an ideal compromise between cost and accuracy, particularly in the case of high Reynolds number separated flows, which are characterised by a significant vorticity production at solid wall boundaries and propagation of such vortical structures through large regions of the computational domain. The two main difficulties associated with DES CFD are 1). the establishment of a robust and reliable criterion to determine the domain portion where a specific approach (RANS or DES) is to be used, and 2). the implementation of a smooth transition between the two models (Piomelli et al., 2003, Sørensen et al., 2011).

## 1.2 Incompressible, low-speed, and multi-speed flows

Many existing CFD codes have been utilised in the aerospace and automotive industry to solve the compressible flow equations required to take into account the important compressibility effects associated with transonic and supersonic Mach numbers. However, from a more general perspective, other important applications, such as those in hydraulic power engineering (Xiao et al., 2013), naval engineering, and biological fluid mechanics do not necessarily require the use of a compressible solver, since there are no compressibility effects. These applications are more frequently dealt with by means of a CFD code solving the incompressible NS equations. The NS incompressible flow equations can be derived by the compressible equations by setting the density equal to a constant value and removing all temporal and spatial derivatives from the equation. When solving the NS equations in conservative form, an equation of state is also needed. A typical example of equation of state for the compressible flow equations is the perfect gas law, which relates pressure, temperature and density. In the case of the incompressible flow equations, the equation of state simply states that the density is constant.

The obvious application of the incompressible flow equations is the flow of an incompressible fluid such that of water in a hydraulic turbomachine, which can be characterised by fairly high flow speeds. However, the incompressible equations can also be used to study the flow of a compressible fluid, such as air, when such flow is characterised by fairly low speeds. This is because in this circumstance, the density variations due to speed variations are so small that they can be neglected in most applications of engineering interest. The use of compressible solvers for the analysis of low-speed compressible flows, however, results in a large disparity between the convective and the acoustic speeds of the flow, and this occurrence leads to reduced accuracy and convergence rates of the compressible solver. As explained and shown in the rest of this thesis, these issues can be circumvented by using a numerical method known as low-speed preconditioning (LSP), one of the main topics of this research.

However, there are many problems which are of a mixed type, and do not fall unambiguously within any of the flow classes discussed above: problems in which one has to accurately assess the variations of the density of an incompressible or low-speed compressible fluid flow due to thermal effects, and problems in which a compressible fluid behaves like

## 1.2 Incompressible, low-speed, and multi-speed flows

incompressible in certain regions, characterised by small fluid velocities, and behaves as compressible in other regions, characterised by high flow speeds. Significant density variations of an incompressible fluid flow occur in the presence of strong heat fluxes. This phenomenon is the key mechanism of natural circulation-based heating systems. A constant pressure combustion process also represents an example in which significant density variations occur as a consequence of thermal effects (heat generated in the combustion process) rather than variations of the fluid velocity.

The second class of mixed flow, which is that of interest to the research of this thesis, is that of the compressible fluid flow problems characterised by regions with very low speeds, where compressibility effects are negligible, and regions characterised by high speeds, where compressibility effects are instead quite significant. In these problems, the density variations are caused primarily by convective speed variations. A typical example of such problems includes transonic flows with regions of low speed near the stagnation points or reverse flow regions. This type of flows is characterised by a wide range of characteristic speeds ranging from the speed of sound of acoustic waves to the convective speeds of eddies and vortices propagating at low particle speeds. One of the representative engineering problems is the Harrier aircraft in near-hover (landing approach) condition (Chaderjian et al., 2002). In this situation, the aircraft's forward velocity is approximately 0.04 Mach; meanwhile the aircraft is on the contrary hovering in the air supported by four high speed jet exhausts downward to the ground. Another example would be the newest multi-megawatt HAWT (Campobasso et al., 2014a) featuring blade heights in excess of 80 m, and thus results in that the local Mach number in the tip region is even higher than 0.3, which is the conventional threshold at which compressibility effects start becoming significant; however the relative Mach number perceived by the blades decreases in a nearly linear fashion from the tip to the root of the blade, where it reaches values of order 0.01 or less and is treated undoubtedly as incompressible flow. Similar phenomena can be also found in the case of the helicopter in forward flight where the rotational speeds of the rotors and the fuselage's forward velocity can be differed by more than 2 orders of magnitude. Two-phase flow mixing between compressible and incompressible or rocket propulsion flow-fields involving low speeds in the combustor and supersonic flow in the nozzle can also be grouped into this category. These problems can be dealt with only by means of compressible flow solvers, due to necessity of modelling the high-speed regions of the flow field at hand.

However, such a wide range of flow speeds poses a severe challenge to even the most advanced compressible CFD algorithms due to the large difference of characteristic speeds. In mixed-speed flow problems, the low speed region would have significant effect on the convergence problems if the low speed region is relatively large. One difficulty of handling such problems lies in the fact that in the low Mach regions, the general time-marching algorithm for computing compressible flows will become ineffective (Choi and Merkle, 1993). As the magnitude of the flow speed decreases and becomes quite small compared to the acoustic speed, a large disparity between the two speeds causes stiff convective terms in the time-dependent equations and consequently hinders the convergence of time-marching method resulting in high computational cost of the simulation. Apart from the negative influence on the convergence, such disparity between the acoustic and particle speeds would also spoil the accuracy of the numerical solution as explained later in the thesis. Therefore in keeping with the broad capability of the time-marching algorithm, it is imperative to develop a proper treatment which could eliminate the convergence and accuracy problems incurred by the low Mach number regions.

## 1.3 Low speed preconditioning

Before providing the analyses of the research of using the compressible algorithm to solve complex flow problems, we would at first introduce an important term called the condition number. For the Euler equations, the condition number is simply defined as the ratio between the smallest and largest wave speeds or absolute eigenvalues. Regarding a simple model of a 1-D Euler equations, which is shown as below,

$$\frac{\partial Q}{\partial t} + A \frac{\partial Q}{\partial x} = 0 \quad (1.1)$$

where  $Q$  stands for the flow variables ( $Q = [\rho, \rho u, \rho E]$  and  $\rho$ ,  $u$  and  $E$  are respectively, the flow density, the x-component of the flow velocity vector  $\hat{v}$  and the total energy per unit mass) and  $A = \partial U / \partial Q$  is the flux Jacobian matrix between the convective flux term  $U$  ( $U = [\rho u, \rho u^2 + p, \rho u H]$  and  $p$  and  $H$  are the pressure and total enthalpy per unit mass) and the flow variable  $Q$ . The eigenvalues for this 1-D system is thus determined by the matrix  $A$  and given as,

$$\lambda_1 = u, \quad \lambda_2 = u + c, \quad \lambda_3 = u - c \quad (1.2)$$

where  $c$  is the speed of the sound.

Since there always exist a complete set of eigenvalues and eigenvectors, the mathematical expression of the condition number  $K$  of the Euler system can be written as,

$$K = \frac{|\lambda|_{max}}{|\lambda|_{min}} \quad (1.3)$$

where  $|\lambda|_{min}$  and  $|\lambda|_{max}$  are the smallest and largest eigenvalues.

The condition number, or so called the characteristic condition number referring to the characteristic speeds of the Euler equations, can often determine the relative stiffness of the system, and the optimum value of the condition number is unity. At such a condition number, all waves would propagate at the same rate, which yields an efficient calculation process. For example, in the explicit local time-stepping, the maximum local time step is restricted by the fastest wave speeds in order to fulfil the requirement of the CFL condition,

$$\Delta t \leq \frac{h}{|\lambda|_{max}} \quad (1.4)$$

where  $h$  represents the mesh width.

As the fastest wave passed the whole mesh width, the slowest wave would only move,

$$\Delta t |\lambda|_{min} = \frac{h}{|\lambda|_{max}} |\lambda|_{min} = \frac{h}{K} \quad (1.5)$$

The essential problem is that the error associated with different wave mode travels out of the domain with specific speed equal to that of its characteristic wave, thus if the wave speeds are largely different, the errors will leave the domain at different times which will consequently slows down the convergence with respect to the case in which all error modes have comparable speeds and leave the domain approximately within the same time. Therefore, a large condition number would have negative influence on the efficiency of the wave propagation and consequently lower the convergence

In case of a subsonic regime ( $M < 0.5$ ) of our research interest in this study, the condition number is determined as  $K = (u + c)/u = 1 + 1/M > 3$ , and it can be easily noticed that as the Mach number approaches to zero (or the difference between the acoustic and particle speeds increases), the condition number will become as large as infinity, which, due to the

above theory, causes a severe convergence issue and lower the computational efficiency dramatically. In addition to this issue, using compressible codes without LSP to solve low Mach number problems suffers an incorrect numerical dissipation which is caused by the large disparity of eigenvalues, and such wrong numerical dissipation can deteriorate the accuracy of the computed solution, thereby confirming our previous statement that it is ineffective to use compressible flow algorithms to solve mix-speed flow problems involving incompressible region.

On the other hand, purely incompressible flow algorithms that are effective for all incompressible fluid flows and compressible fluid low speed flows are usually incapable of handling acoustic and compressibility effects of compressible fluid flows featuring both low and high convective speeds. Therefore, to accurately resolve the above low speed compressible fluid problems and compressible fluid problems with mixed-speed flows, it is impossible to rely on either a single compressible or incompressible solver.

To enable an incompressible code to account for the compressibility effect in a low Mach flow, a method called the artificial compressibility has been first introduced by Chorin (1967) and followed by a wide development and extension (Fiterman et al., 1995, Turkel, 1987, Van Leer et al., 1991), which replaces the standard physical time-derivative terms in the incompressible equations with a set of artificial time-derivatives that eliminate the stiffness difficulties between the wave speeds. Specifically, the method adds a pseudo-time derivative of density into the continuity equation which allows a time-marching algorithm to be applied in the same way as in the momentum equations, and thereby introduces a set of pseudo-acoustic waves that travel at speeds similar to the particle waves. A similar convergence like those obtained with the compressible equations in the transonic flow can now be obtained in the low Mach condition.

Regarding the progress of overcoming the challenges associated with the use of compressible codes, significant efforts have been invested in developing a method called the low speed preconditioning, which aims to reduce the condition number of the system and thus strengthens its numerical capability dealing with the low Mach number problems. Example of such advanced technique and its related theories can be found in refs.(Choi and Merkle, 1993, Turkel, 1987, Weiss and Smith, 1995, Van Leer et al., 1991). As a matter of fact, preconditioning method can be regarded as a viable approach to extend the capability of compressible codes to low Mach number range, by pre-multiplying the time derivative terms

in the Euler/Navier-Stokes equations with local Mach dependent matrices. For example a 1-D preconditioned Euler equations can be modified as,

$$P \frac{\partial Q}{\partial t} + A \frac{\partial Q}{\partial x} = 0 \quad (1.6)$$

where  $P$  is the matrix depending on the local Mach number and is the so-called preconditioner. The new eigenvalues of the system is thus determined by the matrix  $P^{-1}A$  and can be written in a general form as below

$$\lambda_1 = u, \quad \lambda_2 = u + c', \quad \lambda_3 = u - c'' \quad (1.7)$$

where  $c'$  and  $c''$  are two pseudo acoustic speeds and may have different expressions based on the specific choice of the preconditioner  $P$ . With such acoustic speeds being modified to the same order of magnitude as the particle speeds, the condition number of the new system can be greatly reduced for all Mach numbers in the subsonic regime. A comprehensive study of the influence on optimising the condition number with various preconditioning approach can be found in ref. (Hejranfar and Kamali-Moghadam, 2012), and we only present here a simple analysis of optimising the condition number with Choi and Merkle's preconditioner which has also been adopted in our research. The detailed expressions of the preconditioning matrix and eigenvalues are reported in Appendix B.

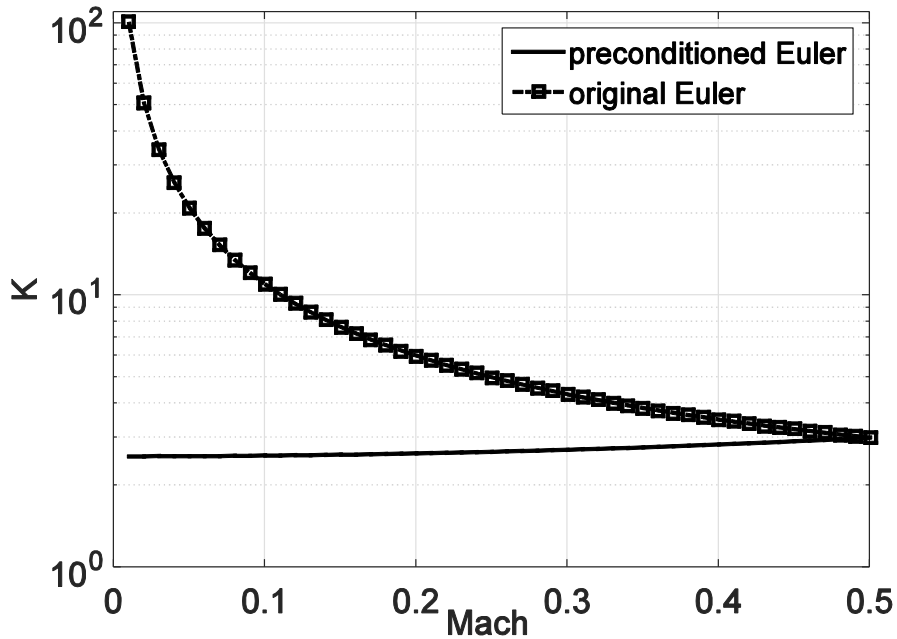


Figure 1.1 Condition number as a function of Mach number for the 1-D Euler equations with and without low speed preconditioning approach

A plot of the condition number as a function of Mach number is shown in Figure 1.1 for both preconditioned and standard (non-preconditioned) Euler equations. Apparently, the LSP approach has greatly optimised the condition number particularly at low Mach numbers by achieving a reduction of more than two orders of magnitude with respect to the non-preconditioned value, and it thus successfully removes the effect of stiffness issues on convergence and enables the algorithm to provide accurate CFD results (the reason why an optimal value of unity is not achieved here can be due to the specific chosen LSP method, and a detailed investigation of various preconditioning approaches on optimising the condition number has been given in Chapter 4). Therefore a compressible flow solver with the preconditioning method can have the advantage of handling problems involving both compressible and incompressible flow regions.

## 1.4 Frequency-domain computational fluid dynamics

Two different approaches have been used to solve the unsteady Reynolds-Averaged Navier-Stokes (URANS) equations in our research. The first and most popular one, applicable to general unsteady flow problems (e.g. transient states) is the classical time-domain method, whereby one starts the solution process at a user-given initial time and marches the solution in time until reaching the specified final time. The other one is the nonlinear frequency-domain (FD) harmonic balance (HB) approach often applied to solve nonlinear periodic flow problems.

In many unsteady periodic flows, one is interested primarily in the characteristics of the periodic flow solution rather than the physical transient leading to that periodic state. For example, the analysis of the periodic flow associated with the horizontal axis wind turbines in yawed wind conditions, requires long simulation time when using the time-domain (TD) approach due to the fact that several rotor revolutions have to be completed to achieve a periodic state. On the other hand, such a high wallclock time required by TD solutions can be substantially reduced with a FD formulation, among which the harmonic balance (HB) NS approach (Hall et al., 2002) to the solution of unsteady periodic flows is one of the most promising methods. The harmonic balance algorithm is an expansion method for determining the periodic solutions of systems of ordinary differential equations (ODEs) in a fairly quick

fashion. The basic idea of the frequency domain method is to represent the solution as a truncated Fourier series with a user-given number of complex harmonics. For a periodic turbulent flow problem which only requires a relatively small number of complex harmonics to represent the time-domain solution accurately, the benefit of method over time-domain method turns out particularly significant, thus yielding a substantial reduction of the computational time without noticeable penalties of the solution accuracy. Aiming at reaching the final periodic solution without the intermediate process of computing the transient flow state like in the case of the time-domain analysis, is one of the main reasons why the harmonic balance solver is substantially faster than the time-domain solver. Another reason is that most of the problems of engineering interest can be accurately represented with a few harmonics even though they are significant nonlinear. It is found in (Hall et al., 2002) who first introduced and developed the harmonic balance approach, that the computational time can be reduced by at least one order of magnitude using this technology with respect to the solution of time-domain method. Therefore this new advanced computational technology has been applied to the prediction of the periodic flow associated with flutter and forced response of turbomachinery blades (Su and Yuan, 2010, Hall et al., 2002, Van Der Weide et al., 2005), and various vibratory motion modes of aircraft configurations (Da Ronch et al., 2013, Sicot et al., 2008).

## 1.5 Motivation, objectives and overview

The research work summarised in the thesis is driven by two major motivations: on one hand, a novel algorithmic and modelling technology has been developed and validated aimed to improve the solution accuracy and computational efficiency of the RANS model-based analysis of general unsteady and periodic turbulent flow problems with mixed or low speed flow regions; on the other hand, incorporation of the above numerical approach into an advanced frequency domain method has been realised and aimed to demonstrate its accuracy and effectiveness of saving computational time by analysing various challenging high-Reynolds number unsteady flows, namely the unsteady aerodynamics analyses of a horizontal axis wind turbine aerofoil and a horizontal axis wind turbine rotor in yawed wind condition.

More specifically, the main objectives associated with the algorithmic work of this research are to:

- extend the low speed preconditioning strategy (i.e. preconditioning matrix, artificial dissipation) to turbulence model and implement it with the fully-coupled integration of the steady, time-domain and harmonic balance RANS and SST turbulence model equations;
- validate and assess the computational efficiency and accuracy achieved by using the turbulent RANS SST harmonic balance LSP-solver by performing time-domain and harmonic balance turbulent analyses of a horizontal axis wind turbine aerofoil and rotor in yawed wind condition, and make comparisons of the computational resources required by the two approaches.

Several elements of novelty on the algorithmic side have been presented in the thesis. The low speed preconditioning approach extended to the two-equation  $k - \omega$  and SST turbulence models and its associated implementations go beyond the purely mathematical analyses given by Venkateswaran and Merkle (1999), but more importantly have been successfully validated on a wide range of challenging problems. . The developed multigrid fully coupled integration of the preconditioned steady and time-domain RANS and SST equations is also a tremendous extension of the frameworks of the steady equations in (Liu and Zheng, 1996) and time-domain analysis given by Yao et al. (2001), as the adaptation of this approach to the SST turbulence model, particularly with the implementation of the low speed preconditioning, and the related theoretical and numerical analyses carried out to optimise the effectiveness of this procedure are one of the novel features reported for the first time in this thesis. On top of that, the extension of the LSP approach has also been made to the fully coupled integration of the turbulent harmonic balance RANS and SST equations, and this is another main novelty presented herein, which, to the best of the author's knowledge, has never been seen in the published literature.

The structure of the thesis is organised as follows. Chapter 2 - *Governing Equations* gives in great details the time-dependent and harmonic balance formulations of the compressible RANS and SST turbulence model equations, forming the fundamental context of developing the LSP method, and it is concluded with the quasi-linear form of the RANS and SST equations.

Chapter 3 - *Solution of the Navier-Stokes Equations* focuses on the numerical approaches, in terms of different aspects, to the solution of RANS and SST equations. It first reports the space discretisation method of the governing equations. The theoretical analyses of the strongly coupled integration method is presented as follows and its implementation in the steady, time-dependent and harmonic balance formulations will also be provided in details in Chapter 3. Description of the farfield boundary conditions is given finally to conclude the chapter. The farfield BCs are formulated in two different forms (Riemann invariants and characteristic variables) and it is highlighted that only the latter form can be implemented with the LSP approach.

An investigation of the preconditioning methods proposed by different researchers (Tukel, Merkle, Van Leer, Roe, Chorin, etc) is provided in Chapter 4 - *Low Speed Preconditioning*, focusing on various treatments of the extended implementation with different turbulence models. This is followed by a detailed review and comparison of two types of integration schemes (implicit and explicit) usually applied in the preconditioned system. Last but not least, the analysis of the preconditioning parameter adopted in different flow problems (steady, time-dependent unsteady, etc) is documented.

Chapter 5 – *Preconditioning of Fully Coupled RANS and SST Equations* focuses on the discussion of several numerical aspects associated with the development and the implementation of the low speed preconditioning into the system. The preconditioned RANS and SST turbulence model equations considered as the fundamental part of the whole scheme is presented at the beginning. To secure the accuracy of the solution for low speed problems, preconditioned artificial dissipation is developed and its detailed analyse is given herein. An optimised farfield boundary condition with LSP implemented is also beneficial to obtain an accurate solution when the computational domain of a small size is used. Therefore the chapter presents the detailed mathematical derivation process of such boundary conditions as well as a numerical analysis to validate its effectiveness. The strongly coupled integration approach to the solutions of different preconditioned formulations (i.e. steady, time-domain and frequency-domain) is also reported herein as a significant extension of those discussed in Chapter 3. Finally we will discuss the preconditioning parameters based on the absolute and relative velocities in the moving grid unsteady problem as such particular choice may affect the solution and convergence rate to some extent. Therefore a mathematical model of the relative velocity based preconditioning parameter is provided herein.

Chapter 6 - *Validation* presents the solution of several turbulent flow problems in subsonic regime, which are used to validate the turbulent flow predictive capabilities of the low speed preconditioning approach. Firstly a steady turbulent flat plate boundary layer is considered: the numerical solution obtained by the CFD solver (COSA) used in our research is compared with available theoretical results for three different Mach numbers. In the second case the flow separation and reattachment caused by a backward facing step is analysed and the simulated results of COSA are compared with both the solution of a well-established research code (CFL3D) and the available experiment data. This is followed by the numerical analyses of a 2D wall-mounted hump experiment where a Glauert-Goldschmied type body is mounted in the lower wall. Experiment data and CFL3D results are used as benchmarks to assess the low speed flow predictive ability of the LSP solver. The last internal flow problem is the 2D simulation of a convex curvature boundary layer in a duct in which we primarily analyse the flow characteristics near the convex wall curvature. The first external problem is a so-called Model-A aerofoil in a low Mach number turbulent flow where characteristics of velocity profiles are measured in the wake at the angle-of-attack of 0 degree. The last test case is the NACA4412 aerofoil in a subsonic turbulent flow featuring a flow reversal in the rear portion of the suction side. The COSA solutions have been compared to available experiment data. In all test cases, comparisons of the numerical solutions of COSA with and without LSP implementation with the experiment data and results of CFL3D analyses are presented, particularly two additional simulations with lower Mach numbers with respect to the original value are included in each problem to further challenge the flow predicting capability of LSP in terms of solution accuracy and stability. It is highlighted that despite the compressibility effect in specific aerofoil cases, solutions of LSP solver have demonstrated an independence of the variation of Mach numbers, and also featured higher numerical accuracy in the low Mach number flow problems due to the correct scaling of the artificial dissipation term.

Chapter 7 - *Results* provides the main computational results of this research, consisting of analyses of two horizontal axis wind turbine applications and one vertical axis wind turbine application. The first one is a thorough comparative analysis of the 30% and 93.5% blade sections of a VESTAS multi-megawatt HAWT working in various regimes (i.e. steady problem where the wind direction is orthogonal to the rotor plane and the unsteady yawed wind condition) and three different freestream Mach numbers, namely the one corresponding to the rated wind speed and two lower Mach numbers for which the flow is required to be treated as incompressible. The main objective for analysing this problem is to assess the

compressibility effect by using LSP to approximate the incompressible solution. Presented results demonstrate the predictive capabilities of the LSP solver for different formulations (steady, time-domain and frequency-domain) and the computational benefits achieved by using the harmonic balance method of the RANS and SST equations rather than the conventional time-domain method through comparing the numerical solutions obtained by these two approaches. The second application is the steady inviscid flow analysis of a NREL multi-megawatt HAWT working in the operating conditions corresponding to both the rated wind speed and fairly low Mach number flow. The main motivation of carrying out this research is to demonstrate the accurate solution achieved by using LSP in analysing the entire three-dimensional wind turbine application. The last application is the time-domain turbulent flow analysis of a vertical axis wind turbine (VAWT), where simulations with and without LSP technology have been performed to the aim of demonstrating the enhanced accuracy achieved by the LSP solver for this particular problem, the necessity of applying the full preconditioning strategy, the important effect of the turbulent kinetic energy on the solution accuracy and the proper implementation of the preconditioning parameter required for an accurate numerical solution to an unsteady moving grid low-speed problem.

The conclusions of the thesis and future work are provided in Chapter 8 - *Conclusion*.

# Chapter 2

## Governing Equations

This chapter outlines the derivation of the differential conservative form of the Unsteady Reynolds-Averaged Navier-Stokes (URANS) equations in a Cartesian reference system. This derivation is a multi-stage process. First the time-dependent equations are averaged on the turbulence time-scales. This results in a new system of Partial Differential Equations (PDEs), which differs from the original time-dependent equations for two reasons: *a*) the new system does no longer have time-derivatives, so it can be used for the numerical solution of steady turbulent flows, and *b*) the new system has additional unknown terms which form the components of a second order tensor, called Reynolds stress tensor. Making use of the Boussinesq approximation and the two-equation turbulence model, such a tensor is assumed to have the same structure as the molecular stress tensor. More precisely, the main part of the Reynolds stress tensor is taken to be proportional to the strain rate tensor through an eddy viscosity parameter  $\mu_T$ . In the Shear Stress Transport (SST) turbulence model considered in this thesis, this parameter, the value of which depends on the position in the computational domain, is determined by the local values of the turbulent kinetic energy  $k$  and the specific dissipation rate  $\omega$ . These two variables are obtained by solving two additional transport equations, one for turbulent kinetic energy  $k$  and the other for  $\omega$ .

The solution of steady turbulent problems is obtained by solving the system of PDE's made up of the Navier-Stokes equations averaged on the turbulence time-scales (i.e. Reynolds Averaged Navier-Stokes (RANS) equations) and the two PDE's associated with the turbulence model. Time-dependent turbulent flows can instead be solved by adding to each RANS PDE and to each PDE of the turbulence model a suitable time-derivative, which refers to time-variations taking place on the characteristic time-scales associated with engineering problem at hand. For example, the main temporal scales in vibrating body problems are the period of the vibration and, possibly, the frequency of vortex shedding. One of the advantages of differential turbulence models over simple algebraic models, is that the former ones allow inertial (time-dependent) and global (through the spatial derivatives of the turbulence model) effects to be taken into account when modelling the effects of turbulence.

## 2.1 Differential conservative form of the time-dependent Navier-Stokes equations

The integral form of the Arbitrary Lagrangian Eulerian (ALE) formulation of the governing equations is also presented in the chapter, which is the fundamental part of the finite volume algorithm used by our research code COSA for problems with moving grids. The chapter is concluded by performing the derivation of the harmonic balance formulation of the governing equations, the great benefits of which, saving computational time and maintain good accuracy, will be demonstrated in Chapter 7 by comparing results with those obtained by time-domain approach.

## 2.1 Differential conservative form of the time-dependent Navier-Stokes equations

The dimensional forms of the PDEs expressing the conservation of mass, momentum and energy of a compressible flow in a three-dimensional Cartesian system are respectively (the *Newtonian* convention of summation over repeated indices is adopted in all the equations presented herein, and a two-dimensional system can be easily obtained by removing the components related to the third direction in each equation):

$$\frac{\partial \rho}{\partial t} + \frac{\partial}{\partial x_j}(\rho u_j) = 0 \quad (2.1)$$

$$\frac{\partial}{\partial t}(\rho u_i) + \frac{\partial}{\partial x_j}(\rho u_j u_i) = -\frac{\partial p}{\partial x_i} + \frac{\partial \tau_{ji}}{\partial x_j} \quad i, j = 1, 2, 3 \quad (2.2)$$

$$\frac{\partial}{\partial t}(\rho E) + \frac{\partial}{\partial x_j}(\rho u_j H) = \frac{\partial}{\partial x_j}[u_i \tau_{ij} - q_j] \quad (2.3)$$

where  $u_{i(j)}$  denotes the Cartesian component of the flow velocity in the direction  $i(j)$ ,  $\rho$  is the fluid density,  $p$  is the thermodynamic pressure,  $E$  is the total energy per unit mass, and  $H$  is the total enthalpy per unit mass. The definitions of  $E$  and  $H$  are respectively:

$$E = e + \frac{u_i u_i}{2}, \quad H = h + \frac{u_i u_i}{2} \quad (2.4)$$

where  $e$  is the internal energy per unit mass (for a calorically perfect gas  $e = c_v T$  with  $T$  being the temperature and  $c_v$  being the specific heat at constant volume), and  $h$  is the static

## 2.1 Differential conservative form of the time-dependent Navier-Stokes equations

enthalpy per unit mass (for a calorically perfect gas  $h = c_p T = e + \frac{p}{\rho}$  with  $c_p$  being the specific heat at constant pressure). The symbol  $\tau_{ij}$  denotes the generic component of the molecular stress tensor. For a Newtonian fluid, its expression is:

$$\tau_{ij} = 2\mu \left[ S_{ij} - \frac{1}{3} \frac{\partial u_k}{\partial x_k} \delta_{ij} \right], \quad S_{ij} = \frac{1}{2} \left[ \frac{\partial u_i}{\partial x_j} + \frac{\partial u_j}{\partial x_i} \right] \quad (2.5)$$

where  $\mu$  is the molecular dynamic viscosity,  $S_{ij}$  is the generic component of the strain rate tensor, and  $\delta_{ij}$  is the Kronecker Delta Function. Sutherland's Law is used to compute  $\mu$ :

$$\mu = \mu_{ref} \left( \frac{T}{T_{ref}} \right)^{\frac{3}{2}} \frac{T_{ref} + S}{T + S} \quad (2.6)$$

where  $\mu_{ref} = 1.716 \cdot 10^{-5} kg \ m^{-1} s^{-1}$ ,  $T_{ref} = 273.15K$  and  $S = 110.4K$ .

The symbol  $q_j$  appearing in Eqn. (2.3) denotes the  $j^{th}$  Cartesian component of the heat flux vector. Its expression is defined by Fourier's law:

$$q_j = -\kappa \frac{\partial T}{\partial x_j} \quad (2.7)$$

in which  $\kappa$  is the thermal conductivity.

The system of PDE's defined so far and used to obtain the solution of three-dimensional problems has 6 unknowns, namely 3 velocity components and 3 thermodynamic variables. The missing condition is an equation of state. For a perfect gas, such an equation is  $p = \rho RT$ .

## 2.2 Differential conservative form of the URANS and Menter's Shear Stress Transport (SST) turbulence model equations

The CFD research code, COSA, adopted in all the simulations appearing in this thesis features both the  $k - \omega$  turbulence model proposed by Wilcox (1988) and  $k - \omega$  Shear Stress Transport (SST) model of Menter (1994), however, we have only focused on the analysis of the latter model, and its different kinds of formulations. The SST model is introduced along

## 2.2 Differential conservative form of the URANS and SST turbulence model equations

with another two-equation turbulence model called Baseline (BSL) model, which is based on the original  $k - \omega$  model and the  $k - \epsilon$  model (Jones and Launder, 1973) with replacing the variable  $\epsilon$  associated with the turbulent energy dissipation rate with the variable  $\omega = \epsilon/k$  associated with the specific dissipation rate of turbulent kinetic energy. In the near wall region the BSL model uses the robust and fairly accurate  $k - \omega$  model, while gradually transits to the standard  $k - \epsilon$  model outside the boundary layer. The advantage of using the  $k - \epsilon$  model outside shear layers lies in the fact that it is substantially less sensitive to the freestream turbulence data,  $\omega$  for example, than the  $k - \omega$  model, whereas the  $k - \omega$  model shows a more accurate predictive capability of flow characteristics in boundary layers than the  $k - \epsilon$  model. For free shear layers the new BSL model performs equally well with the  $k - \epsilon$  model. On the basis of the BSL model, Menter modified the definition of the turbulent eddy viscosity and one constant ( $\sigma_{K1}$ ), yielding the so-called SST model which is based on Bradshaw's assumption that the principal shear-stress is linearly proportional to the turbulent kinetic energy. Such a model has achieved further improvements with respect to the BSL model, particularly when predicting the separated flows in adverse pressure gradient. In terms of the comparison with the original  $k - \omega$  model, the SST model has greatly reduced the sensitivity to the somewhat arbitrary value of the specific dissipation rate enforced at the farfield boundaries of the computational domain, and enhanced the solution accuracy of turbulent flows by improving the capability of the  $k - \omega$  model to predict the onset and amount of separation in adverse pressure flows. The numerical results of Menter (1994) and later comparative analyses performed for internal (Koubogiannis et al., 2003) and external (Ekaterinaris and Menter, 1994) turbulent flows highlight that the SST model achieves both objectives. Other extensions of the original  $k - \omega$  model aiming to achieve the same objectives have also been developed by Wilcox (2008). One-equation eddy viscosity turbulence models (Spalart and Allmaras, 1994) require the solution of only one transport equation. Historically, the development of one-equation models has followed that of two-equation models, and its main motivation has been to reduce the computational cost associated with two-equation models while limiting the accuracy loss with respect to flow simulations based on two-equation models. Several comparative analyses of realistic turbulent flow problems using both one- and two-equation turbulence modelling highlight that, though the results of modern two-equation models often appear to be closer to experimental data, the solution differences between one- and two-equation models are indeed often small. A wider review of turbulence modelling is beyond the scope of this thesis, and

## 2.2 Differential conservative form of the URANS and SST turbulence model equations

the interested reader is referred to the review article (Spalart, 2000) for a wider overview of the present state, challenges and needs of turbulence modelling for engineering applications, and long term projections for the progress in this area.

The URANS equations in dimensional form are:

$$\frac{\partial \bar{\rho}}{\partial t} + \frac{\partial}{\partial x_j} (\bar{\rho} \overline{u_j}) = 0 \quad (2.8)$$

$$\frac{\partial}{\partial t} (\bar{\rho} \overline{u_i}) + \frac{\partial}{\partial x_j} (\bar{\rho} \overline{u_j u_i}) = -\frac{\partial \bar{p}}{\partial x_i} + \frac{\partial \hat{\tau}_{ij}}{\partial x_j} \quad (2.9)$$

$$\frac{\partial}{\partial t} (\bar{\rho} \overline{E}) + \frac{\partial}{\partial x_j} (\bar{\rho} \overline{u_j H}) = \frac{\partial}{\partial x_j} \left[ \overline{u_i \hat{\tau}_{ij}} + (\mu + \sigma_k \mu_T) \frac{\partial \bar{k}}{\partial x_j} - \hat{q}_j \right] \quad (2.10)$$

The system of Eqn. (2.8), (2.9) and (2.10) is formally identical to the system of Eqn. (2.1), (2.2) and (2.3) except for three main features: **a)** all the variables appearing in the URANS equations are time-averaged over the turbulence time-scales and denoted with symbol overbar, and for brevity, the author has dropped the symbols for all other variables in the rest of thesis; **b)** the molecular stress tensor  $\tau_{ij}$  has been replaced by the stress tensor  $\hat{\tau}_{ij}$ , the molecular heat flux vector  $q_j$  has been replaced by the heat flux vector  $\hat{q}_j$ ; **c)** there is an additional diffusive term in the energy equation depending on the eddy viscosity  $\mu_T$  and the components of the gradient of the turbulent kinetic energy  $k$ , and the symbol  $\sigma_k$  in the energy equation denotes one of the constants of the *SST* model.

The stress tensor  $\hat{\tau}_{ij}$  is the sum of the laminar stress tensor  $\tau_{ij}$  and the Reynolds stress tensor  $\tau_{ij}^R$ . Thus

$$\hat{\tau}_{ij} = \tau_{ij} + \tau_{ij}^R \quad (2.11)$$

where the formal definition of the molecular stress tensor  $\tau_{ij}$  is provided by Eqn. (2.5), and

$$\tau_{ij}^R = 2\mu_T \left[ S_{ij} - \frac{1}{3} \frac{\partial u_k}{\partial x_k} \delta_{ij} \right] - \frac{2}{3} \rho k \delta_{ij} \quad (2.12)$$

The formal definition of the strain rate tensor  $S_{ij}$  is the same as in the molecular stress tensor.

The generic component  $\hat{q}_j$  of the heat flux vector results from the sum of a laminar and turbulent contribution. Noting that molecular viscosity, constant pressure specific heat and

## 2.2 Differential conservative form of the URANS and SST turbulence model equations

thermal conductivity are linked by the Prandtl number  $Pr = \frac{\mu c_p}{k}$ , the component  $\hat{q}_j$  can be written as:

$$\hat{q}_j = - \left[ \frac{\mu}{Pr} + \frac{\mu_T}{Pr_T} \right] \frac{\partial h}{\partial x_j} \quad (2.13)$$

$Pr_T$  is the turbulent Prandtl number, relating the turbulent viscosity and the turbulent counterpart of the molecular thermal conductivity.

It should be noted that in the URANS case one can include the turbulent kinetic energy  $k$  in the definition of the total energy and the total enthalpy. By doing so, the definitions of these two variables becomes respectively:

$$E = e + \frac{u_i u_i}{2} + k, \quad H = h + \frac{u_i u_i}{2} + k \quad (2.14)$$

In the case of a perfect gas, the internal energy  $e$  is defined as

$$c_v T = \frac{RT}{\gamma - 1} = \frac{p}{\rho(\gamma - 1)}$$

which implies that the static pressure  $p$  is defined as:

$$p = (\gamma - 1) \left[ \rho E - \frac{1}{2} \rho (u_i u_i) - \rho k \right] \quad (2.15)$$

To be noted that, although  $\gamma$  is the ratio between the specific heat at constant pressure and specific heat at constant volume and can be a function of  $T$  and  $p$  in a general case, however for the calorically perfect gas considered in this thesis, the heat capacity can be treated as constant yielding a constant value of  $\gamma$  equal to 1.4.

It can be seen that the URANS equations contain two additional variables with respect to the non-averaged NS equations, namely the eddy viscosity  $\mu_T$  and the turbulent kinetic energy  $k$ . These two variable establish a strong coupling with the 2 PDEs associated with the SST turbulence model, which, as shown in Chapter 5, requires one to apply the preconditioning method to both RANS and turbulence equations in a rigorous mathematical point of view.

The SST turbulence model consists of two transport equations, one for the turbulent kinetic energy  $k$ , the other for the specific dissipation rate  $\omega$ . These two equations are respectively:

$$\frac{\partial}{\partial t} (\rho k) + \frac{\partial}{\partial x_j} (\rho u_j k) = \tau_{ij}^R \frac{\partial u_i}{\partial x_j} - \beta^* \rho \omega k + \frac{\partial}{\partial x_j} \left[ (\mu + \sigma_k \mu_T) \frac{\partial k}{\partial x_j} \right] \quad (2.16)$$

## 2.2 Differential conservative form of the URANS and SST turbulence model equations

$$\begin{aligned} \frac{\partial}{\partial t}(\rho\omega) + \frac{\partial}{\partial x_j}(\rho u_j \omega) \\ = \frac{\gamma}{\nu_t} \tau_{ij}^R \frac{\partial u_i}{\partial x_j} - \beta \rho \omega^2 + \frac{\partial}{\partial x_j} \left[ (\mu + \sigma_\omega \mu_T) \frac{\partial \omega}{\partial x_j} \right] + CD_{term} \end{aligned} \quad (2.17)$$

where  $CD_{term} = 2\rho(1 - F_1)\sigma_{\omega 2} \frac{1}{\omega} \frac{\partial k}{\partial x_j} \frac{\partial \omega}{\partial x_j}$ .

In Eqn. (2.16), the term  $\tau_{ij}^R \frac{\partial u_i}{\partial x_j}$  leads to the production of the turbulent kinetic energy, and the term  $\beta^* \rho \omega k$  leads to its destruction, whereas in Eqn. (2.17), the term  $\frac{\gamma\rho}{\mu_T} \tau_{ij}^R \frac{\partial u_i}{\partial x_j}$  leads to the production of the specific dissipation rate and the term  $\beta \rho \omega^2$  leads to destruction of the same variable, which are all called the source terms  $\hat{S}$ . Diffusion of the turbulent kinetic energy and the specific dissipation rate are instead enforced by the term  $\frac{\partial}{\partial x_j} \left[ (\mu + \sigma_k \mu_T) \frac{\partial k}{\partial x_j} \right]$  and  $\frac{\partial}{\partial x_j} \left[ (\mu + \sigma_\omega \mu_T) \frac{\partial \omega}{\partial x_j} \right]$ . The turbulent source terms can thus be summarised as,

$$P_k = \tau_{ij}^R \frac{\partial u_i}{\partial x_j}, \quad P_\omega = \frac{\gamma\rho}{\mu_T} \tau_{ij}^R \frac{\partial u_i}{\partial x_j} \quad (2.18)$$

$$D_k = \beta^* \rho \omega k, \quad D_\omega = \beta \rho \omega^2 \quad (2.19)$$

The production terms  $P_k$  and  $P_\omega$  can be also expressed as,

$$P_k = \mu_T P_d - \frac{2}{3} (\nabla \cdot u) \rho k \quad (2.20)$$

$$P_\omega = \gamma \rho P_d - \frac{\gamma \rho}{\mu_T} \frac{2}{3} (\nabla \cdot u) \rho k \quad (2.21)$$

$$P_d = 2 \left( \underline{\underline{S}} - \frac{1}{3} \nabla \cdot u \right) \nabla u \quad (2.22)$$

Since it can be proved that the term  $P_d$  is always positive, the source terms of the turbulent kinetic energy  $k$  – equation and the specific dissipation rate  $\omega$  – equation both feature a term which is always positive (production terms proportional to  $P_d$ ), a term which is always negative (destruction terms  $D_k$  and  $D_\omega$ ) and a term which is either positive or negative depending on the sign of  $\nabla \cdot u$ . Moreover, the source term of the  $\omega$  – equation includes the

## 2.2 Differential conservative form of the URANS and SST turbulence model equations

additional cross-diffusion term  $CD_{term}$  compared with the corresponding source term in the original  $k - \omega$  model, and it can be either positive or negative. As demonstrated in previous studies (Liu and Zheng, 1996, Lin and Sotiropoulos, 1997), the identification of positive and negative source terms is crucially important to the numerical integration of the  $k - \omega$  turbulence model equations. Particularly in terms of applying numerical acceleration techniques such as the explicit multigrid method, the different adoptions of the treatments for the positive and negative turbulent source terms may have various effects on the improvement of the convergence rate of the solution process. More detailed analyses can be found in Chapter 3 and Chapter 5.

The definition of the eddy viscosity  $\mu_T$  in the SST turbulence model is :

$$\mu_T = \frac{\alpha_1 \rho k}{\max(\alpha_1 \omega, \Omega F_2)} \quad (2.23)$$

where  $\alpha_1$  is a constant and  $\Omega$  is the modulus of the vorticity. The variables  $F_1$  and  $F_2$  are blending functions used to combine the  $k - \epsilon$  and  $k - \omega$  models, defined as:

$$F_1 = \tanh(\arg_1^4) \quad (2.24)$$

$$\arg_1^4 = \min \left[ \max \left( \frac{\sqrt{k}}{\beta^* \omega d}, \frac{500 \mu}{\rho \omega d^2} \right), \frac{4 \rho \sigma_{\omega 2} k}{CD_{K\omega} d^2} \right] \quad (2.25)$$

$$CD_{K\omega} = \max \left( 2 \rho \sigma_{\omega 2} \frac{1}{\omega} \frac{\partial k}{\partial x_j} \frac{\partial \omega}{\partial x_j}, 10^{-20} \right) \quad (2.26)$$

$$F_2 = \tanh(\arg_2^2) \quad (2.27)$$

$$\arg_2 = \max \left( \frac{2\sqrt{k}}{\beta^* \omega d}, \frac{500 \mu}{\rho \omega d^2} \right) \quad (2.28)$$

where  $d$  is the distance to the nearest wall.

In order to complete the definition of the SST turbulence model, the turbulent coefficients have to be specified. The final coefficients implemented in the model are defined by the combination of two groups of coefficients using the blending function  $\Phi$ . The constants of the

## 2.2 Differential conservative form of the URANS and SST turbulence model equations

first group are  $\beta_1, \sigma_{k1}, \sigma_{\omega 1}$  and  $\gamma_1$ , and  $\beta_2, \sigma_{k2}, \sigma_{\omega 2}$  and  $\gamma_2$  for the second group, shown in Eqn. (2.29) and (2.30) as below.

$$\text{group 1: } [\beta_1, \sigma_{k1}, \sigma_{\omega 1}, \gamma_1] = [0.0750, 0.85, 0.500, 0.55317] \quad (2.29)$$

$$\text{group 2: } [\beta_2, \sigma_{k2}, \sigma_{\omega 2}, \gamma_2] = [0.0828, 1.00, 0.856, 0.44035] \quad (2.30)$$

Other coefficients used by the model are  $\beta^* = 0.09$ ,  $\kappa = 0.41$  and  $\alpha_1 = 0.31$ . Some of the above coefficients have been optimised and are different from their originally proposed values based on the numerical test. The equation used to calculate the coefficients  $\gamma_1$  and  $\gamma_2$  is:

$$\gamma_1 = \frac{\beta_1}{\beta^*} - \frac{\sigma_{\omega 1} \kappa^2}{\sqrt{\beta^*}}, \quad \gamma_2 = \frac{\beta_2}{\beta^*} - \frac{\sigma_{\omega 2} \kappa^2}{\sqrt{\beta^*}} \quad (2.31)$$

Using the blending function  $\Phi$  defined by equation (2.32), one can compute the coefficients  $\beta$ ,  $\sigma_k$ ,  $\sigma_\omega$  and  $\gamma$  for any area of the computational domain

$$\Phi = F_1 \Phi_1 + (1 - F_1) \Phi_2 \quad (2.32)$$

## 2.3 Integral form of the URANS and Shear Stress Transport (SST) turbulence model equations

The URANS equations (2.8), (2.9) and (2.10) and the turbulence model equations (2.16) and (2.17) can be written in a compact vector form as follows:

$$\frac{\partial \mathbf{U}}{\partial t} + \frac{\partial (\mathbf{E}_c - \mathbf{E}_d)}{\partial x} + \frac{\partial (\mathbf{F}_c - \mathbf{F}_d)}{\partial y} = \mathbf{S} \quad (2.33)$$

where the array  $\mathbf{U}$  collects the conservative flow variables of all transport equations, the arrays  $\mathbf{E}_c$  and  $\mathbf{F}_c$  collect respectively the  $x$ - and  $y$ - components of the convective fluxes of all equations, the arrays  $\mathbf{E}_d$  and  $\mathbf{F}_d$  collect respectively the  $x$ - and  $y$ - components of the diffusive fluxes of all equations, and the array  $\mathbf{S}$  contains the turbulent source terms of the SST equations. The definitions of the arrays  $\mathbf{U}$ ,  $\mathbf{E}_c$  and  $\mathbf{F}_c$  are respectively:

### 2.3 Integral form of the URANS and SST turbulence model equations

$$\mathbf{U} = \begin{bmatrix} \rho \\ \rho u \\ \rho v \\ \rho E \\ \rho k \\ \rho \omega \end{bmatrix}, \quad \mathbf{E}_c = \begin{bmatrix} \rho u \\ \rho u^2 + p \\ \rho uv \\ \rho uE \\ \rho uk \\ \rho u\omega \end{bmatrix}, \quad \mathbf{F}_c = \begin{bmatrix} \rho v \\ \rho vu \\ \rho v^2 + p \\ \rho vE \\ \rho vk \\ \rho v\omega \end{bmatrix} \quad (2.34)$$

where the total energy  $E$  and the total enthalpy  $H$  are defined by Eqn. (2.14). The definitions of the diffusive flux vectors  $\mathbf{E}_d$  and  $\mathbf{F}_d$  are respectively:

$$\mathbf{E}_d = \begin{bmatrix} 0 \\ \tau_{xx} \\ \tau_{xy} \\ u\tau_{xx} + v\tau_{xy} + (\mu + \sigma_k \mu_T) \frac{\partial k}{\partial x} - q_x \\ (\mu + \sigma_k \mu_T) \frac{\partial k}{\partial x} \\ (\mu + \sigma_\omega \mu_T) \frac{\partial \omega}{\partial x} \end{bmatrix} \quad (2.35)$$

$$\mathbf{F}_d = \begin{bmatrix} 0 \\ \tau_{xy} \\ \tau_{yy} \\ u\tau_{xy} + v\tau_{yy} + (\mu + \sigma_k \mu_T) \frac{\partial k}{\partial y} - q_y \\ (\mu + \sigma_k \mu_T) \frac{\partial k}{\partial y} \\ (\mu + \sigma_\omega \mu_T) \frac{\partial \omega}{\partial y} \end{bmatrix} \quad (2.36)$$

The definition of the array  $\mathbf{S}$  is:

$$\mathbf{S} = \begin{bmatrix} 0 \\ 0 \\ 0 \\ 0 \\ P_k - D_k \\ P_\omega - D_\omega + CD_{term} \end{bmatrix} \quad (2.37)$$

where the expressions of all the source terms have been given in Eqns. (2.18) and (2.19).

The integral formulation of the differential divergence form of the conservation laws expressed by system (2.33) is obtained by applying the divergence theorem. Given a fixed control volume  $\mathcal{C}$  with boundary  $S$ , the integral form of the 2D time-dependent RANS equations coupled to the two transport equations of the SST turbulence model is:

$$\frac{\partial}{\partial t} \left( \int_{\mathcal{C}} \mathbf{U} d\mathcal{C} \right) + \oint_S (\hat{\Phi}_c - \hat{\Phi}_d) \cdot d\hat{S} = \int_{\mathcal{C}} \mathbf{S} d\mathcal{C} \quad (2.38)$$

The generalised convective flux vector  $\hat{\Phi}_c$  is

$$\hat{\Phi}_c = \mathbf{E}_c \hat{i} + \mathbf{F}_c \hat{j} \quad (2.39)$$

The generalised diffusive flux vector  $\hat{\Phi}_d$  is

$$\hat{\Phi}_d = \mathbf{E}_d \hat{i} + \mathbf{F}_d \hat{j} \quad (2.40)$$

## 2.4 Arbitrary Lagrangian/Eulerian Integral form of the URANS and Shear Stress Transport (SST) turbulence model equations

Given a time-varying control volume  $\mathcal{C}(t)$  with boundary  $S(t)$ , the Arbitrary Lagrangian-Eulerian integral form of the 2D time-dependent RANS equations coupled to the two transport equations of the SST turbulence model is:

$$\frac{\partial}{\partial t} \left( \int_{\mathcal{C}(t)} \mathbf{U} d\mathcal{C} \right) + \oint_{S(t)} (\hat{\Phi}_c - \hat{\Phi}_d) \cdot d\hat{S} = \int_{\mathcal{C}(t)} \mathbf{S} d\mathcal{C} \quad (2.41)$$

The generalised convective flux vector  $\hat{\Phi}_c$  is:

$$\hat{\Phi}_c = \mathbf{E}_c \hat{i} + \mathbf{F}_c \hat{j} - \hat{v}_b \mathbf{U} \quad (2.42)$$

where the vector  $\hat{v}_b$  is the velocity of the boundary  $S$ , and the flux term  $-\hat{v}_b \mathbf{U}$  is its contribution to the overall flux balance, which is nonzero only in the case of unsteady problems with moving boundaries. In the case of time-varying control volumes, the generalised diffusive flux vector  $\hat{\Phi}_d$  has the same expression of that associated with the case of the motionless control volume, and is thus given by Eqn. (2.40).

## 2.5 Harmonic balance form of URANS and Shear Stress Transport (SST) turbulence model equations

The Harmonic Balance formulation of the RANS equations assumes that the fundamental frequency  $\omega$  of the sought periodic flow field is known. Representing the volume and surface integral of the RANS and turbulence equations (2.41) by  $\mathbf{u}$  and  $\mathbf{h}$  respectively, one can approximate these two variables by means of the truncated Fourier series below:

$$\mathbf{u}(t) \approx \hat{\mathbf{u}}_0 + \sum_{n=1}^{N_H} (\hat{\mathbf{u}}_{2n-1} \cos(\omega nt) + \hat{\mathbf{u}}_{2n} \sin(\omega nt)) \quad (2.43)$$

$$\mathbf{h}(t) \approx \hat{\mathbf{h}}_0 + \sum_{n=1}^{N_H} (\hat{\mathbf{h}}_{2n-1} \cos(\omega nt) + \hat{\mathbf{h}}_{2n} \sin(\omega nt)) \quad (2.44)$$

The time-derivative of  $\mathbf{u}$  is approximated as:

$$\frac{\partial \mathbf{u}(t)}{\partial t} = \sum_{n=1}^{N_H} n\omega (-\hat{\mathbf{u}}_{2n-1} \sin(\omega nt) + \hat{\mathbf{u}}_{2n} \cos(\omega nt)) \quad (2.45)$$

Note the arrays  $\hat{\mathbf{u}}_n$  and  $\hat{\mathbf{h}}_n$  appearing in equations (2.43), (2.44) and (2.45) have length  $N_{PDE}$  and represent respectively the real and imaginary parts of the complex harmonics of the volume and surface integrals of the system of RANS and SST equations, where  $N_{PDE}$  is the number of considered conservation laws. In the case of 2D RANS equations coupled to the SST model equations,  $N_{PDE}$  is equal to 6. Inserting the expressions (2.44) and (2.45) into ALE form of equation (2.41) and balancing harmonics to the same order results in a system of  $N_T = N_{PDE} \times (2N_H + 1)$  equations, which can be expressed as

$$\omega A \hat{\mathbf{u}} + \hat{\mathbf{h}} = 0 \quad (2.46)$$

where  $\hat{\mathbf{u}} = [\hat{u}'_0 \ \hat{u}'_1 \ \dots \ \hat{u}'_{2N_H}]'$ ,  $\hat{\mathbf{h}} = [\hat{h}'_0 \ \hat{h}'_1 \ \dots \ \hat{h}'_{2N_H}]'$  and the superscript  $'$  denotes the transpose operator. The symbol  $A$  denotes a  $N_T \times N_T$  matrix, and it can be expressed as below,

## 2.5 Harmonic balance form of URANS and SST turbulence model equations

$$A = \begin{bmatrix} J_0 & & & & \\ & J_1 & & & \\ & & J_2 & & \\ & & & \dots & \\ & & & & J_{N_H} \end{bmatrix}, J_n = I_{N_{PDE}} \otimes n \begin{bmatrix} 0 & 1 \\ -1 & 0 \end{bmatrix}, n = 0, 1, \dots, N_H \quad (2.47)$$

where the symbol  $\otimes$  denotes the Kronecker tensor product,  $I_{N_{PDE}}$  denotes the identity matrix of size  $(N_{PDE}^2)$ , and blocks  $J_n$  have size  $(2N_{PDE})^2$ . Writing explicitly the equations of the system in Eqn. (2.46), one finds that the unknown harmonic components  $\hat{\mathbf{u}}$  are coupled by the harmonic residuals  $\hat{\mathbf{h}}$ , whereas no coupling occurs through the first term of the equation, since matrix  $A$  is block diagonal. As pointed out by Hall et al. (2002), the computational cost of the HB system in Eqn. (2.46) grows superlinearly with the number of retained harmonics  $N_H$ , and the analytical derivation of the equations becomes extremely complex when dealing with the turbulence models required for high Reynolds number flows. To alleviate these problems, it has been noted that an alternative formulation of the HB equations is obtained by reconstructing the Fourier coefficients of the volume integral  $\hat{\mathbf{u}}$  of the conservation variables and the surface integral  $\hat{\mathbf{h}}$  of the fluxes to become the  $2N_H + 1$  equally spaced snapshots of the sought periodic flow field with period  $T = \frac{2\pi}{\omega}$ . The array  $\tilde{\mathbf{u}}$  containing the snapshots of the volume integral and the array  $\tilde{\mathbf{h}}$  containing the snapshots of the surface integral are given respectively by:

$$\tilde{\mathbf{u}} = \begin{Bmatrix} \mathbf{u}(t_0 + \Delta t) \\ \mathbf{u}(t_0 + 2\Delta t) \\ \vdots \\ \mathbf{u}(t_0 + T) \end{Bmatrix}, \quad \tilde{\mathbf{h}} = \begin{Bmatrix} \mathbf{h}(t_0 + \Delta t) \\ \mathbf{h}(t_0 + 2\Delta t) \\ \vdots \\ \mathbf{h}(t_0 + T) \end{Bmatrix} \quad (2.48)$$

where  $\Delta t = \frac{2\pi}{(2N_H+1)\omega}$ . Through a Fourier matrix  $E^{-1}$ , one can relate the Fourier harmonics with the snapshots shown above,

$$\tilde{\mathbf{u}} = E^{-1} \hat{\mathbf{u}} \quad (2.49)$$

$$\tilde{\mathbf{h}} = E^{-1} \hat{\mathbf{h}} \quad (2.50)$$

Substituting the terms  $\hat{\mathbf{u}}$  and  $\hat{\mathbf{h}}$  in equations (2.46) with the above two expressions yields,

## 2.5 Harmonic balance form of URANS and SST turbulence model equations

$$\omega A E \tilde{\mathbf{u}} + E \tilde{\mathbf{h}} = 0 \quad (2.51)$$

Pre-multiplying the whole equation by the transformation matrix  $E^{-1}$  yields the system,

$$\omega D \tilde{\mathbf{u}} + \tilde{\mathbf{h}} = 0 \quad (2.52)$$

where

$$D = E^{-1} A E \quad (2.53)$$

Inserting the integral definitions of  $\tilde{\mathbf{u}}$  and  $\tilde{\mathbf{h}}$  into equation (2.52) gives the high-dimensional harmonic balance formulation of the RANS and turbulence equations:

$$\omega D \left( \int_{V(t)} \hat{U}_H dV \right) + \oint_{S(t)} (\hat{\Phi}_{c_H} - \hat{\Phi}_{d_H}) dS = \int_{V(t)} \hat{S}_H dV \quad (2.54)$$

where the unknown array  $\hat{U}_H$  is made up of  $2N_H + 1$  flow field snapshots, referring to the equally spaced points of one period:

$$t_n = \frac{n}{(2N_H + 1)} \frac{2\pi}{\omega}, \quad n = 0, 1, \dots, 2N_H \quad (2.55)$$

$$\hat{U}_H = [\hat{U}(t_0), \hat{U}(t_1), \hat{U}(t_2), \dots, \hat{U}(t_{2N_H-1}), \hat{U}(t_{2N_H})]^T \quad (2.56)$$

$$\hat{\Phi}_{c_H} = [\hat{\Phi}_{c_H}(t_0), \hat{\Phi}_{c_H}(t_1), \hat{\Phi}_{c_H}(t_2), \dots, \hat{\Phi}_{c_H}(t_{2N_H-1}), \hat{\Phi}_{c_H}(t_{2N_H})]^T \quad (2.57)$$

Similar expressions hold for  $\hat{\Phi}_{d_H}$  and  $\hat{S}_H$ . As one can see the number of unknowns of the system has been increased from  $N_{PDE}$  to  $N_{PDE} \times (2N_H + 1)$ . Despite the fact that the number of PDE's to be solved has increased, the HB approach allows one to compute unsteady periodic flows at a lower computational cost with respect to the time-domain approach, and detailed analyses of the result will be shown in Chapter 7 of this thesis.

## 2.6 Quasi-linear form of URANS and Shear Stress Transport (SST) turbulence model equations

As shown in Chapter 3, the quasi-linear form of the governing equations is required in determining the eigenvalues and the eigenvectors of the system, and more importantly, in the procedure of implementing the low speed preconditioning reported in Chapter 5, the preconditioned numerical dissipation is also derived based on such kind of formulations. Therefore the 2D time-dependent RANS equations coupled to the two transport equations of the SST turbulence model is written in its quasi-linear form and shown as below:

$$\frac{\partial \hat{U}}{\partial t} + \frac{\partial(\hat{\Phi}_c - \hat{\Phi}_d)}{\partial \hat{U}} \nabla \hat{U} = \hat{S} \quad (2.58)$$

or explicitly,

$$\frac{\partial \hat{U}}{\partial t} + \hat{A} \frac{\partial \hat{U}}{\partial x} + \hat{B} \frac{\partial \hat{U}}{\partial y} = \hat{S} \quad (2.59)$$

where  $\hat{U}$ ,  $\hat{\Phi}_c$ ,  $\hat{\Phi}_d$  and  $\hat{S}$  can be found from equations (2.34), (2.39), (2.40) and (2.37). The symbols  $\hat{A}$  and  $\hat{B}$  are the Jacobian matrices of the flux vector  $\hat{\Phi}$  and they are defined as

$$\hat{A} = \frac{\partial(\hat{E}_c - \hat{E}_d)}{\partial \hat{U}}, \quad \hat{B} = \frac{\partial(\hat{F}_c - \hat{F}_d)}{\partial \hat{U}} \quad (2.60)$$

where  $\hat{E}_c$ ,  $\hat{E}_d$ ,  $\hat{F}_c$  and  $\hat{F}_d$  can be found from equations (2.34), (2.35) and (2.36) respectively.

# Chapter 3

## Solution of the RANS Equations

In seeking the solution to the RANS equations and the two shear stress transport equations used for the turbulence closure, a wide range of numerical methods are adopted in terms of different aspects. This chapter highlights the space discretisation, and the approaches adopted for the solution of the time-domain and the harmonic balance RANS equations by the CFD code adopted for the research work presented in the thesis. The detailed description of each algorithm has been provided focusing on the features which are affected by the LSP technologies developed in this research (see Chapter 5 for corresponding analyses with the LSP implementation).

### 3.1 Space discretisation

In regard to the PDEs of the RANS system and two equations of the SST turbulence model presented in Chapter 2, an analytical solution is rarely found to be plausible, thereby the system has to be solved numerically in general, whereby the space discretisation of the system of RANS and the SST equations is an important stage involved in obtaining the numerical solution. As one of the essential elements of the LSP implementation, this section primarily outlines the space-discretisation of the convective fluxes used to solve the governing equations in the framework of this research, which is performed using Van Leer's second order Monotone Upstream-centred Schemes for Conservation Laws (MUSCL) (Van Leer, 1977) extrapolations and Roe's flux-difference splitting (Van Leer, 1982), while the discretisation of the diffusive fluxes and the turbulent source terms is based on second order finite-differencing, which is described in (Campobasso et al., 2013).

The convective fluxes of Eqn. (2.38) are represented by the term

$$\Phi_{c,f} = (\hat{\Phi}_c \cdot \hat{n}) dS = (E_c n_x + F_c n_y) dS \quad (3.1)$$

where  $dS$  denotes the area of the face across which the flux is being computed, and  $n_x$  and  $n_y$  are respectively the  $x$  – and  $y$  – components of its outward normal vector  $\hat{n}$ . The

numerical estimation of the convective fluxes is performed by means of the flux difference splitting technique and Roe's averaging to compute the numerical dissipation. Using flux difference splitting, the numerical representation of the convective fluxes is:

$$\Phi_{c,f}^* = \frac{1}{2} \left[ \Phi_{c,f}(U_L) + \Phi_{c,f}(U_R) - \left| \frac{\partial \Phi_{c,f}}{\partial U} \right| \delta U \right] \quad (3.2)$$

Here the superscript  $\star$ , the subscript  $f$ , and the subscripts  $L$  and  $R$  denote numerical approximation, face value, and value extrapolated from the left and from the right, respectively. The numerical dissipation depends on the flow state discontinuity across the cell face, defined by  $\delta U = (U_R - U_L)$ , and the generalised flux Jacobian  $K_U$  is evaluated at the face under analysis:

$$(K_U)_f = \frac{\partial \Phi_{c,f}}{\partial U} = \left( \frac{\partial E_c}{\partial U} n_x + \frac{\partial F_c}{\partial U} n_y \right)_f = (An_x + Bn_y)_f \quad (3.3)$$

The symbols  $A$  and  $B$  denote respectively the flux Jacobians of the convective fluxes in the  $x$  – and  $y$  – direction. The subscript  $c$  of  $\Phi_{c,f}$  indicates that this Jacobian refers to the differential form of the conservation laws.

As highlighted by Eqn.(3.2) the numerical dissipation is proportional to  $K_U$ , and this term can also be written as:

$$\delta \Phi = |K_U| \delta U = P |\Lambda| P^{-1} \delta U = P |\Lambda| \delta W \quad (3.4)$$

where  $P$  is the matrix of right eigenvectors of  $K_U$  (more specifically the columns of  $P$  are the right eigenvectors of  $K_U$ ),  $\Lambda$  is the matrix of eigenvalues of  $K_U$  (more specifically  $\Lambda$  is diagonal and its nonzero entries are the eigenvalues of  $K_U$ ), and  $\delta W$  are the discontinuity of characteristic variables, defined by  $\delta W = P^{-1} \delta U$ . The symbol  $P^{-1}$  denotes the matrix of left eigenvectors of  $K_U$ : its rows are the left eigenvectors of  $K_U$ . Eqn.(3.4) highlights that the construction of the numerical dissipation only requires the calculation of the eigenvalues and the eigenvectors of  $K_U$ .

The construction of the numerical dissipation can be simplified by considering the convective terms of the RANS and turbulence equations obtained by writing the equations with respect to a new set of independent variables, namely the primitive variables  $V$  defined as:

$$V = \begin{bmatrix} \rho \\ u \\ v \\ p \\ K \\ \omega \end{bmatrix} \quad (3.5)$$

The aforementioned convective terms expressed with respect to the variables  $V$  are:

$$\tilde{A} \frac{\partial V}{\partial x} + \tilde{B} \frac{\partial V}{\partial y} \quad (3.6)$$

where the symbols  $\tilde{A}$  and  $\tilde{B}$  denote respectively the flux Jacobians of the convective fluxes with respect to the primitive variables in the  $x$  – and  $y$  – direction.

The process of constructing the required numerical dissipation can be simplified by considering the Jacobian  $K_U = \tilde{A}n_x + \tilde{B}n_y$ , and it can be easily shown that,

$$K_U = MK_V M^{-1} \quad (3.7)$$

where  $M$  is the Jacobian matrix of the transformation from primitive to conservative variables, and  $M^{-1}$  is its inverse. Eqn. (3.7) defines a similarity transformation from  $K_U$  to  $K_V$  and vice versa. The matrices  $K_U$  and  $K_V$  are similar, and this implies that they have the same eigenvalues and also that their eigenvectors are related through the transformation  $M$  as shown in the following. Inserting Eqn. (3.7) into Eqn. (3.4), one finds:

$$|K_U| \delta U = M |K_V| M^{-1} \delta U = ML|\Lambda|L^{-1}M^{-1} \delta U = ML|\Lambda|L^{-1} \delta V \quad (3.8)$$

where the columns of  $L$  are the right eigenvectors of  $K_V$ , and the rows of  $L^{-1}$  are the left eigenvectors of  $K_V$ . Comparing Equations (3.4) and (3.8) shows that

$$P = ML \quad (3.9)$$

and

$$\delta W = L^{-1} \delta V \quad (3.10)$$

Given that the calculation of the eigenmodes of  $K_V$  is simpler than the calculation of the eigenmodes of  $K_U$ , the matrix of right eigenvectors  $P$  and the variation of the characteristic variables appearing in Eqn. (3.4), are determined by means of Equations (3.9) and (3.10) respectively, namely by using the matrix of left eigenvalues  $L^{-1}$  and right eigenvectors  $L$ .

The eigenvalues of  $K_U$  and  $K_V$  can thus be determined as:

$$\begin{aligned}
\lambda_1 = \lambda_2 = \lambda_5 = \lambda_6 &= U_n \\
\lambda_3 &= U_n + c \\
\lambda_4 &= U_n - c
\end{aligned} \tag{3.11}$$

where  $U_n$  denotes the component of the flow velocity along the outward face normal vector  $\hat{n}$ ,

$U_n = un_x + vny$ . Eqn. (3.4) can also be written as

$$\delta\Phi = P|\Lambda|\delta\mathbf{W} = \sum_{k=1}^6 |\lambda_k| \delta W_k \mathbf{r}_k \tag{3.12}$$

where  $\delta W_k$  is the  $k^{th}$  component of  $\delta\mathbf{W}$  and  $\mathbf{r}_k$  is the  $k^{th}$  right eigenvector of  $K_U$ , which is also the  $K^{th}$  column of  $P$ .

### 3.1.1 moving grid problems

When dealing with moving-grid problems, the convective fluxes include the contribution associated with the velocity of the cell boundaries  $\hat{v}_b$ . In this circumstance, the array of convective fluxes  $\hat{\Phi}_c$  is given by Eqn. (2.42). The convective fluxes at the boundary of each cell become:

$$\Phi_{c,f} = (\hat{\Phi}_c \cdot \hat{n}) dS = (\mathbf{E}_c n_x + \mathbf{F}_c n_y - \mathbf{U} v_{bn}) dS \tag{3.13}$$

with

$$v_{bn} = \hat{v}_b \cdot \hat{n} \tag{3.14}$$

The expression of the numerical flux at each cell boundary is formally identical to Eqn. (3.2). The only practical differences are that *a*) the analytical fluxes  $\Phi_{c,f}(U_L)$  and  $\Phi_{c,f}(U_R)$  include the flux contribution associated with the boundary velocity, and *b*) the expression of the generalised flux Jacobian  $K_U'$  evaluated at the face under analysis becomes:

$$(K_U')_f = \frac{\partial \Phi_{c,f}}{\partial \mathbf{U}} = \left( \frac{\partial \mathbf{E}_c}{\partial \mathbf{U}} n_x + \frac{\partial \mathbf{F}_c}{\partial \mathbf{U}} n_y \right)_f - I v_{bn} = (K_U)_f - I v_{bn} \tag{3.15}$$

Since the operators  $(K_U')_f$  and  $(K_U)_f$  differ only by a diagonal term, their eigenvalues will differ by the constant offset  $v_{bn}$ , and the eigenvectors are also different due to the same term. More specifically, the eigenvalues of  $(K_U')_f$  are:

$$\begin{aligned}
\lambda_1 = \lambda_2 = \lambda_5 = \lambda_6 &= U_n - v_{bn} \\
\lambda_3 &= U_n - v_{bn} + c \\
\lambda_4 &= U_n - v_{bn} - c
\end{aligned}
\tag{3.16}$$

Consequently, the expression of the flux differences  $\delta\Phi$  for problems with moving grids is formally identical to expression (3.4), and the only difference with respect to problems with motionless grid is the appearance of the boundary velocity term in the eigenvalues of  $(K_U')_f$ .

N.B. Detailed expressions of all matrices and terms can be found in Appendix A.

## 3.2 Numerical integration

To solve numerically the large system of algebraic equations resulting from the space-discretisation of the mean flow and turbulence model equations, either explicit or implicit numerical integration scheme can be applied. As highlighted in the detailed review in Chapter 4 of advantages and disadvantages of both categories implemented with LSP, we would present herein the adopted standard (non-preconditioned) explicit multigrid integration strategy for solving the space-discretised RANS equations and the two equations of the SST turbulence model. Being treated as a single set of strongly coupled systems, the steady RANS equations and the two-turbulence equations are solved iteratively using the same multi-stage Runge-Kutta smoother. The system stiffness issues resulting from the presence of certain source terms in the turbulence equations are resolved by treating implicitly such source terms within the Runge-Kutta integration. General time-dependent flow problems are solved using the so-called dual-time-stepping approach, whereby the physical time-derivatives of the governing equations are discretised by means of second order backward finite-difference leading to a system of nonlinear equations for the flow field at each discrete physical time, and each single system can be treated as a steady problem using the same Runge-Kutta smoother for obtaining a sought steady solution. In cases of unsteady periodic flow problems, the high-dimensional harmonic balance formulation is employed, as this results in substantial reductions of run-times with respect to the case in which the time-domain equations are solved. The harmonic balance RANS and SST equations are solved using the same numerical integration strategy as in steady problems.

## 3.2.1 strongly coupled integration

The space-discretised governing equations will reduce to a set of non-linear ordinary differential equations in time, which can be solved by using the multistage scheme. However, special care must be taken for the time integration of the two turbulence equations. In case of the loosely coupled approach (Liu and Zheng, 1994), the mean flow equations and turbulence equations are marched separately in time, whereby the values of variables of *SST* equations (i.e.  $K$ ,  $\omega$ ,  $\mu_t$ ) are kept frozen while the Navier-Stokes equations are marched in time, and vice versa. More specifically, three evaluations of the viscous terms of the Navier-Stokes equations are performed within a five-stage time-stepping scheme, whereas the *SST* equations are only marched at the first, third and fifth stage when the viscous terms are evaluated for the Navier-Stokes equations. Accelerating techniques, such as multigrid and implicit residual smoothing, are only applied to the flow equations. As a consequence, the convergence of the *SST* equations is found to lag that of the Navier-Stokes equations, which has exerted a dramatically negative influence on the computational efficiency of the time marching scheme of the overall system.

To cope with the above issue, a strongly coupled solution strategy of the Navier–Stokes equations and the two-equation turbulence model equations becomes imperative and is anticipated to result in an improvement of the convergence rate. Therefore, Liu and Zheng (1996) and Lin and Sotiropoulos (1997) have suggested the so-called fully coupled integration method, whereby both the mean flow equations and the *SST* equations are marched in time simultaneously using the same multistage smoother, namely all the variables are updated within the same stage of time stepping and no ‘frozen’ treatment is required. With the equally applied multigrid and residual smoothing, the Navier-Stokes and turbulence model equations are solved as a single system of coupled equations.

In the following sections, a detailed description of the implementation of this strongly coupled integration into steady, time-dependent and harmonic balance problems will be provided, which would form the essential basis for the extension to LSP research.

## 3.2.2 steady problems

For steady problems the time-derivative appearing in Eqn. (2.41) vanishes, and space-discretising all remaining terms on a computational grid consisting of  $N_{cell}$  finite volumes leads to a system of nonlinear algebraic equations of the form:

$$\mathbf{R}_\phi(\mathbf{Q}) = 0 \quad (3.17)$$

The entries of the array  $\mathbf{Q}$  are the unknown flow variables at the  $N_{cell}$  cell centers, and the array  $\mathbf{Q}$  is made up of  $N_{cell}$  subarrays, each of which stores the  $N_{PDE}$  flow unknowns at a particular cell centre. The length of  $\mathbf{Q}$  is therefore  $(N_{PDE} \times N_{cell})$ . The array  $\mathbf{R}_\phi$  stores the cell residuals, and its structure is the same as that of  $\mathbf{Q}$ . For each cell, the  $N_{PDE}$  residuals are obtained by adding the convective fluxes and the diffusive fluxes through all its faces, and for the  $k$  and  $\omega$  residuals, by also adding the associated source terms evaluated at the cell centre.

The RANS and SST equations are solved with a fully coupled time marching algorithm whereby the two sets of equations are time marched simultaneously. The unknown flow vector  $\mathbf{Q}$  is computed by solving iteratively Eqn. (3.17). A fictitious time derivative ( $d\mathbf{Q}/d\tau$ ) premultiplied by the cell volumes is added to this system, which yields:

$$\mathbf{V} \frac{\partial \mathbf{Q}}{\partial \tau} + \mathbf{R}_\phi(\mathbf{Q}) = 0 \quad (3.18)$$

and this fictitious time derivative is then discretised with a four stage Runge-Kutta (RK) scheme. The numerical solution is thus marched in pseudo-time until the steady state is achieved. The convergence rate is enhanced by means of local time-stepping (LTS), variable-coefficient central implicit residual smoothing (IRS) and a full-approximation scheme (FAS) multigrid (MG) algorithm. When solving turbulent problems using a two-equation turbulence model, however, this explicit integration method has a very poor convergence rate, due to the operator stiffness caused by the large negative source terms of the turbulence model, such as  $-D_k$ ,  $-D_\omega$  and, when the velocity divergence is positive,  $-\nabla \cdot \hat{v}$ . To alleviate this problem, a semi-implicit integration strategy (Liu and Zheng, 1996) is adopted whereby the negative source terms of the turbulence equations are treated implicitly within each RK stage. Using this approach (see (Campobasso et al., 2013) for the detailed derivation), the semi-implicit turbulent smoother reads:

$$\begin{aligned}
W^0 &= Q_l \\
(I + \alpha_k \Delta \tau A) W^k &= W^0 + \alpha_k \Delta \tau A W^{k-1} - \alpha_k \Delta \tau V^{-1} L_{IRS} [R_\Phi(W^{k-1}) + f_{MG}] \quad (3.19) \\
Q_{l+1} &= W^{NS}
\end{aligned}$$

where  $\Delta \tau$  is the local pseudo-time-step,  $l$  is the RK cycle counter,  $k$  is the RK stage index, and  $\alpha_k$  is the  $k^{th}$  stage RK coefficient,  $L_{IRS}$  denotes the IRS operator, and  $f_{MG}$  is the MG forcing function, which is nonzero when the smoother (3.19) is used on a coarse level after a restriction step. The diagonal matrix  $V$  stores the volumes of the grid cells. It can be viewed as a block-diagonal matrix of size  $(N_{cell} \times N_{cell})$  with each block being the identity matrix of size  $(N_{PDE} \times N_{PDE})$  multiplied by the volume of the cell the block refers to. The matrix  $A$  is block-diagonal and has size  $(N_{cell} \times N_{cell})$ . The only nonzero elements of each  $(N_{PDE} \times N_{PDE})$  block  $A_i$  on the diagonal of  $A$  are those of the bottom right  $(2 \times 2)$  partition, and this occurrence results in the coupling of the update process of the turbulent variables. The abovesaid partition is:

$$A_i(5:6,5:6) = A_{SST} = \begin{bmatrix} \Delta^+ + \beta^* \omega & \beta^* k \\ \gamma \Delta^+ / \nu_T & 2\beta \omega \end{bmatrix} \quad (3.20)$$

in which  $\Delta^+ = \max\left(0, \frac{2}{3} \nabla \cdot \hat{v}\right)$ , all variables are evaluated at the RK stage  $k-1$ , and the subscript  $i$  identifies the grid cell the matrix block refers to. The cross-diffusion term  $CD_\omega$  can also be positive or negative depending on the local flow conditions, and therefore, when negative, it could be treated like  $\Delta^+$  in the semi-implicit integration. However, this approach would make the implementation substantially more complex and less efficient because the term  $CD_\omega$  depends on  $\nabla k$  and  $\nabla \omega$ . The evaluation of these gradients at stage  $k$  would couple the update process of several cells, thus requiring the inversion of significantly larger systems. For this reason, the integration we have adopted in this research treats the term  $CD_\omega$  explicitly regardless of its sign. It should be noted that this term is absent in the standard  $k - \omega$  model. Another difference between the semi-implicit integration of the standard  $k - \omega$  model and that of the SST model is that, in the former case,  $\rho \omega$  can be updated independently of  $\rho k$ . This is however not possible in the SST case, since  $A_{SST}(2,1)$  is not zero. Hence, a  $(2 \times 2)$  matrix inversion is required at each grid cell to update  $\rho k$  and  $\rho \omega$ . This difference arises from the fact that the expression of the turbulent viscosity of the former model is obtained by setting  $F_2 = 0$  in Eqn. (2.23). This operation results in the relationship  $k/\nu_T = \omega$ , which can be used to remove the dependence of the equation for updating  $\rho \omega$  on  $k$ . By performing this substitution, the bottom right partition of each block of  $A$  becomes:

$$A_i(5:6,5:6) = A_{K-\omega} = \begin{bmatrix} \Delta^+ + \beta^* \omega & \beta^* k \\ 0 & \gamma \Delta^+ + 2\beta \omega \end{bmatrix} \quad (3.21)$$

In general, when using the SST turbulence model, one would adopt Eqn. (3.20) rather than Eqn. (3.21). Numerical experiments, however, reveal that the results computed with either approach present fairly small differences of solutions for low-speed flow problems, such as those analysed in this thesis. Due to the lower computational cost associated with the use of Eqn. (3.21) when solving the HB equations (see below), all analyses presented in this thesis are based on the use of this equation.

### 3.2.3 time-dependent problems

The physical time-derivative of system (2.41) is discretised with a second order backward finite-difference. At each new physical time-level  $n+1$ , the sought flow solution is computed by solving the set of nonlinear algebraic equations resulting from the space- and time-discretization of system (2.41) with the same integration method used for steady problems. This procedure corresponds to Jameson's dual-time-stepping approach to the integration of TD problems. The smoother (3.19) is used for computing the sought flow solution  $Q^{n+1}$  by solving the system of algebraic equations:

$$\mathbf{R}_g(Q^{n+1}) = \frac{3Q^{n+1} - 4Q^n + Q^{n-1}}{2\Delta t} V + \mathbf{R}_\phi(Q) = 0 \quad (3.22)$$

where  $\mathbf{R}_g$  denotes the residual vector which also includes the source terms associated with the discretization of the physical time-derivative  $\partial \mathbf{U} / \partial t$  of Eqn. (2.41), and  $\Delta t$  indicates the user-given physical time-step. Also for TD problems with moving bodies, the matrix  $V$  is independent of the physical time-level because in this report only rigid-body grid motion is considered. This solution procedure may become unstable when the physical time-step  $\Delta t$  is significantly smaller than the pseudo-time-step  $\Delta \tau$ . This instability was reported in (Liou et al., 1993), and investigated in (Melson et al., 1993). The latter study elegantly solved the stability problem by treating implicitly the  $Q^{n+1}$  term of the physical time-derivative within the RK integration process. This strategy has also been implemented in COSA for the fully coupled integration of the TD RANS and SST equations. The TD counterpart of the turbulent steady smoother (3.19) is:

$$\begin{aligned}
\mathbf{W}^0 &= \mathbf{Q}_l \\
&[I + \alpha_k(\beta_{TD}I + \Delta\tau A)]\mathbf{W}^k \\
&= \mathbf{W}^0 + \alpha_k(\beta_{TD}I + \Delta\tau A)\mathbf{W}^{k-1} - \alpha_k\Delta\tau V^{-1}L_{IRS}[\mathbf{R}_g(\mathbf{W}^{k-1}) + \mathbf{f}_{MG}] \\
\mathbf{Q}_{l+1} &= \mathbf{W}^{NS}
\end{aligned} \tag{3.23}$$

where  $\beta_{TD} = 1.5\Delta\tau/\Delta t$ , and  $Q_l$  is shorthand for  $Q_l^{n+1}$ . The matrix multiplying  $W^k$  in Algorithm (3.23) is block-diagonal with  $N_{cell}$  blocks. In each  $(N_{PDE} \times N_{PDE})$  block the top left  $(4 \times 4)$  partition is proportional to the identity matrix through the coefficient  $(1 + \alpha_k\beta_{TD})$ , the bottom right  $(2 \times 2)$  partition is given by the sum of the  $(2 \times 2)$  identity matrix multiplied by  $(1 + \alpha_k\beta_{TD})$  and a non-diagonal  $(2 \times 2)$  matrix given by Eqn. (3.20) or Eqn. (3.21), depending on whether the exact or approximate update of  $\rho\omega$  is used, and all other entries are zero. Similarly to the case of the integration of the steady equations, this structure of the matrix premultiplying  $W^k$  results in the coupling of the update process of the turbulent variables, whereas it still enables the four mean flow variables to be updated without any actual matrix inversion. Due to the fact that the  $Q^{n+1}$  term arising from the backward finite-difference of the physical time-derivative is evaluated at stage  $k$ , algorithm (3.23) is said to be based a point-implicit Runge-Kutta (PIRK) integration of the TD RANS and turbulence equations. The standard fully explicit Runge-Kutta (FERK) integration method is retrieved by setting  $\beta_{TD} = 0$  in this algorithm. Several numerical tests (Campobasso et al., 2013) have highlighted that the turbulent PIRK integration significantly improves the stability of the fully coupled integration, enabling stable pseudo-time-marching with larger CFL numbers than with the standard FERK integration. This yields significant reductions of runtimes, due to the reduction of the overall number of MG cycles required to achieve a user-given reduction of the flow residual.

## 3.2.4 harmonic balance problems

At the differential level, the only difference between system (2.41) and system (2.54) is that the physical time-derivative of the former system is replaced by a volumetric source term proportional to  $\omega$  in the latter system. The set of nonlinear algebraic equations resulting from the space discretization of system (2.54) can thus be solved with the same technique used for

steady problems. The introduction of the derivative with respect to the fictitious time  $\tau$  yields the system of ordinary differential equations shown as below:

$$V_H \frac{dQ_H}{d\tau} + R_{g,H}(Q_H) = 0 \quad (3.24)$$

The smoother (3.19) is used for computing the sought HB flow solution  $Q_H$  by solving the system of algebraic equations:

$$R_{gH}(Q_H) = \omega V_H D_H Q_H + R_{\phi H}(Q_H) \quad (3.25)$$

The array  $Q_H$  is made up of  $N_{cell}$  sets of  $(2N_H + 1)$  flow states, with each state referring to the physical times defined by Eqn. (2.55). Therefore  $Q_H = [Q'_1, Q'_2, \dots, Q'_{N_{cell}}]'$ , where  $Q_i$ , with  $i = 1, \dots, N_{cell}$ , is an array of length  $[N_{PDE} \times (2N_H + 1)]$ . The first  $N_{PDE}$  elements of  $Q_i$  contain the flow state at  $t = t_0$ , the next  $N_{PDE}$  elements contain the flow state at  $t = t_1$ , and the last  $N_{PDE}$  elements contain the flow state at  $t = t_{2N_H}$ . The arrays  $R_{gH}$  and  $R_{\phi H}$  have the same structure of  $Q_H$ . The  $2N_H + 1$  states of a subarray  $(R_{\phi})_i$  contain the cell residuals associated with the convective fluxes, the diffusive fluxes and the turbulent source terms at the physical times defined by Eqn. (2.55). The residual subarray  $(R_g)_i$  includes also the source term  $\omega V_i D Q_i$ , where  $V_i$  is the product of the volume of the  $i^{th}$  grid cell and  $I_{N_{eqs}}$ , the identity matrix of size  $(N_{eqs} \times N_{eqs})$  with  $N_{eqs} = [N_{PDE} \times (2N_H + 1)]$ . The diagonal matrix  $V_H$  is a block-diagonal matrix with blocks given by the matrices  $V_i$  defined above, and the block-diagonal matrix  $D_H$  is defined as  $D_H = I_{N_{cell}} \otimes D$ .

It is found that the use of the non-turbulent counterpart of the smoother (3.19) for solving the HB equations describing certain periodic Euler and laminar flows results in numerical instabilities of the solver that prevent its convergence, unless unacceptably low CFL numbers are used. The aforementioned flows include the periodic transonic flow fields past an oscillating aerofoil reported in (Da Ronch et al., 2013), analysed with the COSA HB solver and the implicit HB solver of the PMB CFD code. This instability is likely to be the FD counterpart of the TD problem, discussed in the preceding subsection. A stabilised point-implicit HB smoother was therefore developed and implemented in the COSA HB solver (Campobasso and Baba-Ahmadi, 2012), and this allowed the calculation of the transonic flows reported in (Da Ronch et al., 2013) with the typical maximum CFL values of the numerical scheme used by COSA. The stabilization process can be generalised and extended to the turbulent case, and used to improve the numerical stability of the turbulent HB MG

solver. The fundamental step of the stabilization process requires treating implicitly the source term of Eqn.(3.25) within each RK stage. By doing so, one obtains the following HB-counterpart of the turbulent TD smoother (3.23):

$$\begin{aligned}
 \mathbf{W}_H^0 &= (\mathbf{Q}_H)_l \\
 [I + \alpha_k(\beta_H D_H + \Delta\tau_H A_H)]\mathbf{W}_H^k &= \mathbf{W}_H^0 + \\
 \alpha_k(\beta_H D_H + \Delta\tau_H A_H)\mathbf{W}_H^{k-1} - \alpha_k\Delta\tau_H V_H^{-1} L_{IRS,H}[\mathbf{R}_{gH}(\mathbf{W}_H^{k-1}) + \mathbf{f}_{MG,H}] & \quad (3.26) \\
 (\mathbf{Q}_H)_{l+1} &= \mathbf{W}_H^{NS}
 \end{aligned}$$

where the  $N_{cell}$  subarrays of  $\Delta\tau_H$  have length  $(2N_H + 1)$ . Each subarray contain the local time steps for the  $2N_H + 1$  flow states. One also has  $\beta_H = \omega\Delta\tau_H$ . The array of the HB MG forcing term  $\mathbf{f}_{MG,H}$  has the same structure as  $\mathbf{Q}_H$ . The matrix  $A_H$  can be viewed as a  $(N_{cell} \times N_{cell})$  block-diagonal matrix. Each block  $A_{H,i}$  of size  $(N_{eqs} \times N_{eqs})$  with  $N_{eqs} = [N_{PDE} \times (2N_H + 1)]$ , also has a block-diagonal structure. Its  $(2N_H + 1)$  nonzero  $(N_{PDE} \times N_{PDE})$  blocks provide the matrices  $A_i$ 's for the flow states referring to the times defined by Eqn. (2.55). The HB IRS operator has the same block structure of  $A_H$ . The use of the turbulent PIRK HB smoother (3.26) enables the use of significantly larger CFL numbers than the use of its FERK counterpart. Moreover, the higher stability achieved by PIRK with respect to the FERK iteration increases significantly with  $N_H$ .

When using the approximation provided by Eqn. (3.21) for updating  $\rho k$  and  $\rho\omega$ , the structure of the matrix premultiplying  $\mathbf{W}_H^k$  at the second line of Algorithm (3.26) is such that, for each grid cell, the update of the  $[N_{PDE} \times (2N_H + 1)]$  unknowns requires the inversion of  $3[(2N_H + 1) \times (2N_H + 1)]$  subblock of  $[I + \alpha_k(\beta_H D_H + \Delta\tau_H A_H)]$ . Such overhead results in the computational cost of the HB analysis growing in a moderately superlinear fashion with  $N_H$ . Despite this feature, the computational cost of the HB analysis remains competitive with that of the TD analysis. If the exact update of the turbulent variables provided by Eqn. (3.20) were used, the computational cost of the turbulent PIRK smoother would be significantly higher than the cost incurred by using Eqn. (3.21). As a matter of fact, the update of the four RANS variables in the former case would require the same inversion of a  $[(2N_H + 1) \times (2N_H + 1)]$  matrix as in the latter case, but the update of the two turbulence variables would require an inversion of a  $[2(2N_H + 1) \times 2(2N_H + 1)]$  matrix, because of the equation coupling due to all entries of  $A_{SST}$  being not zero. Since these matrices are dense and unstructured, Gaussian elimination is used for their inversion, and the computational cost of

such inversions is proportional to the third power of the matrix size. Therefore, the use of Eqn. (3.21) rather than Eqn. (3.20) for updating the harmonics of the SST turbulence variables with the turbulent PIRK HB smoother yields a reduction of the computational cost of eight times. For highly nonlinear periodic flows, requiring values of  $N_H$  of at least five for a satisfactory time-resolution, this cost reduction would turn out to be even more significant.

### 3.3 Farfield boundary conditions

For numerical simulation of aerodynamic problems, the implementation of the farfield Boundary Conditions (BCs) plays an essential role. The standard implementation of the farfield BCs can be based either on the multi-dimensional compatibility equations and differential form of the characteristic variables, or the one-dimensional Riemann invariants. The reason why we have considered herein these two different formulations of the farfield BC is that the first one based on characteristic variables is the only formulation amenable to the straightforward integration into LSP framework, while the other one using Riemann invariants is more widespread and has been already implemented in the previous research.

Based on the differential form of the 2D characteristic variables, the 2D compatibility equations in the absence of source terms yield:

$$\begin{aligned}
\delta W_1 &= \delta\rho - \frac{1}{c^2} \delta p = 0 & \text{along } C_1: \frac{dl}{dt} &= U_n \\
\delta W_2 &= \rho n_y \delta u - \rho n_x \delta v = 0 & \text{along } C_2: \frac{dl}{dt} &= U_n \\
\delta W_3 &= \frac{\delta p}{2c^2} + \frac{\rho \delta U_n}{2c} = 0 & \text{along } C_3: \frac{dl}{dt} &= U_n + c \\
\delta W_4 &= \frac{\delta p}{2c^2} - \frac{\rho \delta U_n}{2c} = 0 & \text{along } C_4: \frac{dl}{dt} &= U_n - c \\
\delta W_5 &= \rho \delta K = 0 & \text{along } C_5: \frac{dl}{dt} &= U_n \\
\delta W_6 &= \rho \delta \omega = 0 & \text{along } C_6: \frac{dl}{dt} &= U_n
\end{aligned} \tag{3.27}$$

where  $l$  denotes the curvilinear coordinate along the 'trajectory' of each characteristic. Here it is assumed that the unit vector  $\hat{n}_b$  normal to the farfield boundary points outside the domain. Given this choice of the orientation of  $\hat{n}_b$ , inflow boundaries are characterised by negative

values of  $U_{nb}$ , the flow velocity component normal to the farfield boundary, whereas outflow boundaries are characterised by positive values of  $U_{nb}$ . Therefore, in the case of subsonic flow conditions at the farfield boundary, the acoustic characteristic with speed  $U_n + c$  always leaves the domain, whereas the acoustic characteristic with speed  $U_n - c$  always enters the domain. In the following two sections, the subscript  $b$  denotes sought flowfield values at the farfield boundary, the subscript  $i$  denotes computed flow field values extrapolated from the interior of the physical domain (the cells adjacent to the boundary of the computational domain in the discretised representation of the problem), and the subscript  $\infty$  denotes given farfield values. A sketch of the farfield boundary for both subsonic inflow and outflow is depicted in Figure 3.1.

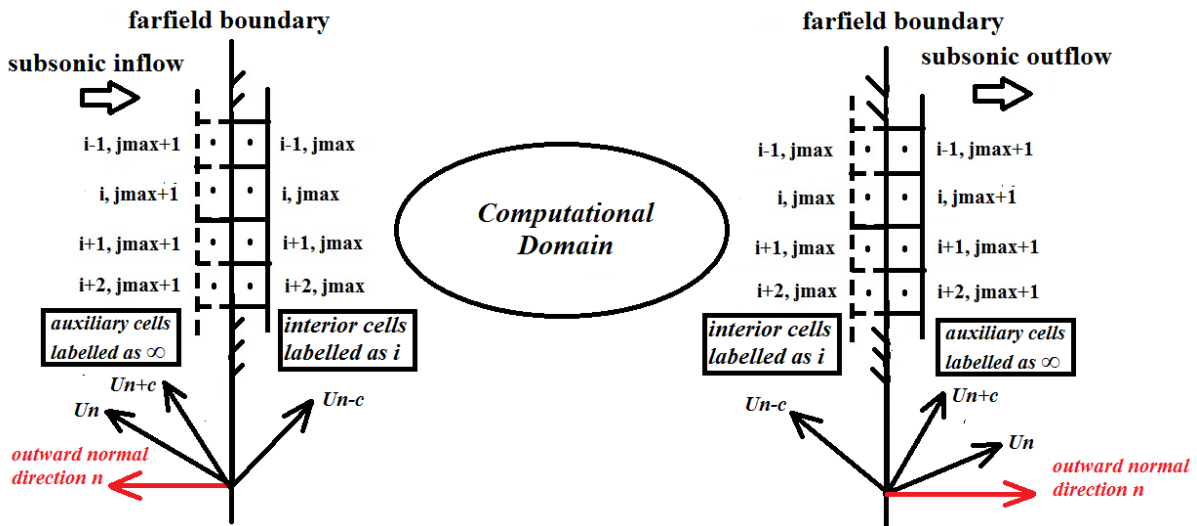


Figure 3.1 A SKETCH OF THE FARFIELD BOUNDARY

### 3.3.1 BCs based on multi-dimensional compatibility equations

Taking into account the direction of propagation, and imposing the compatibility constraint of the outgoing and incoming acoustic characteristics across the farfield boundary yields:

$$(U_{nb} - U_{ni}) + \frac{1}{\rho c} (p_b - p_i) = 0 \quad (3.28)$$

and

### 3.3.1 BCs based on multi-dimensional compatibility equations

$$(U_{nb} - U_{n\infty}) - \frac{1}{\rho c} (p_b - p_\infty) = 0 \quad (3.29)$$

Adding and subtracting Equations (3.28) and (3.29) yield respectively

$$U_{nb} = \frac{U_{ni} + U_{n\infty}}{2} + \frac{1}{\rho c} \left( \frac{p_i - p_\infty}{2} \right) \quad (3.30)$$

$$p_b = \frac{p_i + p_\infty}{2} + \rho c \left( \frac{U_{ni} - U_{n\infty}}{2} \right) \quad (3.31)$$

which can be used to determine the normal velocity component and the static pressure at the farfield boundaries. The product  $\rho c$  appearing in these two equations can be approximated with the value at the interior point adjacent to the boundary  $\rho c \approx \rho_i c_i$  or using the given farfield data  $\rho c \approx \rho_\infty c_\infty$ . Eqn. (3.30) and (3.31) can be used both at inflow and outflow boundaries.

In the case of a subsonic inflow, the characteristics  $W_1$  and  $W_2$  enter the computational domain, and therefore two additional conditions must be prescribed using the given farfield data. One condition is that the entropy at the farfield boundary should be the prescribed freestream value, and the other condition is that the tangential component of the given freestream velocity is equal to that of the flow velocity at the farfield boundary. Imposing the freestream entropy conditions yields:

$$\frac{p_\infty}{\rho_\infty^\gamma} = S_\infty = \frac{p_b}{\rho_b^\gamma} \quad (3.32)$$

The density at the boundary is thus

$$\rho_b = \rho_\infty \left( \frac{p_b}{p_\infty} \right)^{\frac{1}{\gamma}} \quad (3.33)$$

Denoting by  $\hat{U}_b$  the flow velocity vector at the farfield boundary and by  $\hat{U}_\infty$  the given freestream velocity, the constraint on the tangential velocity component can be written as:

$$\hat{U}_b - (\hat{U}_b \cdot \hat{n}) \hat{n} = \hat{U}_\infty - (\hat{U}_\infty \cdot \hat{n}) \hat{n} \quad (3.34)$$

which yields:

$$\hat{U}_b = \hat{U}_\infty + (U_{nb} - U_{n\infty}) \hat{n} \quad (3.35)$$

### 3.3.1 BCs based on multi-dimensional compatibility equations

The two sought Cartesian components of the flow velocity vector at the farfield boundary are thus:

$$u_b = u_\infty + (U_{nb} - U_{n\infty}) n_x, \quad v_b = v_\infty + (U_{nb} - U_{n\infty}) n_y \quad (3.36)$$

Since also the characteristics associated with the two turbulent variables enter the domain, the values of these two variables at the boundary are taken to be the given freestream values:

$$k_b = k_\infty, \quad \omega_b = \omega_\infty \quad (3.37)$$

In the case of a subsonic outflow, the characteristics  $W_1$  and  $W_2$  leave the computational domain, and therefore two additional conditions must be prescribed extrapolating the computed data from the interior point adjacent to the farfield boundary. One condition is that the entropy at the farfield boundary is extrapolated from the interior of the domain, and the other condition is that the tangential velocity component extrapolated from the interior is equal to that of the flow velocity at the farfield boundary. Imposing the extrapolated entropy conditions yields:

$$\frac{p_i}{\rho_i^\gamma} = S_i = \frac{p_b}{\rho_b^\gamma} \quad (3.38)$$

The density at the boundary is thus

$$\rho_b = \rho_i \left( \frac{p_b}{p_i} \right)^{\frac{1}{\gamma}} \quad (3.39)$$

The procedure to impose the constraint on the tangential velocity component is the same as shown in the subsonic inflow case. Denoting by  $U_{ni}$  the tangential component of the flow velocity vector extrapolated from the interior, the sought Cartesian components of the flow velocity vector at the farfield boundary are:

$$u_b = u_i + (U_{nb} - U_{ni}) n_x, \quad v_b = v_i + (U_{nb} - U_{ni}) n_y \quad (3.40)$$

Since also the characteristics associated with the two turbulent variables leave the domain, the values of these two variables at the boundary are taken to be extrapolated values too:

$$k_b = k_i, \quad \omega_b = \omega_i \quad (3.41)$$

### 3.3.2 BCs based on one-dimensional Riemann invariants

Integrating the 1-D compatibility equations of the entropy characteristic ( $W_1$ ), the two acoustic characteristics ( $W_3$  and  $W_4$ ), and the two characteristics associated with the convection of the turbulence variables ( $W_5$  and  $W_6$ ), one obtains the so-called Riemann invariants. The expression of the 1-D Riemann invariants is found to be:

$$R_1 = S, \quad R_3 = U_n + \frac{2c}{\gamma - 1}, \quad R_4 = U_n - \frac{2c}{\gamma - 1}, \quad R_5 = k, \quad R_6 = \omega \quad (3.42)$$

Computing the value of the outgoing invariant  $R_3$  using extrapolated flow data, and the value of the incoming invariant  $R_4$  using given farfield flow data, the unknown values of  $U_{nb}$  and the sound speed  $c_b$  at the farfield boundary can be obtained by combining the expressions of  $R_3$  and  $R_4$ :

$$U_{nb} = \frac{R_{3i} + R_{4\infty}}{2}, \quad c_b = \frac{R_{3i} - R_{4\infty}}{4(\gamma - 1)} \quad (3.43)$$

These two equations are valid both for the inflow and the outflow cases, and the sign of the computed value of  $U_{nb}$  can be used to determine if an inflow or outflow condition occurs.

In the inflow case ( $U_{nb} < 0$ ), two additional constraints must be enforced using given freestream data. One is the freestream entropy, and the other is the tangential component of the freestream velocity. The freestream entropy constraint is expressed by Eqn. (3.32), and it yields a constant entropy:

$$S_\infty = \frac{p_\infty}{\rho_\infty^\gamma} \quad (3.44)$$

noting that the nondimensionalised equation of state used by COSA is  $p\gamma = \rho T$ , one gets:

$$\rho_b = \left( \frac{T}{\gamma S_\infty} \right)^{\frac{1}{\gamma-1}} = \left( \frac{c_b^2}{\gamma S_\infty} \right)^{\frac{1}{\gamma-1}} \quad (3.45)$$

The static pressure at the farfield boundary is instead given by:

$$p_b = \frac{\rho_b c_b^2}{\gamma} \quad (3.46)$$

### 3.3.2 BCs based on one-dimensional Riemann invariants

The velocity components and turbulence variables at the inflow farfield boundary are determined with the same approach adopted in the case of BCs based on the differential form of the compatibility equations. Therefore the flow velocity components and the turbulent flow variables at the farfield boundary are given by Equations (3.36) and (3.37) respectively.

For the case of subsonic outflow ( $U_{nb} > 0$ ), the entropy and the tangential velocity component to be imposed at the farfield boundary are extrapolated from the interior. Following the same procedure adopted in the inflow case, one finds:

$$\rho_b = \left( \frac{T}{\gamma S_i} \right)^{\frac{1}{\gamma-1}} = \left( \frac{c_b^2}{\gamma S_i} \right)^{\frac{1}{\gamma-1}} \quad (3.47)$$

where the extrapolated entropy constant is defined as

$$S_i = \frac{p_i}{\rho_i^\gamma} \quad (3.48)$$

The static pressure at the farfield boundary is defined in the same way as Eqn. (3.46), and the flow velocity components and the turbulent flow variables at the farfield boundary are given by Equations (3.40) and (3.41) respectively.

## *Chapter 4*

# Low Speed Preconditioning

## 4.1 Low-speed preconditioner

In the past decades, the amount of research on low speed preconditioning has seen a dramatic growth since the method is an effective means to ensuring that time-marching algorithms remain well-conditioned in terms of both accuracy and efficiency in a wide range of flow speeds (Tukel, 1999, Weiss and Smith, 1995). In the case of a steady flow problem, a pseudo-time derivative is usually added to the time-marching system, while for unsteady or time-dependent analyses, one often adopts the algorithm called the dual-time-stepping, which is firstly suggested by (Jameson, 1991) and later developed and incorporated into the preconditioning system (Venkateswaran and Merkle, 1995). In this strategy, the physical transient process is modelled by means of time marching the physical time derivatives, whereas pseudo-time-derivatives or fictitious time-derivatives are used to perform an inner iteration to determine the flow field at each physical time. As explained in more details below, in the case of time-dependent problems the LSP (or the preconditioning matrix) is only applied to the fictitious time derivative in order to remain the time accuracy. The performance of the preconditioned algorithm is thus predominated by the choice of such a matrix in particular, which directly affects the numerical solution procedure in terms of the convergence optimisation and the accuracy improvement.

Among all the efforts devoted to developing the LSP algorithm, some have extended the preconditioning method in a more generalised sense for all Mach number range, while others concentrate on the problems of low speed flows. Concerning the former case, Tukel (1987) had discussed the application of preconditioning to both incompressible and compressible flows and mathematically proven (Tukel et al., 1993) that the limit of the compressible equations for Mach number approaching to zero is the incompressible equations. van Leer et al. (1992) had applied the preconditioning into multistage scheme for multigrid computations. Tukel (1987) and van Leer et al. (1992) primarily discuss the method from a purely theoretical point of view without providing detailed systematic studies of the effectiveness of

the preconditioning in solving realistic problems, while Choi and Merkle (1993) has dealt with a series of low Mach number restricted issues by using the preconditioning approach and proceeds primarily from an implementation point of view.

The first published work on using low-speed preconditioning is presented in (Briley et al., 1983), in which a constant diagonal preconditioning matrix is employed to alter the time-marching scheme and demonstrated to improve the convergence for a low Mach number case. It is followed by a large amount of study on developing the structure of low speed preconditioning matrix for inviscid flow problems by different researchers. Turkel (1987) used the entropy as the primitive variable to derive the system and introduces additional parameters to reduce the condition number. The generalised preconditioning matrix which depends on the local flow velocity is built on the basis of the artificial compressibility proposed by Chorin (1967). A 2-D system of the preconditioned equations using Turkel's approach is shown below,

$$\Gamma \frac{\partial Q}{\partial t} + A \frac{\partial Q}{\partial x} + B \frac{\partial Q}{\partial y} = 0 \quad (4.1)$$

$$Q = [p, u, v, S]^T$$

where A and B are the flux Jacobian matrix in x- and y- directions respectively,  $p$ ,  $u$ ,  $v$ , and  $S$  denote the pressure, x- and y- components of the flow velocity and entropy. The preconditioner  $\Gamma$  is defined as

$$\Gamma = \begin{bmatrix} \frac{c^2}{\beta^2} & 0 & 0 & \delta \\ \frac{\alpha u}{\rho \beta^2} & 1 & 0 & 0 \\ \frac{\alpha v}{\rho \beta^2} & 0 & 1 & 0 \\ 0 & 0 & 0 & 1 \end{bmatrix} \quad (4.2)$$

In which  $\beta$  is known as the artificial compressibility parameter while  $\alpha$  and  $\delta$  are two free parameters. The parameter  $\delta$  has no effect on the eigenvalues of the system thus the optimisation of the condition number and convergence rate is independent of  $\delta$ , and it can be usually neglected only except a particular requirement for determining the eigenvectors. When the local Mach number approaches zero, a singularity problem occurs due to the standard definition of  $\beta^2 = \min[c^2, u^2 + v^2]$ , therefore a cutoff value must be introduced in order to circumvent the issue. The optimal condition number of such preconditioned system can be achieved with  $\alpha = 1$ .

In contrast to the approach proposed by Turkel, other researchers have chosen to base the preconditioning matrices on the temperature as the dependent variable. Choi and Merkle (1993), for example, had adopted a similar form of the preconditioner as Briley et al. (1983) and enhanced the convergence by using the local velocity, which can be expressed in a 2-D preconditioned system as below,

$$\Gamma \frac{\partial Q}{\partial t} + A \frac{\partial Q}{\partial x} + B \frac{\partial Q}{\partial y} = 0 \quad (4.3)$$

$$Q = [p, u, v, T]^T$$

with

$$\Gamma = \begin{bmatrix} \frac{1}{ac^2} & 0 & 0 & 0 \\ \frac{u}{ac^2} & \rho & 0 & 0 \\ \frac{1}{ac^2} & 0 & \rho & 0 \\ \frac{H}{ac^2} - 1 & \rho u & \rho v & \rho C_p \end{bmatrix} \quad (4.4)$$

where  $a$  is the only parameter used in the preconditioner. It is noted that the preconditioning matrix (4.4) is derived from the Jacobian matrix  $\partial U/\partial Q$  between conservative variables  $U$  and primitive variables  $Q$ , by replacing the term  $\rho_p$  in the first column of the latter matrix with  $1/ac^2$  through which the acoustic wave can be modified to travel at the speeds of the same order of magnitude with respect to the particle wave, and also by neglecting the term  $\rho_T$  in the fourth column.

On the other hand, though Weiss and Smith (1995) had adopted the same procedure as that of Choi and Merkle (1993), they chose to keep the  $\rho_T$  term instead while replacing the preconditioning parameter  $1/ac^2$  with a more complex term, shown in the following 2-D example (the system of the preconditioned governing equations can be referred to Eqn. (4.3)),

$$\Gamma = \begin{bmatrix} \Theta & 0 & 0 & \rho_T \\ \Theta u & \rho & 0 & \rho_T u \\ \Theta v & 0 & \rho & \rho_T v \\ \Theta H - 1 & \rho u & \rho v & \rho_T H + \rho C_p \end{bmatrix} \quad (4.5)$$

where parameter  $\Theta$  is defined as  $\Theta = \left( \frac{1}{U_r^2} - \frac{\rho_T}{\rho C_p} \right)$ , and  $U_r$  is the reference velocity with the definition depending on the specific flow region,

$$U_r = \begin{cases} \epsilon c, & |v| < \epsilon c \\ |v|, & \epsilon c < |v| < c \\ c, & |v| > c \end{cases} \quad (4.6)$$

The coefficient  $\epsilon$  is usually a small constant and prevents  $U_r$  from becoming zero (singularity) at the stagnation points. They also claim that with retaining the  $\rho_T$  term in the matrix, the definition of  $\Theta$  can simplify the eigenvalues of the system with respect to those in the case of Choi and Merkle (1993).

In addition to the above methods, Van Leer et al. (1991) had developed another symmetric preconditioning matrix or the so-called Van Leer-Lee-Roe (VLR) preconditioner which is often referred to as optimal since it equalises eigenvalues across all Mach numbers and yields an optimal reduction of the condition number. Based on the flow variables  $dU$  denoted below, they derived the preconditioning matrix from the Euler equations and set the system coordinate align to the local flow velocity.

$$dU = \begin{pmatrix} \frac{dp}{\rho c} \\ du \\ dv \\ dp - a^2 d\rho \end{pmatrix} \quad (4.7)$$

The expression of the preconditioning matrix is,

$$\Gamma = \begin{bmatrix} \frac{\tau}{\beta^2} M^2 & -\frac{\tau}{\beta^2} M^2 & 0 & 0 \\ -\frac{\tau}{\beta^2} M^2 & \frac{\tau}{\beta^2} + 1 & 0 & 0 \\ 0 & 0 & \tau & 0 \\ 0 & 0 & 0 & 1 \end{bmatrix} \quad (4.8)$$

where  $\beta$  and  $\tau$  are defined as,

$$\beta = \begin{cases} \sqrt{1 - M^2}, & M < 1 \\ \sqrt{M^2 - 1}, & M \geq 1 \end{cases} \quad (4.9)$$

$$\tau = \begin{cases} \sqrt{1 - M^2}, & M < 1 \\ \sqrt{1 - M^{-2}}, & M \geq 1 \end{cases}$$

An investigation and review of these preconditioners has been reported in the work of Choi (1989) primarily for the Euler equations, and detailed analyses for Navier-Stokes equations are presented in (Lee, 1996) and (Tukel, 1999). Brief comparisons between the above proposed preconditioning matrices can be made in assessing three numerical aspects:

- convergence: as the VLR preconditioner yields the lowest condition number in theory, it thus ensures the most optimal convergence rate among all choices, which has been demonstrated in the numerical analyses (Hejranfar and Kamali-Moghadam, 2012) of two inviscid aerofoil flow problems. In this study, the preconditioning matrix proposed by Turkel is used to replace the VLR preconditioner since it gives the same optimal condition number of unity as that of the latter when the parameter  $\alpha$  equals 1. However, the numerical analyses highlight that though Turkel's preconditioner has demonstrated a better convergence rate of the solution compared to all the other studied approaches, its performance shows a large dependence on  $\alpha$  of which the optimal value is determined by the specific problem at hand, thereby it increases the complexity when one applies the knowledge obtained in the theoretical study to a realistic application.
- accuracy: despite the different derivation procedures of the preconditioning matrices, all these approaches have shown an almost equivalent effect on improving the accuracy as presented in the study of Hejranfar and Kamali-Moghadam (2012), primarily because the eigenvalues in all preconditioned systems are correctly rescaled in the same level, which results in comparable effects on the accuracy preservation of the numerical dissipation and final solutions obtained.
- robustness: although the VLR preconditioner is devoted to optimising the wave speeds for all Mach numbers, it suffers a severe robustness issue due to the strong dependence on the flow angle. On the contrary, the one proposed by Weiss and Smith only suffers from the singularity of the stagnation point, which can be simply eliminated by imposing the restriction on the preconditioning parameter in these regions. Moreover, it also demonstrates high robustness while analysing the sensitivity to flow angle and outer boundary or resolving problems with sonic point regions.

Besides low speed preconditioning, another method based on the perturbed form of the equations can also be used to eliminate the eigenvalue stiffness problem. In references (Choi, 1989, Merkle and Choi, 1988), by using an expansion of the flow variables in terms of the Mach number squared, the authors manage to replace the physical acoustic wave with a set of pseudo acoustic mode whose magnitude is comparable to the particle wave speed. The method is effective for both inviscid and viscous flow problems and has been widely applied to many areas of engineering. However, despite the fact that this perturbation method is fairly robust in calculation, its use is limited by the nature of perturbation to subsonic flow regime

only. Specifically, the method is inadequate for solving transonic flow problems, which makes it less competitive compared to the preconditioning method when dealing with a general flow problem with multispeed flows involved. Choi and Merkle (1993) and Venkateswaran and Merkle (1999) have thus worked on developing the preconditioning matrix taking advantage of the robustness exhibited by the perturbation expansion approach, and extended its application to transonic flows. To be more specific, a small parameter  $\epsilon$  obtained from the non-dimensionalisation of the governing equations is used to expand the pressure in its power series, where the zeroth order component  $p_0$  can be demonstrated as constant and is usually the reference pressure, while the perturbation pressure, on the other hand, which is orders of magnitude smaller than the thermodynamic pressure  $p_0$ , is the only solved pressure field. By modifying the partial derivative of density with respect to the pressure taking into account the effect of the small parameter  $\epsilon$ , one can equalise the time derivative of pressure and all the other terms in the continuity equation to the same order of magnitude and thus be able to update the pressure field even for very low Mach number.

A comprehensive study of the low-speed preconditioning approach for inviscid flows has been conducted by Choi (1989) for Euler equations, and the attempt of its extension to the case of viscous flows was made firstly by Choi and Merkle (1993), although only the study of the effects on convergence rate is reported in details. Regarding the extension of the preconditioning to the Navier-Stokes equations, a new parameter, Reynolds number, appears in the equations, which in its discretised form, is one of the key quantities in the system called cell Reynolds number  $Re_h$ . However, the extension procedure is not straightforward, since the wave speeds become complex as a result of the dissipative terms. To further investigate this problem, a dispersion relation analysis between the complex frequency  $\omega$  and wave number  $k$  has been provided in (Venkateswaran and Merkle, 1999) for the analytical solution of the Navier-Stokes equations. Based on the roots ( $\omega/k$ ) calculated for the complex frequency, it is found that in the case of a high Reynolds number ( $Re \gg 1$ ), the values of these roots become to the same particle and acoustic eigenvalues of the Euler equations, whereas in the viscous-dominated flow ( $Re \ll 1$ ), at least one of the above three roots yields an imaginary value depending on another parameter called the ‘acoustic’ Reynolds number ( $Re_c = c/\nu k = Re/M$ ), which directly links to the damping mode of the corresponding wave and is apparently due to the viscous terms of the momentum and energy equations. Therefore, determined by the Mach number and the ‘acoustic’ Reynolds number, the Navier-Stokes equations shows a much more complex physical process compared with the Euler equations,

which has also pointed to the fact that for high values of  $Re_h$ , there is less concern about designing new preconditioning approach rather than for low values of  $Re_h$  where the original ‘Euler approach’ would fail.

A summary of preconditioning methods used for different flow models (inviscid, laminar, turbulent) has been made by Lee (1996) focusing on theoretical aspect with only a limited number of numerical tests of validation. In Refs. (Lee et al., 1997, Lee, 1998) the authors have proposed an optimised preconditioning matrix in order to circumvent the singularity issues near the stagnation point as well as two specific methods for extending the local Euler preconditioning matrix to the Navier-Stokes equations, namely by adding the viscous entries arising in block-Jacobi preconditioning to deal with the stiff source terms and large cell aspect ratios, and introducing cell-Reynolds-number dependence in the entries of the Euler preconditioner based on the Navier-Stokes dispersion analysis. Meanwhile various types of improved preconditioning approaches have been proposed by different researchers (Fiterman et al., 1995, Venkateswaran and Merkle, 2000, Venkateswaran and Merkle, 1999, Weiss et al., 1999) and been successfully applied to solve complex viscous problems. HAKIMI (1997) has investigated and compared the preconditioning methods developed by Turkel (1987) and Choi and Merkle (1993), and also proposed the extension form of the preconditioning matrix to  $k - \epsilon$  turbulence model. Jespersen et al. (1997) made the enhancement to a compressible solver with the low Mach preconditioning algorithm aimed at the improvement of the numerical dissipation (solution accuracy) and the convergence rate, and the implementation of the preconditioned Roe-scheme is validated in both inviscid and high Reynolds number turbulent cases. Such modification of the artificial dissipation has indeed resulted in the beneficial effect of accuracy enhancement brought by the preconditioning. Recently, Li et al. (2009) have derived an all-speed Roe-scheme which results from the combination of the ‘classical’ Roe-scheme and Low-Speed-Roe scheme through a function of local Mach number. With theoretical analyses of its improvement achieved over the traditional preconditioned-Roe scheme and the above two counterparts in terms of the robustness and convergence acceleration, it is demonstrated with an all speed flow predictive capability of capturing shocks and simulating low speed flows.

However, despite the fact that significant progress on LSP research has been done in terms of the inviscid and viscous laminar flow problems, there still remains a large unexplored area regarding its application to high-Reynolds turbulent problems, particularly when using the Reynolds-averaged Navier-Stokes equations in conjunction with two-equation turbulence

models, such as Wilcox's  $k - \omega$  model (Wilcox, 1993) or Menter's Shear-Stress-Transport (SST) model (Menter, 1994). Regarding the analysis of the implementation of LSP in RANS solvers augmented with turbulence models, two important features require to be emphasised. The first one is the method called the fully coupled integration approach (Liu and Zheng, 1996), which solves the RANS equations and turbulence model equations simultaneously, and has shown a significant improvement compared to the loosely couple counterpart in terms of the computational efficiency (see Section 3.2 for the theory). Venkateswaran and Merkle (1999) have analysed the important influence of this fully coupled integration scheme on preconditioned equations. The other one is to derive the preconditioning matrix applied to both the flow equations and turbulence model equations, which is due to the fact that the RANS and turbulence equations have already been coupled at the mathematical level through the turbulence kinetic energy in the total energy (with reference to Eqn. (2.10)), which results in the necessity of obtaining a single convective flux Jacobian for both RANS and turbulence equations and implementing the LSP to the whole system uniformly. The detailed analysis of this turbulence preconditioning matrix are first given in Ref. (Venkateswaran and Merkle, 1999), but in a purely theoretical point of view and no numerical results have been provided to validate the assumption. One essential reason for implementing the fully coupled method when solving the preconditioned Navier-Stokes and turbulence system is that it is important to consider the effect of the turbulence kinetic energy term in the pressure gradient of the momentum equation (2.9) as well as in the total energy of the energy equation (2.10). To be more specific, it is not the comparison of the magnitude of the pressure and turbulent kinetic energy that matters, but rather the comparison of the gradient of both variables. Particularly for low speed flows in some cases, the gradient of the turbulent kinetic energy can be of the same order or even larger than that of the pressure. Therefore, with the turbulent kinetic energy terms in the fluid equations (momentum and energy equations), the coupling of the RANS and the turbulence equations becomes straightforward and imperative, which as a consequence has resulted in the generation of the specific form of the preconditioning matrix for the turbulent flows.

Unfortunately, no more study seems to be found thereafter on the incorporation of the fully coupled multigrid integration into the system where both the flow and turbulence equations are preconditioned. For example, Zheng et al. (1997) and Liu et al. (1998) solve the incompressible RANS equations by using the pseudo-compressibility approach of Chorin (1967), and only precondition the RANS equations, although the fully coupled approach is

used to solve the systems of RANS and turbulence equations of  $k - \omega$  model, which may only be applicable to incompressible solvers, as the momentum and energy equations are decoupled, and the latter one is not solved in this reference. Therefore unlike in the compressible case, no contribution of turbulent kinetic energy to the numerical dissipation of the momentum equation has been taken into account, which allows the fully coupled integration approach to be used without the need to precondition the turbulence equations. They claim no preconditioning is needed for the turbulence equations since the wave speed of the two characteristics associated with the two turbulence equations is already equal to the convective velocity, which is lack of strict theoretical demonstration and would require further analysis. Similar simplified implementation of the preconditioning method with two-equation turbulence models have also been found in (Gleize and Costes, 2003, Le Pape and Gleize, 2006), where the authors choose the preconditioning method of Choi and Merkle (1993) and incorporate its original form into various turbulence models (for example, two-equation  $k - l$  model suggested by Brian (1994), two-equation  $k - \epsilon$  model of Launder and Sharma and the  $k - \omega$  model of Wilcox), and solve the turbulence flow equations apart from the Navier-Stokes system.

Therefore, based on the above findings, one can conclude that almost no validated implementation of the preconditioning method for both the Navier-Stokes system and two-equation turbulence model equations in the framework of the strongly coupled integration approach has been made or published. More importantly, according to the research progress achieved by Buelow (2014), it has been confirmed that in the analysis of the combustion problem where large areas of mixed high speed and low speed flows can often occur, the turbulence kinetic energy has exerted a significant effect on the solution, providing us a strong evidence of validating the Venkateswaran and Merkle (1999)'s theory.

## 4.2 LSP in Implicit and explicit CFD

In order to solve the system of non-linear algebraic equations resulting from the space-discretisation of the convective and diffusive terms of the steady RANS and SST equations, and the source terms of the SST equations, one can adopt either an implicit or explicit time-marching scheme. The type of time-marching method is determined by how the time-

derivative of the unknown flow variables is re-introduced into the system of the above algebraic equations, which, often through a suitable time discretisation of the time derivative, yields a system of ODEs. A convenient initial solution is required at the beginning of the time-marching method to achieve the steady sought solution. Denoting the space-discretised system of the  $N$ -unknown flow equations by  $f(\hat{Q})$ , and  $\hat{Q}$  represents the array storing  $N$  unknowns  $Q_1, Q_2, \dots, Q_N$ , the solution of the steady equations can thus be obtained by time-marching the following system of ODEs:

$$\frac{\Delta \hat{Q}}{\Delta t} + f(\hat{Q}) = 0 \quad (4.10)$$

The sought steady solution can be obtained when  $f(\hat{Q})$ , the residual of the steady equations, equals to zero.

An explicit time-marching method can be implemented by solving the ODEs and evaluating the residual term  $f(\hat{Q})$  at time level  $n$ , and approximating the time-derivative with a first order finite difference scheme:

$$\hat{Q}^{n+1} = \hat{Q}^n - \Delta t f(\hat{Q}^n) \quad (4.11)$$

where  $\hat{Q}^n$  is the value of  $\hat{Q}$  computed at time level  $n$  ( $t = n\Delta t$ ).

Whereas regarding the implicit time-marching method, the residual term is instead evaluated at the time level  $n + 1$ , and the time derivative is discretised using a backward finite difference. Referring to the ODE system (4.10), the implicit time-marching approach yields,

$$\hat{Q}^{n+1} = \hat{Q}^n - \Delta t f(\hat{Q}^{n+1}) \quad (4.12)$$

thus computing the solution of  $f(\hat{Q}) = 0$  requires to solve a system of equations at time level  $n + 1$ .

Before proceeding to the further discussion on the implicit and explicit time-marching approaches, an introduction of the iteration methods used in a single time level is provided first, which are usually classified as the so-called non-iterative and iterative methods, whereby the latter one can degenerate to the non-iterative time-marching method if only one iteration is performed at each time step. However, the non-iterative time marching method is subject to the loss of temporal accuracy unless extremely small physical time steps are used, particularly analysing the complex flow problems involving strong non-linear behaviour such

as shock waves or combustion problems (Venkateswaran and Merkle, 1995). Worse still, its physical time step size also suffers a severe limitation due to stability issues associated with stretched grids (Buelow et al., 1997) and errors associated with the approximate-inversion methods that are typically used in the implicit scheme. Therefore iterative procedures are usually adopted and applied at each physical time-level, which, in case of the implicit schemes, greatly eliminates the linearization and approximate factorization errors and ensures a good temporal accuracy.

The approximate-Newton iterative procedure (Rai, 1993) and the dual-time-stepping approach (Jameson, 1991, Shuen et al., 1992) are the two iterative methods commonly used in the unsteady calculation. Both methods feature ‘inner’ or ‘sub’ iterations at each physical time step, and the dual time stepping approach which is more general, introduces an additional ‘pseudo’ time derivative to drive out errors in the physical transient and ensure well converged solutions in the inner iterations. One advantage of dual time stepping lies in the fact that the pseudo time derivative terms can be optimised to improve the convergence of the inner iteration, for example with the implementation of the preconditioning technique for low Mach number flow problems. The other benefit (Buelow et al., 1997) is that the physical time step can be chosen independently of the iterative method. The dual-time stepping method can be applied to both explicit (Jameson, 1991, Weiss and Smith, 1995) and implicit (Shuen et al., 1992, Venkateswaran and Merkle, 1995) time-marching schemes. A potential drawback of using the explicit integration is that it suffers an instability issue in the presence of highly stretched grids, thereby causing poor convergence in the inner iteration. The implicit methods, on the other hand, have shown a good capability of dealing with the stretched grids (Buelow et al., 1994) and produce satisfactory convergence results (Venkateswaran and Merkle, 1995). Hence, to solve Eqn. (4.12) iteratively using an implicit time-marching method, requires the update of the solution of a large system of equations at time level  $n + 1$ , which is apparently a disadvantage with respect to the explicit methods, however, it still possesses a significant attractiveness to many researchers by the fact that the maximum time step size  $h$  available in the implicit time-marching method is substantially higher than that of the explicit case demonstrated in the stability analysis. Therefore, a largely reduced number of time-steps is required in the implicit method, yielding a comparable computational cost with respect to the explicit approach.

To illustrate in more details the steady solution obtained with the implicit time-marching method, a linearised form of the equation (4.12) is given as,

$$\left(\frac{I}{h} + A\right) \Delta \hat{Q} = -f(\hat{Q}^n) \quad (4.13)$$

where

$$\Delta \hat{Q} = \hat{Q}^{n+1} - \hat{Q}^n \quad (4.14)$$

and the Jacobian matrix  $A$  is defined as,

$$A = \frac{\partial f(\hat{Q}^n)}{\partial \hat{Q}^n} \quad (4.15)$$

To solve the above system (4.15), one needs to solve the system of linear equations at the time step  $n + 1$  using an effective linear solver, and the solution can thus be updated as:

$$\hat{Q}^{n+1} = \hat{Q}^n + \Delta \hat{Q} \quad (4.16)$$

It should be noted that, with a very large time step  $h$  chosen in this approach, the term proportional to  $1/h$  in (4.13) is thus neglected and it becomes the Newton's method, the convergence of which is quadratic and therefore extremely favourable. However, the Newton's method usually requires a fairly close initial solution to the final sought steady solution, making it difficult to develop a stable solution procedure. Therefore, a relatively small time step  $h$  has to be adopted in the starting procedure of the implicit time march by most CFD codes based on the Newton's method.

Another implicit time-marching strategy often adopted for solving the RANS and turbulence model equations denoted by (4.13) is the so-called Approximate Factorisation Alternating Direction Implicit technique (AF-ADI), which approximates the matrix operator on LHS of equation (4.13) by the product of 2 (two-dimensional) or 3 (three-dimensional) simple matrices (e.g. tridiagonal matrices), and solves iteratively these 2 (or 3) simple systems at each iteration. At the end of each iteration, the residual term  $f(\hat{Q}^n)$  on the RHS of equation (4.13) is updated using the obtained solution of  $\hat{Q}^{n+1}$ .

As for the implementation of the LSP in the above implicit methods, Venkateswaran and Merkle (1995) conducted a von Neumann stability analysis and found that in the two extreme cases of small and large physical time steps, different choices of preconditioning matrix are required to ensure an optimal CFL number and convergence, and none of them is appropriate to be used in the intermediate choice of time-step. Therefore a wavenumber-dependent preconditioning parameter is suggested to overcome the damping issues for a wide range of

physical time steps as well as the most difficult - low wavenumber region. Buelow et al. (1997) have made a more detailed analysis of the preconditioning approach in implicit time-marching schemes. A diagonalised form of ADI method (Pulliam and Chaussee, 1981) is introduced aimed at reducing the computational cost by simplifying the block inversion of the left hand side to the scalar tri-diagonal inversion and matrix multiplication and extended to include the time-derivative preconditioning. To resolve the challenge of properly treating the inverted physical time term on the left hand side while implementing the preconditioning in the diagonalised ADI algorithm, they replace the traditional way of applying the inversion of a block penta-diagonal system with the ADI factorisation which leads to one dimensional implicit sweeps in the computational domain and a more efficient block tri-diagonal inversion. While taking into account the preconditioning matrix in the inversion of LHS, the additional term associated with the physical time derivative can hinder a straightforward diagonalisation, and one effective way is to group the pseudo- and physical- time derivatives in a single term before applying factorisation and diagonalisation methods. Another point to be noted is the way of diagonalising the linearized viscous term, whereby the authors replace the LHS viscous coefficient matrices with their spectral radii times the identity matrix, though such simplified treatment may have negative effect on the convergence for low Reynolds number flow. They also claim that despite an inconsistent modal analysis between the LHS and RHS after performing the diagonalisation of the above resulting LHS, it is demonstrated to work well in the preconditioned system. A further analysis of the implicit iterative method and the above modified ADI factorisation used in dual-time stepping can be found in (Venkateswaran and Merkle, 1999) with more details and its implementation of solving practical problems (such as a round-jet in a low-Mach number cross-flow with ground-effect) is presented by Pandya et al. (2003).

Despite the stability benefits achieved by using the implicit scheme, it is also found that in order to achieve the purpose of using ADI technique, a mixed-second derivative term of the variable difference has to be dropped yielding a potential stability issue (Lerat et al., 1982), and the associated approximate-factorisation error, which relates to the size of the physical time step or the CFL number, may have dominating effect on the convergence particularly when the CFL number becomes way larger than unity. On the contrary, though the marching time step size  $h$  of the explicit integration is bounded with the scheme-dependent and problem-dependent threshold due to the stability concern, no additional complex matrix is required to be built or stored with respect to the implicit method within each step of its time

marching procedure, which saves a great amount of floating points operations (FLOPs) and is thereby more convenient in terms of the memory usage.

Therefore using the explicit method, the equation (4.11) can be solved in an iterative fashion by updating  $\hat{Q}^{n+1}$  until the procedure converges and the obtained value of  $\hat{Q}^{n+1}$  is regarded as the sought steady solution. One widely adopted explicit time-marching strategy is the explicit multi-stage Runge-Kutta strategy, which is first proposed by Jameson et al. (1981) to solve the Euler equations. The extension of the method has been later made to solve the Navier-Stokes equations (Belov et al., 1995) as well as the RANS equations augmented with various turbulence models (Mavriplis and Martinelli, 1994, Liu and Zheng, 1996, Lin and Sotiropoulos, 1997). However, due to the previously mentioned stability limitation on the CFL number, the iteration numbers required to assure the converged sought solution may become very large. In order to improve the computational efficiency, certain kinds of accelerating techniques are imperative to be introduced, such as implicit residual smoothing (Jameson, 1983, Blazek et al., 1991, Blazek et al., 1993, Swanson and Rossow, 2009) and full approximation storage (FAS) multigrid method (Douglas, 1996, Wesseling, 1995, Briggs and McCormick, 2000). Therefore with the above techniques implemented, the overall amount of FLOPs required to obtain a steady flow solution can be comparable or even smaller than implicit methods, although the overall number of FLOPs and/or the run-time required by explicit and implicit time-marching methods for a user defined reduction of the residual are still case-dependent in general. However, the fact of particular interest to our research is that the implementation of the explicit integration scheme in the preconditioned system tends to be more straightforward and convenient than the implicit one, which consequently makes it attractive to be adopted by many commercial (such as NUMECA etc.) or research CFD codes (Gleize and Costes, 2003, Campobasso et al., 2014a, Coutier-Delgosha et al., 2005, Weiss and Smith, 1995, Turkel and Vatsa, 2003, Heinrich and Schwarze, 2014) implemented with LSP.

To be noted that, the true benefits of low speed preconditioning can only be fully achieved with a well modified Runge-Kutta multistage scheme adapted to the numerical dissipation and space discretisation terms of a specific flow solver. In (Liu et al., 1998) the authors have devised a new update formula with implementing the preconditioner and treating implicitly the unsteady physical time-dependent terms, namely by introducing an intermediate step, the update of the solution at a given stage can be achieved with the yielded intermediate value. In terms of optimising the multistage coefficients, most attempts have been made with empirical

model, or geometric methods, or based on questionably defined functions for classical Runge-Kutta methods instead of a more advantageous modified version. Hosseini and Alonso (2004) have performed the numerical and analytical optimisation of different parameters and coefficients to achieve the optimum convergence for preconditioned Euler equations and aimed to find out the limitation and correlation of using both methods. Darmofal and Siu (1999) on the other hand choose to include a cell residual preconditioner in the multi-stage integration, thus to guarantee the good damping of high frequency errors for the semi-coarsening multigrid algorithm. The extension of the same kind of treatment is made by Moinier and Giles (2002) to solve the 3D compressible RANS equations with Spalart-Allmaras turbulence model, and the matrix preconditioner will have contributions from both inviscid and viscous flux terms, as well as the linearised source terms of the turbulence model. Turkel and Vatsa (2003) have conducted detailed analyses of the impact of variable choices on the preconditioned explicit Runge-Kutta scheme, through comparing the results obtained with implementing the conservation variables, primitive variables and a mixed combination of the two. In the recent published work of Campobasso et al. (2014a), the preconditioned turbulence equations with SST model is solved with the explicit Runge-Kutta time-marching algorithm in a strongly coupled integration manner, which will be detailed in Chapter 5.

### 4.3 Preconditioning parameter analysis

For the low speed preconditioning approach, apart from a well-defined matrix and associated numerical integration scheme, another crucial problem lies in the definition of preconditioning velocity scale applied in building the matrix. In Euler computations, preconditioning schemes often suffer severe robustness issues, which is due to the fact that local Mach number would approach zero near a stagnation point, therefore Venkateswaran and Merkle (1999) and Darmofal and Siu (1999) suggest a pressure-gradient based velocity scale at a specific cell in defining the preconditioning parameter.

A 2-D example of the preconditioning parameter (Venkateswaran and Merkle, 1999) used in the preconditioned equations is illustrated as below (based on the primitive variable  $Q_p = [p, u, v, T]^T$ ),

$$\Gamma = \begin{bmatrix} \rho_p' & 0 & 0 & \rho_T' \\ u\rho_p' & \rho & 0 & u\rho_T' \\ v\rho_p' & 0 & \rho & v\rho_T' \\ h_0\rho_p' - (1 - \rho h_p) & \rho u & \rho v & h_0\rho_T' + \rho h_T \end{bmatrix} \quad (4.17)$$

where the entry (1,1) is crucially important to control the performance of the whole preconditioning system based on the perturbation analyses and therefore requires particular attention when determining the preconditioning parameters for this term. It is scaled by  $1/V_p^2$  and  $V_p = \text{Min}(V_{inv}, c)$ , where  $V_{inv} = \sqrt{u^2 + v^2}$ , and it turns out that the preconditioned artificial speed equals the particle wave speed for subsonic flow and the acoustic wave speed for supersonic flow. With the implementation of the pressure gradient based velocity scale  $V_{pgr}$ , it becomes  $V_p = \text{Min}[\text{Max}(V_{inv}, V_{pgr}), c]$ , where  $V_{pgr} = \sqrt{|\Delta p|/\rho}$ , and the pressure variation can be determined as either the maximum or the average values across each of the cell faces,  $|\Delta p| = \text{Max}(|P_R - P_L|)$  or  $\text{Avg}(|P_R - P_L|)$ .

For high Reynolds number turbulent problems, the lack of robustness arises in low Reynolds number regions, which is because the preconditioning technique is designed to eliminate the stiffness issue related to the propagative disparities in the low Mach region, while in terms of the viscous flow, the diffusion process acts a dominating role in the boundary layer, and the basic unmodified preconditioning parameter would result in a large number of time steps required to resolve these regions. Therefore a local diffusion velocity scale  $V_{vis}$  is introduced in (Venkateswaran and Merkle, 1999) and the new preconditioning parameter is given as  $V_p = \text{Min}[\text{Max}(V_{inv}, V_{pgr}, V_{vis}), c]$ . The viscous velocity scale  $V_{vis}$  is defined as below

$$V_{vis} = \text{Max} \left[ \frac{M_x^2 \left( \frac{1}{Re_{\Delta x}} - 1 \right)}{Re_{\Delta x} \left[ 1 + M_x^2 \left( \frac{1}{Re_{\Delta x}} - 1 \right) \right]}, \frac{M_y^2 \left( \frac{1}{Re_{\Delta y}} - 1 \right)}{Re_{\Delta y} \left[ 1 + M_y^2 \left( \frac{1}{Re_{\Delta y}} - 1 \right) \right]} \right] \cdot c \quad (4.18)$$

Where  $M_x$  and  $M_y$  are the Mach number based on the x- and y- component of the velocity respectively, and  $Re_{\Delta x}$  and  $Re_{\Delta y}$  are respectively the cell Reynolds numbers  $u\Delta x/\nu$  and  $v\Delta y/\nu$  based on the cell length  $\Delta x$  and  $\Delta y$  in the x- and y- directions. However, it is found that such modification appears to be insufficient and produce divergent solutions for intake separation computations. One robust formulation is suggested by Turkel (1999), whereas it is still subject to difficult prescription of the reference Mach number value used in defining this restriction, as the crosswind inlet flow develops at speed varying significantly from the boundary layer to the intake region. Therefore another isentropic Mach number based

cutoff/restriction approach (Colin et al., 2011) is introduced to account for a wide range of complex turbulent applications.

Venkateswaran et al. (2003) have later performed a systematic numerical analyses of various steady preconditioning velocity scales: 1) the global preconditioning simply based on the multiple of free stream velocity, 2) local velocity based preconditioning, the one using the maximum value of the velocity in the neighbourhood of cells of concern. In order to overcome the singularity problem near the stagnation point, additional cutoff values of different types (pressure gradient or free stream velocity based) have been applied to the specific preconditioning method. The analysis focuses on the inviscid situations and results have shown an advantage of the local maximum preconditioning over the others in terms of the straightforward implementation, robustness and efficiency.

Turkel (2002) claims that the cut-off to prevent the stagnation-point singularity would be large and problem-dependent in difficult cases to ensure the robustness, which coincides with what we have found in our research. Besides, to take into account the viscous effect, they have not chosen the same manner as Venkateswaran et al. (2003) of incorporating a viscous correction into the local Mach number, but only make the corrections after calculating an inviscid value including all cut-offs. Followed by another published work (Turkel and Vatsa, 2005), in which they consider the use of two separate preconditioning parameters aiming to improve the convergence rate and accuracy of the artificial dissipation. The former one used in the update stage does not affect accuracy and can be chosen only to improve the convergence rate, while the latter one is designed ideally to be as small as possible without destroying convergence so as to gain accuracy. As a consequence, the positive effect on accuracy improvement will deteriorate as the physical time step increases. Besides, a parametric study (Unrau et al., 1997) on the implementation of Weiss-Smith preconditioner, has revealed that the optimal value of lower limit(or cutoff as mentioned before) used to prevent the preconditioning parameter from becoming zero in stagnation region is dependent on the angle of attack and the grid.

In cases of the unsteady computations, Venkateswaran and Merkle (1999) introduce a characteristic length  $l_x$  and  $l_y$  in multi directions determining the unsteady preconditioning velocity scale  $V_{uns}$ , therefore the preconditioned velocity is now defined as  $V_p = \text{Min}[\text{Max}(V_{ins}, V_{pgr}, V_{vis}, V_{uns}), c]$ , and  $V_{uns}$  is given as,

$$V_{uns} = \text{Max} \left[ \frac{l_x}{\pi \Delta t}, \frac{l_y}{\pi \Delta t} \right] \quad (4.19)$$

where  $l_x$  and  $l_y$  are usually chosen as the physical dimensions of the modelled geometrical configurations.

As for problems involved of moving objects, different treatment of defining the preconditioning parameters as well as the associated approach has been suggested. Liu et al. (1998) has modified the general preconditioning matrix of Chorin, Turkel and van Leer used to solve unsteady incompressible equations to the form taking into account the moving grid velocity, and the absolute velocity term in the preconditioning parameter is replaced by the relative velocity. Similar modification has also been found in (Gleize and Le Pape, 2006), where the selected preconditioning method of Choi and Merkle (1993) is changed in the same manner by replacing the velocity terms. Moreover, detailed analyses of reference Mach used in preconditioning parameter are provided for different cases (helicopter rotors in forward flight or wind turbine), and a ratio between the free stream and the rotating Mach number is introduced to assess the effect of the variation of the reference section on the local Mach considered. However, the modification of the preconditioning matrix by Gleize and Le Pape (2006) is not mathematically correct and motivated, provided that the velocity components in the flow variables are denoted in the absolute frame of reference. Particularly when adopting the approach of Choi and Merkle (1993), the preconditioning matrix is in fact the variation form of the Jacobian matrix of the primitive and conservative variables after performing the pressure perturbation analysis, therefore all velocity related entries in the matrix are only determined by these two sets of flow variables implemented in the governing equations, regardless of the type of the flows. Supporting evidence of the above statement is found in (Wang et al., 2005, Sheng, 2011), where the governing equations are cast in the relative frame of reference to solve the rotating flow problems and a constant diagonal preconditioning matrix (Briley et al., 2003) is introduced with its original form. However due to the instability issues encountered in cases where a high rotating speed occurs, a rotating Mach number based on the characteristic rotating speed and reference length scale is employed as part of the reference Mach number to equivalently account for both flow and rotational speeds in determining the preconditioning parameter, which yields a good re-scale of the eigenvalues and reduces the characteristic condition number of rotating flows. Similar finding is also reported by Xiao et al. (2007), who has implemented the preconditioning matrix of Weiss and Smith (1995) to the unsteady Navier-Stokes equations, while a modified

### 4.3 Preconditioning parameter analysis

preconditioning parameter based on Venkateswaran et al. (2003) is suggested to adapt to the moving grid problem.

## Chapter 5

# Preconditioning of Fully Coupled RANS and SST Equations

In the case of inviscid steady low-speed flows, a large disparity between the convective and acoustic eigenvalues of the flux Jacobian  $\partial\Phi_{i,f}/\partial U$  exists. This results in unbalanced amounts of numerical dissipation (Turkel et al., 1993, Venkateswaran and Merkle, 1999), and this occurrence spoils the accuracy of the solution. When using explicit time-marching methods, the local time-step also depends on the eigenvalues of the flux Jacobian, and the abovesaid eigenvalue disparity impairs the convergence rate of the solver. An analogous disparity among the eigenvalues of the Jacobian of the governing equations also occurs in the case of viscous steady and unsteady low-speed problems. These issues can be circumvented by using low-speed preconditioning (Turkel et al., 1997, Venkateswaran and Merkle, 1999). The LSP approach reported in Venkateswaran and Merkle (1999) is implemented in the COSA code, and the analyses of this method for laminar steady and TD problems has been reported in Campobasso and Baba-Ahmadi (2012). The extension of this preconditioning approach to steady and TD turbulent flow problems solved with the fully coupled multigrid integration is reported here.

## 5.1 Governing equations (2D)

To build the COSA LSP-solver, we introduce a new set of primitive variables defined as  $V_p = [p, u, v, T, k, \omega]^T$ . Eqn. (2.33) becomes

$$\bar{\Gamma}_p^{-1} \frac{\partial V_p}{\partial t} + \frac{\partial(\mathbf{E}_c - \mathbf{E}_d)}{\partial x} + \frac{\partial(\mathbf{F}_c - \mathbf{F}_d)}{\partial y} = \mathbf{S} \quad (5.1)$$

with  $\bar{\Gamma}_p^{-1}$  being the Jacobian matrix  $\frac{\partial U}{\partial V_p}$ . Replacing this Jacobian matrix by the preconditioning matrix  $\Gamma_p^{-1}$  one obtains

$$\Gamma_p^{-1} \frac{\partial \mathbf{V}_p}{\partial t} + \frac{\partial(\mathbf{E}_c - \mathbf{E}_d)}{\partial x} + \frac{\partial(\mathbf{F}_c - \mathbf{F}_d)}{\partial y} = \mathbf{S} \quad (5.2)$$

Reverting to conservative variables, the pseudo time derivative  $d\mathbf{U}/dt$  is premultiplied by a preconditioning matrix  $P_c^{-1}$ , where  $P_c^{-1} = \Gamma_p^{-1} \bar{\Gamma}_p$ .

$$P_c^{-1} \frac{\partial \mathbf{U}}{\partial t} + \frac{\partial(\mathbf{E}_c - \mathbf{E}_d)}{\partial x} + \frac{\partial(\mathbf{F}_c - \mathbf{F}_d)}{\partial y} = \mathbf{S} \quad (5.3)$$

This results in a rescaling of the eigenvalues of the preconditioned sum of the convective and viscous flux Jacobians which restores the correct levels of numerical dissipation and allows one to maintain high convergence rates even in low-speed problems. The preconditioner  $P_c$  for inviscid/laminar steady and TD flows has dimension  $[(2 + pd) \times (2 + pd)]$  ( $pd = 2$  in two- and  $pd = 3$  in three-dimensional problems), and is reported in Venkateswaran and Merkle (1999). When using the fully coupled integration of the RANS and SST equations, it is not possible to apply the LSP only to the RANS equations without the introduction of questionable approximations in the mathematical form of the governing equations. One of the most important reasons is that restricting the use of LSP to the RANS equations only when using the fully coupled integration is prohibited by the presence of the turbulent kinetic energy term  $k$  in the definition of the total energy. Due to such term, the numerical dissipation of the momentum and energy equations features contributions of the turbulent kinetic energy even without LSP, which thereby forms a strong coupling of the RANS and SST equations in calculating the numerical dissipations and leads them to be treated as a single system when implementing the LSP. On the other hand, using a  $(N_{PDE} \times N_{PDE})$  preconditioning matrix having the  $[(2 + pd) \times (2 + pd)]$  laminar preconditioner in the top left and the  $(2 \times 2)$  identity matrix in the bottom right corner (which corresponds to the case that no preconditioning is applied to the SST equations) yields complex eigenmodes of the preconditioned  $(N_{PDE} \times N_{PDE})$  convective flux Jacobian unless the turbulent kinetic energy is removed from the definition of the total energy, which means changing the original set-up of the RANS SST turbulence model and would cause significant accuracy uncertainty for complex flow problems. In order to demonstrate the necessity of the full preconditioning approach whereby both RANS and SST equations are applied with the LSP through the coupling of the turbulent kinetic energy, we have also tested two simplified preconditioning counterparts, both of which remove the turbulent kinetic energy in the total energy yielding the decoupling of the two systems of equations. One simplified version only preconditions the flow equations whereas the other one follows a rigorous mathematical derivation process

and applies the LSP to both systems (however with a different preconditioning matrix  $P_c$  with respect to that of the full preconditioning approach). The expression of the preconditioner  $P_c$  used by the fully coupled integration of COSA and the two simplified approaches are both reported in the Appendix C, and the comparative analyses of the computational results among the above choices are performed for the applications of the horizontal axis wind turbine blade and vertical axis wind turbine shown in Chapter 7.

Based on the above statement, LSP must be applied equally to the two systems of the equations and the dimension of the preconditioning matrix  $P_c$  increases to  $(N_{PDE} \times N_{PDE})$  with  $N_{PDE} = 4 + pd$ . The matrix  $P_c$  depends on a parameter  $M_p$ . For low speed flows, the parameter  $M_p$  is,

$$M_p = \min(\max(M, M_{pg}, M_{vis}, \epsilon), 1) \quad (5.4)$$

where  $M$  is the actual local Mach number,  $M_{pg}$  is a cut-off value based on the local pressure gradient (Weiss et al., 1999, Darmofal and Siu, 1999), and  $M_{vis}$  is the viscous cut-off value proposed by Buelow (1995). The parameter  $\epsilon$  is a small cut-off parameter that prevents the preconditioner from becoming singular at stagnation points. The choice  $M_p = 1$  yields no preconditioning, and it allows us to make a very strict validation of the LSP implementation against the default solver without LSP. Based on the derivation process of LSP presented in this chapter and the preconditioning parameter  $M_p$  set to 1, we can assess individually each part of the code affected by LSP, such as the eigenvectors required for numerical dissipation, the preconditioned characteristics, eigenvalues and residual, the farfield boundary conditions and the numerical integration, therefore it can be regarded as one crucially important algorithmic feature of the way we derive and validate the LSP implementation in our research.

## 5.2 Artificial dissipation

Artificial dissipation is one of the most essential elements to CFD algorithm which aims to damp out the high order frequency errors during the solution process. Artificial dissipation models can be generalised into two categories: the first one is the central difference scheme wherein the dissipation is introduced as a higher order derivative terms through an explicit step; the second one is the so-called upwind scheme, whereby the dissipation is an inherent

part of the space discretisation. As the upwind flux difference scheme is the one adopted in our research, the low speed preconditioning analysis presented in the section is based on this scheme only. Given an explicit form of the matrix dissipation of upwind scheme, it has been demonstrated (Venkateswaran and Merkle, 1999) that with the implementation of LSP, some of the dissipation terms can be properly modified yielding all the terms of the dissipation matrix to the same order of magnitude and well-proportioned, thus guarantying a good accuracy at all Mach numbers.

For simplicity reason, the steady inviscid formulation is considered. Multiplying Eqn. (5.3) by  $P_c$  yields

$$\frac{\partial \mathbf{U}}{\partial t} + P_c \left( \frac{\partial E}{\partial x} + \frac{\partial F}{\partial y} \right) = 0 \quad (5.5)$$

and the associated integral form reads

$$\int \frac{\partial U}{\partial t} dV + \oint P_c (\hat{F} \cdot d\hat{S}) = \int \frac{\partial U}{\partial t} dV + \oint P_c \mathcal{F} dS = 0 \quad (5.6)$$

where

$$\hat{F} = E\hat{i} + F\hat{j}, \quad \mathcal{F} = Ek_x + Fk_y, \quad d\hat{S} = (k_x\hat{i} + k_y\hat{j})dS \quad (5.7)$$

and

$$k_x^2 + k_y^2 = 1 \quad (5.8)$$

The use of Roe's scheme yields the numerical flux

$$\mathcal{F}^* = \frac{1}{2} P_c (\mathcal{F}_L + \mathcal{F}_R) - \frac{1}{2} |P_c K| \delta U \quad (5.9)$$

with

$$K = \frac{\partial \mathcal{F}}{\partial U} = \frac{\partial E}{\partial U} k_x + \frac{\partial F}{\partial U} k_y \quad (5.10)$$

The finite volume space-discretised version of Eqn. (5.6) becomes:

$$\int \frac{\partial U}{\partial t} dV + \sum \frac{1}{2} [P_c (\mathcal{F}_L + \mathcal{F}_R) - |P_c K| \delta U] dS = 0 \quad (5.11)$$

Premultiplying equation (5.11) by  $P_c^{-1}$  yields

$$\int P_c^{-1} \frac{\partial U}{\partial t} dV + \sum \frac{1}{2} [(F_L + F_R) - P_c^{-1} |P_c K| \delta U] dS = 0 \quad (5.12)$$

Therefore the numerical dissipation term that needs to be calculated is

$$\frac{1}{2} P_c^{-1} |P_c K| \delta U \quad (5.13)$$

In order to implement the preconditioned numerical dissipation given by Eqn. (5.13), one would need to compute the eigenmodes of  $P_c K$ . It turns out, however, that it is simpler to work with the eigenmodes of  $\Gamma_p \frac{\partial \mathcal{F}}{\partial V_p}$ , and  $\Gamma_p$  is the preconditioning matrix related to the primitive variables  $V_p$ .

Rewritten in terms of the above preconditioned Jacobian, it becomes as

$$|P_c K| = \left| \left( \frac{\partial U}{\partial V_p} \Gamma_p \right) \left( \frac{\partial \mathcal{F}}{\partial V_p} \frac{\partial V_p}{\partial U} \right) \right| = \left| (\bar{\Gamma}_p)^{-1} \Gamma_p \left( \frac{\partial \mathcal{F}}{\partial V_p} \bar{\Gamma}_p \right) \right| \quad (5.14)$$

where  $\bar{\Gamma}_p$  is the Jacobian matrix between primitive variable  $V_p$  and conservative variable  $U$ .

As proved in the Appendix D, Eqn. (5.14) can be written as,

$$|P_c K| = (\bar{\Gamma}_p)^{-1} \left| \Gamma_p \frac{\partial \mathcal{F}}{\partial V_p} \right| \bar{\Gamma}_p \quad (5.15)$$

which leads to the sought expression of the numerical dissipation

$$\frac{1}{2} P_c^{-1} |P_c K| \delta U = \frac{1}{2} \Gamma_p^{-1} \bar{\Gamma}_p (\bar{\Gamma}_p)^{-1} \left| \Gamma_p \frac{\partial \mathcal{F}}{\partial V_p} \right| \bar{\Gamma}_p \delta U = \frac{1}{2} \Gamma_p^{-1} \left| \Gamma_p \frac{\partial \mathcal{F}}{\partial V_p} \right| \bar{\Gamma}_p \delta U \quad (5.16)$$

## 5.2.1 construction of numerical dissipation

The first step consists of diagonalising the Jacobian matrix  $\Gamma_p \frac{\partial \mathcal{F}}{\partial V_p}$ ,

$$\left| \Gamma_p \frac{\partial \mathcal{F}}{\partial V_p} \right| = \hat{R} |\Lambda| \hat{R}^{-1} = \hat{L} |\Lambda| \hat{L}^{-1} \quad (5.17)$$

where  $\hat{R}$  and  $\hat{L}^{-1}$  are respectively the matrix of right and left eigenvectors of  $\Gamma_p \frac{\partial \mathcal{F}}{\partial V_p}$ . Note that

$\hat{R} = \hat{L}$ . From Eqn. (5.16) it follows that

$$\frac{1}{2} P_c^{-1} |P_c K| \delta U = \frac{1}{2} \Gamma_p^{-1} \hat{R} |\Lambda| \hat{R}^{-1} \bar{\Gamma}_p \delta U = \frac{1}{2} \Gamma_p^{-1} \hat{L} |\Lambda| \hat{L}^{-1} \bar{\Gamma}_p \delta U \quad (5.18)$$

This term can be rewritten as:

$$\frac{1}{2}P_c^{-1}|P_c K|\delta U = \frac{1}{2}\mathcal{R}|\Lambda|\mathcal{L}^{-1}\delta U \quad (5.19)$$

where

$$\mathcal{R} = \Gamma_p^{-1}\hat{R}, \quad \mathcal{L}^{-1} = \hat{L}^{-1}\bar{\Gamma}_p \quad (5.20)$$

When the Mach number  $M$  tends to 1, then  $\mathcal{R} \rightarrow \mathcal{L}$ . For  $M < 1$ ,  $\mathcal{R} \neq \mathcal{L}$ , because  $\Gamma_p \neq \bar{\Gamma}_p$ .

Let us now consider the  $i^{th}$  flux difference ( $i = 1$  corresponds to the continuity equation,  $i = 2$  and  $i = 3$  correspond to the x- and y-component of the momentum equation,  $i = 4$  corresponds to the energy equation,  $i = 5$  and  $i = 6$  correspond to the two SST turbulence model equations with respect to turbulent kinetic energy and dissipation rate). The  $i^{th}$  flux difference  $\delta f_i$  is given by

$$\delta f_i = \sum_j r_{ij} \alpha_j |\lambda_j| \quad (5.21)$$

where  $\hat{r}_j$  is the  $j^{th}$  column of  $\mathcal{R}$  and  $\lambda_j$  is the  $j^{th}$  entry of  $\Lambda$ . The scalars  $\alpha_j$  ( $j = 1, 6$ ) are given by  $\alpha_j = \delta W = (L_\star^{-1})_j \delta V$ , where  $\delta V$  is the array of the standard primitive variables  $\delta[\rho, u, v, p, K, \omega]^T$  and  $(L_\star^{-1})_j$  is the  $j^{th}$  row of the matrix  $L_\star^{-1}$ , which is defined as

$$L_\star^{-1} = \mathcal{L}^{-1}M \quad (5.22)$$

in which  $M$  is the Jacobian matrix  $M = \frac{\partial U}{\partial V}$ .

Expressions of all the above matrices are provided in details in the Appendix B.

## 5.3 Farfield BCs (2D)

Although the standard nonpreconditioned form of the farfield boundary conditions can be based both on the multi-dimensional compatibility equations and differential form of the characteristic variables, or the one-dimensional Riemann invariants, the preconditioned characteristic-based farfield BCs can be built only by using the differential form of the preconditioned characteristics, obtained by considering the multi-dimensional preconditioned compatibility equations.

### 5.3.1 mathematical model

The preconditioned characteristic variables for the turbulent NS equations coupled to the SST turbulence model equations have been derived in Appendix B. Based on Eqn. (B.17), the preconditioned compatibility equations for turbulent problems are:

$$\begin{aligned}
\delta W_1 &= \delta\rho - \frac{1}{c^2} \delta p = 0 & \text{along } C_1: \frac{dl}{dt} &= U_n \\
\delta W_2 &= \rho n_y \delta u - \rho n_x \delta v = 0 & \text{along } C_2: \frac{dl}{dt} &= U_n \\
\delta W_3 &= \frac{\delta p - \rho \delta U_n (\lambda_4 - U_n)}{c(\lambda_3 - \lambda_4)} = 0 & \text{along } C_3: \frac{dl}{dt} &= U'_n + c' \\
\delta W_4 &= \frac{\delta p - \rho \delta U_n (\lambda_3 - U_n)}{c(\lambda_3 - \lambda_4)} = 0 & \text{along } C_4: \frac{dl}{dt} &= U'_n - c' \\
\delta W_5 &= \rho \delta k = 0 & \text{along } C_5: \frac{dl}{dt} &= U_n \\
\delta W_6 &= \rho \delta \omega = 0 & \text{along } C_6: \frac{dl}{dt} &= U_n
\end{aligned} \tag{5.23}$$

where  $\lambda_3 = U'_n + c'$ ,  $\lambda_4 = U'_n - c'$ ,  $U'_n = \frac{(1+M_p^2)}{2} U_n$ ,  $c' = \sqrt{c^2 M_p^2 + a_m^2 U_n^2}$ ,  $a_m = \frac{(1-M_p^2)}{2} c$  stands for the sound speed while  $c'$  is the artificial sound speed.

Inserting the expressions of  $\lambda_3$  and  $\lambda_4$  into the compatibility equations of  $W_3$  and  $W_4$  yields:

$$\begin{aligned}
\delta W_1 &= \delta\rho - \frac{1}{c^2} \delta p = 0 & \text{along } C_1: \frac{dl}{dt} &= U_n \\
\delta W_2 &= \rho n_y \delta u - \rho n_x \delta v = 0 & \text{along } C_2: \frac{dl}{dt} &= U_n \\
\delta W_3 &= \frac{\rho(a_m U_n + c')}{2cc'} \left( \delta U_n + \frac{c' - a_m U_n}{\rho c^2 M_p^2} \delta p \right) = 0 & \text{along } C_3: \frac{dl}{dt} &= U'_n + c' \\
\delta W_4 &= -\frac{\rho(a_m U_n + c')}{2cc'} \left( \delta U_n - \frac{c' + a_m U_n}{\rho c^2 M_p^2} \delta p \right) = 0 & \text{along } C_4: \frac{dl}{dt} &= U'_n - c' \\
\delta W_5 &= \rho \delta k = 0 & \text{along } C_5: \frac{dl}{dt} &= U_n \\
\delta W_6 &= \rho \delta \omega = 0 & \text{along } C_6: \frac{dl}{dt} &= U_n
\end{aligned} \tag{5.24}$$

Taking into account the direction of propagation, and imposing the compatibility constraint of the outgoing  $W_3$  and incoming  $W_4$  acoustic characteristics across the farfield boundary (the

definitions of the incoming the outgoing flows and all the related subscripts, ' $n'$ ', ' $b'$ ', ' $i'$ ', ' $\infty'$ ' appearing in the following equations can be found in Section 3.3 of Chapter 3) yields:

$$\delta U_n + \frac{c' - a_m U_n}{\rho c^2 M_p^2} \delta p = (U_{nb} - U_{ni}) + \frac{c' - a_m U_n}{\rho c^2 M_p^2} (p_b - p_i) = 0 \quad (5.25)$$

and

$$\delta U_n - \frac{c' + a_m U_n}{\rho c^2 M_p^2} \delta p = (U_{nb} - U_{n\infty}) - \frac{c' + a_m U_n}{\rho c^2 M_p^2} (p_b - p_\infty) = 0 \quad (5.26)$$

Adding and subtracting Eqn. (5.25) and (5.26) yield respectively

$$U_{nb} = \frac{U_{ni} + U_{n\infty}}{2} + \frac{1}{\rho c'} \frac{p_i - p_\infty}{2} + \frac{a_m U_n}{c'} \frac{U_{ni} - U_{n\infty}}{2} \quad (5.27)$$

$$p_b = \frac{p_i + p_\infty}{2} + \frac{\rho M_p^2 c^2}{c'} \frac{U_{ni} - U_{n\infty}}{2} - \frac{a_m U_n}{c'} \frac{p_i - p_\infty}{2} \quad (5.28)$$

which can be used to determine the normal velocity component and the static pressure at the farfield boundaries. The density  $\rho$  and the sound speed  $c$  appearing in the two equations above can be approximated with the value at the interior point adjacent to the boundary ( $\rho \approx \rho_i$  &  $c \approx c_i$ ) or the given farfield data ( $\rho \approx \rho_\infty$  &  $c \approx c_\infty$ ). As for the artificial sound speed  $c'$ , the estimate of this variable also requires the approximation of  $U_n$ . Equations (5.27) and (5.28) can be used both at inflow and outflow boundaries. The density, all velocity components, and two turbulence variables at the farfield boundary are determined using the same expressions and equations reported in subsection 3.3.1.

## 5.3.2 validation

In order to validate the implementation of the preconditioned characteristic-based farfield boundary conditions, we have considered here an inviscid flow past the NACA0012 aerofoil at the AoA of  $1^\circ$ , and three free stream Mach numbers are specified, namely 0.1, 0.01 and 0.001 respectively. The steady inviscid flow analyses have also been performed using the MIT incompressible panel code XFOIL (Drela, 1989). This code also uses a Karman-Tsien compressibility correction that allows good compressible flow predictions all the way from incompressible ( $M_\infty = 0$ ) to sonic ( $M_\infty \approx 1$ ) conditions. A layout of the boundary

conditions imposed in the simulations is displayed in Figure 5.1. Aiming to demonstrate the beneficial effect of the preconditioned farfield boundary condition on the solution accuracy particularly for a small size of computational domain, a fairly small distance of 20 chords and large distance of 50 chords have been chosen between the aerofoil and farfield boundary in the simulations. Both preconditioned and non-preconditioned characteristic farfield BCs are implemented and compared, while an inviscid slip wall condition is specified on the aerofoil surface.

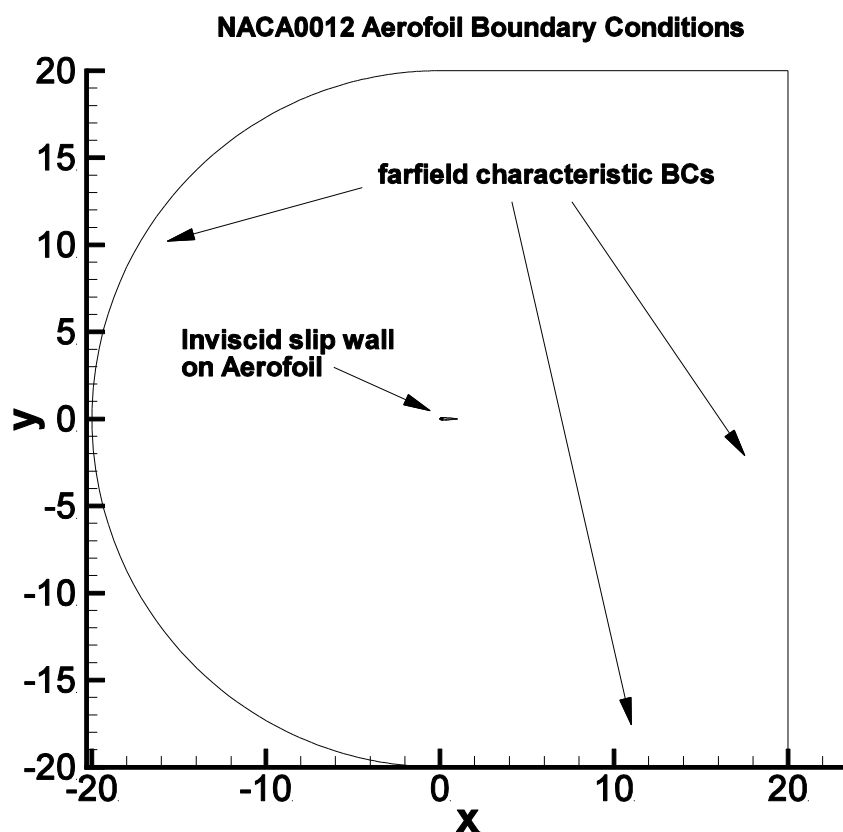


*Figure 5.1 IMPOSED BOUNDARY CONDITIONS FOR NACA0012 AEROFOIL CASE (20 CHORDS)*

A 2D C-type structured grid is adopted here for all flow simulations. The grid is stretched in the normal wall direction, and the clustering is maintained in the wake region. An over view of the adopted grid is given in Figure 5.2 (since we have applied the same mesh size and clustering for grids of both farfield boundary distances, only the one with 20 chords of farfield boundary distance is displayed herein for clarity), where stretched grid spacing can be seen in the wall-normal direction and the wake. Figure 5.3, on the other hand, provides an

enlarged view in the aerofoil region, of which 176 mesh intervals are along the aerofoil surface, 40 intervals are along the wake from the aerofoil trailing edge to the outflow boundary, and 160 intervals are in the normal-like direction, giving a total number of cells of 40960. A preliminary mesh refinement analysis has been made and no significant difference is observed between the solutions obtained with a finer mesh and the one shown here, thus the latter one has been adopted in all the simulations presented in the section.

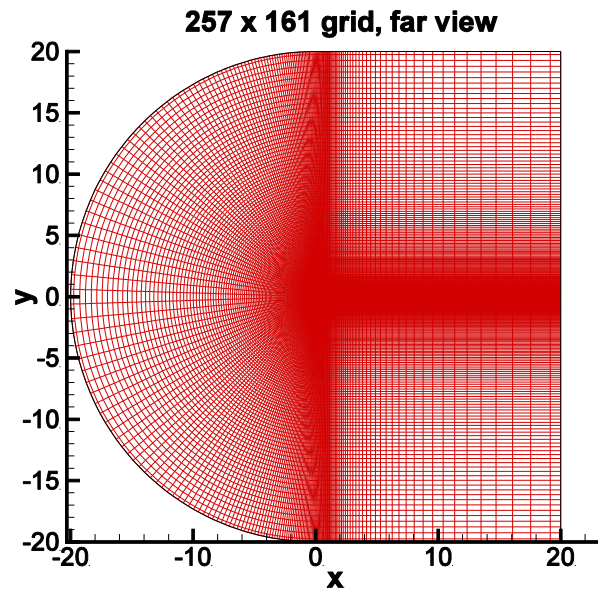


Figure 5.2 GRID VIEW IN FARFIELD REGION FOR NACA0012 AEROFOIL CASE (20 CHORDS)

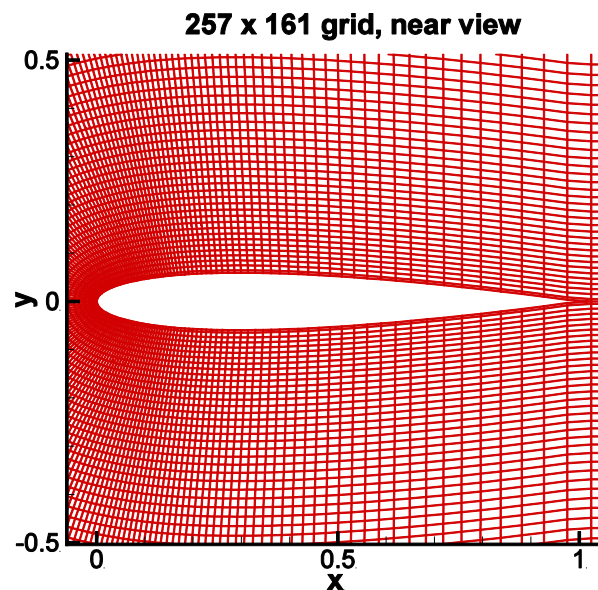


Figure 5.3 GRID VIEW IN NEAR AEROFOIL REGION (20 CHORDS)

The analysed variable of interest in this validation is the static pressure coefficient on the aerofoil surface, a profile comparison of which is shown in Figure 5.4 regarding the solutions obtained with the grid of 20 chords. The left subplot of the figure reports the comparisons of XFOIL and three LSP estimates of the static pressure coefficient  $c_p$  along the chord obtained in the simulations with preconditioned farfield characteristic BCs, whereas the same comparative analysis of XFOIL and LSP estimated values obtained with non-preconditioned BCs are depicted in the right subplot. Inspection of the  $c_p$  profiles in the left subplot yields that unnoticeable differences exist in both the leading edge (LE) and trailing edge (TE) between the XFOIL  $M_\infty = 0.1$  profile and those obtained by fully preconditioned approach associated with the three values of  $M_\infty$ . More importantly, the feature emerging from the  $c_p$  profiles obtained without preconditioned farfield BCs is that the results for the two lower values of  $M_\infty$  display significant non-physical oscillations at both LE and TE with respect to the solution of XFOIL, which on the other hand is successfully removed in the full LSP calculations as a result of the optimised farfield boundary condition. Figure 5.5, on the other hand, depicts the comparison of  $c_p$  profiles obtained with the larger mesh of 50 chords. Through the comparative analysis of both figures, it can be noticed that increasing the farfield distance or the size of the domain can improve slightly the accuracy of the solution obtained without the preconditioned farfield BCs for low speed flow problem (i.e. the solution near the LE of  $M_\infty = 0.001$ ), which, however, results in a significantly higher computational expense. The preconditioned farfield boundary conditions, on the other hand, have demonstrated equivalent benefits of preserving the solution accuracy in both cases and are thus less sensitive to the variation of the farfield boundary distance than the non-preconditioned counterpart, which provides us a strong evidence of the enhanced accuracy of the solution to the low speed flow problems by using the preconditioned farfield BCs, particularly with a relatively small computational domain.

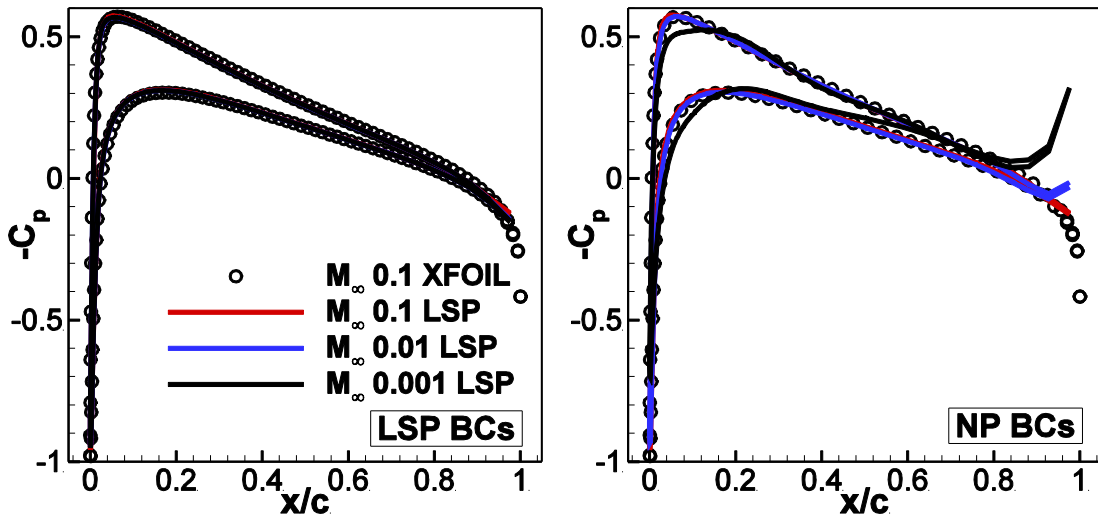


Figure 5.4 COMPARISON OF PRESSURE COEFFICIENT  $c_p$  AT THREE VALUES OF  $M_\infty$  0.1, 0.01, 0.001, OBTAINED BY XFOIL AND COSA LSP-ENHANCED SOLVER WITH AND WITHOUT PRECONDITIONED FARFIELD BCs (GRID OF 20 CHORDS). RIGHT SUBPLOT:  $c_p$  OBTAINED WITH XFOIL AND PRECONDITIONED FARFIELD BCs. LEFT SUBPLOT:  $c_p$  OBTAINED WITH XFOIL AND NON-PRECONDITIONED FARFIELD BCs

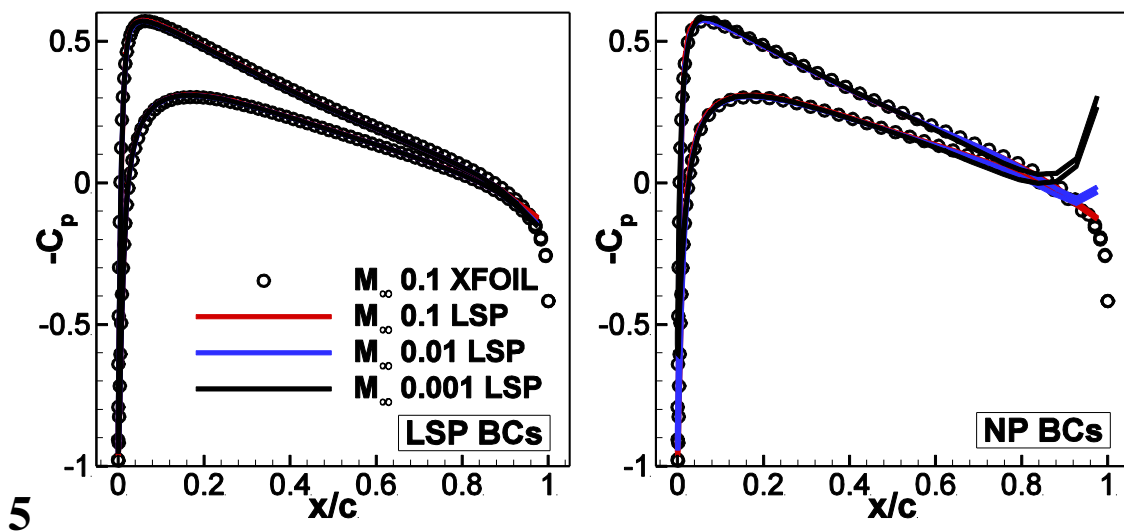


Figure 5.5 COMPARISON OF PRESSURE COEFFICIENT  $c_p$  AT THREE VALUES OF  $M_\infty$  0.1, 0.01, 0.001, OBTAINED BY XFOIL AND COSA LSP-ENHANCED SOLVER WITH AND WITHOUT PRECONDITIONED FARFIELD BCs (GRID OF 50 CHORDS).

## 5.4 Numerical integration

Starting from the standard numerical integration methods provided in the previous chapter for non-preconditioned analyses, we have made a brief description of their counterparts for the integration of the steady, time-dependent and harmonic balance preconditioned systems.

### 5.4.1 time-dependent problems

The general form of the point-implicit Runge-Kutta (PIRK) MG iteration to solve low-speed TD problems, obtained by premultiplying the fictitious time-derivative  $dQ/d\tau$  by  $P_c^{-1}$  and applying the stabilization process of Melson et al. (1993), is:

$$\begin{aligned}
 \mathbf{W}^0 &= \mathbf{Q}_l \\
 & (I + P_c \alpha_k (\beta_{TD} I + \Delta\tau A)) \mathbf{W}^k \\
 &= \mathbf{W}^0 + \alpha_k P_c (\beta_{TD} I + \Delta\tau A) \mathbf{W}^{k-1} - \alpha_k \Delta\tau V^{-1} P_c L_{IRS} [\mathbf{R}_g(\mathbf{W}^{k-1}) + \mathbf{f}_{MG}] \\
 \mathbf{Q}_{l+1} &= \mathbf{W}^{NS}
 \end{aligned} \tag{5.29}$$

The matrix premultiplying  $\mathbf{W}^k$  is block-diagonal, but its blocks are not diagonal because of the preconditioner  $P_c$ , which is a fully populated matrix, and also because of the off-diagonal terms of  $A$ . Therefore the update process requires the inversion of an  $N_{PDE} \times N_{PDE}$ -matrix for each cell of the computational domain. The standard fully explicit Runge-Kutta (FERK) integration algorithm of the TD equations is retrieved by setting  $\beta_{TD} = 0$  in Algorithm (5.29). The integration scheme of the steady equations is instead obtained by also replacing  $R_g$  with  $R_\Phi$  in Algorithm (5.29).

### 5.4.2 harmonic balance problems

In the case of frequency-domain problems, the pseudo-time derivative of Eqn. (3.24) is premultiplied by a  $[(2N_H + 1) \times (2N_H + 1)]$ -diagonal-block-matrix  $P_{c,H}^{-1}$ , and the nonzero blocks  $P_{c,n}^{-1}$  with  $n = 0, 1, \dots, 2N_H$  are simply instantiations of the preconditioning matrix  $P_c^{-1}$

discussed above at the times defined by Eqn. (2.55). The use of the same stabilization process of the RK cycle used in the TD problems yields the following PIRK MG iteration scheme for HB cases:

$$\begin{aligned}
\mathbf{W}_H^0 &= (\mathbf{Q}_H)_l \\
[I + \alpha_k P_{c,H}(\beta_H D_H + \Delta\tau_H A_H)] \mathbf{W}_H^k &= \mathbf{W}_H^0 + \\
\alpha_k P_{c,H}(\beta_H D_H + \Delta\tau_H A_H) \mathbf{W}_H^{k-1} - \alpha_k \Delta\tau_H V_H^{-1} P_{c,H} L_{IRS,H} [\mathbf{R}_{gH}(\mathbf{W}_H^{k-1}) + \mathbf{f}_{MG,H}] & \\
(\mathbf{Q}_H)_{l+1} &= \mathbf{W}_H^{NS}
\end{aligned} \tag{5.30}$$

The matrix pre-multiplying  $\mathbf{W}_H^k$  is block-diagonal, but its blocks are not diagonal because the preconditioner  $P_c$ , the matrix  $D$  and the matrix  $A$  are not diagonal. Each of these  $N_{cell}$  blocks has size of  $((2N_H + 1) \times N_{PDE})^2$ , and the update process of the whole solution requires the inversion of all such blocks. Due to this feature, the computational cost of HB analyses is moderately superlinear with respect to  $N_H$ . All numerical analyses carried out thus far, however, show that the computational speed of the HB analysis remains significantly higher than that of the TD despite the abovesaid overhead. The standard fully FERK integration algorithm of the HB equations can be retrieved by setting  $\beta_H = 0$  in Algorithm (5.30).

## 5.5 Preconditioning parameter for moving grid problem

For time-dependent moving grid problems, the definition of the preconditioning parameter  $M_p$  in Eqn.(5.4) should be treated differently from the steady cases by taking into account the grid moving velocity. Analyses and implementations of such modified parameters based on the relative flow velocity have been given in (Xiao et al., 2007) and (Liu et al., 1998) for general unsteady compressible and incompressible flow problems, while Gleize and Le Pape (2006) have provided a detailed numerical analysis with particular emphasis on the horizontal axis wind turbine application. As a consequence, the preconditioning parameter is defined as,

$$M_p = \min(\max(M_{ref}, M_{pg}, M_{vis}, \epsilon), 1) \tag{5.31}$$

where  $M_{ref} = |\hat{V} - \hat{V}_g|/c$  is the relative local Mach number, and  $\hat{V}$  and  $\hat{V}_g$  are the flow velocity and moving grid velocity in vector forms respectively.

## 5.5 Preconditioning parameter for moving grid problem

In the analysis of the vertical axis wind turbine application (see Section 7.3), we have found a noticeable improvement achieved in the solution of the torque coefficient by using the relative preconditioning parameter. However, based on the experience obtained in our study, the cutoff value  $\epsilon$  should be always set fairly high (i.e. 3 to 5 times the free stream Mach number) for the complex turbulent problems in order to get rid of the stability issue often occurring in the low Mach flow region (a similar conclusion has also been reported in the work of Turkel (2002)), which, to some extent, results in all the other preconditioning parameters less ‘active’, thus yielding a potential problem that the nice factors in the definition of the preconditioning parameter only work well for simpler test case of the same type as those used to develop them, while regarding the real flows (high Reynolds number, stretched grids, significant separations) which are substantially more complex than the simple idealised flows often used for developing elegant algorithms, the various variables appearing in the definition of the preconditioning parameters tend to be less important and beneficial. Therefore, to work out an approach that can properly balance the stability and accuracy for solving turbulent problems would still require further analyses in our future research.

## Chapter 6

# Validation

This chapter outlines numerical results computed for various internal and external flow problems. These test cases are considered to validate all aspects of the developed fully-coupled low-speed preconditioning technology

Firstly a steady turbulent flat plate boundary layer is considered: the numerical solution of COSA is compared with available theoretical results for three different Mach numbers. In the second case the flow separation and reattachment caused by a backward facing step is analysed and the simulated results of COSA are compared with both the solution of a well-established American CFD code (CFL3D) and the available experiment data. This is followed by the numerical analyses of a NASA 2D wall-Mounted hump experiment where a Glauert-Goldschmied type body is mounted in the lower wall. Experimental data and CFL3D results are used as benchmarks to assess the low speed flow predictive ability of the COSA LSP solver. The last internal flow problem is the 2D convex curvature boundary layer in a duct in which we primarily analyse the flow characteristics near the convex wall curvature. The first external flow problem considered in the chapter is the flow past a so-called Model-A aerofoil in a low Mach number turbulent flow for which measured velocity profiles in the wake are available for an angle-of-attack of 0 degree. The last test case is the NACA4412 aerofoil in a subsonic turbulent flow featuring a flow reversal in the rear portion of the suction side. The COSA solutions have been compared to available detailed hot-wire boundary layer measurements.

In all test cases, comparisons of the numerical solutions of COSA with and without LSP implementation, the experiment data and results of CFL3D analyses are presented. Additionally, for each test case two simulations with lower Mach numbers with respect to the original value are included to further challenge the flow predicting capability of the LSP-enhanced code in terms of solution accuracy and stability. It is highlighted that despite the compressibility effect in specific aerofoil cases, the solutions of the LSP solver have demonstrated an independence on the variation of Mach numbers, and also feature higher numerical accuracy in the normal subsonic flow problems due to the correct scaling of the artificial dissipation terms.

## 6.1 Steady turbulent flat plate boundary layer

The turbulent flow over a flat plate leading to the formation of a turbulent boundary layer is considered. The computational domain is rectangular and the flat plate lies on the lower horizontal boundary. The leading edge (LE) of the flat plate is in the origin of the Cartesian system, and its trailing edge (TE) is at  $x = 1$ , where the (vertical) outlet boundary is positioned. The inlet boundary is at  $x = -1/3$ , and the upper horizontal side is a farfield boundary positioned at  $y = 1$ . The computational mesh is shown in Figure 6.1 and only every second line is plotted for clarity.

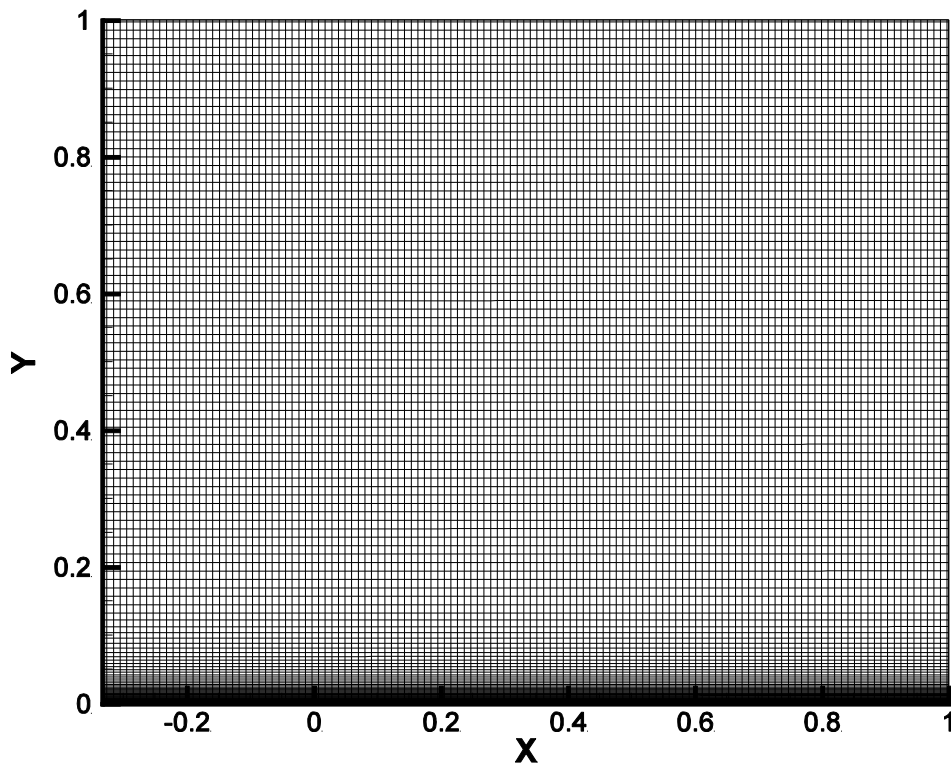


*Figure 6.1: Grid for turbulent flat plate*

The adopted Cartesian grid has 384 mesh intervals along  $y$ , and the size of these intervals increases from the lower horizontal boundary to the upper horizontal boundary starting from a minimum value of  $2.5 \cdot 10^{-7}$  yielding a non-dimensionalised wall distance  $y^+$  less than 1. The grid has 256 equal mesh intervals along  $x$ ; 192 are on the flat plate and 64 in the space between the LE and the inlet boundary. The freestream Reynolds number  $Re$  is  $6 \cdot 10^6$ . A

mesh refinement analysis has revealed that the solution computed with the grid defined above presents negligible differences from the solution computed by using grids with substantially higher spatial refinement. All simulations discussed below have been performed using the so-called *improved auxiliary state* farfield BCs for internal flows (Campobasso and Baba-Ahmadi, 2011) on the vertical left and right boundaries of the computational domain, and a standard external-flow characteristic based farfield condition on the top horizontal boundary. Symmetry conditions are imposed on the portion of the lower horizontal boundary between the inlet boundary and the LE of the flat plate, and a no-slip condition is applied on the flat plate.

From a physical standpoint, the effects of compressibility are expected to be negligible for  $M_\infty$  of order 0.1 or less. When using the compressible formulation without LSP, however, both the convergence rate of explicit solvers and the accuracy of the solution are expected to worsen as the Mach number decreases. To assess the effectiveness of the developed turbulent LSP technique, this test case has been solved for three values of  $M_\infty$ , namely 0.1, 0.01 and 0.001, and for each value a simulation with LSP and one without have been performed. All simulations have been run for 3,000 MG cycles with three grid levels and  $CFL = 3$ . The three profiles of the nondimensionalised velocity component parallel to the flat plate on a line orthogonal to the flat plate itself at  $x = 0.5$ , computed with and without LSP are reported in the left and right subplot of Figure 6.2 respectively (the label ‘NP’ in the top left corner of the right subplot denotes simulations performed without LSP).

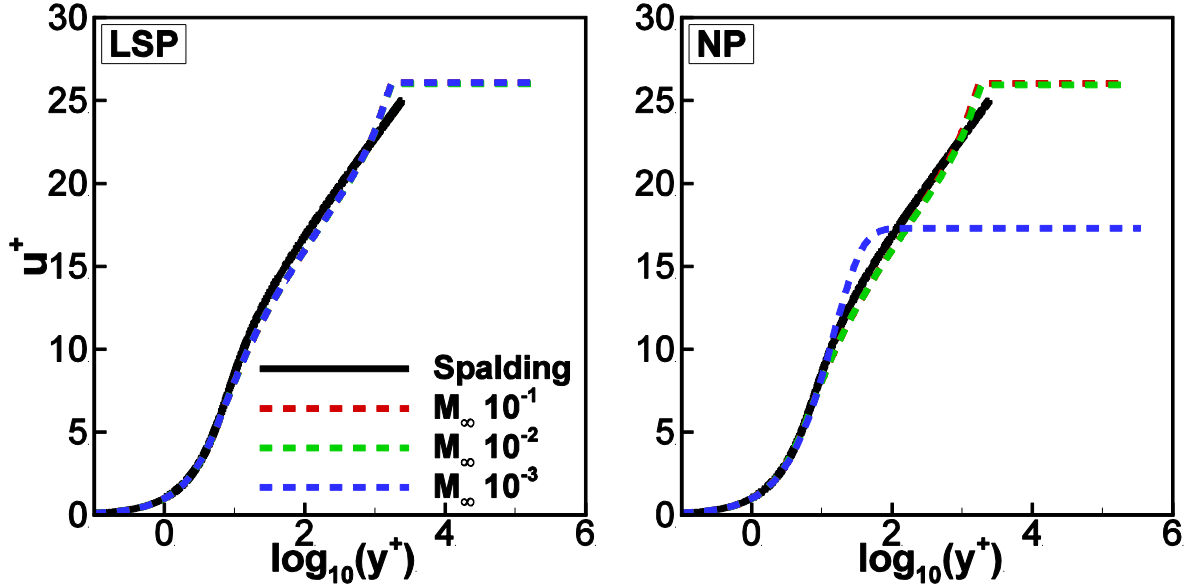


Figure 6.2 COMPARISON OF SPALDING'S VELOCITY PROFILE AND FLAT PLATE VELOCITY PROFILES EXTRACTED FROM FLAT PLATE FLOW SIMULATIONS FOR  $M_\infty = 0.1$ ,  $M_\infty = 0.01$ , AND  $M_\infty = 0.001$ . LEFT SUBPLOT: CFD SOLUTIONS WITH LSP. RIGHT SUBPLOT: CFD SOLUTIONS WITHOUT LSP.

The variable on the x-axis is the logarithm in base 10 of  $y^+$ , the nondimensionalised wall distance, and its expression is  $y^+ = (u_\tau d)/\nu_w$ . The variable on the y-axis is  $u^+$ , the nondimensionalised velocity component  $u_{||}$  parallel to the wall, which, in this case, is the  $x$ -component of the velocity vector. Its expression is  $u^+ = u_{||}/u_\tau$ . Both subplots also report Spalding's profile, which is a power-series interpolation of experimental data joining the linear sublayer to the logarithmic region of the turbulent boundary layer occurring on a flat plate in the absence of a streamwise pressure gradient. The left subplot of Figure 6.2 shows that the LSP solutions associated with the three values of  $M_\infty$  are superimposed, as expected on the basis of physical evidence, and in very good agreement with Spalding's velocity profile. The right subplot of Figure 6.2 shows that the CFD solutions without LSP are not independent of the Mach number, as the solution associated with  $M_\infty = 0.001$  differs both from the other two CFD results and Spalding's estimate. The theoretical value of the drag coefficient  $c_D$  for the considered configuration is  $3.14 \cdot 10^{-3}$ , whereas the values of  $c_D$  obtained with the three LSP simulations and the three simulations not using LSP are reported in the second and third columns of Table 6.1, respectively. These data emphasise that the  $c_D$  predicted by the LSP analysis remains constant as  $M_\infty$  decreases, and is equal to the theoretical value. Conversely, the drag coefficient estimate of the analysis without LSP deviates substantially from the theoretical prediction as  $M_\infty$  is reduced, due to the numerical

## 6.1 Steady turbulent flat plate boundary layer

errors associated with the use of the compressible solver without LSP at low Mach number levels.

$M_\infty$	LSP	NP
$1 \cdot 10^{-1}$	$3.14 \cdot 10^{-3}$	$3.14 \cdot 10^{-3}$
$1 \cdot 10^{-2}$	$3.14 \cdot 10^{-3}$	$3.24 \cdot 10^{-3}$
$1 \cdot 10^{-3}$	$3.14 \cdot 10^{-3}$	$6.87 \cdot 10^{-3}$

*Table 6.1 COMPARISON OF DRAG COEFFICIENTS EXTRACTED FROM FLAT PLATE FLOWSIMULATIONS FOR  $M_\infty = 0.1$ ,  $M_\infty = 0.01$  AND  $M_\infty = 0.001$  WITH AND WITHOUT LSP.*

The results of Table 6.1 and Figure 6.2 point to the necessity of using LSP to preserve the accuracy of the solution when solving low-speed flows with the compressible equations. The improvements of the convergence properties of the explicit multigrid compressible solver featuring LSP is highlighted in Figure 6.3. Its six subplots report the convergence histories of the continuity equation (subplot labelled  $\rho$ ), the  $x$  –component of the momentum equation (subplot labelled  $\rho u$ ), the  $y$  – component of the momentum equation (subplot labelled  $\rho v$ ), the energy equation (subplot labelled  $\rho E$ ), the turbulent kinetic energy equation (subplot labelled  $\rho k$ ), and the specific dissipation rate equation (subplot labelled  $\rho \omega$ ). In all plots, the variable on the  $x$  –axis is the number of multigrid iterations, and the variable  $\Delta l_r$  on the  $y$  –axis is the logarithm in base 10 of the root mean square of all cell-residuals for the considered conservation equation normalised by the residual of the 1<sup>st</sup> iteration. Each subplot reports the convergence history of the CFD runs with and without LSP for the three selected values of  $M_\infty$ .

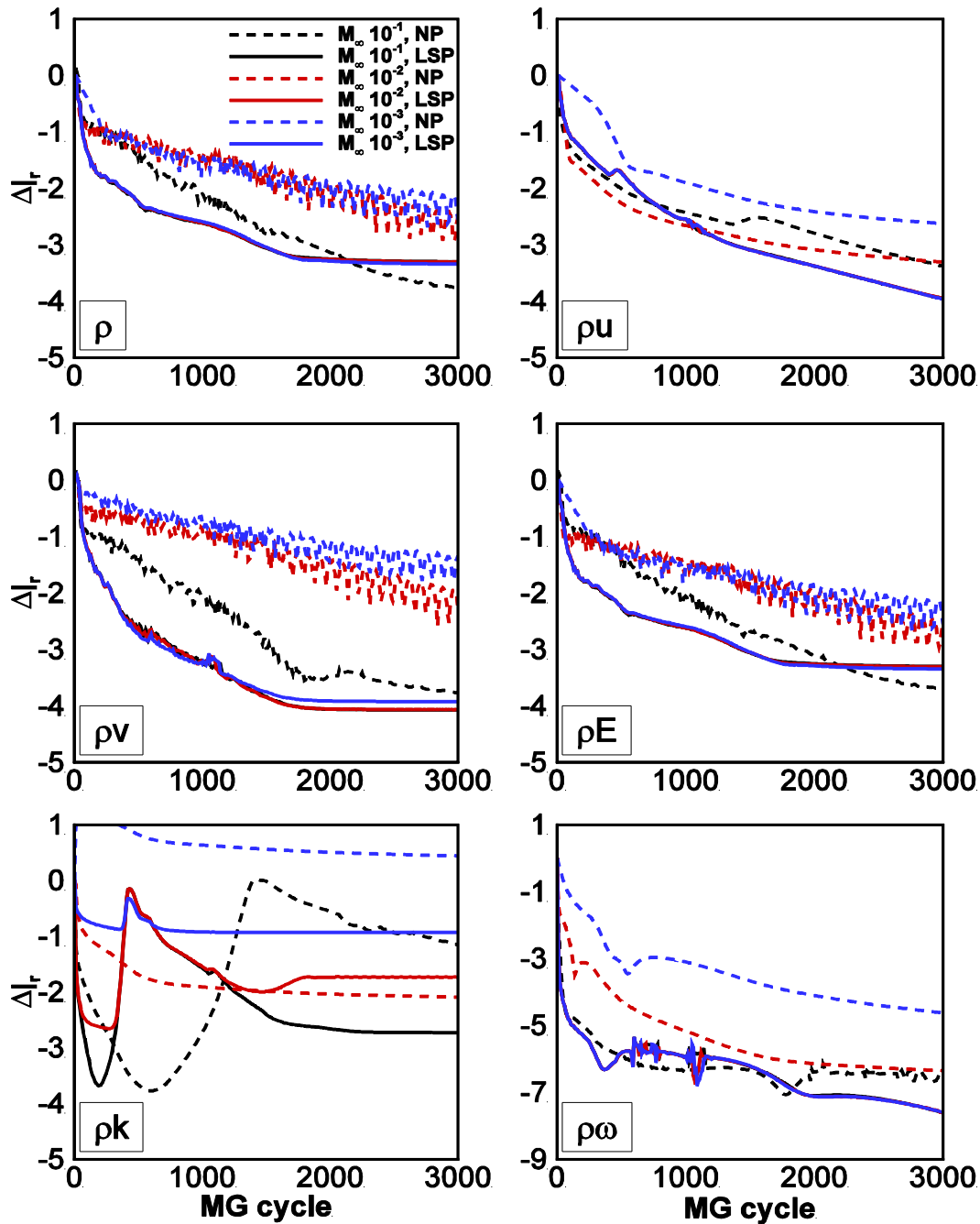


Figure 6.3 CONVERGENCE HISTORIES OF FLAT PLATE FLOW SIMULATIONS WITH AND WITHOUT LSP  $M_\infty = 0.1$ ,  $M_\infty = 0.01$  AND  $M_\infty = 0.001$ . TOP LEFT SUBPLOT: CONTINUITY EQUATION. TOP RIGHT SUBPLOT:  $x$ -COMPONENT OF MOMENTUM EQUATION. MIDDLE LEFT SUBPLOT:  $y$ -COMPONENT OF MOMENTUM EQUATION. MIDDLE RIGHT SUBPLOT: ENERGY EQUATION. BOTTOM LEFT SUBPLOT: TURBULENT KINETIC ENERGY EQUATION. BOTTOM RIGHT SUBPLOT: SPECIFIC DISSIPATION RATE EQUATION.

Inspection of the residual histories of the RANS and the  $\omega$  equations highlights that both the convergence rate and the overall residual drop of all three LSP simulations is independent of  $M_\infty$ , as expected on the basis of theoretical analyses. The general pattern of the convergence history of the  $k$ - equation of the three LSP simulations also shows an independent overall

drop of the residuals of this equations as  $M_\infty$  decreases, however the smaller order of magnitude of the drop of residuals compared with other flow variables is seen as a common problem for this turbulence model and noticed by many researchers. Figure 6.3 also shows that both the convergence rate and the overall drop of all residual histories of the three simulations without LSP vary significantly with  $M_\infty$ , denoting an increasing disparity between the characteristic acoustic and convective speeds as  $M_\infty$  decreases.

## 6.2 2D Backward facing step

In this case, a turbulent boundary layer encounters a sudden back step, causing flow separation. The flow then reattaches and recovers downstream of the step. The Reynolds number based on boundary layer momentum thickness prior to the step is 5000. This corresponds to a Reynolds number of approximately 36,000 based on step height  $H$ . The boundary layer thickness prior to the step is approximately  $1.5H$ . The boundary conditions adopted for the simulation of this problem are shown in Figure 6.4. Other than a short region with symmetry conditions imposed (to avoid possible incompatibilities between freestream inflow and wall BCs), both bottom and top walls are treated as viscous walls. In this case, the inflow length prior to the area of interest (near  $x=0$ ) has been adjusted so that the naturally developing turbulent boundary layer on the lower wall in the CFD solution grows to approximately the correct thickness and yields approximately the correct wall skin friction coefficient prior to the step. The back pressure is adjusted to yield approximately the correct Mach number ( $M=0.128$ ) upstream of the step.

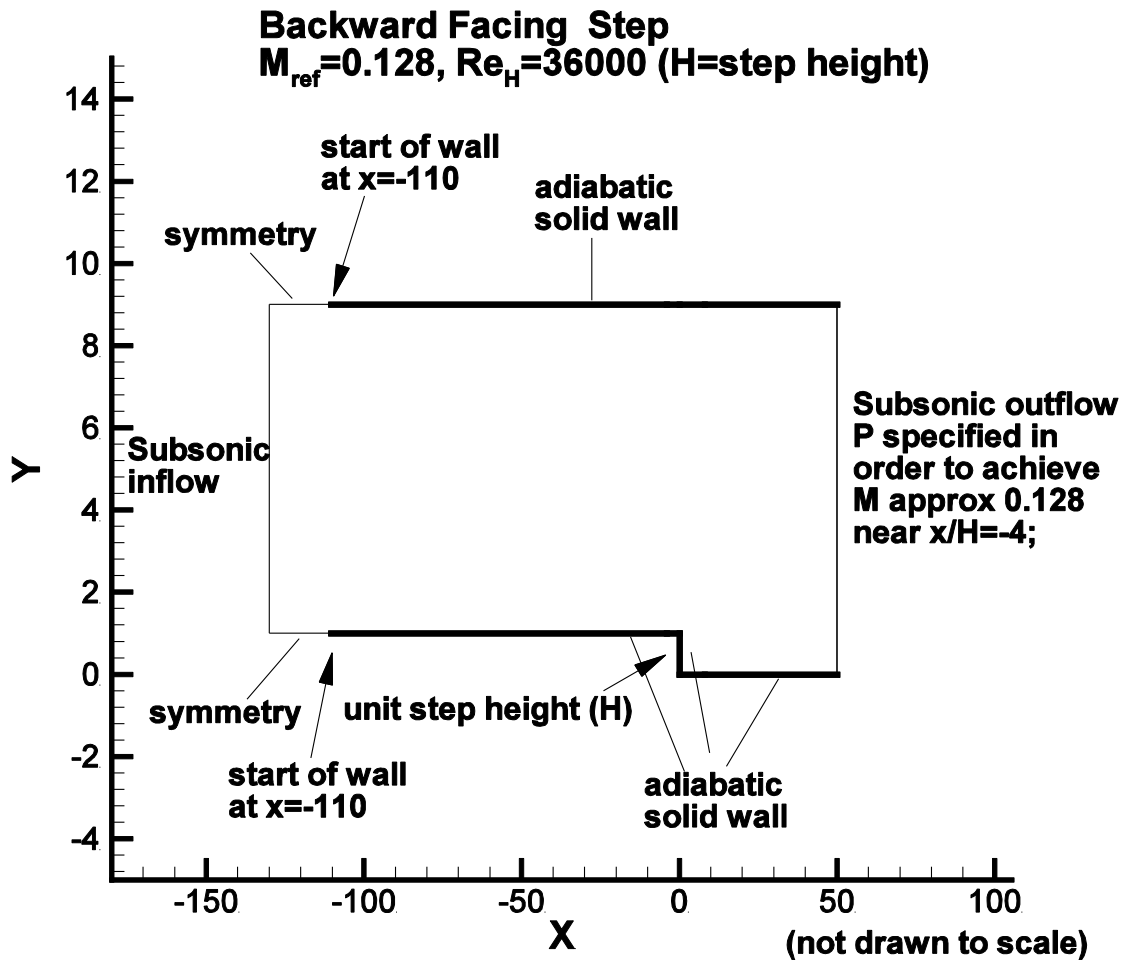


*Figure 6.4 IMPOSED BOUNDARY CONDITIONS FOR BACKWARD FACING STEP*

A series of 5 nested 2-D grids, non-dimensionalised by the step height  $H$ , are provided on NASA Research Centre website ([http://turbmodels.larc.nasa.gov/backstep\\_grids.html](http://turbmodels.larc.nasa.gov/backstep_grids.html)). Each coarser grid is exactly every-other-point of the next finer grid. As shown in the figure above, the computational domain is made up of two rectangular subdomains and the backward facing step is placed at  $x = 0$  on the lower wall. Figure 6.5 provides an enlarged view of the grid portion in the middle region. For visual clarity, only every second line of both grid line sets is plotted. The structured grid comprises 4 different zones, which are connected in a one to one fashion (for example, zone 1 and 2 prior to the step can easily be combined into one zone as they share the same number of cells in the normal direction; and zone 3 and 4 after the step can be combined into one zone for the same reason). Each zone of the grid has different number of cells, namely zone 1 with 129 grid points in both directions, zone 2 with 129 grid points in the normal direction and 49 points in the horizontal direction respectively, zone 3 with 225 and 193 grid points in the normal and horizontal directions and zone 4 with

225 and 65 grid points in the normal and horizontal directions respectively. The grid is stretched from both top and bottom walls to the centre of the domain in the normal wall direction and the clustering is maintained in both wall regions.

A preliminary mesh refinement analysis has revealed that the solution computed with the grid defined above presents negligible differences from the solution computed by using grids with higher spatial refinement. It should be noted that, the CFD results of CFL3D presented below is obtained by using the grid which is finer than that used in COSA (or the grid used in COSA simulations is exactly every-other-point of that in CFL3D), and no significant difference can be observed in the first case analysis of  $M_\infty = 0.128$ , which can be regarded as an advantage of the COSA solver to achieve a higher computational efficiency without any accuracy penalty.

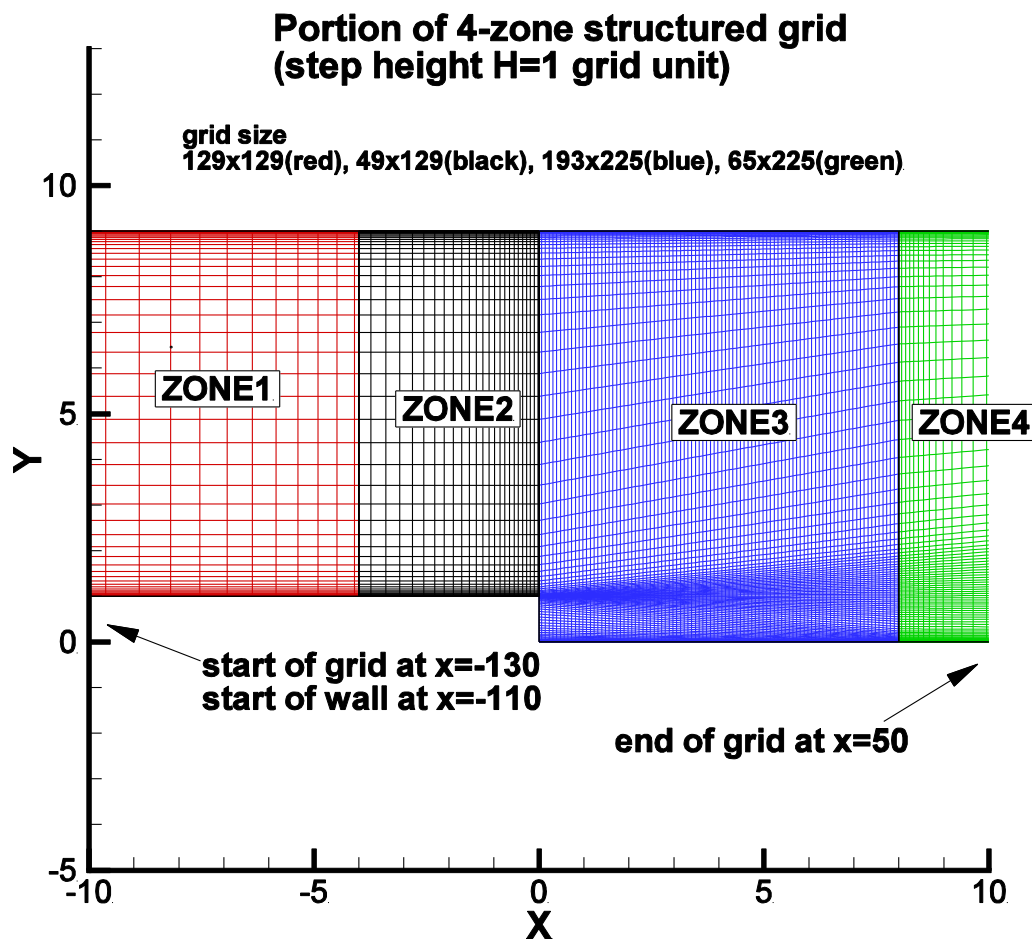


Figure 6.5 GRID VIEW IN BACKWARD FACING STEP REGION.  
([http://turbmodels.larc.nasa.gov/backstep\\_grids.htm](http://turbmodels.larc.nasa.gov/backstep_grids.htm))

Figure 6.6 and Figure 6.7 show the velocity profiles, skin friction coefficient and pressure coefficient of interest chosen at the following  $x/H$  locations, upstream of step  $x/H=-4$ , and downstream of the step  $x/H=1, 4, 6, 10$ . All the results compared in this section are obtained by CFL3D (Krist et al., 1998), a Navier-Stokes compressible CFD code developed at NASA Langley Research Centre for solving 2-D or 3-D flows on structured grids, by COSA with and without LSP and the experimental data provided by Driver and Seegmiller (1985) respectively. The  $U_{ref}$ , used to nondimensionalise the velocity profiles, is the reference velocity at the centre-channel near location  $x/H=-4$ , therefore velocity profile with respect to this particular location has been plotted in Figure 6.6 being a critical assessment of yielding the proper flow field while the back pressure is adjusted. The skin friction coefficient and pressure coefficient data are also measured and analysed with respect to conditions near this location. Note that all the plotted pressure coefficient data (experiment and CFD results) have been shifted so that  $c_p$  is 0 near the position  $x/H=40$ , and same modification is also done by Eça and Hoekstra (2008). Another important reason for shifting the plotted  $c_p$  profiles, which also applies to the other two internal flow problem analyses, is that the static pressure coefficient defined as  $c_p = (p - p_{ref}) / (0.5\rho M_\infty^2)$ , is in fact the pressure difference divided by a constant head, however the reference pressure value  $p_{ref}$  is somehow dependent on the imposed subsonic inflow and outflow conditions and may be different from the one used in the experiment, therefore we have shifted uniformly all the computed  $c_p$  profiles and achieve the same values as the experiment data for a specific location, thus ensuring a better presentation and analysis of the results.

The simulation results of COSA depicted in top, middle, and bottom subplot rows of Figure 6.6 refer to the value of  $M_\infty$  of 0.128, 0.0128 and 0.00128 respectively, and each subplot provides the velocity profile of the simulations with and without LSP, while the experiment data and CFL3D results are always with respect to the value of  $M_\infty$  of 0.128. The term ‘SST’ appearing in the legend stands for the turbulence model applied in both CFL3D and COSA solver, while  $129 \times 129$  and  $256 \times 256$  represent the grid size of the 1<sup>st</sup> ZONE in two adopted meshes used by both solvers. This figure highlights that the velocity profile chosen at the locations of interest predicted by the compressible analysis without LSP starts being affected by significant errors already at  $M_\infty = 0.0128$ . The LSP-enhanced solver, however, has demonstrated a highly accurate predictive ability of the velocity profile compared with the two benchmark data in case  $M_\infty$  0.128 regardless of the variation of the Mach number.

A similar conclusion can also be drawn by analysing the plots of skin friction coefficient  $c_f$  and pressure coefficient  $c_p$  shown in Figure 6.7, where results obtained using COSA with and without LSP at three different Mach numbers are displayed in the top, middle and bottom rows respectively. More importantly, as one key measure of success for this flow field is the prediction of reattachment point downstream of the step, which is determined (by laser oil-flow interferometer measurements of skin-friction and interpolation of the zero skin-friction location) to be:  $x/H_{reattach} = 6.26 \pm 0.10$  in the experiment, an accurate prediction of the reattachment point has shown to be well maintained for a wide range of Mach numbers with implementing the LSP approach.

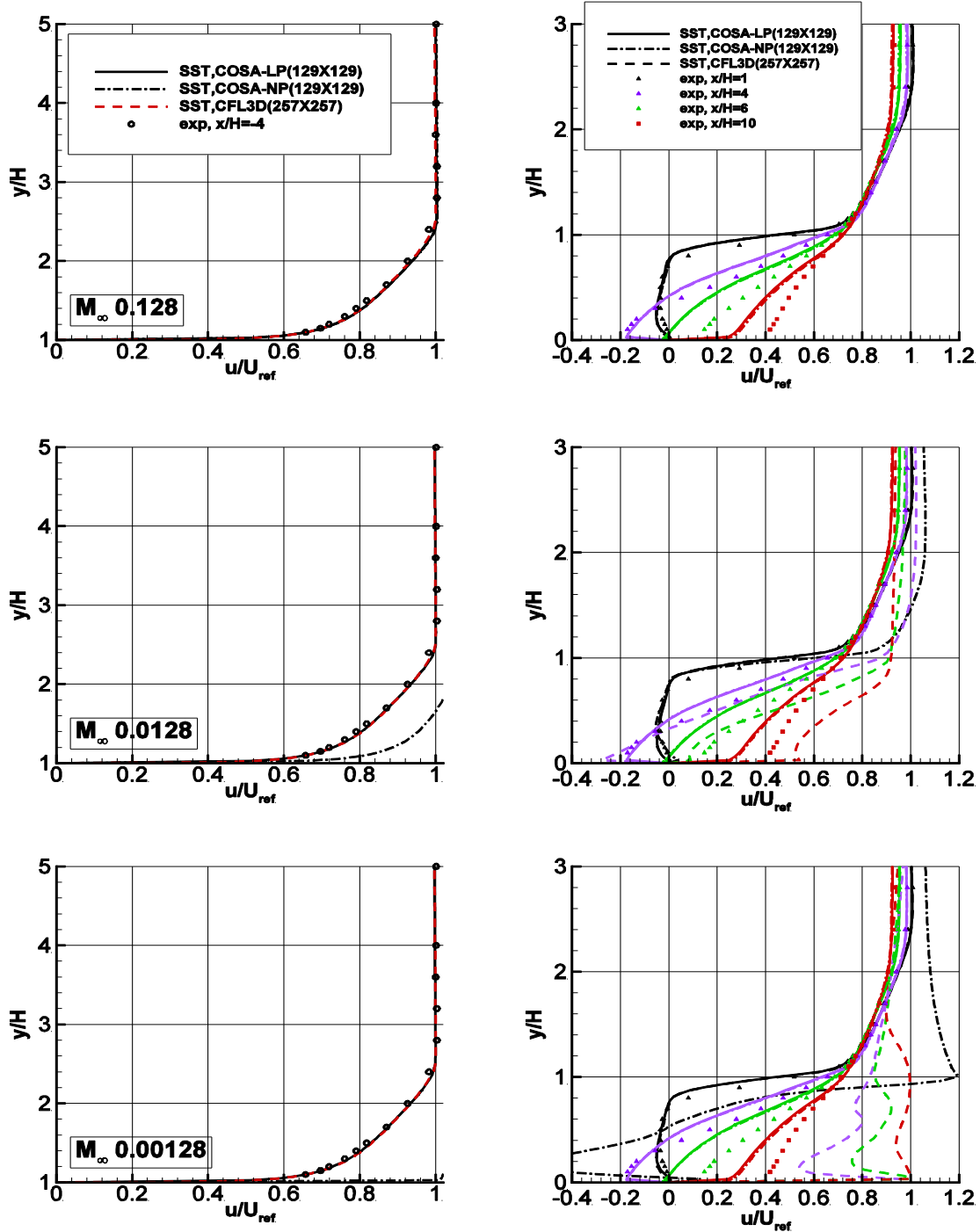


Figure 6.6 COMPARISON OF VELOCITY PROFILE NEAR THE BOUNDARY LAYER NORMALISED BY THE REFERENCE VELOCITY AT THREE VALUES OF  $M_\infty$  OBTAINED BY CFL3D, COSA WITH AND WITHOUT LSP AND EXPERIMENT DATA. TOP LEFT SUBPLOT: VELOCITY PROFILE AT  $x/H=-4$ ,  $M_\infty = 0.128$ . MIDDLE LEFT SUBPLOT: VELOCITY PROFILE AT  $x/H=-4$ ,  $M_\infty = 0.0128$ . BOTTOM LEFT SUBPLOT: VELOCITY PROFILE AT  $x/H=-4$ ,  $M_\infty = 0.00128$ . TOP RIGHT SUBPLOT: VELOCITY PROFILE AT  $x/H=1,4,6,10$ ,  $M_\infty = 0.128$ . MIDDLE RIGHT SUBPLOT: VELOCITY PROFILE AT  $x/H=1,4,6,10$ ,  $M_\infty = 0.0128$ . BOTTOM RIGHT SUBPLOT: VELOCITY PROFILE AT  $x/H=1,4,6,10$ ,  $M_\infty = 0.00128$ .

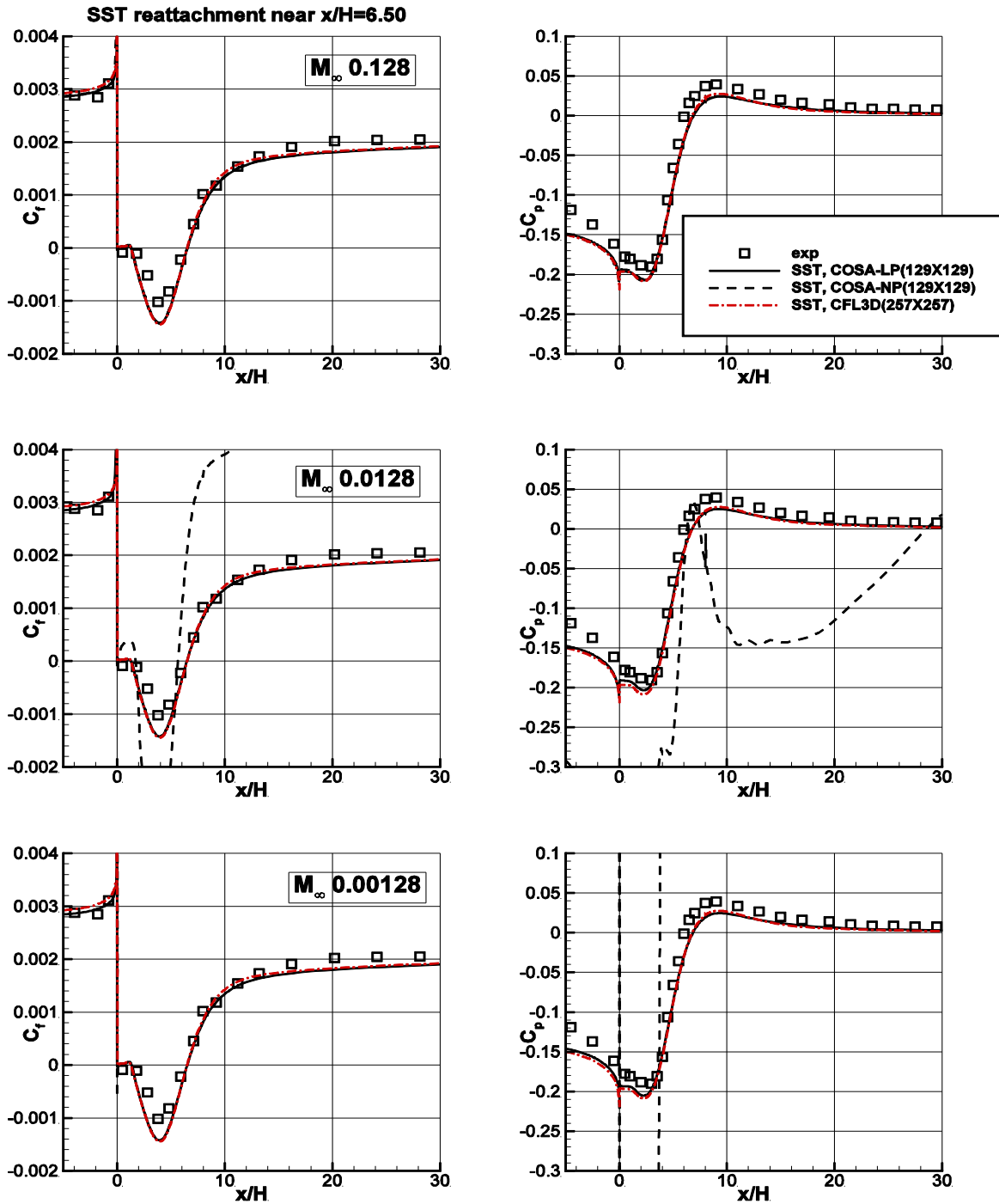


Figure 6.7 COMPARISON OF SKIN FRICTION COEFFICIENT  $c_f$  AND PRESSURE COEFFICIENT  $c_p$  AT THREE VALUES OF  $M_\infty$  OBTAINED BY CFL3D, COSA WITH AND WITHOUT LSP AND EXPERIMENT DATA. TOP LEFT SUBPLOT: SKIN FRICTION COEFFICIENT  $c_f$ ,  $M_\infty = 0.128$ . MIDDLE LEFT SUBPLOT: SKIN FRICTION COEFFICIENT  $c_f$ ,  $M_\infty = 0.0128$ . BOTTOM LEFT SUBPLOT: SKIN FRICTION COEFFICIENT  $c_f$ ,  $M_\infty = 0.00128$ . TOP RIGHT SUBPLOT: PRESSURE COEFFICIENT  $c_p$ ,  $M_\infty = 0.128$ . MIDDLE RIGHT SUBPLOT: PRESSURE COEFFICIENT  $c_p$ ,  $M_\infty = 0.0128$ . BOTTOM RIGHT SUBPLOT: PRESSURE COEFFICIENT  $c_p$ ,  $M_\infty = 0.00128$

## 6.3 2D NASA wall-mounted hump

A NASA wall-Mounted hump experiment is considered here for validating the ability of the LSP implementation of our CFD solver to predict separated 2D flows. A Glauert-Goldschmied type body is mounted in the lower wall, and the whole model is fixed between two glass endplate frames, of which both the leading and trailing edges are faired smoothly with a wind tunnel splitter plate, such that it can be treated as a two-dimensional experiment for CFD validation. A more detailed description of the experiment is provided in NASA (2004). This test case focuses primarily on assessing the ability of turbulence models to predict 2-D separation from a smooth body caused by adverse pressure gradient as well as subsequent reattachment and boundary layer recovery, moreover, the validation of the LSP capability is also performed by analysing the test cases of extremely low Mach numbers.

The reference freestream velocity in this case is taken at the position  $x/c=-2.14$ , which is approximately 34.6 m/s ( $M_\infty = 0.1$ ) and the incoming fully turbulent boundary layer is regarded to develop fully at the same position with thickness of approximately 35 mm, or about 8%c (the bump "chord" is 420 mm). The back pressure has been adjusted to yield the above desired flow. A sufficient upstream length is chosen to ensure the natural development of the fully turbulent boundary layer as well as the correct boundary layer thickness achieved approximately upstream of the hump. In Figure 6.8, an overview of the adopted BCs is shown for the case, while Figure 6.9 provides the detailed layout near the slot. A small contour is included in the upper wall surface to approximately account for the blockage caused by the end plates in the experiment. In terms of the inlet and outlet boundary conditions, "Pt" stands for the total pressure, "P" refers to the static pressure, and "Tt" represents the total temperature. The Reynolds number based on the bump chord for this case is determined to be 936000. To be noted that, the test case can be run either with or without the plenum/chamber (the plenum was present in the experiment and only for the no-flow-control purpose). Although it is not crucial to include the plenum in the numerical analysis, we have chosen to adopt the same mesh with such structure by which the simulation results of CFL3D is obtained.

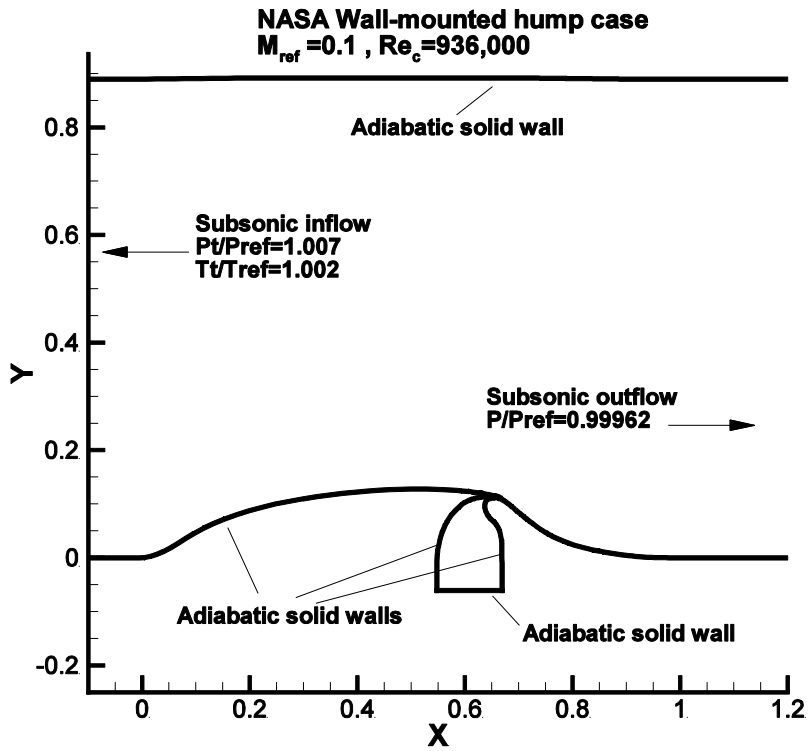


Figure 6.8 IMPOSED BOUNDARY CONDITIONS FOR NASA WALL-MOUNTED HUMP CASE

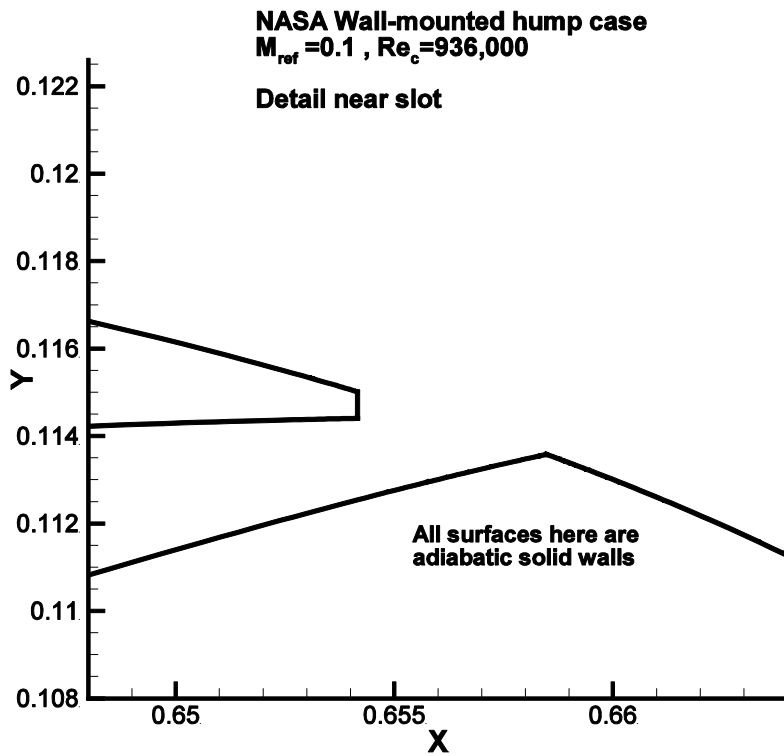


Figure 6.9 IMPOSED BOUNDARY CONDITIONS NEAR THE SLOT FOR NASA WALL-MOUNTED HUMP CASE

There are two computational meshes supplied by NASA workshop (NASA, 2004) for the wall-mounted hump case, which are called the "fine" and "medium" levels of structured grid, containing 210,060 grid points and 52,952 grid points respectively (the 'medium' one is obtained by taking exactly every other point from the fine grid in each coordinate direction).. The finest grid has minimum wall distance of approximately  $y = 8 \cdot 10^{-6}$ , yielding an approximate average  $y^+$  between 0.1 and 0.2 over the hump. A general description is given in Figure 6.10 for the coarser "medium" grid, where stretched grid spacing can be seen in the wall-normal direction. Figure 6.11 and Figure 6.12, on the other hand, show the local view of the grid near the chamber and slot. Same as in the backward facing step case, negligible difference is found between the solutions computed with the two levels of grid mentioned above through a mesh refinement analysis. Therefore, the medium grid is adopted for all calculations performed by COSA in purpose of higher computational efficiency.

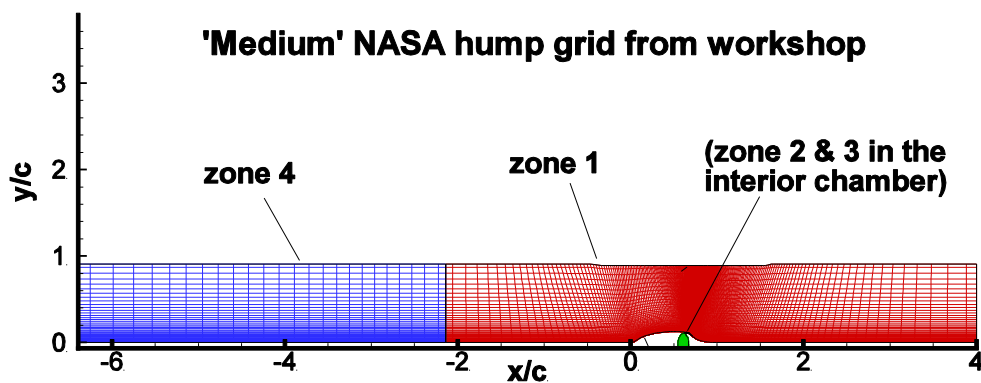


Figure 6.10 OVERALL GRID VIEW FOR MEDIUM NASA HUMP GRID (NASA, 2004)

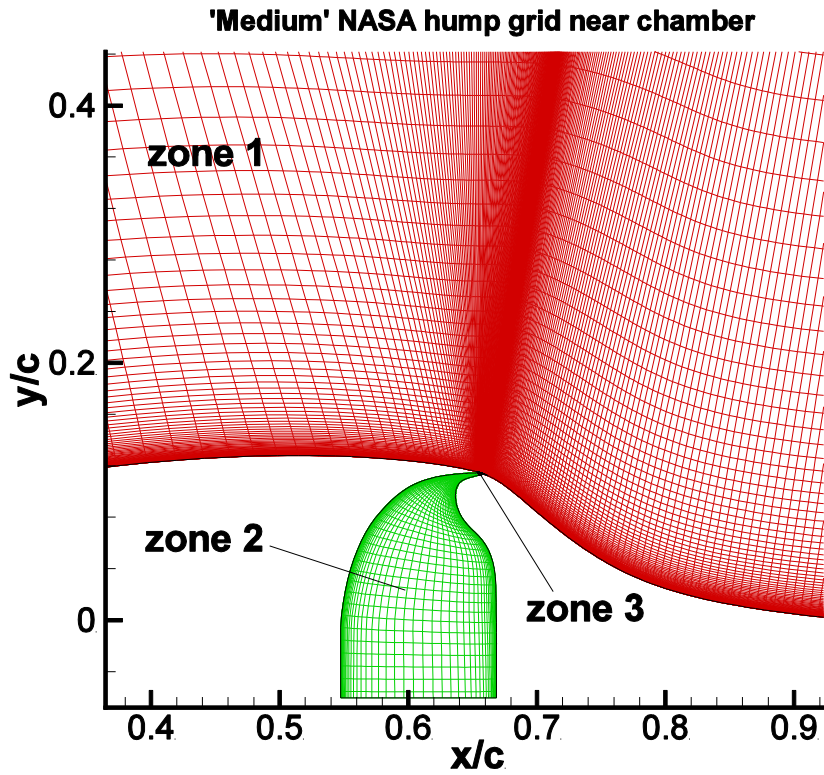


Figure 6.11 GRID VIEW NEAR CHAMBER FOR MEDIUM NASA HUMP GRID

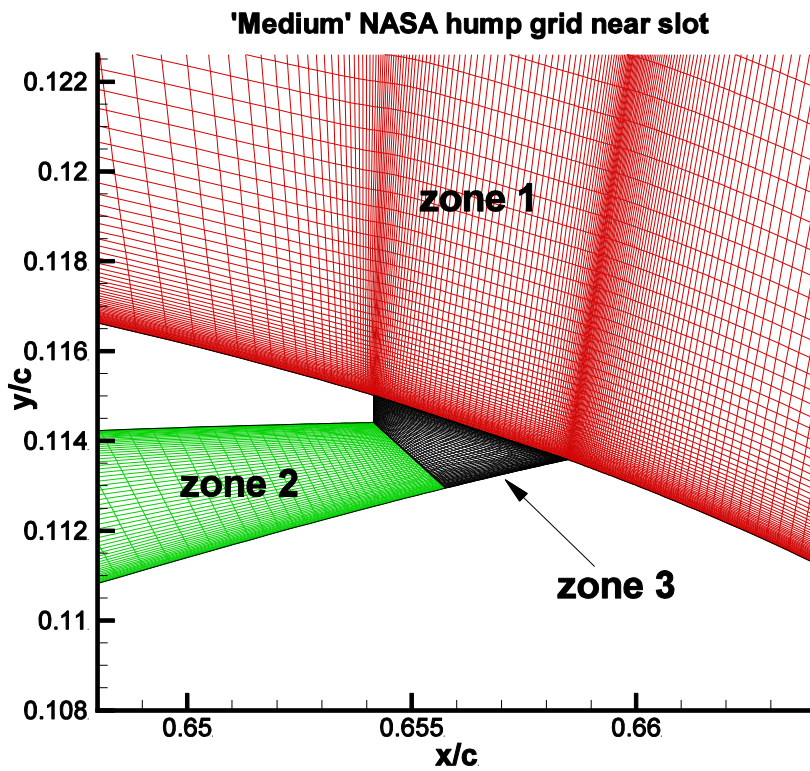


Figure 6.12 GRID VIEW NEAR SLOT FOR MEDIUM NASA HUMP GRID

Comparisons of the CFD results (COSA and CFL3D) and experiment data (Greenblatt et al., 2004) are displayed in Figure 6.13 and Figure 6.14, in terms of the velocity profiles, skin friction coefficient and pressure coefficient chosen at the following  $x/c$  locations of interest, upstream of hump  $x/c=-2.14$ , and downstream of  $x/c=0.65, 0.9, 1.1, 1.3$ . Note that all the CFD pressure coefficient data have been plotted being shifted uniformly so that  $c_p$  can better match the experiment reference value of the upstream.

The simulated results of COSA depicted in top, middle, and bottom subplot rows of Figure 6.13 refer to the value of  $M_\infty$  of 0.1, 0.01 and 0.001 respectively, and each subplot provides the velocity profile of the simulations with and without LSP, while the experiment data and CFL3D results are always with respect to the value of  $M_\infty$  of 0.1. The term ‘SST’ appearing in the legend stands for the turbulence model applied in both CFL3D and COSA solver, while 52k and 210k represent the grid size or grid points of the two different levels of meshes adopted by each solver. The figure again highlights that the velocity profile chosen at the locations of interest predicted by the compressible analysis without LSP starts being affected by significant errors already at  $M_\infty = 0.01$ . The LSP-enhanced solver, however, has demonstrated a highly accurate predictive ability of the velocity profile compared with the two benchmark data of  $M_\infty$  0.1, particularly in the most difficult case of the lowest Mach number of 0.001, no significant difference can be spotted. The same conclusion is also achieved after analysing the plots of skin friction coefficient  $c_f$  and pressure coefficient  $c_p$  shown in Figure 6.14, where results obtained using COSA with and without LSP at three different Mach numbers are displayed in the top, middle and bottom rows respectively. Regardless of the variation of the Mach number, the skin friction coefficient and pressure coefficient are both accurately predicted using the LSP-enhanced solver, which has demonstrated an independent flow predictive ability of free stream Mach number being consistent with the theoretical analyses (the LSP approach should yield the same solutions regardless of the change of flow velocity).

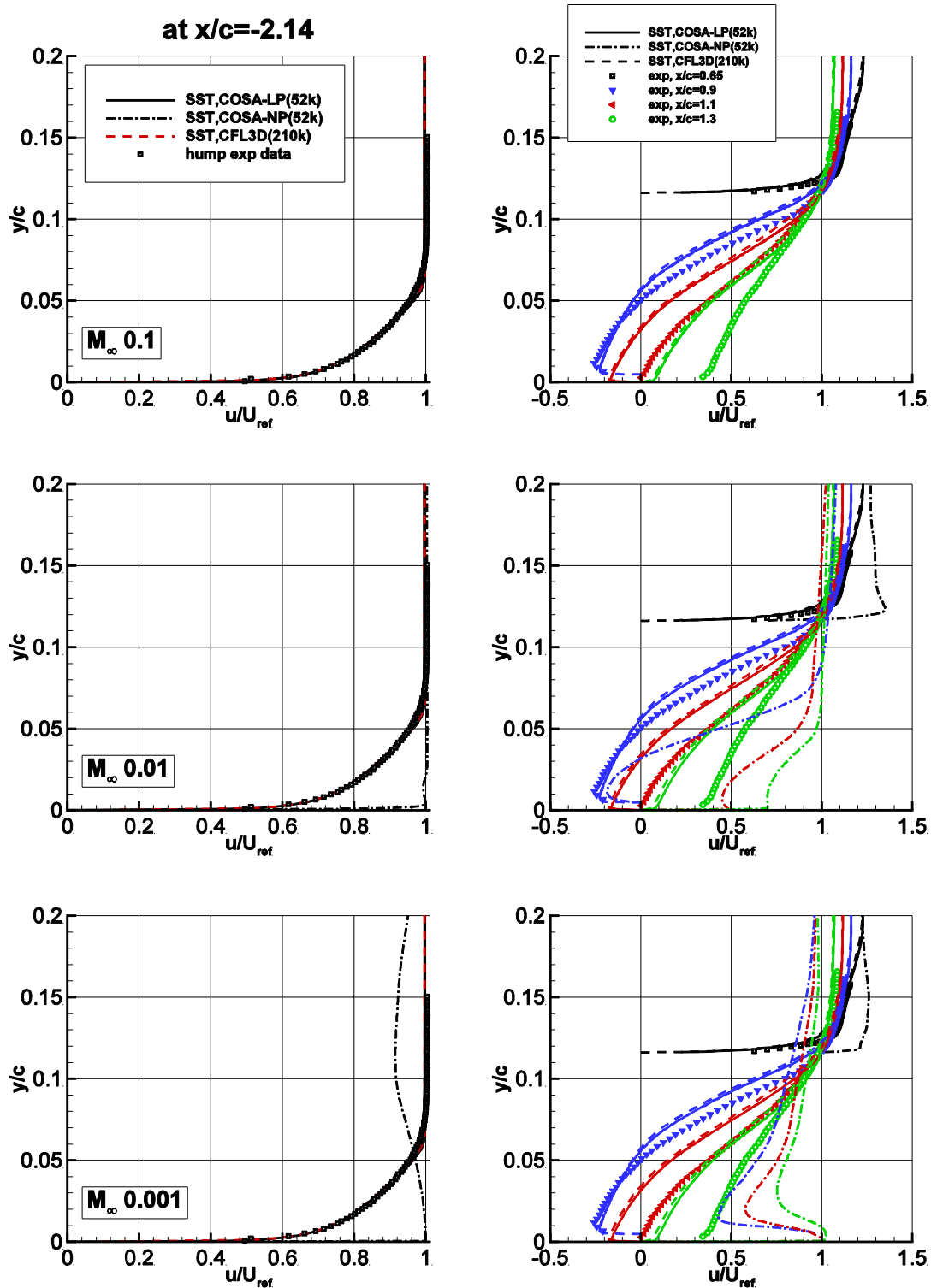


Figure 6.13 COMPARISON OF VELOCITY PROFILE NEAR THE BOUNDARY LAYER NORMALISED BY THE REFERENCE VELOCITY OBTAINED BY CFL3D, COSA WITH AND WITHOUT LSP AND EXPERIMENT DATA. TOP LEFT SUBPLOT: VELOCITY PROFILE AT  $X/C=-2.14$ ,  $M_\infty = 0.1$ . MIDDLE LEFT SUBPLOT: VELOCITY PROFILE AT  $X/C=-2.14$ ,  $M_\infty = 0.01$ . BOTTOM LEFT SUBPLOT: VELOCITY PROFILE AT  $X/C=-2.14$ ,  $M_\infty = 0.001$ . TOP RIGHT SUBPLOT: VELOCITY PROFILE AT  $X/C=0.65, 0.9, 1.1, 1.3$ ,  $M_\infty = 0.1$ . MIDDLE RIGHT SUBPLOT: VELOCITY PROFILE AT  $X/C=0.65, 0.9, 1.1, 1.3$ ,  $M_\infty = 0.01$ . BOTTOM RIGHT SUBPLOT: VELOCITY PROFILE AT  $X/C=0.65, 0.9, 1.1, 1.3$ ,  $M_\infty = 0.001$

### 6.3 2D NASA wall-mounted hump

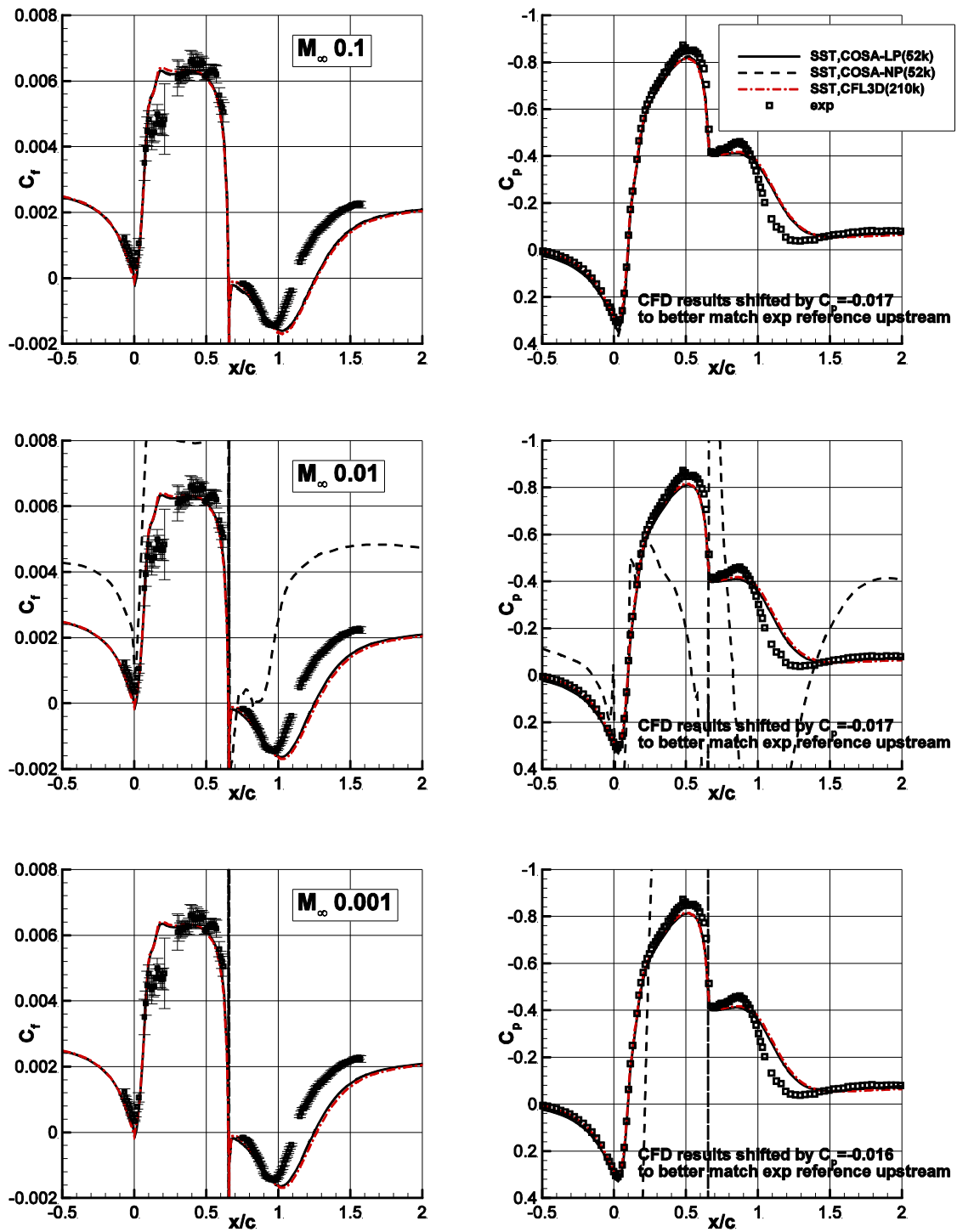


Figure 6.14 COMPARISON OF SKIN FRICTION COEFFICIENT  $c_f$  AND PRESSURE COEFFICIENT  $c_p$  OBTAINED BY CFL3D, COSA WITH AND WITHOUT LSP AND EXPERIMENT DATA. TOP LEFT SUBPLOT: SKIN FRICTION COEFFICIENT  $c_f$ ,  $M_\infty = 0.1$ . MIDDLE LEFT SUBPLOT: SKIN FRICTION COEFFICIENT  $c_f$ ,  $M_\infty = 0.01$ . BOTTOM LEFT SUBPLOT: SKIN FRICTION COEFFICIENT  $c_f$ ,  $M_\infty = 0.001$ . TOP RIGHT SUBPLOT: PRESSURE COEFFICIENT  $c_p$ ,  $M_\infty = 0.1$ . MIDDLE RIGHT SUBPLOT: PRESSURE COEFFICIENT  $c_p$ ,  $M_\infty = 0.01$ . BOTTOM RIGHT SUBPLOT: PRESSURE COEFFICIENT  $c_p$ ,  $M_\infty = 0.001$ .

## 6.4 2D Convex Curvature Boundary Layer

The 2D convex curvature boundary layer case considered here refers to the experiment carried out by Smits et al. (1979), which utilises a constant area square duct of height 0.127m with a 30 degree bend in the middle section of the duct (inner radius of curvature is 0.127 m). The primary focus of the original case is to assess turbulence models for convex wall curvature (the lower wall in this case), in addition to this purpose we also aim to validate the implementation of LSP for solving problems of lower Mach numbers. The challenge of this case is that the turbulence level and the thickness of the boundary layer will increase as a result of the destabilised boundary layer near the concave wall. The quasi-stable Gortler vortices generally formed in concave curvature can lead to steady or slowly varying large-scale spanwise variations in the boundary layer, which has been verified by significant spanwise variations of the skin friction measured in experiment of Smits et al. (1979). Considering the nature of streamwise flow in concave curvature, the differences noticed between the CFD solution and experiment data in this region should be interpreted by accounting for both the uncertainty in the test results and the impossibility of capturing the effects of Gortler vortices in a 2D steady state simulation. The reference freestream velocity ( $U_{ref}$ ) in this case is taken near the inlet, which is approximately 31.9 m/s ( $M_\infty = 0.093$ ). The back pressure has been adjusted to yield the above desired flow. A sufficient upstream length is chosen to ensure the natural development of the fully turbulent boundary layer as well as the correct boundary layer thickness achieved approximately upstream of the bend. Both upper and lower boundaries are modelled as adiabatic solid walls.

An overview of the adopted BCs is shown for the case in Figure 6.15. In terms of the inlet and outlet boundary conditions, "Pt" stands for the total pressure, "P" refers to the static pressure, and "Tt" represents the total temperature. The Reynolds number based on the grid unit length for this case is determined to be  $2.1 \cdot 10^6$ . Since all simulation results shown below are plotted against the x-axis value in a Cartesian coordinate rather than the distance value  $s$  along the curved duct wall, a formulation used to translate the two types of distances can be derived based on the coordinate system given in Figure 6.16:

$$\text{if } s < -0.066497, x = -0.0635 + (s + 0.0665) \cos 30 \quad (6.1)$$

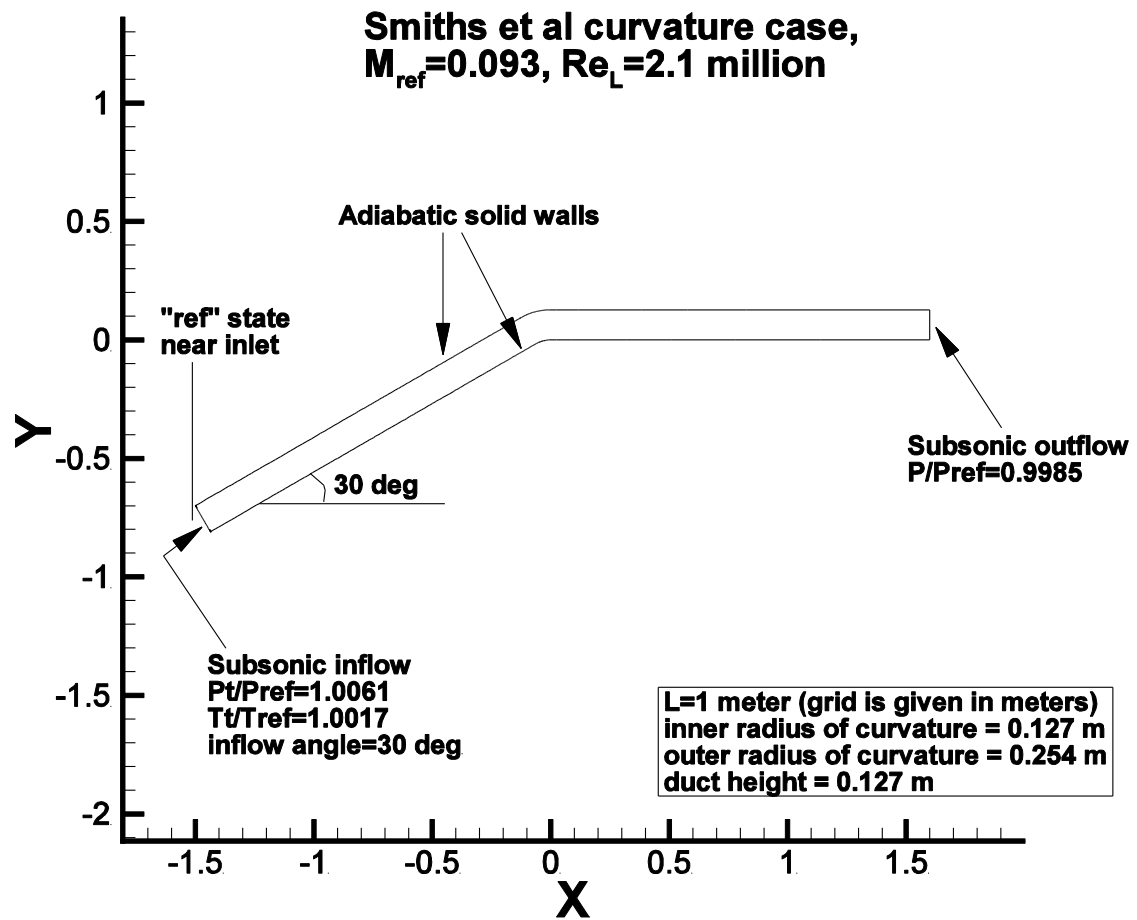


Figure 6.15 IMPOSED BOUNDARY CONDITIONS FOR 2D CONVEX CURVATURE BOUNDARY LAYER CASE

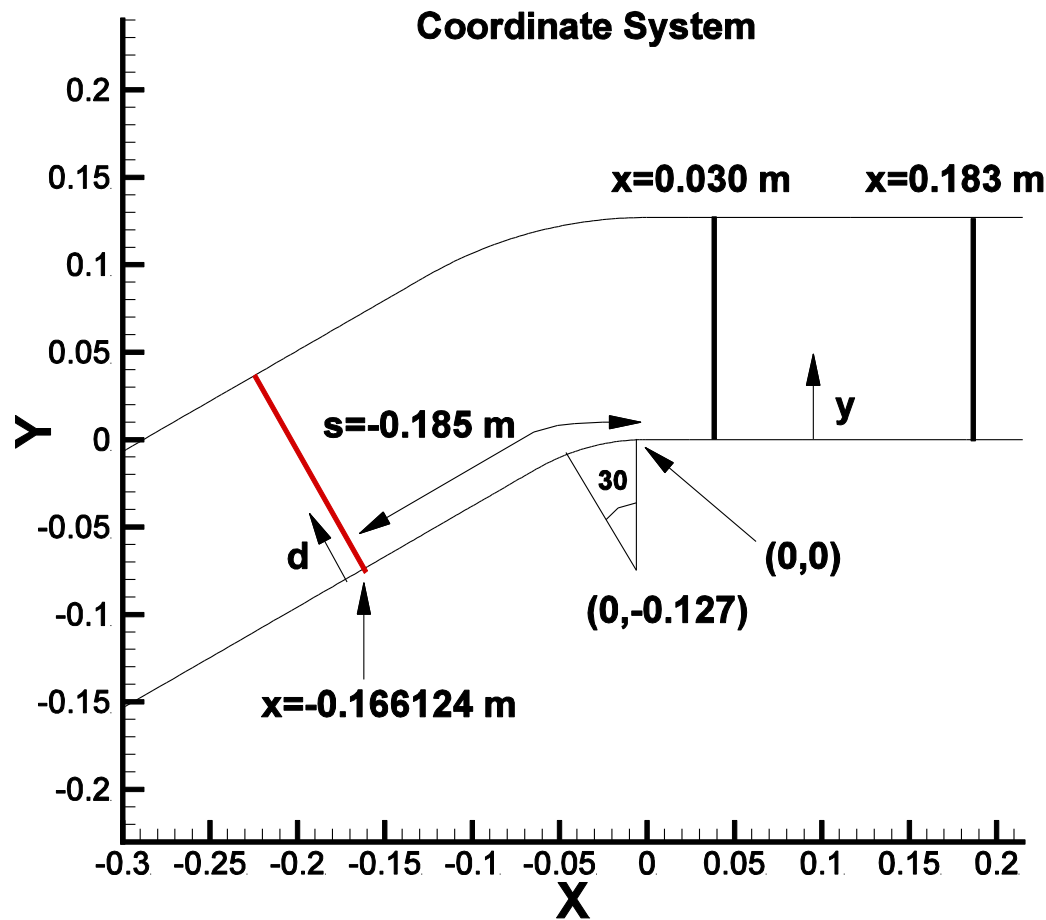
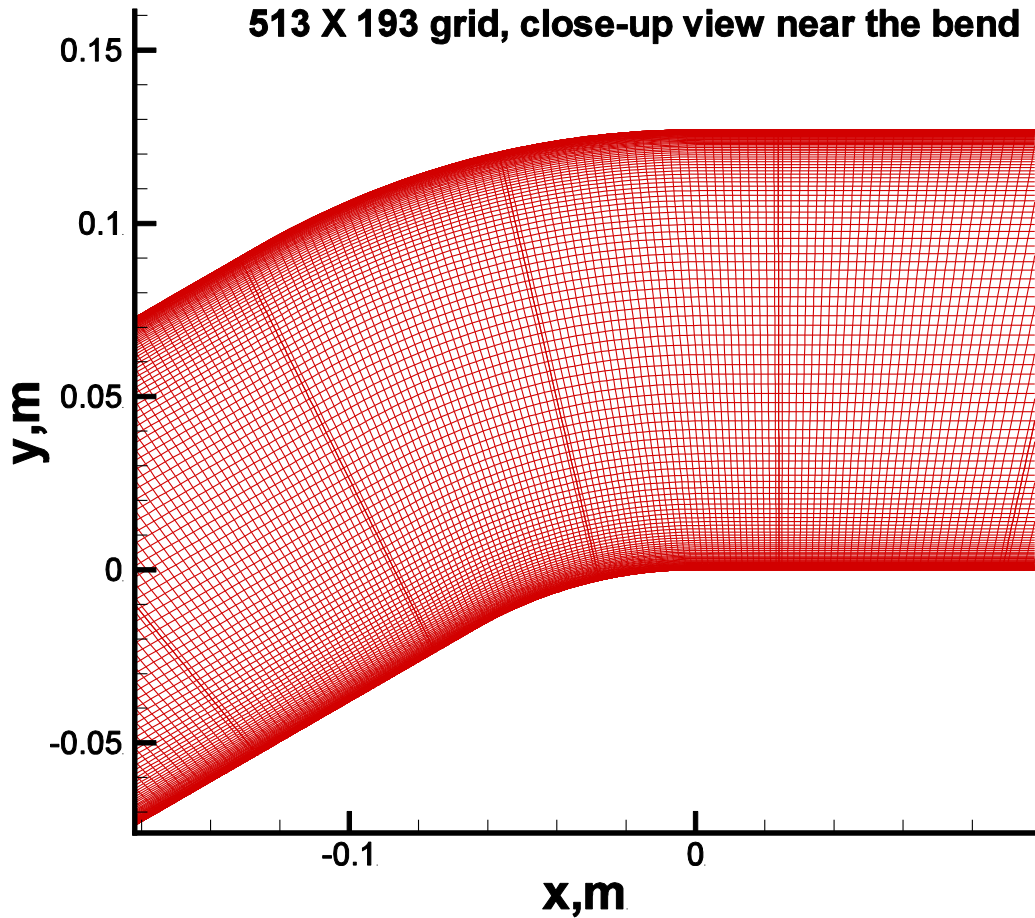


Figure 6.16 COORDINATE SYSTEM VIEW NEAR THE BEND

A series of 5 nested 2D grids are provided on NASA Langley Research Centre website ([http://turbmodels.larc.nasa.gov/smitscurve\\_grids.html](http://turbmodels.larc.nasa.gov/smitscurve_grids.html)) for the Convex Curvature case. Each coarser grid is obtained by maintaining exactly every-other-point of the current finer grid, ranging from the finest  $1025 \times 385$  (defined by the product of the grid point number in the streamwise direction times that in the normal wall direction) to the coarsest  $65 \times 25$  grid. The finest grid has minimum wall distance of about  $y = 1.1 \cdot 10^{-6}$ , giving an approximate average  $y^+$  of less than 0.1 at the Reynolds number specified. The grid is stretched from both walls in the wall-normal direction, and there is some stream-wise clustering near the bend. A mesh refinement analysis has yielded an insignificant difference between the solutions computed with the finest grid  $1025 \times 385$  and the grid of the second coarser level  $513 \times 193$ , therefore both CFL3D and COSA have adopted the coarser mesh in all simulations, and a near-field view is shown in Figure 6.17 for the particular bend section of this grid.



*Figure 6.17 GRID VIEW FOR CONVEX CURVATURE BOUNDARY LAYER CASE NEAR THE BEND  
([http://turbmodels.larc.nasa.gov/smitscurve\\_grids.html](http://turbmodels.larc.nasa.gov/smitscurve_grids.html))*

Comparisons of the CFD results (COSA and CFL3D) and experiment data (Smits et al., 1979) are displayed in Figure 6.18 and Figure 6.19, in terms of the velocity profiles chosen at the following locations of interest, upstream of the bend  $x=-0.166124\text{m}$  (all distance values presented in this section are in the unit of meters), and downstream of  $x=0.030\text{m}$ ,  $0.183\text{m}$ ,  $0.335\text{m}$ ,  $0.635\text{m}$ ,  $1.25\text{m}$  and skin friction coefficient and pressure coefficient along the wall. For the velocity profile plotted upstream of the bend where  $x=-0.166124\text{ m}$ , particular attention should be paid to the velocity component  $u_p$  which is parallel to the wall and canted at 30 degree relative to x-axis in Cartesian coordinates, therefore a formulation to compute this variable  $u_p$  using the velocities in the Cartesian system is given as below,

$$u_p = u \cos \theta + v \sin \theta \quad (6.2)$$

where  $\theta$  is the inflow angle (30 degree in this case). The distance  $d$  appearing as the  $y$ -component is measured in the normal wall direction across the channel at the upstream location.

Note that all CFD results of the pressure coefficient have been plotted being uniformly shifted so that  $c_p$  can better match the experiment reference value of the upstream. The simulated results of COSA depicted in top, middle, and bottom subplot rows of Figure 6.18 refer to the value of  $M_\infty$  of 0.093, 0.0093 and 0.00093 respectively, and each subplot provides the velocity profile of the simulations with and without LSP, while the experiment data and CFL3D results are always with respect to the value of  $M_\infty$  of 0.093. The term ‘‘SST’’ appearing in the legend stands for the turbulence model applied in both CFL3D and COSA solver, while ‘‘513X193’’ represent the grid size of the mesh adopted by the two solvers. The figure again highlights that the velocity profile chosen at the locations of interest predicted by the compressible analysis without LSP starts being affected by significant errors already at  $M_\infty = 0.0093$ . The LSP-enhanced solver, however, has demonstrated a highly accurate predictive ability of the velocity profile compared with the two benchmark data of  $M_\infty = 0.093$ , particularly in the case of the lowest Mach number of 0.00093, indistinguishable difference is found between the solutions of COSA-LSP solver and those of CFL3D and the experiment data for  $M_\infty = 0.093$ . The same conclusion is also verified by analysing the plots of the skin friction coefficient  $c_f$  and the pressure coefficient  $c_p$  shown in Figure 6.19, where results obtained using COSA with and without LSP at three different Mach numbers are displayed in the top, middle and bottom rows respectively. Regardless of the variation of the Mach number, the skin friction coefficient and pressure coefficient are both accurately predicted using the LSP-enhanced solver, which has demonstrated an independent flow predictive ability of free stream Mach number consistent with the theoretical analyses.

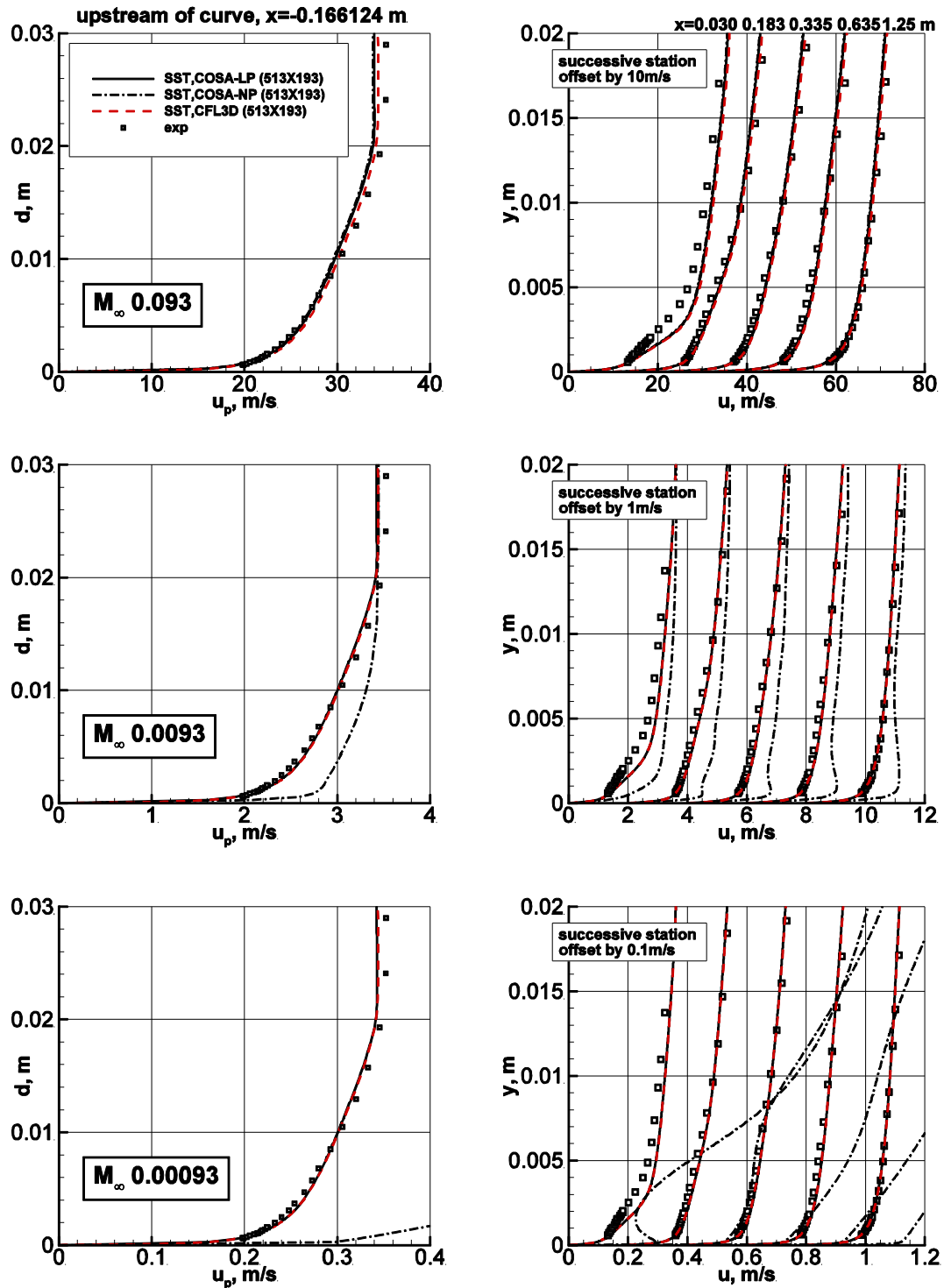


Figure 6.18 COMPARISON OF VELOCITY PROFILE NEAR THE BOUNDARY LAYER AT THREE VALUES OF  $M_\infty$  OBTAINED BY CFL3D, COSA WITH AND WITHOUT LSP AND EXPERIMENT DATA. TOP LEFT SUBPLOT: VELOCITY PROFILE AT  $X=-0.166124m$ ,  $M_\infty = 0.093$ . MIDDLE LEFT SUBPLOT: VELOCITY PROFILE  $X=-0.166124m$ ,  $M_\infty = 0.0093$ . BOTTOM LEFT SUBPLOT: VELOCITY PROFILE  $X=-0.166124m$ ,  $M_\infty = 0.00093$ . TOP RIGHT SUBPLOT: VELOCITY PROFILE AT  $X=0.030, 0.183, 0.335, 0.635, 1.25m$ ,  $M_\infty = 0.093$ . MIDDLE RIGHT SUBPLOT: VELOCITY PROFILE AT  $X=0.030, 0.183, 0.335, 0.635, 1.25m$ ,  $M_\infty = 0.0093$ . BOTTOM RIGHT SUBPLOT: VELOCITY PROFILE AT  $X=0.030, 0.183, 0.335, 0.635, 1.25m$ ,  $M_\infty = 0.00093$ .

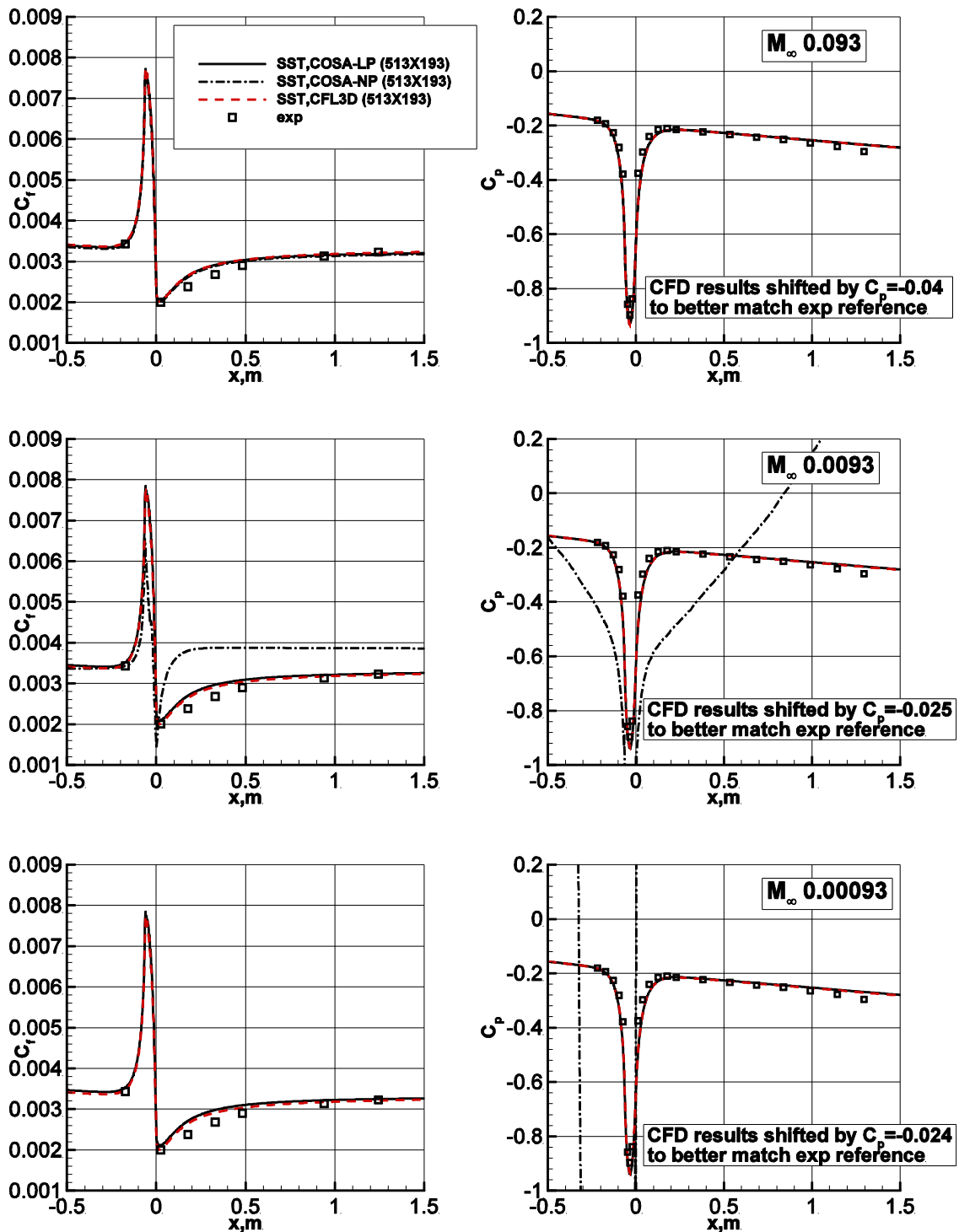
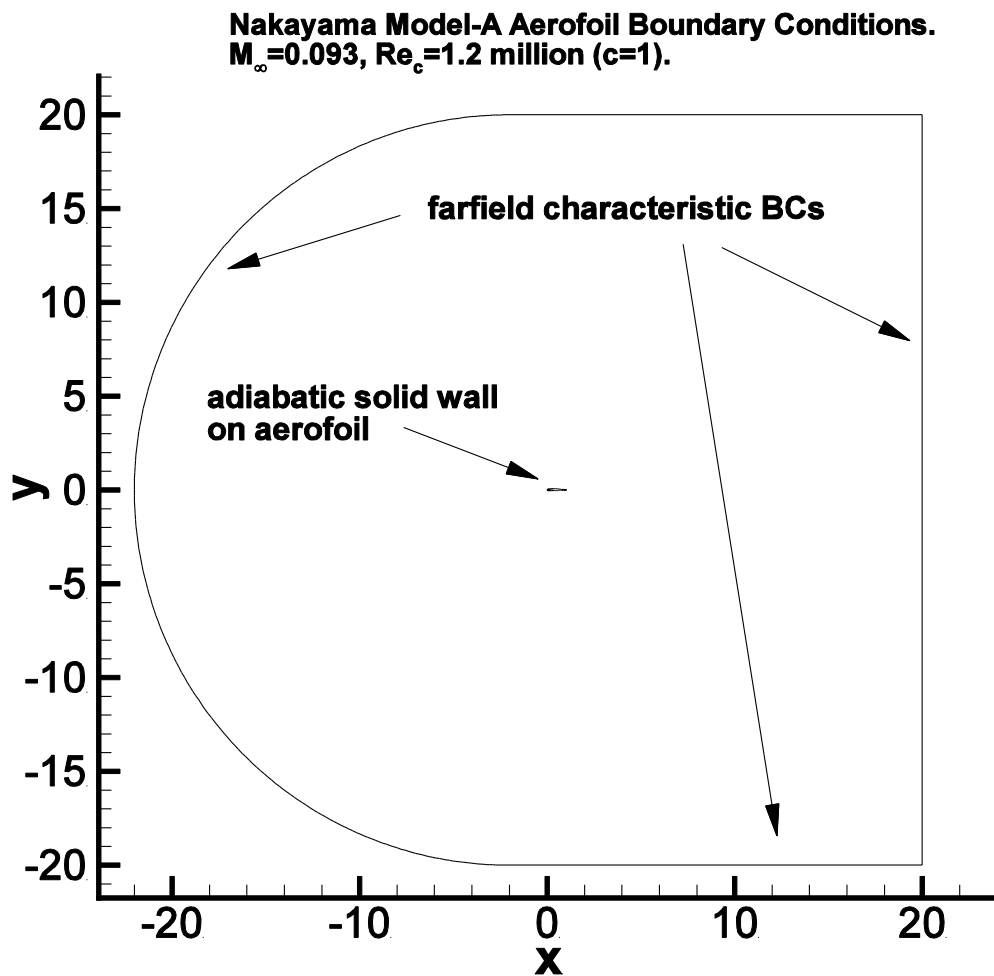


Figure 6.19 COMPARISON OF SKIN FRICTION COEFFICIENT  $c_f$  AND PRESSURE COEFFICIENT  $c_p$  AT THREE VALUES OF  $M_\infty$  OBTAINED BY CFL3D, COSA WITH AND WITHOUT LSP AND EXPERIMENT DATA. TOP LEFT SUBPLOT:  $c_f$  at  $M_\infty = 0.093$ . MIDDLE LEFT SUBPLOT:  $c_f$  at  $M_\infty = 0.0093$ . BOTTOM LEFT SUBPLOT:  $c_f$  at  $M_\infty = 0.00093$ . TOP RIGHT SUBPLOT:  $c_p$  at  $M_\infty = 0.093$ . MIDDLE RIGHT SUBPLOT:  $c_p$  at  $M_\infty = 0.0093$ . BOTTOM RIGHT SUBPLOT:  $c_p$  at  $M_\infty = 0.00093$ .

## 6.5 2D Nakayama Model-A aerofoil case

A non-symmetric 10%-thick conventional aerofoil (referred to as the "Model-A aerofoil") is involved in this 2D experiment (Nakayama, 1985) considered here. Wake characteristics (of velocity profiles) are measured at an angle-of-attack of 0 degree. The Reynolds number was 1.2 million per aerofoil chord based on a freestream Mach number  $M_\infty$  of 0.088. Both the upper and lower boundary layers were tripped in the experiment (16%c upper surface and 5%c lower surface). However, the fully turbulence boundary layer is employed in all CFD simulations due to the fact that this may yield better results than forcing laminar flow upstream of the trip locations (Rumsey, 2013). It should be noted that in the experiment the trailing edge of the original aerofoil has a thickness of approximately 0.001c, while the aerofoil definition has been modified slightly in CFD computations so it closes at chord=1 with a sharp trailing edge instead. Figure 6.20 shows the layout of the boundary conditions adopted in the simulation, where the farfield boundary is placed at about 20 chords from the aerofoil and the characteristic-based farfield boundary conditions are imposed (see Section 5.3 for the related theory).



*Figure 6.20 IMPOSED BOUNDARY CONDITIONS FOR MODEL-A AERFOIL CASE*

5 nested 2D grids are provided on NASA Langley Research Centre website ([http://turbmodels.larc.nasa.gov/airfoilwake\\_grids.html](http://turbmodels.larc.nasa.gov/airfoilwake_grids.html)) for the Nakayama Model-A aerofoil case (with sharpened trailing edge). A so-call ‘C-grid’ topology is adopted for each grid, whereby the grid wraps around the aerofoil starting from the downstream farfield, passing around the lower aerofoil surface to the upper, and back to the downstream farfield again, thus the grid connects to itself in a 1-to-1 fashion in the cut.

Each coarser grid is obtained by maintaining exactly every-other-point of the current finer grid, ranging from the finest  $2241 \times 385$  (defined by the product of the total grid point number on the aerofoil and grid cut times that in the normal-like direction) to the coarsest  $141 \times 25$  grid. The finest grid has minimum wall distance of  $2.5 \cdot 10^{-6}$ , giving an approximate average  $y^+$  between 0.1 and 0.2 over the aerofoil at the Reynolds number specified. The grid is stretched in the normal wall direction, and the clustering is maintained in the wake region. A

mesh refinement analysis has yielded an insignificant difference between the solutions computed with the second finest grid  $1121 \times 193$  and grid of the coarser level  $561 \times 97$  for COSA, therefore despite the fact that the CFL3D results to be compared are obtained with the finer grid, we adopt the coarser grid in all simulations performed by COSA to achieve higher computational efficiency. A general description is given in Figure 6.21 for the coarser  $561 \times 97$  grid, where stretched grid spacing can be seen in the wall-normal direction and the wake. Figure 6.22, on the other hand, provides an enlarged view of the adopted grid in the aerofoil region, of which 256 mesh intervals are along the aerofoil surface, 152 intervals are along the wake from the aerofoil trailing edge to the outflow boundary, and 96 intervals are in the normal-like direction.

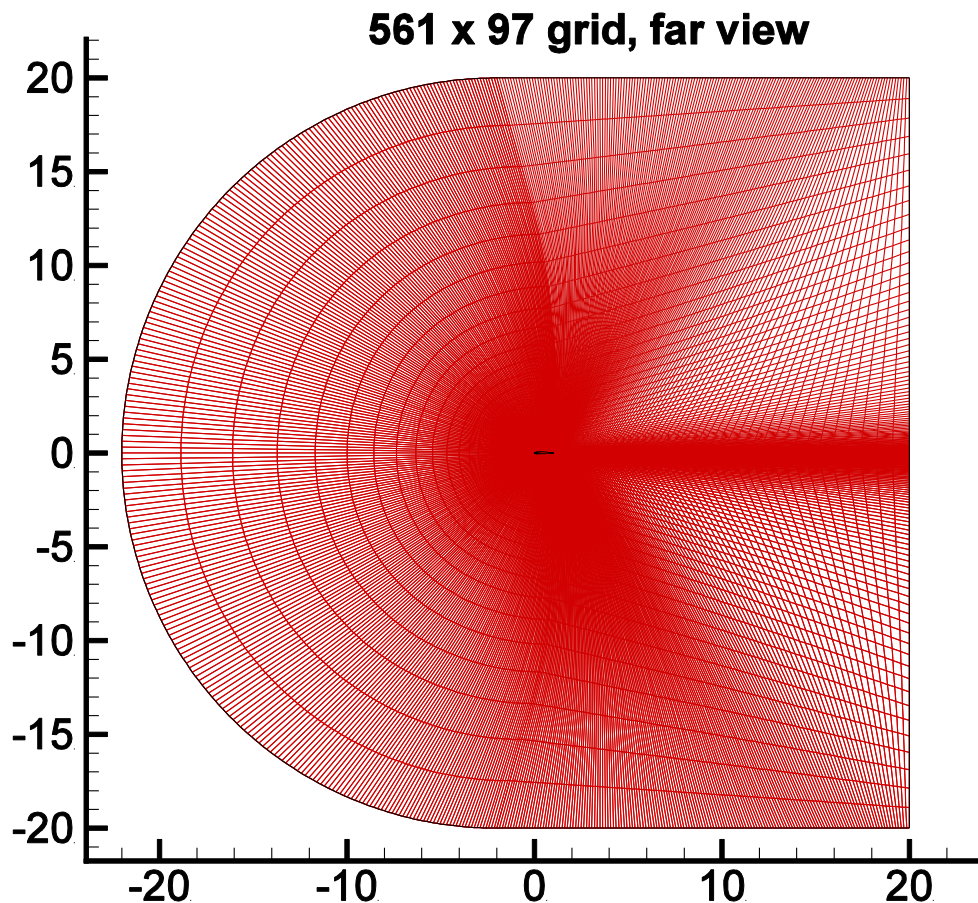


*Figure 6.21 GRID VIEW IN FARFIELD REGION FOR MODEL-A AERFOIL CASE  
([http://turbmodels.larc.nasa.gov/airfoilwake\\_grids.html](http://turbmodels.larc.nasa.gov/airfoilwake_grids.html))*

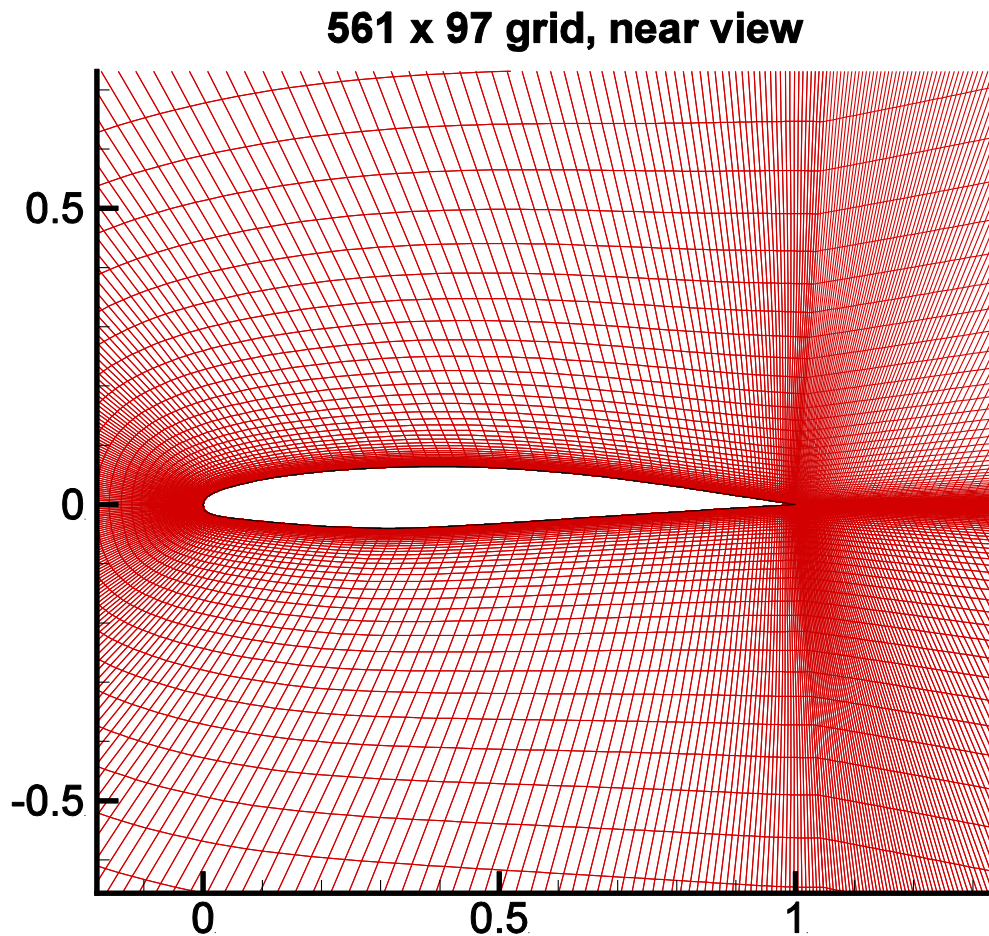


*Figure 6.22 GRID VIEW IN AEROFOIL REGION*

The second and third columns of Table 6.2 report respectively the lift coefficient  $C_l$  and the drag coefficient  $C_d$  computed with the LSP analysis for the three values of  $M_\infty$ . The fourth and fifth columns report instead the estimates of the same force coefficients obtained by the analysis without LSP. Several interesting observations can be made by cross-comparing the data of this table. Firstly, one notes that the difference between the LSP lift force estimates for  $M_\infty = 8.8 \cdot 10^{-3}$  and  $M_\infty = 8.8 \cdot 10^{-4}$  is significantly smaller than the difference estimates for  $M_\infty = 8.8 \cdot 10^{-2}$  and  $M_\infty = 8.8 \cdot 10^{-3}$ . This occurrence points to the existence of slight compressibility effects in the flow field considered herein. The comparison of the LSP- and the NP-estimate of a given force component for the same  $M_\infty$  highlights that the difference between LSP and NP predictions increases significantly as  $M_\infty$  decreases, as expected. It is also noted that, though relatively small, the difference between the LSP- and the NP estimate of the two force coefficients at  $M_\infty = 8.8 \cdot 10^{-2}$  is larger than the difference between the LSP- and the NP-estimate of the flat plate drag coefficient at  $M_\infty = 0.1$ . This is

presumably due to the higher complexity of the aerofoil flow field with respect to the zero-pressure gradient flat plate boundary layer. In the aerofoil problem, a rapid growth of the boundary layer on the aerofoil suction side (SS) occurs between the peak-velocity point and the TE. The accuracy of the LSP simulation in this low-speed and low-Reynolds number boundary layer region is likely to be higher than the solver without LSP due to the optimised LSP numerical dissipation. The same phenomenon is also reported in (Vatsa and Turkel, 2004), which compares the viscous drag of the RAE aerofoil for an angle of attack of  $2.79^\circ$  at  $M_\infty = 0.2$  and  $Re = 6.5 \cdot 10^6$  obtained from the compressible RANS analyses with and without LSP. The steady flow analyses commented above of  $M_\infty = 8.8 \cdot 10^{-2}$  have also been performed using two NASA compressible codes, CFL3D and another fully unstructured Navier-Stokes research code FUN3D (Langley, 2015). Like the COSA simulations reported above, the two NASA analyses have been performed assuming fully turbulent boundary layer. The force coefficients computed by both codes for the considered values of  $M_\infty$  are provided in Table 6.3. A fairly closer agreement of the force coefficients is found between COSA-LSP solver and the two NASA codes with respect to its NP counterpart, which has further demonstrated the above conclusion of better accuracy yielded by the LSP optimised numerical dissipation. Based on the results presented in the two tables, one can conclude that the force coefficients predicted by the LSP analysis almost remain constant as  $M_\infty$  decreases, and shows a good agreement with the solutions of other well-developed CFD research codes. Conversely, the force coefficient estimates of the analysis without LSP deviates substantially from the reference values as  $M_\infty$  is reduced, due to the numerical errors associated with the use of the compressible solver without LSP at low Mach number levels, which points to the necessity of using LSP to preserve the accuracy of the solution when solving low-speed flows with the compressible equations even for  $M_\infty$  of order 0.1.

$M_\infty$	COSA-LSP		COSA-NP	
	$C_l$	$C_d$	$C_l$	$C_d$
$8.8 \cdot 10^{-2}$	0.1541	0.01033	0.1596	0.01061
$8.8 \cdot 10^{-3}$	0.1536	0.01036	0.1699	0.01548
$8.8 \cdot 10^{-4}$	0.1535	0.01052	0.1435	0.06550

*Table 6.2 COMPARISONS OF LIFT COEFFICIENT  $C_l$  AND DRAG COEFFICIENT  $C_d$  FOR  $M_\infty = 8.8 \cdot 10^{-2}$ ,  $M_\infty = 8.8 \cdot 10^{-3}$ , AND  $M_\infty = 8.8 \cdot 10^{-4}$  OBTAINED WITH AND WITHOUT LSP.*

$M_\infty$	CFL3D		FUN3D	
	$C_l$	$C_d$	$C_l$	$C_d$
$8.8 \cdot 10^{-2}$	0.1574	0.01011	0.1556	0.01015

*Table 6.3 COMPARISONS OF LIFT COEFFICIENT  $C_l$  AND DRAG COEFFICIENT  $C_d$  FOR  $M_\infty = 8.8 \cdot 10^{-2}$  OBTAINED BY CFL3D AND FUN3D*

Comparisons of the CFD results (COSA and CFL3D) and experiment data (Nakayama, 1985) are displayed in Figure 6.23, in terms of the velocity profiles chosen at the following locations in the wake,  $x/c=1.01, 1.05, 1.20, 1.40, 1.80, 2.19$ . The simulated results of COSA depicted in top, middle, and bottom subplot rows of Figure 6.23 refer to the value of  $M_\infty$  of 0.088, 0.0088 and 0.00088 respectively, and each subplot provides the velocity profile of the simulations with and without LSP, while the experimental data and CFL3D results are always with respect to the value of  $M_\infty$  of 0.088. The term ‘‘SST’’ appearing in the legend stands for the turbulence model applied in both CFL3D and COSA solver, while ‘‘561  $\times$  97’’ and ‘‘1121  $\times$  193’’ represent the size of the two different meshes adopted by COSA and CFL3D respectively. The figure highlights that the velocity profile chosen at the locations of interest predicted by the compressible analysis without LSP starts being affected by significant errors already at  $M_\infty = 0.0088$ . The LSP-enhanced solver, however, has demonstrated a highly accurate predictive ability of the velocity profile compared with the two benchmark data of  $M_\infty = 0.088$ , particularly in the most difficult case of the lowest Mach number of 0.00088, no significant difference is spotted.

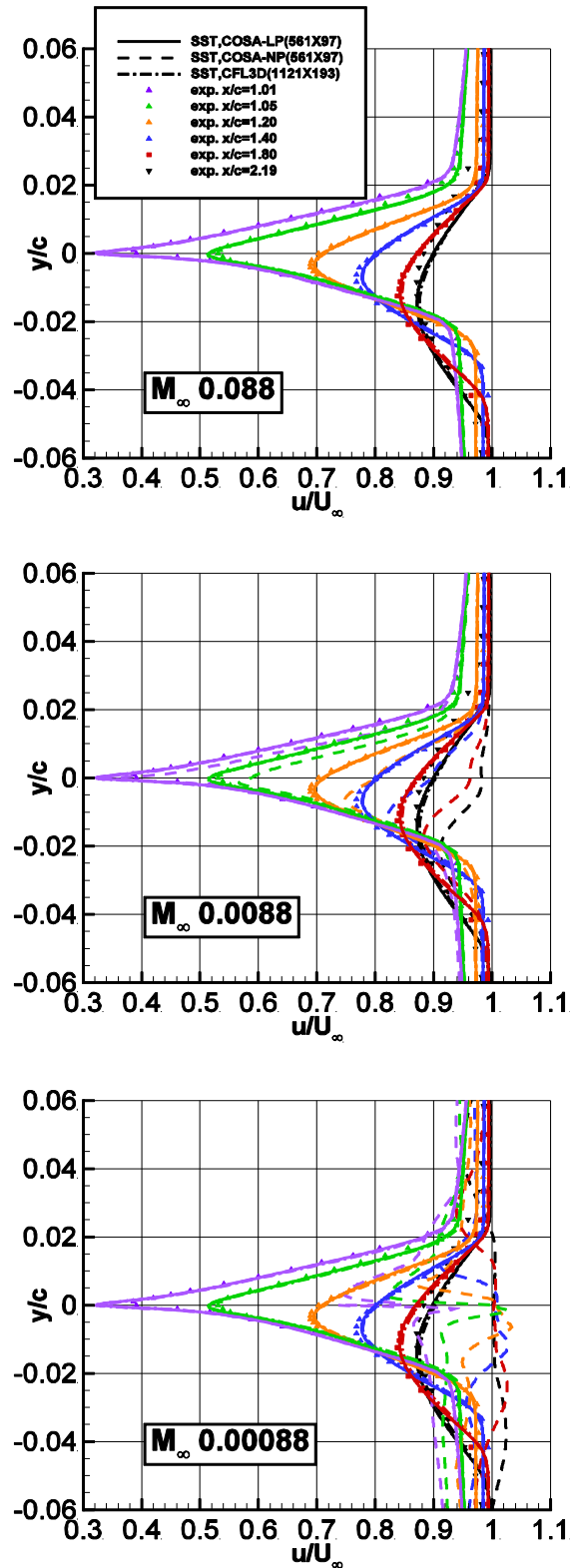
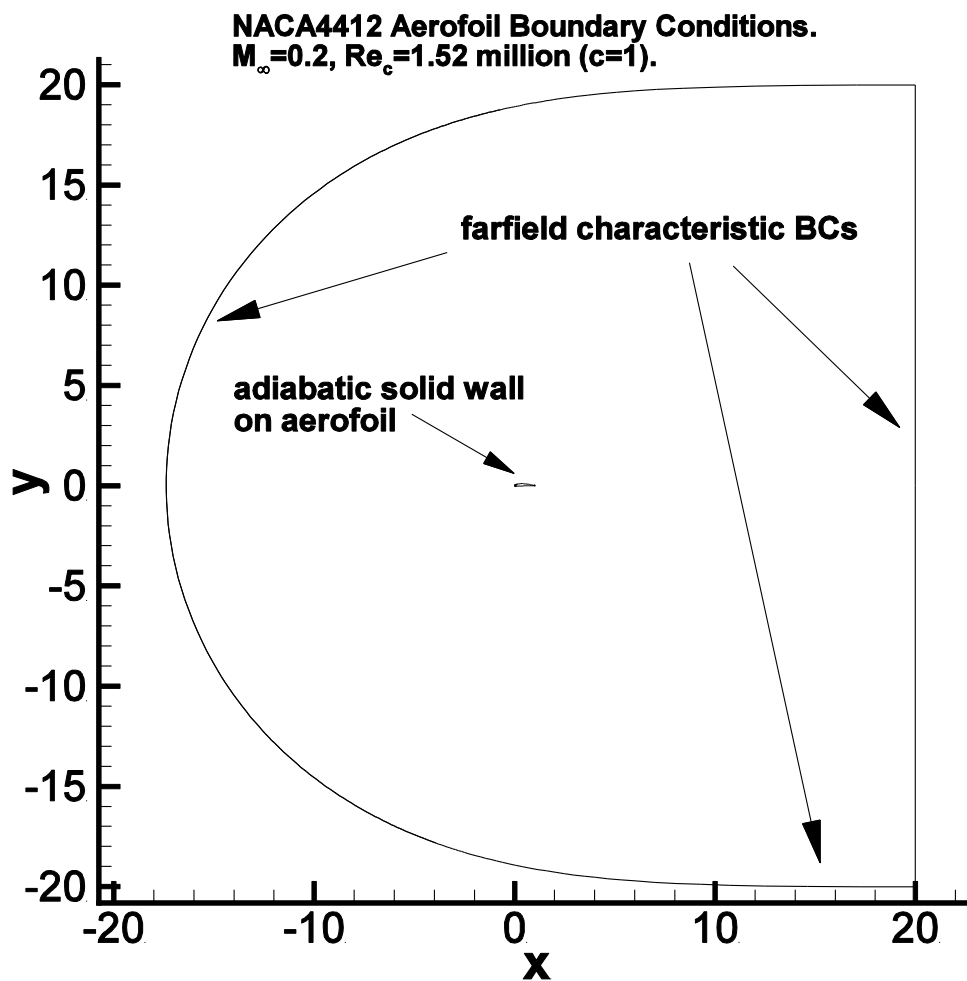


Figure 6.23 COMPARISON OF VELOCITY PROFILE IN THE WAKE NORMALISED BY THE FREESTREAM VELOCITY AT THREE VALUES OF  $M_\infty$  OBTAINED BY CFL3D, COSA WITH AND WITHOUT LSP AND EXPERIMENT DATA. TOP SUBPLOT: VELOCITY PROFILE AT  $x/c=1.01, 1.05, 1.20, 1.40, 1.80, 2.19$ ,  $M_\infty = 0.088$ . MIDDLE SUBPLOT: VELOCITY PROFILE AT  $M_\infty = 0.0088$ . BOTTOM SUBPLOT: VELOCITY PROFILE AT  $M_\infty = 0.00088$

## 6.6 NACA4412 aerofoil case

In contrast to the relatively simple aerofoil case with an angle of attack of zero degree discussed in the previous section, we have considered herein the turbulent flow field past the NACA4412 aerofoil at the AoA of  $13.87^\circ$  where a maximum lift force is achieved and a large separation area is generated in the trailing edge. The free-stream Mach number  $M_\infty$  is 0.2, and the Reynolds number based on the aerofoil chord and the free-stream velocity is  $1.52 \cdot 10^6$ . The experimental data we refer to in this section is from the hot-wire boundary layer measurements performed by Coles and Wadcock (1979) at NASA Ames. Similar numerical analyses can also be found in the work of Moryossef and Levy (2006) and Menter (1994). In all our CFD simulations, a fully turbulent boundary layer is enforced, which corresponds to the turbulent intensity at the far-field boundary equal to 1% and the ratio between turbulent viscosity and laminar viscosity  $\mu_T/\mu$  of  $10^{-4}$ . A layout of the boundary conditions adopted in the simulation is displayed in Figure 6.24, where the farfield boundary is placed at about 20 chords from the aerofoil and the characteristic farfield boundary condition is specified.



*Figure 6.24 IMPOSED BOUNDARY CONDITIONS FOR NACA4412 AEROFOIL CASE*

A 2D C-type structured grid is provided on the website of NASA CFD code - CFL3D (Rumsey, 2013) and is thus adopted here for all our numerical simulations in order to provide better comparison of the solutions obtained with different codes. The grid has a minimum wall distance (defined by the distance of the first grid points off the aerofoil surface) of  $4 \cdot 10^{-5}c$ , yielding an approximate average  $y^+$  of less than 1 over the aerofoil at the Reynolds number specified. The grid is stretched in the normal wall direction, and the clustering is maintained in the wake region. An overview of the adopted grid is given in Figure 6.25, where stretched grid spacing can be seen in the wall-normal direction and the wake. Figure 6.26, on the other hand, provides an enlarged view in the aerofoil region, of which 176 mesh intervals are along the aerofoil surface, 40 intervals are along the wake from the aerofoil trailing edge to the outflow boundary, and 80 intervals are in the normal-like direction, giving a total number of cells of 20480.

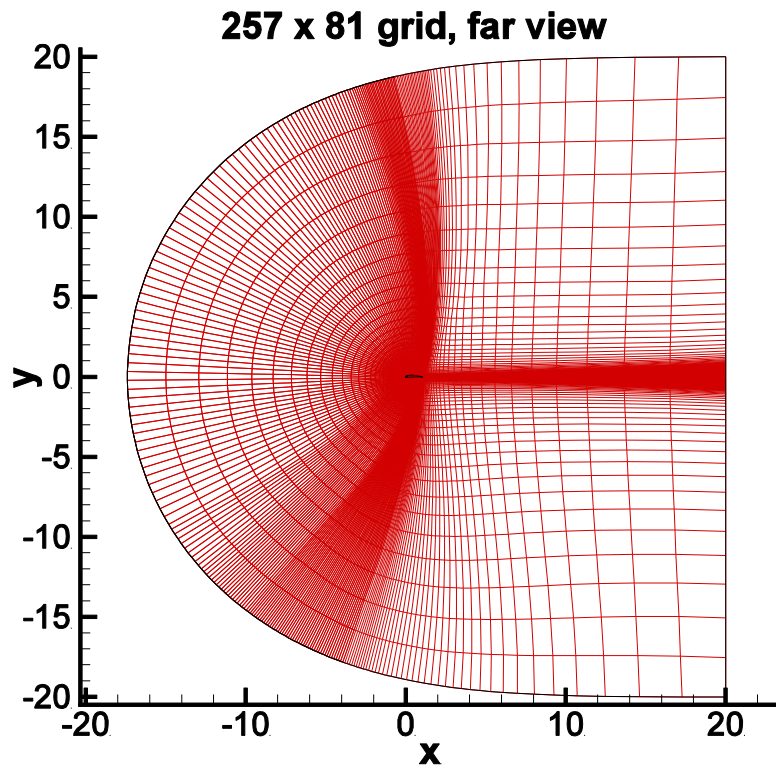


Figure 6.25 GRID VIEW IN FARFIELD REGION FOR NACA4412 AEROFOIL CASE (Rumsey, 2013)

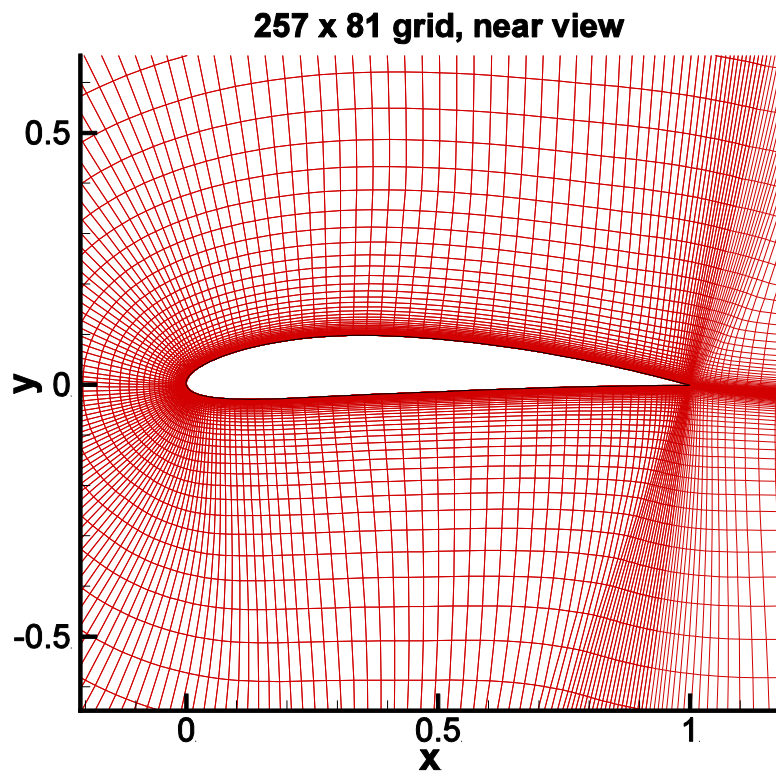


Figure 6.26 GRID VIEW IN NEAR AEROFOIL REGION

The second and third columns of Table 6.4 report the lift coefficient  $C_l$  and the drag coefficient  $C_d$  computed with the LSP analysis for the three values of  $M_\infty$ , while the fourth and fifth columns report instead the estimates of the same force coefficients obtained by the analysis without LSP and the last column represents the experiment data of  $C_l$  at  $M_\infty = 0.2$ .

Through cross-comparing the lift coefficient  $C_l$  obtained by COSA LSP-solver, NP-solvers and the experiment value for  $M_\infty = 0.2$ , a closer and better agreement is found between the LSP-estimate and measured data with respect to the NP-estimate value, and we can therefore demonstrate that better prediction of the flow properties can be provided with the LSP-enhanced solver even for a relatively high Mach number. Secondly, one finds that the difference between the LSP  $C_d$  estimates for  $M_\infty = 0.02$  and  $M_\infty = 0.002$  is significantly smaller than the difference estimates for  $M_\infty = 0.2$  and  $M_\infty = 0.02$ . This phenomenon relates to the existence of compressibility effects in the flow field at  $M_\infty = 0.2$ . The comparison of the LSP- and the NP-estimate of a given force component for the same  $M_\infty$  particularly the  $C_d$ , highlights that the difference between LSP and NP predictions increases significantly as  $M_\infty$  decreases, as expected. Therefore these data emphasise that the force coefficients predicted by the LSP analysis remains almost as a constant as  $M_\infty$  decreases, and is equal to the experiment data. Conversely, the force coefficient estimates of the analysis without LSP deviates substantially from the measured data as  $M_\infty$  is reduced, due to the numerical errors associated with the use of the compressible solver without LSP at low Mach number levels, and it points again to the necessity of using LSP to preserve the accuracy of the solution when solving low-speed flows with the compressible equations even for levels of  $M_\infty$  above 0.1.

$M_\infty$	COSA-LSP		COSA-NP		EXP
	$C_l$	$C_d$	$C_l$	$C_d$	$C_l$
$2 \cdot 10^{-1}$	1.670	0.0390	1.698	0.0369	1.669
$2 \cdot 10^{-2}$	1.666	0.0362	1.694	0.0566	
$2 \cdot 10^{-3}$	1.670	0.0371	1.791	0.163	

*Table 6.4 COMPARISONS OF LIFT COEFFICIENT  $C_l$  AND DRAG COEFFICIENT  $C_d$  FOR  $M_\infty = 2 \cdot 10^{-1}, 2 \cdot 10^{-2}, 2 \cdot 10^{-3}$  OBTAINED WITH AND WITHOUT LSP AND EXPERIMENT DATA*

Comparisons of the COSA NP- and LSP- estimate results and experiment data (Coles and Wadcock, 1979) are displayed in Figure 6.27 and Figure 6.28 respectively, in terms of the velocity profiles chosen at the following six locations near the trailing edge,  $x/c=0.62, 0.731,$

0.786, 0.842, 0.897, 0.953. The simulated results of COSA depicted in top, middle, and bottom subplot rows of Figure 6.27 refer to the value of  $M_\infty$  of 0.2, 0.02 and 0.002 at the first three locations mentioned above respectively, and velocity profiles of the simulations with and without LSP are provided in the left and right columns. The experiment data are always with respect to the value of  $M_\infty$  of 0.2. Comparisons of the velocity profiles for the other three locations are shown in Figure 6.28. Analysing the two figures shows that the velocity profile at the specified locations predicted by the compressible analysis without LSP starts being affected by significant errors already at  $M_\infty = 0.02$ . The LSP-enhanced solver, however, has demonstrated a highly accurate predictive ability of the flow characteristics compared with the experiment data of  $M_\infty = 0.2$ , by displaying the accurate velocity profile even at an extremely low Mach number of 0.002. Despite the fact that differences can be still spotted between the two LSP results of  $M_\infty$  below 0.02, its significantly smaller magnitude compared to that between the two higher Mach numbers has demonstrated again the previously mentioned compressibility effect in force coefficient analyses.

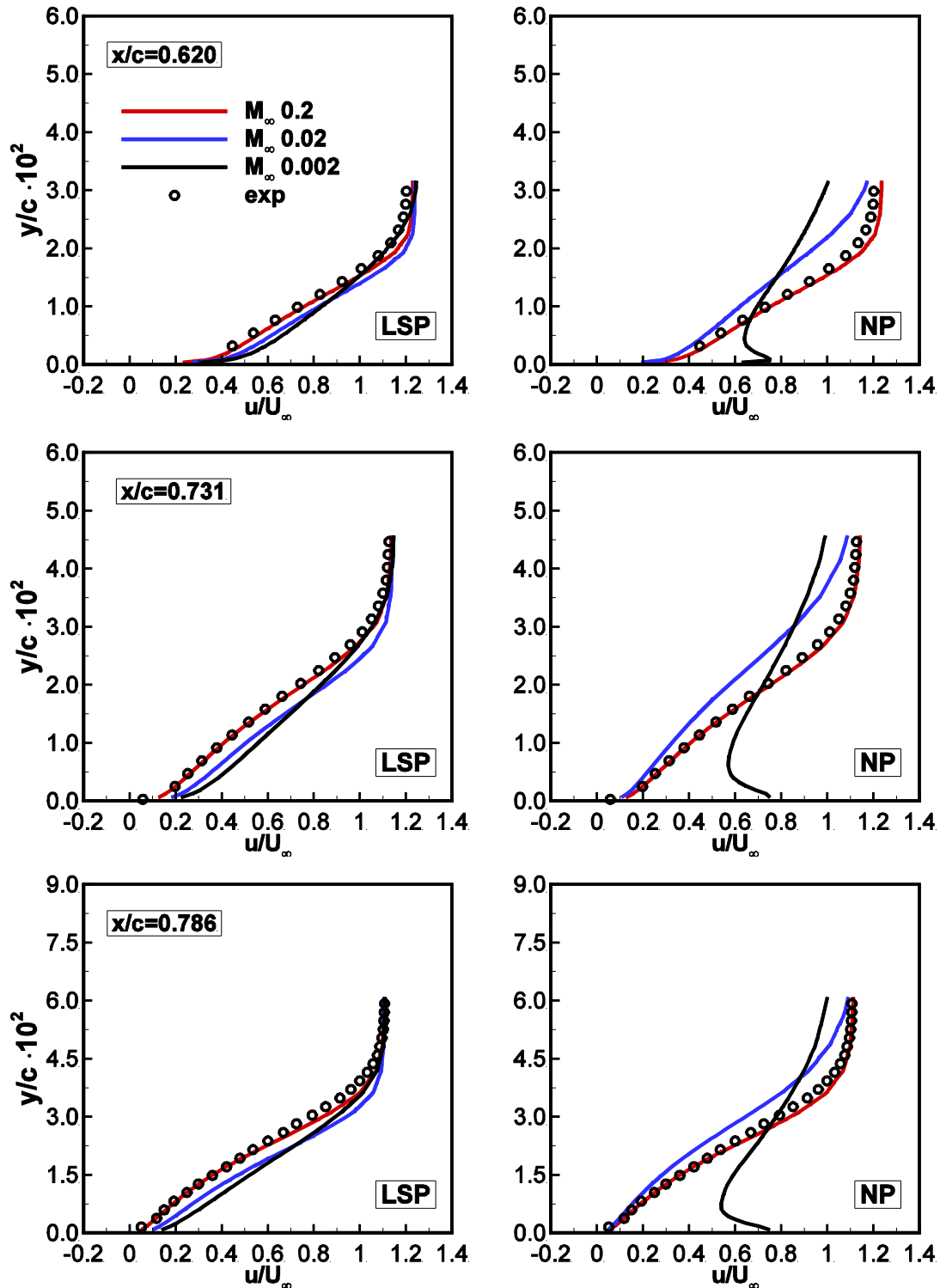


Figure 6.27 COMPARISON OF VELOCITY PROFILE NEAR THE TRAILING EDGE NORMALISED BY THE FREESTREAM VELOCITY AT THREE VALUES OF  $M_\infty$ , 0.2, 0.02, 0.002, OBTAINED BY COSA WITH AND WITHOUT LSP AND EXPERIMENT DATA. TOP LEFT SUBPLOT: VELOCITY PROFILE WITH LSP AT  $x/c=0.620$ . MIDDLE LEFT SUBPLOT: VELOCITY PROFILE WITH LSP AT  $x/c=0.731$ . BOTTOM LEFT SUBPLOT: VELOCITY PROFILE WITH LSP AT  $x/c=0.786$ . TOP RIGHT SUBPLOT: VELOCITY PROFILE WITHOUT LSP AT  $x/c=0.620$ . MIDDLE RIGHT SUBPLOT: VELOCITY PROFILE WITHOUT LSP AT  $x/c=0.731$ . BOTTOM RIGHT SUBPLOT: VELOCITY PROFILE WITHOUT LSP AT  $x/c=0.786$ .

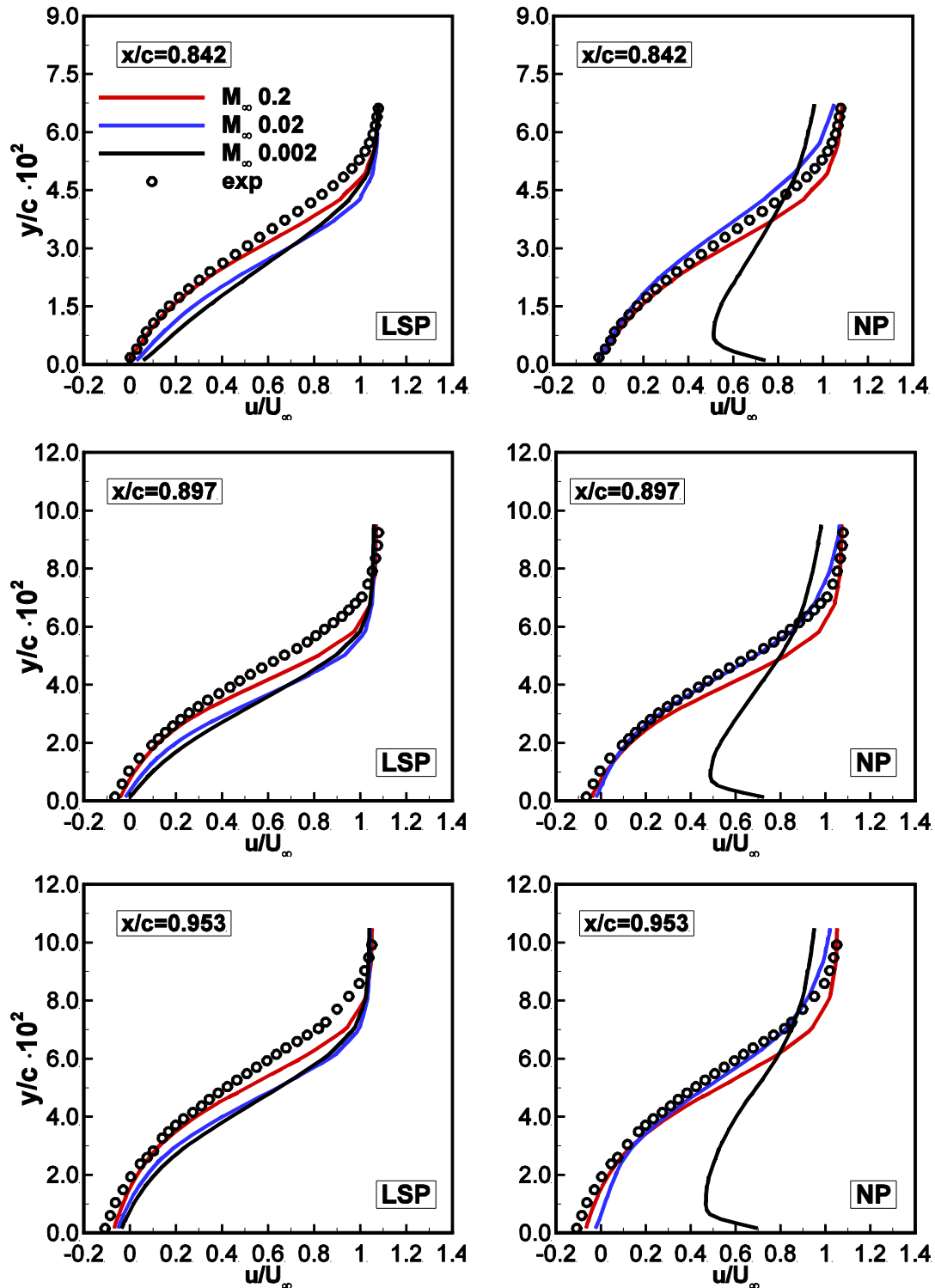


Figure 6.28 COMPARISON OF VELOCITY PROFILE NEAR THE TRAILING EDGE NORMALISED BY THE FREESTREAM VELOCITY AT THREE VALUES OF  $M_\infty$ , 0.2, 0.02, 0.002, OBTAINED BY COSA WITH AND WITHOUT LSP AND EXPERIMENT DATA. TOP LEFT SUBPLOT: VELOCITY PROFILE WITH LSP AT  $x/c=0.842$ . MIDDLE LEFT SUBPLOT: VELOCITY PROFILE WITH LSP AT  $x/c=0.897$ . BOTTOM LEFT SUBPLOT: VELOCITY PROFILE WITH LSP AT  $x/c=0.953$ . TOP RIGHT SUBPLOT: VELOCITY PROFILE WITHOUT LSP AT  $x/c=0.842$ . MIDDLE RIGHT SUBPLOT: VELOCITY PROFILE WITHOUT LSP AT  $x/c=0.897$ . BOTTOM RIGHT SUBPLOT: VELOCITY PROFILE WITHOUT LSP AT  $x/c=0.953$ .

The left subplot of Figure 6.29 reports the three LSP estimates of the static pressure coefficient  $C_p$  along the chord, whereas the estimates obtained without LSP are depicted in the right subplot. Inspection of the LSP  $C_p$  profiles confirms that significant differences exist between the  $M_\infty = 0.2$  profiles and those associated with the other two values of  $M_\infty$ , and also that the profiles associated with the two lower values are indistinguishable. This finding has also provided evidence for this problem that compressibility effects are fairly significant at the Mach number considered herein. Another main feature emerging from the  $C_p$  profiles obtained without LSP is that the result for the lowest value of  $M_\infty = 0.002$  features significant non-physical oscillations at both the LE and the TE, which is successfully removed in the LSP calculations as a result of the optimised numerical dissipation.

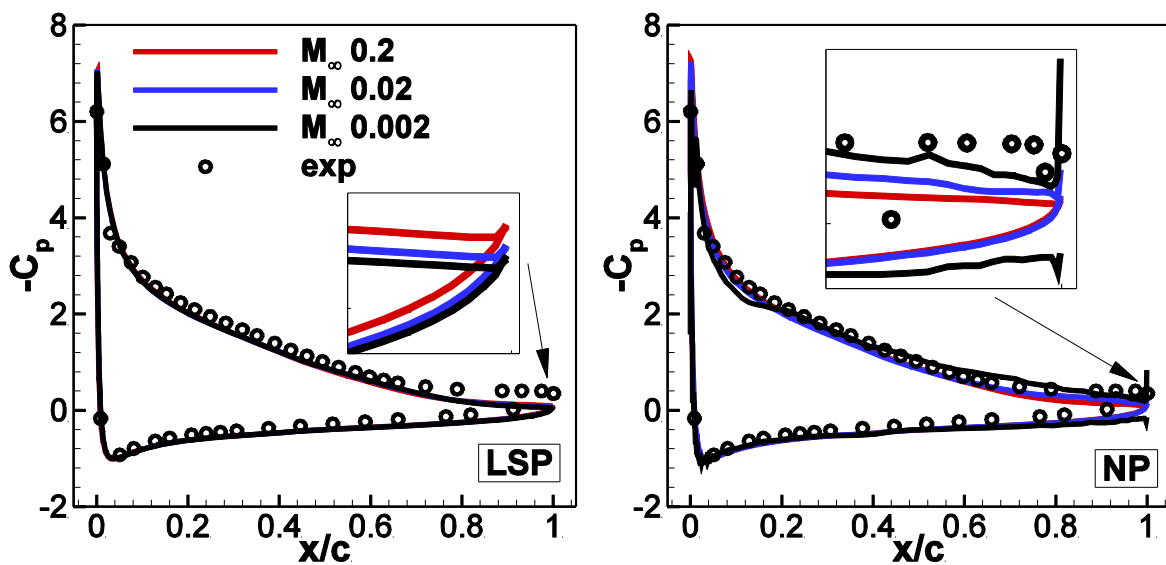


Figure 6.29 COMPARISON OF PRESSURE COEFFICIENT  $c_p$  AT THREE VALUES OF  $M_\infty$  0.2, 0.02, 0.002, OBTAINED BY COSA WITH AND WITHOUT LSP AND EXPERIMENT DATA. RIGHT SUBPLOT: PRESSURE COEFFICIENT  $c_p$  OBTAINED WITH LSP. LEFT SUBPLOT: PRESSURE COEFFICIENT  $c_p$  OBTAINED WITHOUT LSP

## 6.7 Summary

The predictive capabilities of the CFD compressible solver - COSA using the presented turbulent preconditioning strategy are assessed by computing the turbulent flows for different values of  $M_\infty$  in various challenging test cases, and has shown a highly reliable accuracy of the solutions regardless of the variation of Mach number, thereby demonstrating a great advantage over its non-preconditioned (standard) compressible solver while dealing with the low speed flow problems. Based on the above successful demonstration and validation of the predictive capability of the LSP solver, we can thus be able to proceed to solve more realistic engineering problems, such as those involved in the wind turbine applications presented in Chapter 7.

# Chapter 7

## Results

HAWT and VAWT are the two representatives of the modern energy engineering problems. This chapter therefore provides the main computational results regarding to these two substantially different energy applications of our research. The first case is a comparative analysis of specific blade sections of a VESTAS multi-megawatt HAWT working in various regimes (i.e. steady problem where the wind direction is orthogonal to the rotor plane and the unsteady yawed wind condition). The CFD simulations are performed in three different freestream Mach numbers, namely the one corresponding to the rated wind speed and two lower Mach numbers for which the flow is required to be treated as incompressible, and the results obtained in various Mach numbers are used to compare and assess the compressibility effect by using LSP to approximate the incompressible solution. Presented results highlight the inaccurate solutions obtained by the non-preconditioned solver for low Mach number flow problems and hence demonstrate the predictive capabilities of the LSP approach for solving low-speed problems with different formulations (steady, time-domain and frequency-domain) and the computational benefits achieved by using the harmonic balance method of the RANS and SST equations rather than the conventional time-domain method through comparing the numerical solutions obtained by these two approaches. The second application is the steady inviscid flow analysis of a NREL multi-megawatt HAWT working in the operating conditions corresponding to both the rated wind speed and fairly low Mach number flow. This type of subsonic problem is used to analyse both the aerodynamic characteristics of particular blade sections and of the whole rotor. The main motivation of carrying out this research is to demonstrate the accurate solution achieved by using LSP in analysing the entire wind turbine application in a realistic flow condition. The last application is the time-domain turbulent aerodynamics analysis of the VAWT. We firstly demonstrate the necessity of applying the preconditioning method to solve such a flow problem by comparing the results obtained with and without LSP technology, and secondly the comparative analysis of different kinds of implementation of the preconditioning approaches is performed by

neglecting the turbulent kinetic energy term in the total energy, thereby verifying the essential part of the turbulent kinetic energy in the coupling of the RANS and SST equations of the preconditioned system. Last but not the least, two sets of preconditioning parameters have been selected to analyse to the aim of demonstrating a proper implementation of the preconditioning parameter in solving an unsteady moving grid problem.

## 7.1 Horizontal axis wind turbine aerodynamics (2D)

Large-scale electricity production from the wind is primarily based on the use of multi-megawatt horizontal axis wind turbines (HAWTs). The dimensions of these machines keep increasing, and one of the them having already become operational in 2014 has a rotor radius of about 82 m. HAWT rotor design is an inherently multidisciplinary task as it involves fluid dynamics, structural mechanics, aeroelasticity and also aeroacoustics. The aerodynamic module of modern industrial systems for HAWT aeromechanical design (Hansen et al., 2006) is often still based on the blade element momentum (BEM) theory. BEM codes are very fast, but unfortunately their results may be affected by significant level of uncertainty due to the use of several semi-empirical and correlation-based models, and also because these codes are also used for flow regimes which violate the underlying assumptions of the BEM theory (i.e. yawed flows). Moreover, BEM codes rely on the availability of reliable two-dimensional (2D) aerofoil force data for a wide range of Reynolds number and angle of attack (AoA). This feature limits the exploration of the design space, possibly preventing the adoption of new and more efficient HAWT configurations. Conversely, the use of computational fluid dynamics (CFD) solvers based on the Navier-Stokes (NS) equations allows the aforementioned limitations to be greatly reduced and often removed. These codes can use any user-given three-dimensional (3D) blade geometry and solve the 3D aerodynamic flow field around the entire turbine (Mo et al., 2013, Gómez-Iradi et al., 2009). NS solvers require substantially higher run-times with respect to BEM solvers, but the present rapid growth of novel high-performance computing devices, such as Graphics Processing Units, the development of faster methods for the integration of periodic flows (Campobasso et al., 2014b, Campobasso and Baba-Ahmadi, 2012) and progress on how best to exploit modern multi-core processors (Jackson and Campobasso, 2011) are making the NS technology for HAWT design increasingly affordable.

When using the NS CFD technology for HAWT rotor aerodynamics, one can use either the incompressible (Bechmann et al., 2011, Sørensen et al., 2002) or the compressible (Gómez-Iradi et al., 2009, Le Pape and Gleize, 2006) formulation of the conservation laws. Newest multi-megawatt HAWT rotors can feature rotor radii in excess of 80 m, and blade tip speeds in the region of 0.3, which is the conventional threshold at which compressibility effects start becoming significant. Therefore, one may wonder whether the use of compressible NS solvers for multi-megawatt rotor aerodynamics may yield more reliable answers. Preliminary tests for this type and size of turbine point to the fact that compressibility effects produce differences of less than 1% between the annual energy production (AEP) estimated using a compressible or an incompressible flow analysis. Fairly small differences between the aerodynamic loads estimated with either approach are also found. The differences arising from using either the compressible or the incompressible flow analysis, however, are likely to be more significant when analysing HAWT aeroacoustic noise generation and propagation. One popular approach consists of using the blade static pressure distribution predicted by a Reynolds-averaged Navier-Stokes solver (RANS) as an input for an aeroacoustic code based on the acoustic analogy (Williams and Hawkings, 1969) that predicts the spatial noise propagation around the turbine (Ranft et al., 2010). Using this approach, an inaccurate blade static pressure prediction due to the use of an incompressible rather than a compressible solver, may yield significant errors in the prediction of the propagated noise. Furthermore, a NS code may also be used for directly simulating the near-field aeroacoustics of the turbine (Arakawa et al., 2005). A review of HAWT aeroacoustic noise propagation and generation, a fairly comprehensive review of high-fidelity simulation technologies for HAWT noise analysis and further considerations on the use of compressible or incompressible NS CFD for HAWT aeroacoustics can be found in Morris et al. (2004).

The discussion above points to the appropriateness of using compressible NS solvers for the analysis of new multi-megawatt HAWT rotor aeroacoustics. The relative Mach number perceived by the blades, however, decreases in a nearly linear fashion from the tip to the root of the blade, where it reaches values of order 0.01 or less. At these low speeds, unfortunately, a large disparity between acoustic and convective speeds arises, and this results in a reduction of the solution accuracy of compressible NS solvers. When an explicit integration approach is used, a significant reduction of the convergence rate is also experienced. Low-speed preconditioning (LSP) (Venkateswaran and Merkle, 1999, Turkel et al., 1997) is a mathematical method that allows both problems to be solved or greatly reduced. The use of

LSP allows the nominal accuracy of the compressible solver to be maintained also at very low flow speeds. Moreover, based on theoretical analysis and numerical solution of relatively simple test cases, the convergence rate of compressible NS solvers using LSP is independent of the freestream Mach number  $M_\infty$ . In view of their use for HAWT aeroacoustics, one of the main objectives of this analysis is to quantify the differences between the compressible and the incompressible solution of HAWT aerodynamic flows based on the NS technology. To this aim, the compressible RANS research code COSA (Campobasso and Baba-Ahmadi, 2012, Campobasso et al., 2013, Campobasso and Drofelnik, 2012) featuring the  $k - \omega$  shear stress transport (SST) turbulence model of Menter (Menter, 1994) is used. The compressible and incompressible solutions of realistic steady and time-dependent HAWT flows featuring a compressible Mach number are compared with an emphasis on the prediction of the blade and near field static pressure. Since the incompressible flow equations have been shown to be the limit of the compressible flow equations as the Mach number tends to zero (Tukel et al., 1993), the incompressible flow solution is here approximated with that of the compressible LSP-enhanced solver obtained by reducing the actual value of  $M_\infty$  by a factor 100.

### 7.1.1 yawed wind modelling

The *TD* and *HB* analyses reported in this section refer to the yawed flow past the blades of a large HAWT rotor. The periodic flow regime experienced by the aerofoils of a HAWT blade in yawed wind depends on the freestream wind speed  $V_{fs}$ , the turbine rotational speed  $\omega$ , the angle  $\delta$  between  $V_{fs}$  and the normal to the rotor plane (*yaw angle*), the chord  $c$  of the aerofoil and its distance  $R$  from the rotational axis. The left and right plots of Figure 7.1 respectively depict the top and front views of a HAWT in yawed wind, and highlight some of the aforementioned parameters. The circumferential position of a blade is defined by the angle  $\theta$ , which is taken to be zero when the blade is vertical and descending (position *A*). The four plots of Figure 7.2 report the velocity triangles associated with a blade aerofoil for the positions labelled *A* to *D* in the right plot of Figure 7.1. The modulus of the axial velocity component is  $V_{fs} \cos \delta$ , and is the same for all radial and circumferential positions. The modulus of the entrainment velocity  $\omega \times R$  varies linearly with  $R$ , and is therefore the same in all four triangles of Figure 7.2. The velocity  $W_i$  and the angle  $\alpha_i$  ( $i = A, B, C, D$ ) denote

respectively the freestream velocity and inflow angle observed by the blade section at radius  $R$ , and both parameters vary with the circumferential position  $\theta = \omega t$ . Each velocity triangle is contained in the plane tangent to the cylinder of radius  $R$  centred on the rotational axis, and therefore it neglects any radial (i.e. along the blade axis) velocity component. The magnitude of the discarded radial component varies with  $\theta$ : no component is discarded when the blade is vertical (positions  $A$  and  $C$ ), as the entire vector  $V_{fs}$  is contained in the tangent plane; the entire radial component  $V_{fs} \sin \delta$  is instead neglected when the blade is horizontal (positions  $B$  and  $D$ ), as the radial component of  $V_{fs}$  is orthogonal to the tangent plane.

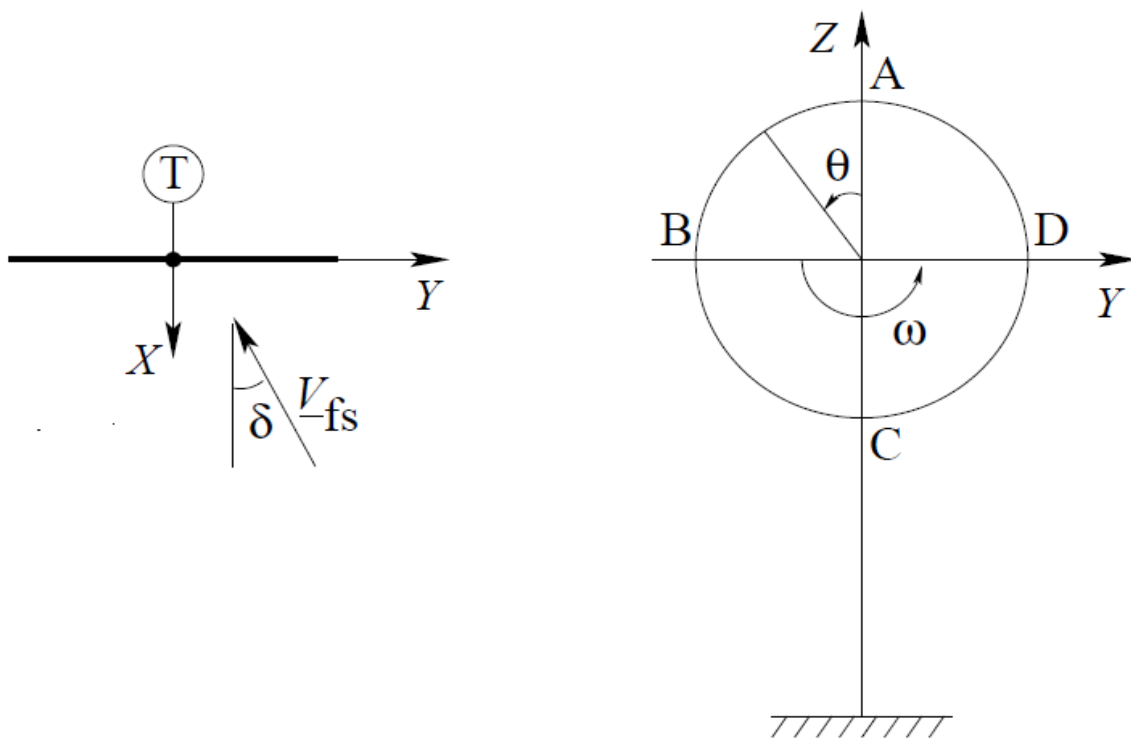


Figure 7.1 SCHEMATIC VIEWS OF HAWT IN YAWED WIND. LEFT PLOT: TOP VIEW; RIGHT PLOT: FRONT VIEW.

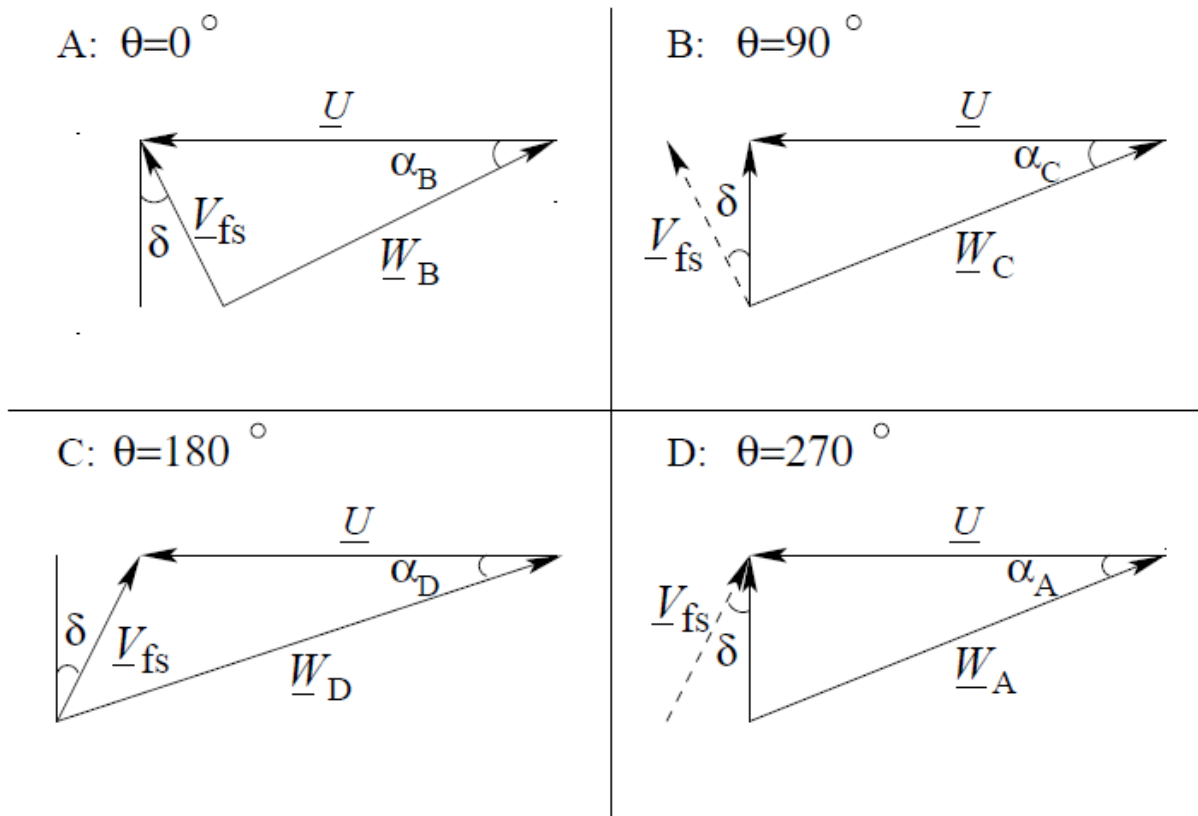


Figure 7.2 VELOCITY TRIANGLES OF HAWT BLADE SECTION FOR POSITIONS LABELED A TO D IN Figure 7.1.

Within the limits of these approximations, the axial and circumferential components of the freestream velocity perceived by each blade section are respectively:

$$W_x = V_{fs} \cos(\delta), \quad W_\theta = \omega R - V_{fs} \sin(\delta) \cos(\theta) \quad (7.1)$$

which define a time-dependent velocity vector  $\widehat{W}$ . The angle  $\alpha$  formed by  $\widehat{W}$  and the rotor plane is:

$$\alpha = \arctan(W_x/W_\theta) \quad (7.2)$$

The 2D simulation of the unsteady flow past the blade aerofoil of the HAWT in yawed wind could be performed by using a motionless domain and enforcing the time-dependent freestream velocity defined by conditions (7.1). Alternatively, one could also use a moving-grid simulation with steady farfield freestream conditions and suitably defined grid motion. The modulus  $W_\infty$  and the orientation  $\alpha_\infty$  of the uniform freestream are obtained by removing the time-dependent term of Eqn. (7.1), and their expressions are respectively:

$$W_{\infty} = \sqrt{(V_{fs} \cos \delta)^2 + (\omega R)^2} \quad (7.3)$$

$$\alpha_{\infty} = \arctan[(V_{fs} \cos \delta) / \omega R] \quad (7.4)$$

When using steady farfield boundary conditions, the variability of the inflow state associated with the case of motionless domain can be replaced by the conditions such that the aerofoil and the grid experience a horizontal sinusoidal motion with time-dependent displacement  $h(t)$  defined by

$$h(t) = h_0 \sin(\theta) \quad \text{with} \quad \theta = \omega t \quad (7.5)$$

$$h_0 = V_{fs} \sin \delta / \omega$$

where  $\theta$  denotes the azimuthal position of the blade.

The moving domain model has been adopted for the analyses presented in the section, and it could also be used to perform 2D experimental measurements aimed at studying the aerodynamic characteristics of HWAT aerofoils in yawed wind. A typical HAWT aerofoil twisted by an angle  $\gamma$  is depicted in the left plot of Figure 7.3 along with an indication of the harmonic motion. The right plot provides a representation of Eqn. (7.5) and the four positions  $A$  to  $D$  correspond to those labelled with the same symbols in Figure 7.1 and Figure 7.2.

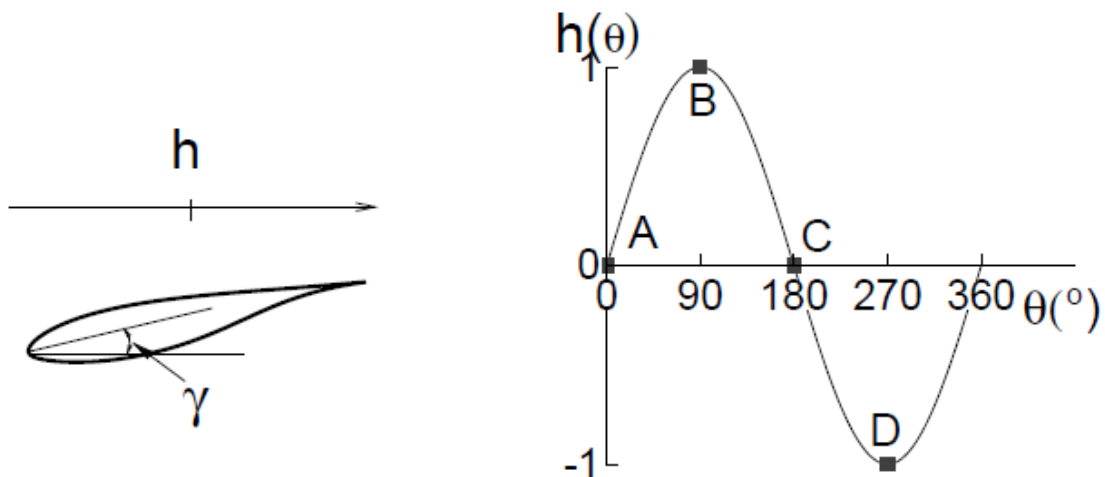


Figure 7.3 HARMONIC MOTION OF HAWT BLADE SECTION CORRESPONDING TO YAWED WIND CONDITION.

The sectional force coefficients considered herein are made up of the horizontal force coefficient  $C_x$ , the vertical force coefficient  $C_y$ , and the constant-head pitching moment coefficient  $C_m'$  defined respectively as:

$$C_x = \frac{F_x}{0.5\rho_\infty W_\infty^2 c}, \quad C_y = \frac{F_y}{0.5\rho W_\infty^2 c}, \quad C_m' = \frac{M}{0.5\rho W_\infty^2 c^2} \quad (7.6)$$

To be noted, the  $x$ - and  $y$ - directions appearing in the force coefficients are defined differently from those in the velocity components: they are both regarding the system of 2D simulations, and  $x$ - corresponds to the direction orthogonal to the rotation axis in the rotation plane, whereas  $y$ - corresponds to the direction parallel to the rotation axis. The horizontal force per unit blade length  $F_x$  is the tangential force component that results in useful torque; the vertical force per unit blade length  $F_y$  is the axial force component that results in rotor thrust; the pitching moment  $M$  per unit blade length results in a torsional load on the blade.

## 7.1.2 simulation set-up

The 2D steady and TD turbulent flow fields past the aerofoil of a rotating HAWT blade are considered in this section. The steady analysis refers to the case in which the wind direction is orthogonal to the rotor plane, and the TD analysis refers to a yawed wind condition. The rotor radius is 82.0m, the freestream wind velocity  $V_\infty$  is 13m/s, and the rotor speed is 12.0RPM, which corresponds to a value of  $\omega$  of about 1.26rad/s. The considered blade section is at 93.5% rotor radius, and features a NACA64-618 aerofoil with a chord  $c$  of 2.41m and a twist  $\gamma_p$  of 0.37° on the rotor plane.

The inflow angle  $\alpha_\infty = 7.68^\circ$  of the steady regime is obtained from Eqn. (7.4) using  $\delta = 0^\circ$  and the values of  $V_\infty$ ,  $\omega$  and  $R$  provided above. The relative AoA  $\Phi_\infty = 7.31^\circ$  for the 2D simulations is instead obtained by subtracting the twist  $\gamma_p$  to the inflow angle  $\alpha_\infty$ . Using the value of  $W_\infty$  obtained by inserting the required data into Eqn. (7.3) and the standard temperature of 288K, yields a freestream Mach number  $M_\infty = 0.286$ . The Reynolds number based on the standard density of 1.22kg/m<sup>3</sup>, the velocity  $W_\infty$ , the aerofoil chord and the air viscosity at standard temperature is  $1.6 \cdot 10^7$ .

In the unsteady regime associated with yawed wind, a yaw angle  $\delta$  of  $45^\circ$  is assumed. Eqn. (7.4) yields  $\alpha_\infty = 5.45^\circ$ , and therefore,  $\Phi_\infty = \alpha_\infty - \gamma_p = 5.08^\circ$ . Using the value of  $W_\infty$  obtained by inserting the required data into Eqn. (7.3) and the standard temperature of 288K, yields a freestream Mach number  $M_\infty = 0.285$ . The Reynolds number, calculated as in the steady case, is still  $1.6 \cdot 10^7$ . The reduced frequency  $\lambda = \omega c / W_\infty$  is 0.0313. The main physical parameters of the steady and TD simulations analysed in this section are reported in Table 7.1.

Yaw( $\delta$ )	Mode	$M_\infty$	AoA( $\Phi_\infty$ )	$\lambda$	$Re$
$0^\circ$	Steady	0.286	$7.31^\circ$	0	$1.6 \cdot 10^7$
$45^\circ$	TD	0.285	$5.08^\circ$	0.0313	$1.6 \cdot 10^7$

*Table 7.1 MAIN PHYSICAL PARAMETERS OF STEADY AND TD FLOW SIMULATIONS OF HAWT BLADE SECTION AT 93.5% RADIUS.*

The 524,288-cell C-grid adopted for all simulations has 512 mesh intervals along the aerofoil, 256 intervals in the grid cut, and 512 intervals in the normal-like direction. The farfield boundary is placed at about 50 chords from the aerofoil, and the distance  $d_w$  of the first grid points off the aerofoil surface from the surface itself is about  $10^{-6}c$ . The non-dimensional minimum distance from the wall is  $y_w^+ = (u_\tau d_w) / \nu_w$ , where  $u_\tau$  is the friction velocity and  $\nu_w$  is the kinematic viscosity at the wall. In all the simulations reported below, the maximum value of  $y_w^+$  was always smaller than 1. Figure 7.4 provides an enlarged view of the adopted grid in the aerofoil region. The aerofoil and the whole grid are inclined by the twist angle  $\gamma_p$  on the horizontal direction in both the steady and the TD simulations. In the latter case, the whole grid also undergoes a sinusoidal motion defined by Eqn. (7.5), with amplitude  $h_0$  equal to  $3.03c$ . All TD analyses reported below have been performed using 128 time-intervals per period or rotor revolution. These TD simulations have been run until the maximum  $C_x$ ,  $C_y$  and  $C_m'$  differences over two consecutive oscillation cycles became less than 0.1% of their maxima over the latter cycle of the cycle pair.

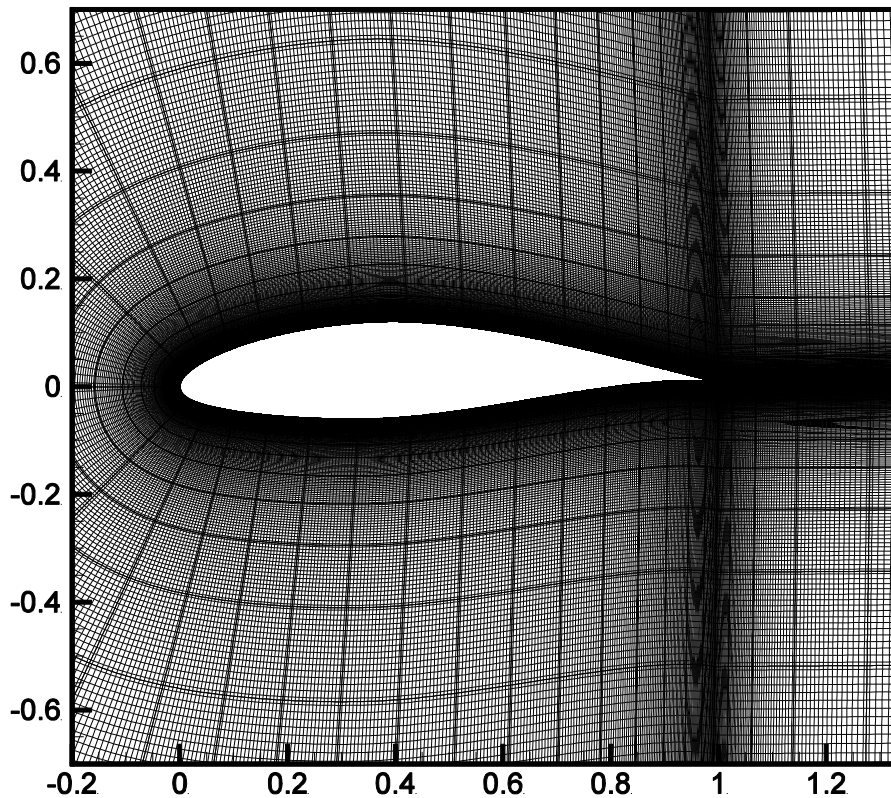


Figure 7.4 GRID VIEW IN AEROFOIL REGION. (Campobasso et al., 2014a)

### 7.1.3 steady flow analysis

In order to assess the effects of compressibility on the steady flow field past the considered HAWT section, such a flow field has been computed with the LSP-enhanced solver for three values of  $M_\infty$ , namely the value of  $2.86 \cdot 10^{-1}$  corresponding to the real flow conditions, and the lower values of  $2.86 \cdot 10^{-2}$  and  $2.86 \cdot 10^{-3}$ . All other physical control parameters of the three simulations are instead those given before. One of objectives of the comparative analysis of these three simulations is to highlight the differences between the prediction of compressible CFD solvers, namely that for  $M_\infty = 2.86 \cdot 10^{-1}$ , and that of incompressible CFD solvers, here taken to correspond to the limit of the LSP-enhanced solution of COSA for  $M_\infty \rightarrow 0$ . Moreover, in order to further assess the benefits of LSP on the solution accuracy,

the simulations for the three values of  $M_\infty$  have also been performed without LSP and compared to their LSP counterparts.

$M_\infty$	LSP			NP		
	$C_l$	$C_d$	$C'_m$	$C_l$	$C_d$	$C'_m$
$2.86 \cdot 10^{-1}$	1.350	0.01380	0.1283	1.355	0.01330	0.1289
$2.86 \cdot 10^{-2}$	1.301	0.01292	0.1261	1.336	0.01220	0.1327
$2.86 \cdot 10^{-3}$	1.298	0.01306	0.1256	1.312	0.03382	0.1379

*Table 7.2 COMPARISON OF FORCE COEFFICIENTS OF BLADE SECTION AT 93.5% RADIUS IN STEADY REGIME FOR  $M_\infty = 2.86 \cdot 10^{-1}$ ,  $M_\infty = 2.86 \cdot 10^{-2}$ , AND  $M_\infty = 2.86 \cdot 10^{-3}$  WITH AND WITHOUT LSP.*

$M_\infty$	$C_l$	$C_d$	$C'_m$
$2.86 \cdot 10^{-1}$	1.334	0.01206	0.1143
$2.86 \cdot 10^{-2}$	1.299	0.01130	0.1187
$2.86 \cdot 10^{-3}$	1.298	0.01129	0.1187

*Table 7.3 FORCE COEFFICIENTS OF BLADE SECTION AT 93.5% RADIUS IN STEADY REGIME FOR  $M_\infty = 2.86 \cdot 10^{-1}$ ,  $M_\infty = 2.86 \cdot 10^{-2}$ , AND  $M_\infty = 2.86 \cdot 10^{-3}$  COMPUTED BY XFOIL*

The second, third and fourth columns of Table 7.2 report respectively the lift coefficient  $C_l$ , the drag coefficient  $C_d$  and the pitching moment coefficient  $C'_m$  computed with the LSP analysis for the three values of  $M_\infty$ . The fifth, sixth and seventh columns report instead the estimates of the same force coefficients obtained by the analysis without LSP. Several interesting observations can be made by cross-comparing the data of this table. Firstly, one notes that the difference between the LSP force estimates for  $M_\infty = 2.86 \cdot 10^{-2}$  and  $M_\infty = 2.86 \cdot 10^{-3}$  is significantly smaller than the difference of the LSP force estimates for  $M_\infty = 2.86 \cdot 10^{-1}$  and  $M_\infty = 2.86 \cdot 10^{-2}$ . This occurrence points to the existence of significant compressibility effects in the outboard regions of large HAWT rotors of the type considered herein. Based on the LSP predictions for the highest and lowest values of  $M_\infty$ , it emerges that the use of an incompressible CFD solver is likely to underestimate by nearly 4% of its real value the lift force on the blade section. The comparison of the LSP- and the NP-estimate of a given force component for the same  $M_\infty$  highlights that the difference between LSP and NP predictions increases significantly as  $M_\infty$  decreases, as expected. This points to the necessity of using LSP even for levels of  $M_\infty$  of order 0.01, which is representative of the relative speeds observed at the roots of HAWT blades. It is also noted that, though relatively small,

the difference between the LSP- and the NP estimate of the three force coefficients at  $M_\infty = 2.86 \cdot 10^{-1}$  is larger than the difference between the LSP- and the NP-estimate of the flat plate drag coefficient at  $M_\infty = 0.1$ . This is presumably due to the higher complexity of the aerofoil flow field with respect to the zero-pressure gradient flat plate boundary layer. In the aerofoil problem, a rapid growth of the boundary layer on the aerofoil suction side (SS) occurs between the peak-velocity point and the TE. The accuracy of the LSP simulation in this low-speed and low-Reynolds number boundary layer region is likely to be higher than the solver without LSP due to the optimised LSP numerical dissipation. The same phenomenon is also reported in Vatsa and Turkel (2004), which compares the viscous drag of the RAE aerofoil for an AoA of  $2.79^\circ$  at  $M_\infty = 0.2$  and  $Re = 6.5 \cdot 10^6$  obtained from the compressible RANS analyses with and without LSP. We have also performed the  $M_\infty = 2.86 \cdot 10^{-1}$  turbulent simulation with and without LSP replacing the NACA64-618 with the thinner NACA0012 aerofoil. By doing so, it has been found that the difference between the LSP- and the NP estimates of the force coefficients become substantially smaller than in the NACA64-618 aerofoil case, which corroborates the above assumptions of low-speed effects even for relatively high freestream Mach numbers.

The steady flow analyses commented above have also been performed using the MIT incompressible panel code XFOIL (Drela, 1989). This code also uses a Karman-Tsien compressibility correction that, for steady and attached laminar, viscous and transitional regimes, allows good compressible flow predictions all the way from incompressible ( $M_\infty = 0$ ) to sonic ( $M_\infty \approx 1$ ) conditions. Like the COSA simulations reported above, the three XFOIL analyses have been performed assuming fully turbulent boundary layer. The force coefficients computed by XFOIL for the three considered values of  $M_\infty$  are provided in Table 7.3. These results highlight sensitivities of the force coefficients to variations of  $M_\infty$  of the same order of those obtained from the COSA results. Moreover, a fairly good agreement of the force coefficients predicted by the two codes is observed.

The profiles of the skin friction coefficients  $c_f$  along the aerofoil chord obtained with the LSP analysis for the three values of  $M_\infty$  are reported in the top left subplot of Figure 7.5 whereas those obtained with the analysis without LSP are provided in the top right subplot. The bottom left subplot reports the three LSP estimates of the static pressure coefficient  $c_p$  along the chord, whereas the estimates obtained without LSP are depicted in the bottom right subplot of Figure 7.5. Inspection of the LSP  $c_f$  and  $c_p$  profiles confirms that significant

differences exist between the  $M_\infty = 2.86 \cdot 10^{-1}$  profiles and those associated with the other two values of  $M_\infty$ , and also that the profiles associated with the two lower values are indistinguishable. This confirms that, for this problem, compressibility effects exist at the real operating conditions. The top right subplot of Figure 7.5 highlights that the  $c_f$  profile for the lowest freestream Mach number is wrong, whereas those for  $M_\infty = 2.86 \cdot 10^{-2}$  and  $M_\infty = 2.86 \cdot 10^{-1}$  appear to be closer than observed in the LSP results. The main feature emerging from the  $c_p$  profiles obtained without LSP is that the result for the lowest value of  $M_\infty$  features significant non-physical oscillations at both the LE and the TE.

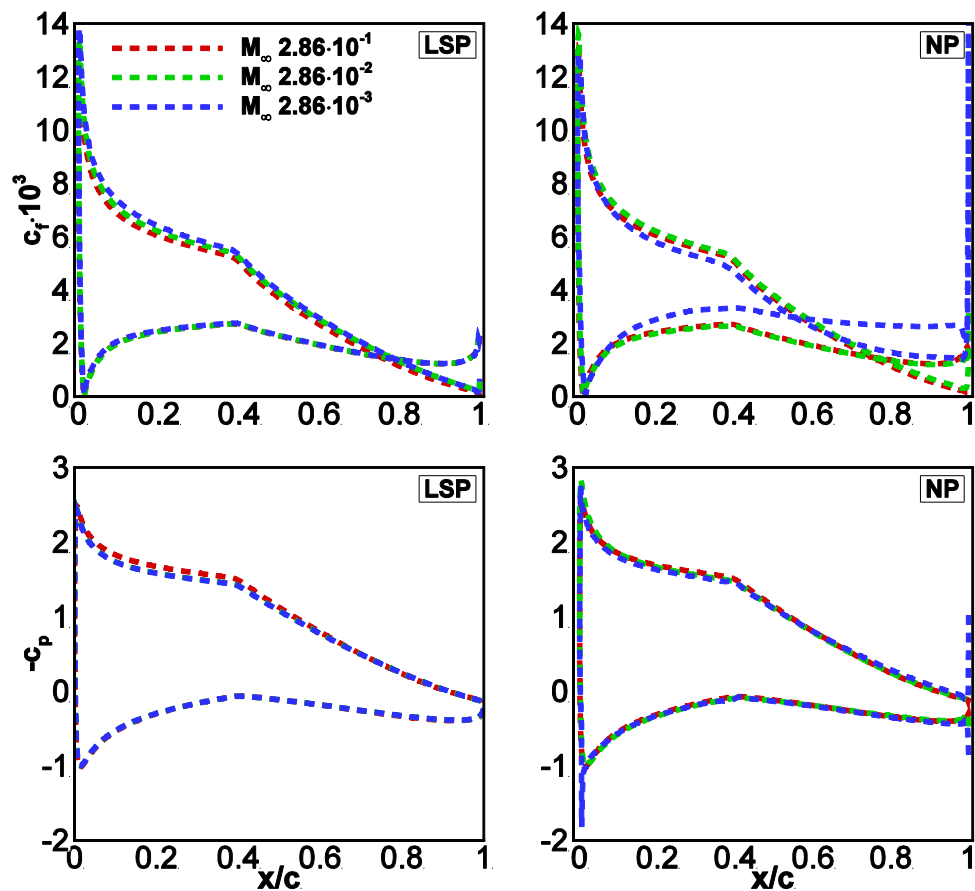


Figure 7.5 COMPARISON OF SKIN FRICTION COEFFICIENT ( $c_f$ ) AND PRESSURE COEFFICIENT ( $c_p$ ) OF BLADE SECTION AT 93.5% RADIUS IN STEADY REGIME FOR  $M_\infty = 2.86 \cdot 10^{-1}$ ,  $M_\infty = 2.86 \cdot 10^{-2}$ , AND  $M_\infty = 2.86 \cdot 10^{-3}$ . TOP LEFT SUBPLOT:  $c_f$  PROFILES FROM SIMULATIONS WITH LSP. BOTTOM LEFT SUBPLOT:  $c_p$  PROFILES FROM SIMULATIONS WITH LSP. TOP RIGHT SUBPLOT:  $c_f$  PROFILES FROM SIMULATIONS WITHOUT LSP. BOTTOM RIGHT SUBPLOT:  $c_p$  PROFILES FROM SIMULATIONS WITHOUT LSP.

It should be noted that the improvements of the solution accuracy achievable by using LSP in the compressible flow analysis of HAWT flows are even higher than reported above and in the next subsection when separated flow regions exist. The compressible  $M_\infty$  0.044 RANS

analyses of the S809 aerofoil reported in work of Le Pape and Lecanu (2004), for example, point to the fact that significant improvements of the prediction of the stall characteristics can be achieved by using LSP in the compressible solver.

## 7.1.4 yawed wind analysis with time-domain approach

In order to assess the effects of compressibility on the time dependent flow field past the considered HAWT section caused by the assumed yaw error of  $45^\circ$ , also such a flow field has been computed with the LSP-enhanced solver for three values of  $M_\infty$ , namely the value of  $2.85 \cdot 10^{-1}$  corresponding to the real flow conditions, and the lower values of  $2.85 \cdot 10^{-2}$  and  $2.85 \cdot 10^{-3}$ . All other physical control parameters of the three simulations are instead those given at the beginning of this section. As in the steady case, one of the objectives of comparing these three simulations is to highlight the differences between the prediction of compressible CFD solvers, namely that for  $M_\infty = 2.85 \cdot 10^{-1}$ , and that of incompressible CFD solvers, here taken to correspond to the limit of the LSP-enhanced solution of COSA for  $M_\infty \rightarrow 0$ . Moreover, in order to further assess the benefits of LSP on the solution accuracy, the simulations for the three values of  $M_\infty$  have also been performed without LSP and compared to their LSP counterparts.

The hysteresis loops of the horizontal force coefficients  $C_x$ , the vertical force coefficient  $C_y$  and the pitching moment coefficient  $C_m'$  predicted by the three LSP simulations are depicted in the top left, middle left and bottom left subplots of Figure 7.6 respectively. The variable along the horizontal axis of these subplots is the angle  $\Phi$  between the time-dependent freestream velocity  $\widehat{W}$  defined by Eqn. (7.1) and the chord over one period. One has  $\Phi = \alpha - \gamma_p$ , with  $\alpha$  defined by Eqn. (7.2). The  $C_x$ ,  $C_y$  and  $C_m'$  hysteresis loops predicted by the three simulations without LSP are instead reported in the top right, middle right and bottom right subplots respectively. Examination of the hysteresis loops obtained with the LSP analyses point to significant compressibility effects for the real operating conditions of  $M_\infty = 2.85 \cdot 10^{-1}$ , since the force loops for this value of the freestream Mach number differ significantly from those corresponding to the two lower values of  $M_\infty$ . Such effects are particularly noticeable in the  $C_x$  loops, which highlight an increment of about 5% of the mean tangential

#### 7.1.4 yawed wind analysis with time-domain approach

force acting on the blade section caused by compressibility effects. The  $C_y$  loops also highlight increments of about 5% of the mean axial thrust coefficient due to compressibility effects. These results underline the importance of including compressibility effects in the unsteady analysis of HAWT rotor aerodynamics, particularly in view of estimating the energy production and the structural loads on the turbine in yawed flow conditions. Cross comparison of the left and right subplots of Figure 7.6 also reveals that, while the force loops for the highest value of  $M_\infty$  computed with and without LSP are in reasonably good agreement, the analyses without LSP fail to predict the correct trend of the hysteresis cycles as  $M_\infty$  decreases.

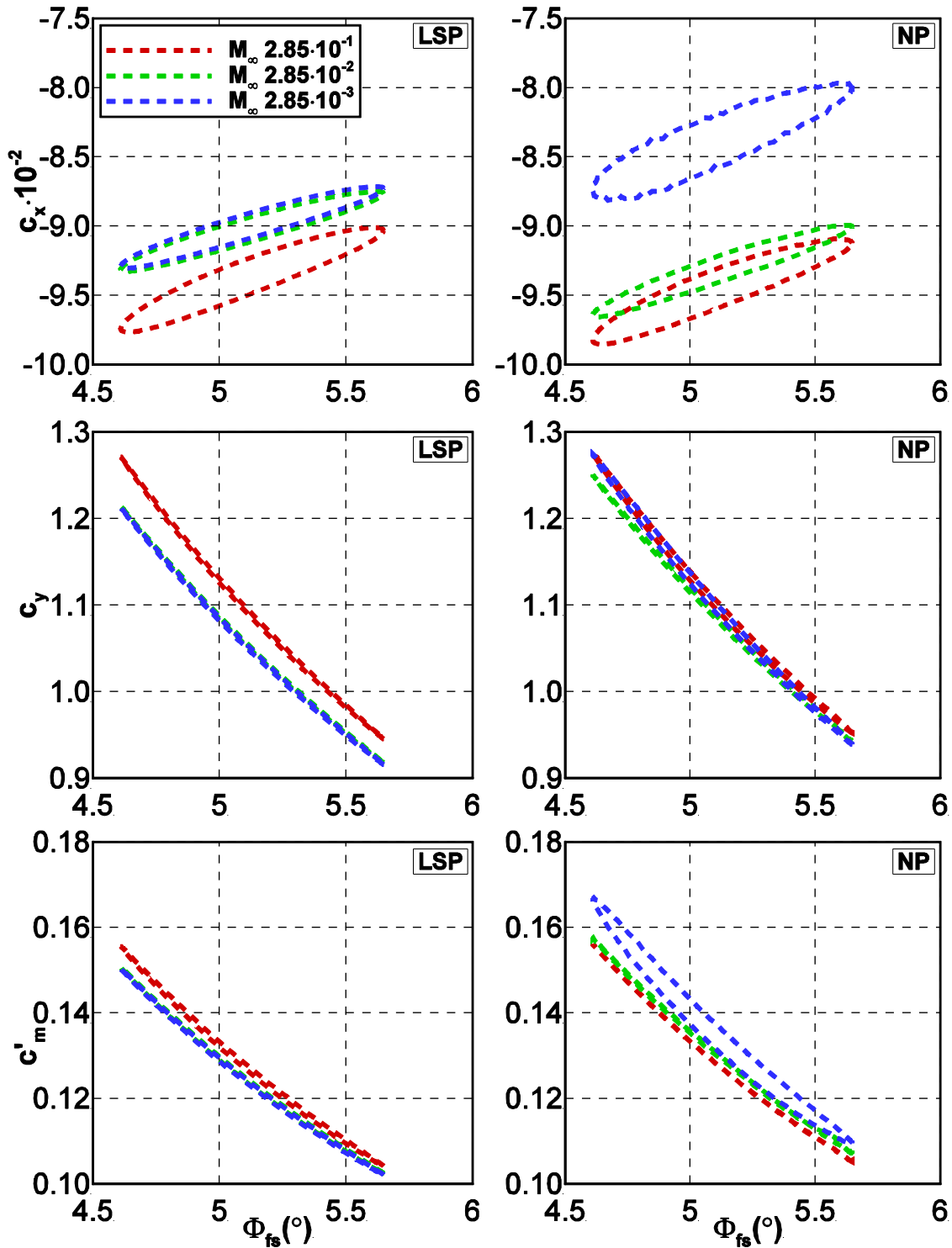
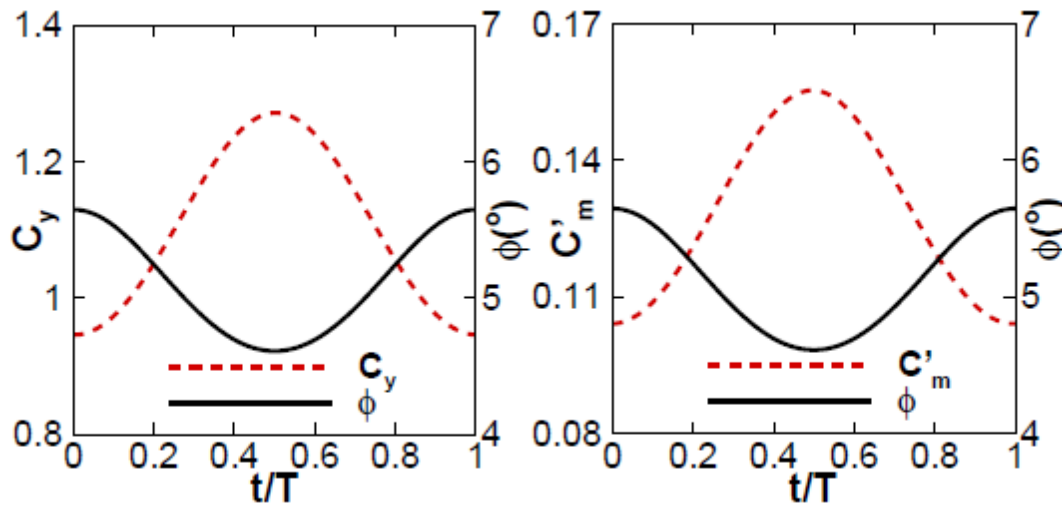


Figure 7.6 HYSTERESIS LOOPS OF HORIZONTAL FORCE COEFFICIENT ( $C_x$ ), VERTICAL FORCE COEFFICIENT ( $C_y$ ), AND CONSTANHEAD PITCHING MOMENT COEFFICIENT ( $C_m'$ ) OF BLADE SECTION AT 93.5 % RADIUS IN YAWED FLOW FOR  $M_\infty = 2.85 \cdot 10^{-1}$ ,  $M_\infty = 2.85 \cdot 10^{-2}$ , AND  $M_\infty = 2.85 \cdot 10^{-3}$  TOP LEFT SUBPLOT:  $C_x$  LOOP WITH LSP. MIDDLE LEFT SUBPLOT:  $C_y$  LOOP WITH LSP. BOTTOM LEFT SUBPLOT:  $C_m'$  LOOP WITH LSP. TOP RIGHT SUBPLOT:  $C_x$  LOOP WITHOUT LSP. MIDDLE RIGHT SUBPLOT:  $C_y$  LOOP WITHOUT LSP. BOTTOM RIGHT SUBPLOT:  $C_m'$  LOOP WITHOUT LSP.

### 7.1.4 yawed wind analysis with time-domain approach

Figure 7.7 reports the  $C_y$  and  $C_m'$  force coefficients, and the freestream AoA  $\Phi$  against the percentage time of the rotor revolution  $t/T$ . The values  $t/T = 0$  and  $t/T = 0.5$  correspond to the blade at its highest and lowest point respectively. It is therefore observed that the maximum value of both force coefficients occurs when the blade is at its lowest position, whereas the minimum value occurs when the blade is at its highest position. It has been shown in Campobasso et al. (2014b) that, for the considered blade section, the maximum and the minimum of the  $C_y$  and  $C_m'$  force coefficients occur, respectively, when the blade is vertical and rotates against the circumferential yawed wind component, and when the blade is vertical and rotates with the circumferential yawed wind component.



*Figure 7.7 TIME-EVOLUTION OF FORCE COEFFICIENTS OF BLADE SECTION AT 93.5% RADIUS IN YAWED FLOW (LSP SIMULATION FOR  $M_\infty = 2.85 \cdot 10^{-1}$ ). LEFT PLOT: VERTICAL FORCE COEFFICIENT ( $C_y$ ) RIGHT PLOT: CONSTANT-HEAD PITCHING MOMENT COEFFICIENT ( $C_m'$ ).*

The contours of the static pressure coefficient past the aerofoil LE and TE computed for  $M_\infty = 2.85 \cdot 10^{-1}$  and  $M_\infty = 2.85 \cdot 10^{-3}$  using the LSP-enhanced solver are depicted in Figure 7.8. Both snapshots refer to the beginning of the periodic motion defined by Eqn. (7.5) (0% of the period). The left subplot shows the portion of the aerofoil from the LE to its 25% chord, whereas the right subplot shows the portion of the aerofoil from 75% chord to the TE. The noticeable differences between the constant pressure lines of the two solutions visible in both subplots confirm the significant compressibility effects highlighted by the cross comparison of the hysteresis loops above.

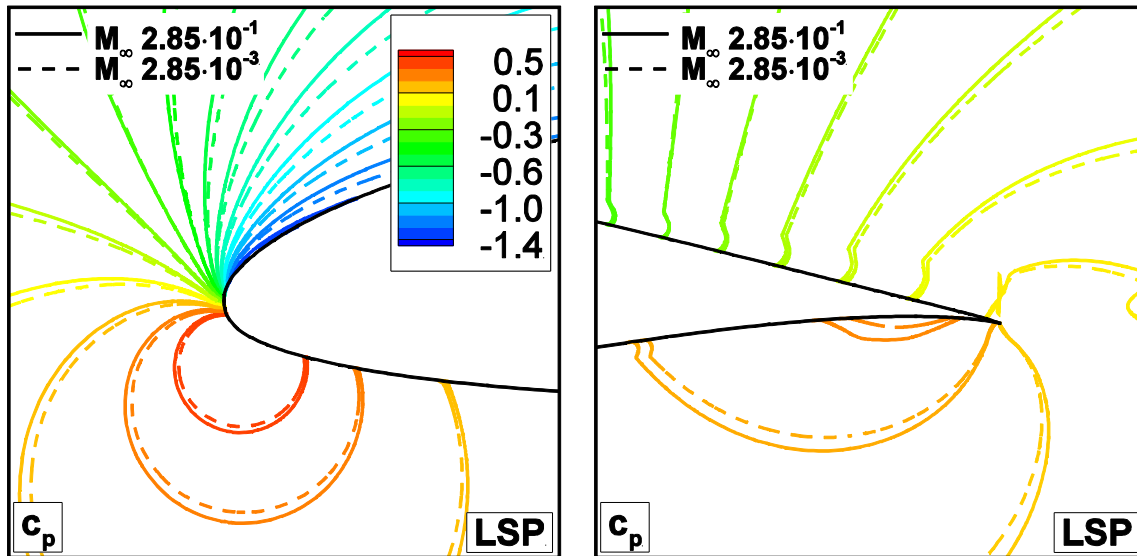


Figure 7.8 COMPARISON OF STATIC PRESSURE COEFFICIENT  $c_p$  CONTOURS AT  $M_\infty = 2.85 \cdot 10^{-1}$ , AND  $M_\infty = 2.85 \cdot 10^{-3}$  OBTAINED WITH LSP-ENHANCED CFD SOLVER.

The  $c_p$  contours past the aerofoil LE and TE computed for all three values of  $M_\infty$  with and without LSP are depicted in Figure 7.9. Also these snapshots refer to the beginning of the periodic motion defined by Eqn.(7.5). The top, middle and bottom subplot rows refer to the values of  $M_\infty$  of  $2.85 \cdot 10^{-1}$ ,  $2.85 \cdot 10^{-2}$  and  $2.85 \cdot 10^{-3}$  respectively, and each subplot provides the  $c_p$  contours of the simulations with and without LSP. This figure highlights that the local static pressure around the aerofoil edges predicted by the compressible analysis without LSP starts being affected by significant errors already at  $M_\infty = 2.85 \cdot 10^{-2}$ . A very accurate prediction of the near-aerofoil static pressure field is an essential requirement for accurate predictions of the noise generated by the blades. Hence, these results emphasise the necessity of using compressible solvers with LSP for accurately predicting the blade noise generation along the entire span of the blades. A significant amount of noise generation is typically ascribed to the outboard part of the blade, where relative speeds are fairly high. Nevertheless, off-design conditions and very high wind speeds may result in significant amount of flow separations also on the outboard part of the blade. In these circumstances, both the aerodynamic loads and the accurate prediction of noise generation are very likely to require the use of LSP when performing these analyses by means of a compressible RANS solver.

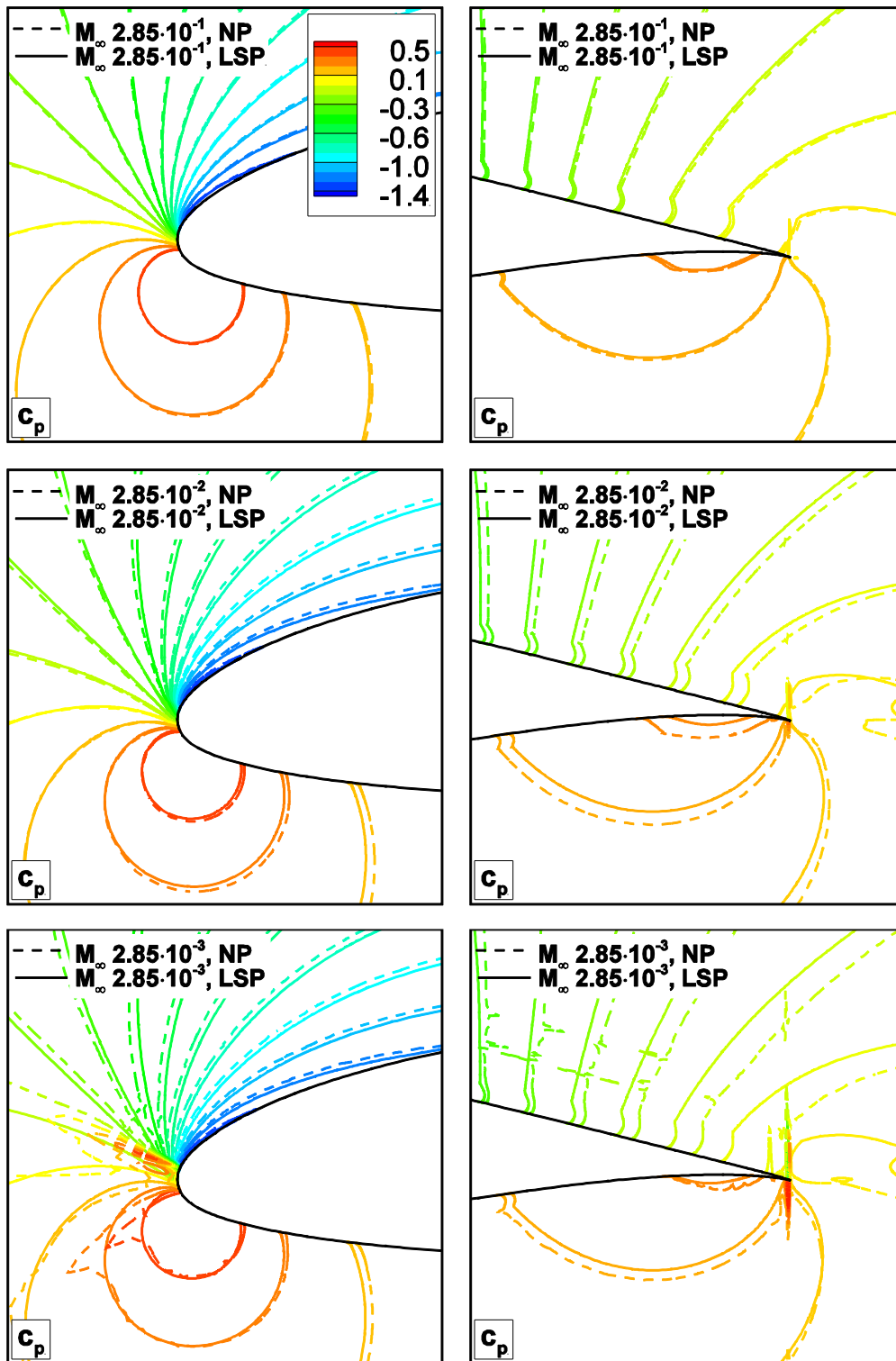


Figure 7.9 COMPARISON OF STATIC PRESSURE COEFFICIENT  $c_p$  CONTOURS OF BLADE SECTION AT 93.5% RADIUS IN YAWED FLOW AT THREE VALUES OF  $M_\infty$  OBTAINED WITH AND WITHOUT LSP. TOP LEFT SUBPLOT: LE AREA,  $M_\infty = 2.85 \cdot 10^{-1}$ . MIDDLE LEFT SUBPLOT: LE AREA,  $M_\infty = 2.85 \cdot 10^{-2}$ . BOTTOM LEFT SUBPLOT: LE AREA,  $M_\infty = 2.85 \cdot 10^{-3}$ . TOP RIGHT SUBPLOT: TE AREA,  $M_\infty = 2.85 \cdot 10^{-1}$ . MIDDLE RIGHT SUBPLOT: TE AREA,  $M_\infty = 2.85 \cdot 10^{-2}$ . BOTTOMRIGHT SUBPLOT: TE AREA,  $M_\infty = 2.85 \cdot 10^{-3}$ .

## 7.1.5 yawed wind analysis with frequency-domain approach

Based on the successful demonstration of the use of the turbulent HB RANS technology for unsteady HAWT aerodynamics in the non-preconditioned study reported in the paper of Campobasso et al. (2014b), we have considered herein a periodic flow past the blade section that is analysed in that paper, namely that at 30% blade length of the same blade to which the section analysed in the previous section belongs. This has been done to validate the harmonic balance LSP implementation of the COSA code developed in this research. The operating conditions of the wind turbine periodic flow simulated with the LSP harmonic balance analysis are similar to those of the time-dependent problem discussed in the previous section (rotor speed  $12RPM$  or  $\omega = 1.26 \text{ rad/s}$ , freestream wind speed  $V_{fs} = 13m/s$ , yaw angle  $\delta = 45^\circ$ ). However, here we consider the blade section at 30% blade length, which features a DU99W350 aerofoil with a chord  $c$  of 5.2m and a twist angle  $\gamma_p$  of  $10.4^\circ$ . Therefore, the relative angle of attack  $\Phi_\infty (= \alpha_\infty - \gamma_p = 6.12^\circ)$  for the 2D simulations is obtained by subtracting the twist  $\gamma_p$  to the inflow angle  $\alpha_\infty = 16.56^\circ$  obtained from Eqn.(7.4). Using the value of  $W_\infty$  obtained by inserting the required data into Eqn. (7.3) and the standard temperature of 288K, yields a freestream Mach number  $M_\infty = 0.095$ . The Reynolds number based on the standard density of  $1.22kg/m^3$ , the velocity  $W_\infty$ , the aerofoil chord and the air viscosity at standard temperature is  $1.15 \cdot 10^7$ , and the reduced frequency  $\lambda = \omega c/W_\infty$  is 0.203.

The 524,288-cell C-grid adopted for all simulations has 512 mesh intervals along the aerofoil, 256 intervals in the grid cut, and 512 intervals in the normal-like direction. The farfield boundary is placed at about 50 chords from the aerofoil, and the distance  $d_w$  of the first grid points off the aerofoil surface from the surface itself is about  $10^{-6}c$ , which yields the maximum value of the non-dimensional minimum wall distance  $y_w^+$  always smaller than 1 in all simulations reported below. Figure 7.10 provides an enlarged view of the adopted grid in the aerofoil region. The aerofoil and the whole grid are inclined by the twist angle  $\gamma_p$  on the horizontal direction. The whole grid also undergoes a sinusoidal motion defined by Eqn. (7.5) with amplitude  $h_0$  equal to  $1.4c$ . The only TD analyses reported below have been performed using 128 time-intervals per period or rotor revolution, which, according to the time-refinement aerodynamic analysis (Campobasso et al., 2014b), is the minimum number of

### 7.1.5 yawed wind analysis with frequency-domain approach

time-intervals required to accurately predict the lift, drag and pitching moment coefficients without a further increment of the time resolution, and the simulation has been run until the maximum  $C_x$ ,  $C_y$  and  $C_m'$  differences over two consecutive oscillation cycles become less than 0.1% of their maxima over the latter cycle of the cycle pair.

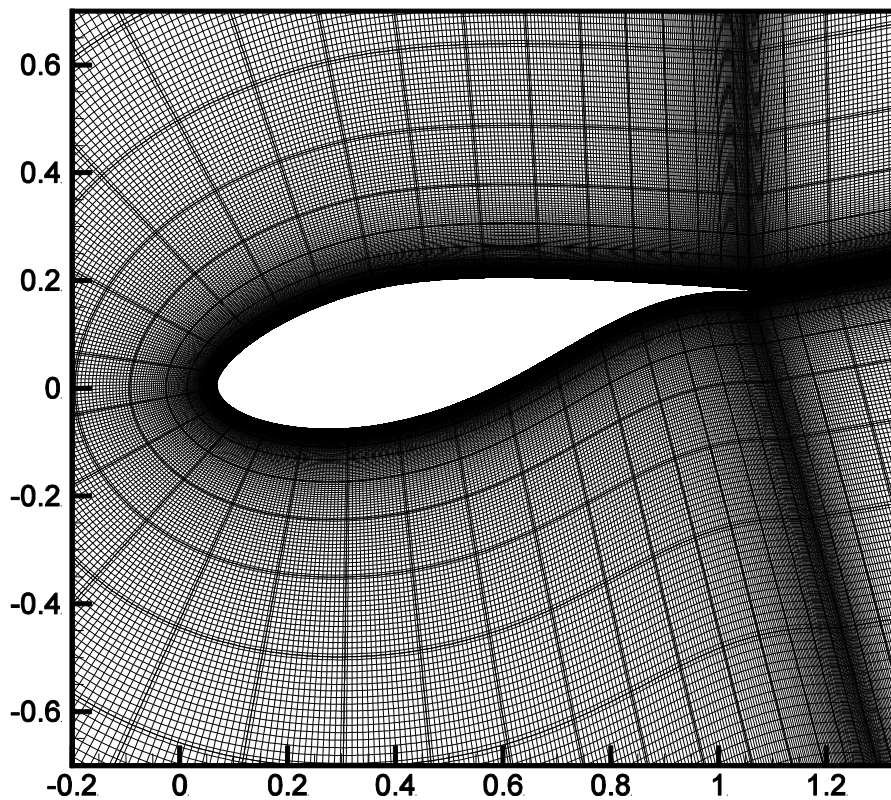
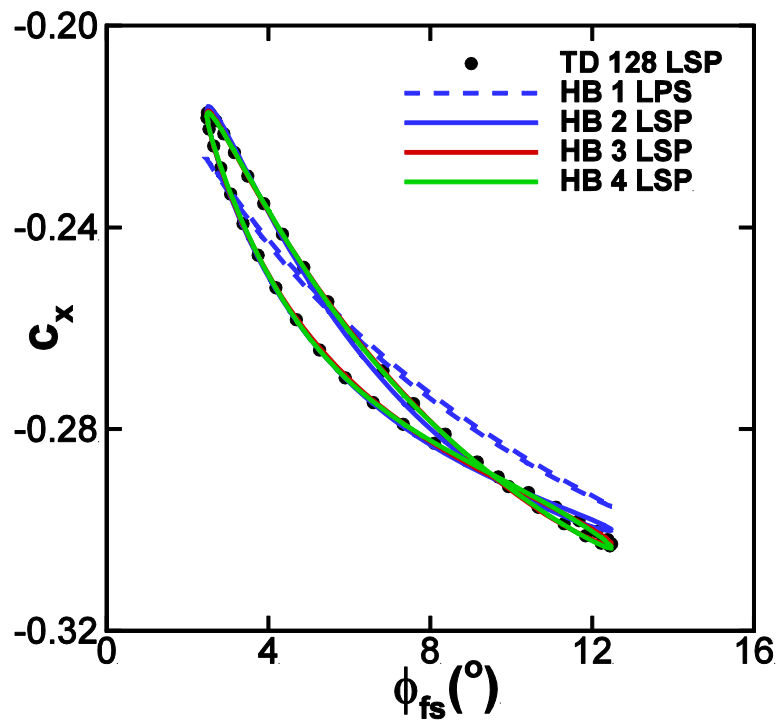


*Figure 7.10 GRID VIEW IN AEROFOIL REGION.(Campobasso et al., 2014b)*

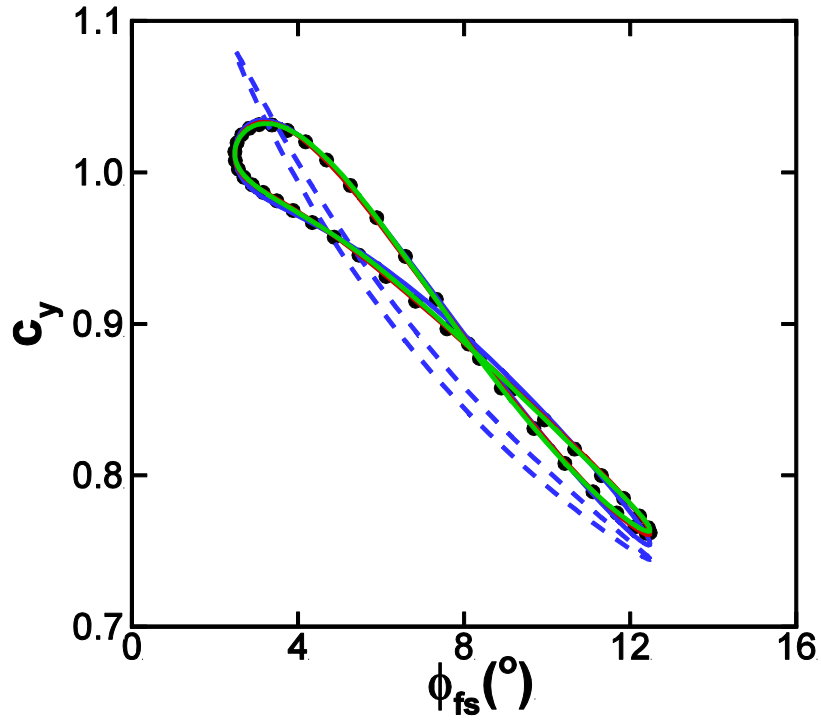
Having established the reference time-domain analysis as a term of comparison, the next important step is to determine the minimum harmonic number necessary to capture the flow unsteady characteristics with the harmonic balance solver and provide a comparable solution to the above TD 128 solution. Thus four HB simulations have been performed. The number of harmonics  $N_H$  for the simulations are 1, 2, 3 and 4, and they are denoted by the acronym *HB* followed by the value of  $N_H$ . All HB analyses have been run for 10,000 MG iterations, since this is the minimum value required for the convergence of all force components of all harmonics retained by the four HB analyses. Each physical time-step of the TD 128 analysis has instead used 3,000 MG iterations, as this value has been sufficient for the convergence of

### 7.1.5 yawed wind analysis with frequency-domain approach

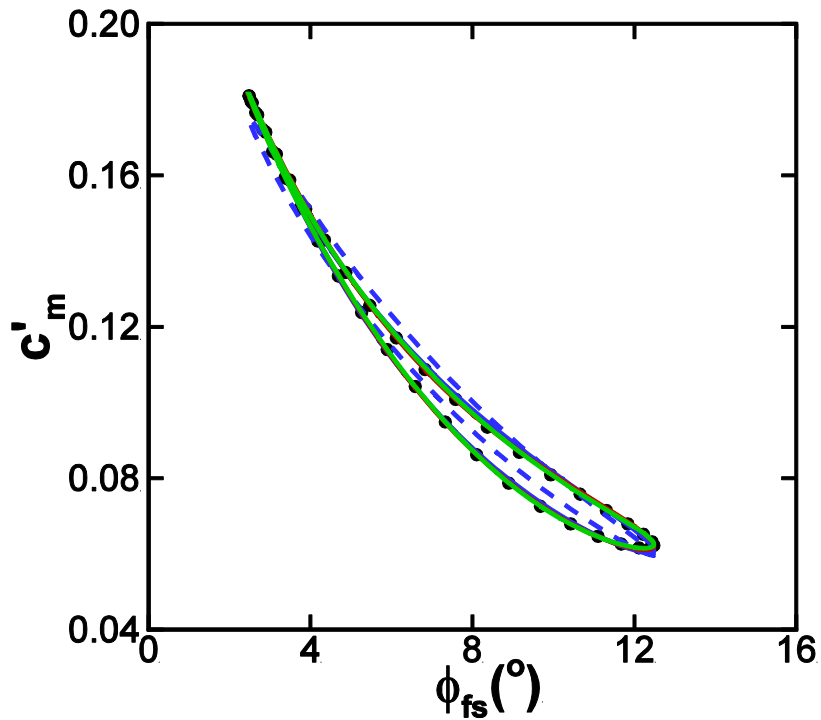
all force components. In order to reduce the periodicity error below the 0.1 % threshold defined at the beginning, five periods have to be simulated starting from a freestream initial condition. The hysteresis loops of the force coefficients of  $C_x$ ,  $C_y$  and  $C_m'$  computed by the four HB LSP analyses and one TD LSP analyses are plotted against  $\Phi_{fs}$  in the three subplots of Figure 7.11. Same conclusion is discovered in these results as in the reference that at least 3 complex harmonics are required to achieve a frequency-domain resolution of all force components comparable to that of the TD 128 simulation, since only negligible differences is found between the HB 3 and the HB 4 force loops, whereas the loops of  $C_x$  and  $C_y$  computed with the HB 2 and HB 3 analyses present some discrepancies for the highest values of  $\Phi_{fs}$ .



a)



b)



c)

Figure 7.11 HYSTERESIS FORCE LOOPS OF BLADE SECTION AT 30 % RADIUS IN YAWED FLOW FOR  $M_\infty = 9.5 \cdot 10^{-2}$ , COMPUTED WITH TD LSP SOLVERS AND FOUR HB LSP ANALYSES: a) HORIZONTAL FORCE COEFFICIENT ( $c_x$ ), b) VERTICAL FORCE COEFFICIENT ( $c_y$ ), c) CONSTANT-HEAD PITCHING MOMENT COEFFICIENT ( $c_m^E$ ).

### 7.1.5 yawed wind analysis with frequency-domain approach

Before proceeding to the results of LSP HB simulations for more challenging problems, a computational efficiency analyses is provided below. Since all the HB analyses reported herein could be performed with the FERK MG iteration rather than the PIRK algorithm given by Eqn.(5.30), the computational time of one HB MG iteration increases in a moderately superlinear fashion with  $N_H$ , resulting in the cost of one MG cycle for a HB- $N_H$  simulation being higher than  $2N_H + 1$  times the cost of the same MG cycle in the steady simulation. This overhead is due to the calculation of the HB source term  $\omega V_H D_H Q_H$  appearing in Eqn. (3.25), and is proportional to  $(2N_H + 1)^2$ . By calculating the ratio of measured CPU-time per MG iteration between the HB  $N_H$  analysis and the steady analysis and dividing it by  $2N_H + 1$ , one can quantify this overhead which is labelled  $C_{MG}$  below. This variable has been reported in the second row of Table 7.4. It is concluded that the overhead for the calculation of the HB source term with the HB-3 analysis makes the average CPU time of one HB MG cycle for calculating one HB snapshot about 80% higher than that of one steady MG cycle. The sixth column of Table 7.4 reports  $C_{MG}$  for the TD simulation, and the small overhead of 9% is that required for the calculation of the source term  $1.5Q^{n+1}/\Delta t$  appearing in Eqn. (3.22).

The HB speed-up parameter, defined as the ratio between the wallclock time of the TD 128 simulation and that of the four HB analyses is reported in the third row of Table 7.4. It is seen that a fairly accurate estimate of the time dependent loads associated with the considered yawed condition can be obtained with HB 3 analysis while only at the cost of as low as 6% of the CPU-time required in the TD 128 analysis.

	HB 1	HB 2	HB 3	HB 4	TD 128	steady
$C_{MG}$	1.25	1.74	1.81	1.82	1.09	1.00
speed-up	54.3	24.1	16.5	12.7	1	

*Table 7.4 ACCELERATION FACTORS OF HB ANALYSES WITH RESPECT TO TIME-DOMAIN ANALYSIS FOR THE 30% BLADE SECTION.*

In order to further assess the benefits of LSP on the accuracy of the HB analysis, two additional simulations at lower Mach numbers  $M_\infty = 9.5 \cdot 10^{-3}$  and  $9.5 \cdot 10^{-4}$  have been performed with and without LSP and compared to the results obtained at the highest Mach number. The hysteresis loops of the horizontal force coefficients  $C_x$ , the vertical force coefficient  $C_y$  and the constant-head pitching moment coefficient  $C_m'$  predicted by the three LSP simulations are plotted against the angle of attack  $\Phi_{f_s}$  and depicted in the top left, middle left and bottom left subplots of Figure 7.12 respectively, whereas the estimates of

### 7.1.5 yawed wind analysis with frequency-domain approach

three force coefficients without LSP are instead reported in the top right, middle right and bottom right subplots respectively. Cross comparisons of the hysteresis loops obtained with and without the LSP analyses in the left and right subplots of Figure 7.12 show that while the force loops for the highest value of  $M_\infty$  computed with and without LSP are in reasonably good agreement, the analyses without LSP fail to predict the correct trend of the hysteresis cycles as  $M_\infty$  decreases, and more importantly negligible differences are noticed between the results of three LSP simulations, which points to the fact that a Mach-independent solution to a non-linear flow problem can be provided using HB LSP analysis and satisfactory accuracy is thus well maintained even in the region of extremely low Mach number.

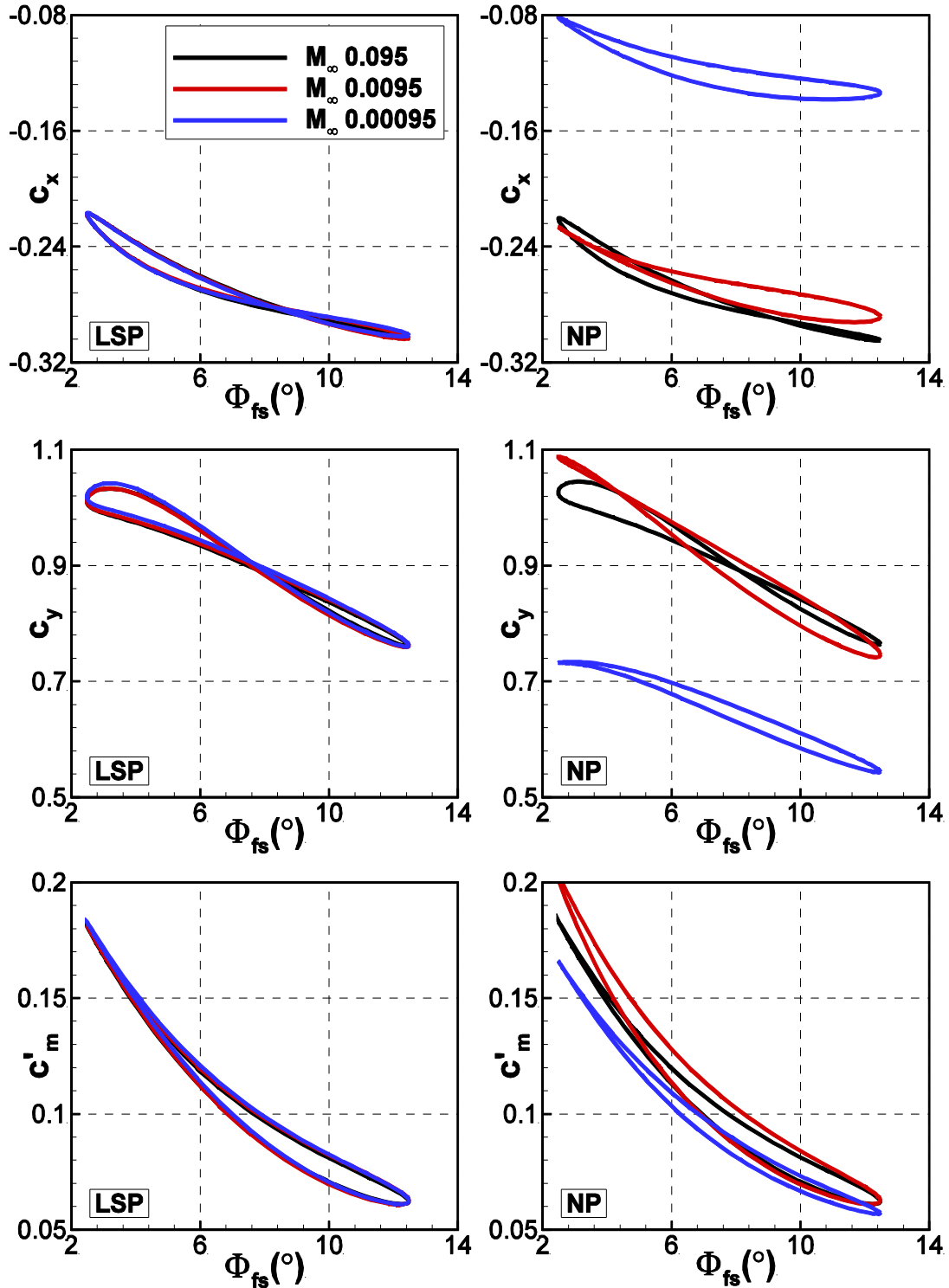


Figure 7.12 HYSTERESIS LOOPS OF HORIZONTAL FORCE COEFFICIENT ( $C_x$ ), VERTICAL FORCE COEFFICIENT ( $C_y$ ), AND CONSTANHEAD PITCHING MOMENT COEFFICIENT ( $C_m'$ ) OF BLADE SECTION AT 30 % RADIUS IN YAWED FLOW FOR  $M_\infty = 9.5 \cdot 10^{-2}$ ,  $M_\infty = 9.5 \cdot 10^{-3}$ , AND  $M_\infty = 9.5 \cdot 10^{-4}$  TOP LEFT SUBPLOT:  $C_x$  LOOP WITH LSP. MIDDLE LEFT SUBPLOT:  $C_y$  LOOP WITH LSP. BOTTOM LEFT SUBPLOT:  $C_m'$  LOOP WITH LSP. TOP RIGHT SUBPLOT:  $C_x$  LOOP WITHOUT LSP. MIDDLE RIGHT SUBPLOT:  $C_y$  LOOP WITHOUT LSP. BOTTOM RIGHT SUBPLOT:  $C_m'$  LOOP WITHOUT LSP.

## 7.2 Horizontal axis wind turbine aerodynamics (3D)

The aerodynamic analyses reported in this section refer to the steady inviscid flow field past the rotating NREL 5MW HAWT. The steady analysis refers to the case in which the wind direction is orthogonal to the rotor plane. The rotor radius  $R$  is 63.0m, the freestream wind velocity  $V_\infty$  is 11.4m/s, yielding a freestream Mach number  $M_\infty = 0.0335$  based on the standard temperature 288K, and the rotor speed is 12.1RPM, which corresponds to a value of  $\omega$  of about 1.27rad/s and a Mach number at the blade tip equal to 0.235. The tip speed ratio ( $TSR = \omega R / M_\infty$ ) is hence calculated as 7.015. The results to be analysed and compared corresponds to the blade sections of 25% and 89% of the whole rotor blade respectively. The main physical parameters of the steady simulations analysed in this case are reported in Table 7.5.

Yaw( $\delta$ )	Mode	$M_\infty$	$TSR$
0°	Steady	0.335	7.015

*Table 7.5 MAIN PHYSICAL PARAMETERS OF THE STEADY FLOW SIMULATION OF NREL 5MW HAWT*

The adopted structured mesh for all simulations has a multi-block C–H topology with 1473751 cells in total. It represents one azimuthal sector around a single blade. Thanks to the implementation of the periodicity boundary condition, the computational domain can be restricted to one 120° azimuthal sector as shown in Figure 7.13. The configuration considered in this work is the blade without the root which is also presented in Figure 7.13. The grid extension in the wind direction is  $\pm 20R$  upstream and downstream of the wind turbine and  $6R$  in the spanwise direction, ensuring an undisturbed flow field near the domain boundaries. Due to the fact that this is our first attempt to analyse a 3D wind turbine test case, the flow field is assumed to be inviscid and therefore no particular requirement has been specified when defining the wall distance of the first grid points off the wall. The TD solutions reported below have been obtained using 360 time-intervals per period or rotor revolution. These TD simulations have been run until the maximum lift and momentum coefficient differences over two consecutive oscillation cycles became less than 0.1% of their maxima over the latter cycle of the cycle pair.

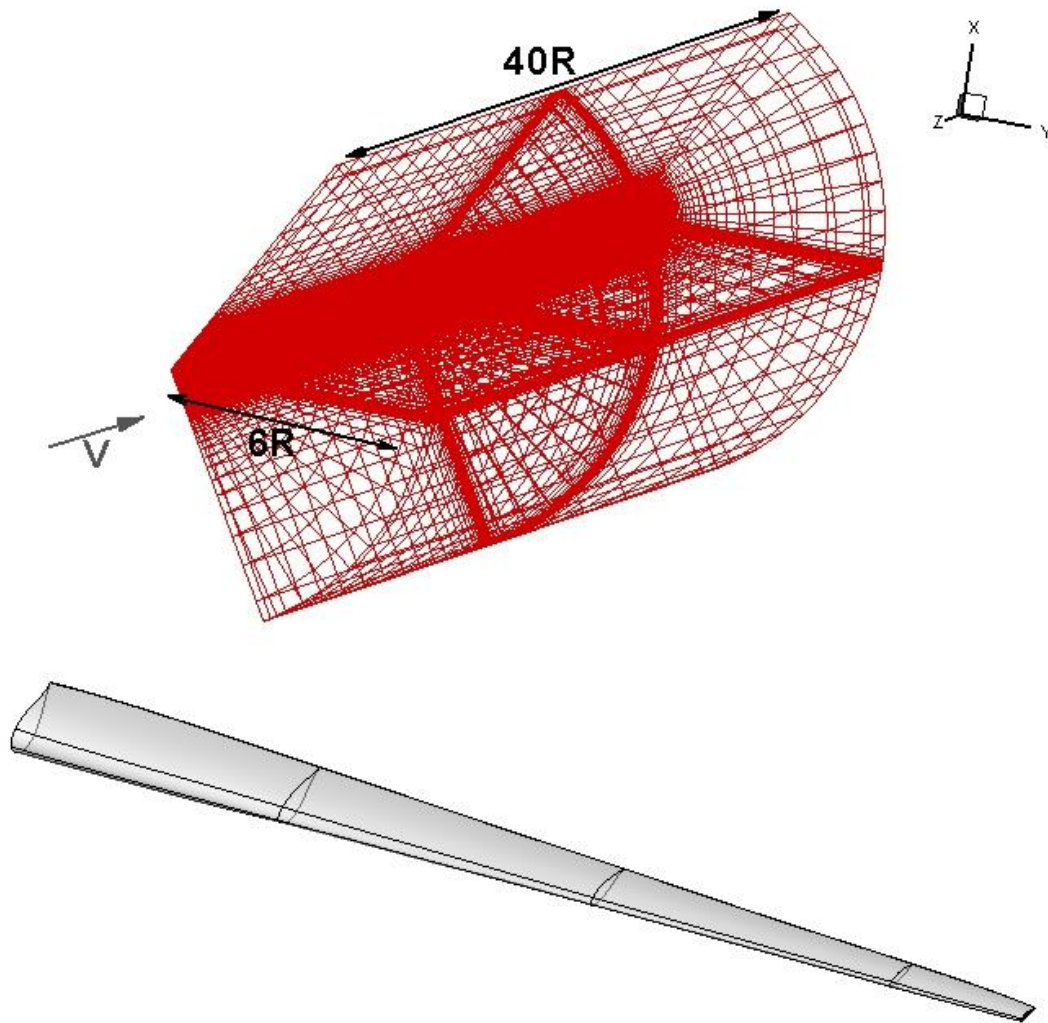


*Figure 7.13 C-H GRID OF A SINGLE BLADE OF WIND TURBINE*

In order to demonstrate the necessity of using LSP-enhanced solver to predict the flow field past the HAWT, the simulations have been performed for two values of  $M_\infty$ , namely the value of  $3.35 \cdot 10^{-2}$  corresponding to the real flow conditions, and the lower value of  $3.35 \cdot 10^{-3}$ . One primary objective of the comparative analysis of the simulations with and without LSP is to assess the benefits of LSP to the solution accuracy by highlighting its solution independence of the variation of freestream Mach number  $M_\infty$ . Moreover, the effects of compressibility on the steady flow field past the outbound section (89% in our case) of the blade can be assessed by analysing the differences between the prediction of compressible CFD solver, namely that for  $M_\infty = 3.35 \cdot 10^{-2}$  (note that the relative local Mach in this section can be as high as 0.238), and that of incompressible CFD solvers, here taken to correspond to the limit of the LSP-enhanced solution of COSA for  $M_\infty \rightarrow 0$ .

The  $c_p$  contours past the LE and TE of the aerofoil at 25% blade length computed with and without LSP for the two indicated values of  $M_\infty$  are depicted in Figure 7.14. The left subplots show the portion of the aerofoil from the LE to its 25% chord, whereas the right subplots show the portion of the aerofoil from 75% chord to the TE. The top and middle subplot rows refer to the  $c_p$  contours of the simulations with and without LSP for the values of  $M_\infty$  of  $3.35 \cdot 10^{-2}$  and  $3.35 \cdot 10^{-3}$  respectively, and the bottom subplot rows depict the contours of static pressure coefficient computed for  $M_\infty = 3.35 \cdot 10^{-2}$  and  $M_\infty = 3.35 \cdot 10^{-3}$  using the LSP-enhanced solver only. Similar comparisons of the  $c_p$  contours past the aerofoil at 89% blade length are depicted in Figure 7.15. These two figures highlight that even for the outbound blade section where the local Mach number is relatively high, the local static pressure around the aerofoil edges predicted by the compressible analysis without LSP starts being affected by noticeable errors already at  $M_\infty = 3.35 \cdot 10^{-2}$ , which corresponds to the normal operating condition for the wind turbine. A very accurate prediction of the near-aerofoil static pressure field is an essential requirement for accurate predictions of the noise generated by the blades. Hence, these results emphasise the necessity of using compressible solvers with LSP for accurately predicting the blade noise generation along the entire span of the blades. Moreover, a significant amount of noise generation and flow separations is typically ascribed to the outboard part of the blade as a result of the fairly high relative speeds. In these circumstances, both the aerodynamic loads and the accurate prediction of noise generation are very likely to require the use of LSP when performing these analyses by means of a compressible RANS solver. On the other hand, the noticeable differences between the constant static pressure lines of the two LSP solutions at 89% blade section visible in the bottom subplots of Figure 7.15 is due to the compressibility effect in the real operating condition at  $M_\infty = 3.35 \cdot 10^{-2}$  as the maximum local Mach number is found to be above the compressibility threshold of 0.3.

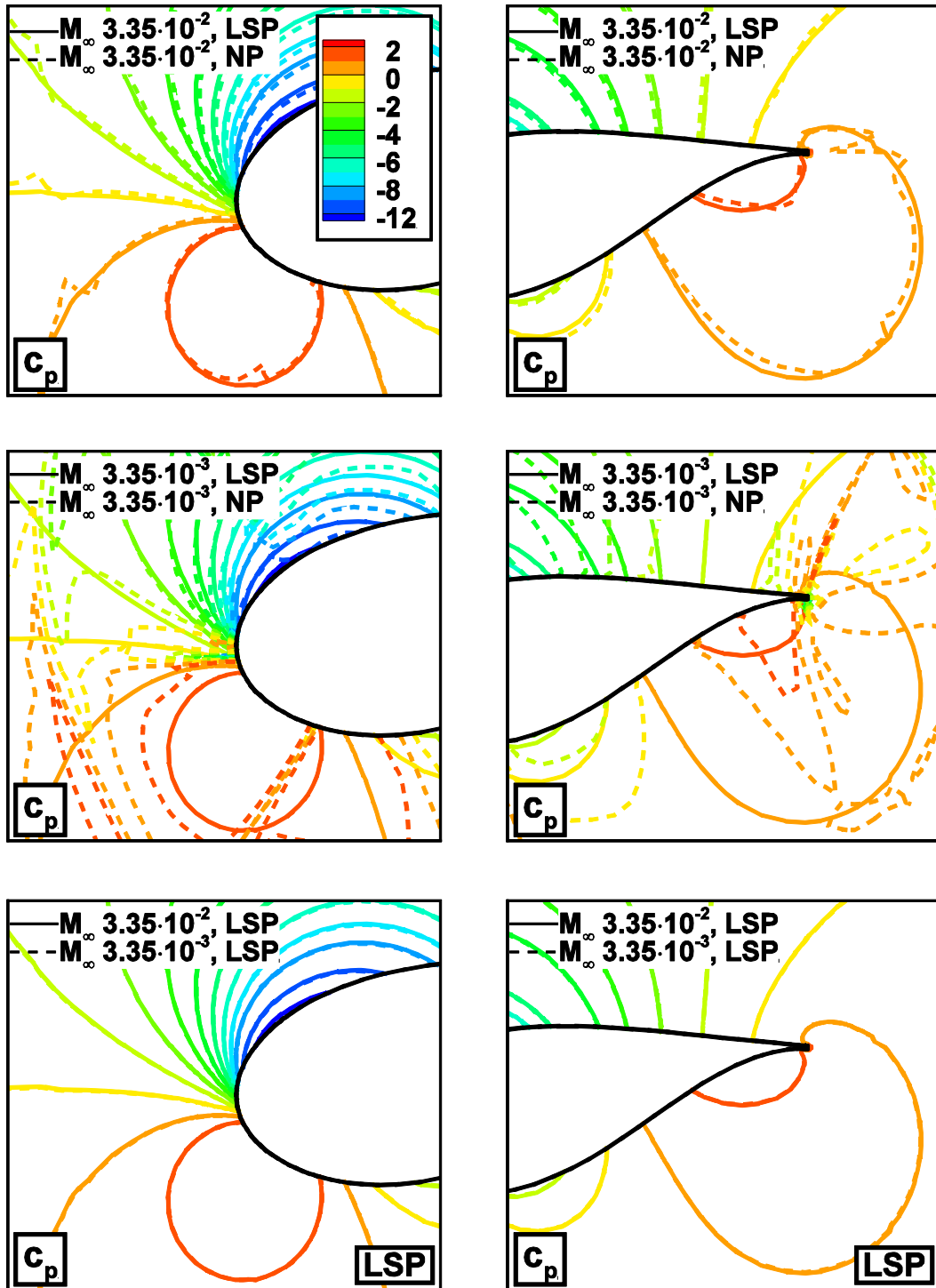


Figure 7.14 COMPARISON OF STATIC PRESSURE COEFFICIENT  $c_p$  CONTOURS OF BLADE SECTION AT 25% RADIUS IN STEADY REGIME AT TWO VALUES OF  $M_\infty$  OBTAINED WITH AND WITHOUT LSP. TOP LEFT SUBPLOT: LE AREA,  $M_\infty = 3.35 \cdot 10^{-2}$ . MIDDLE LEFT SUBPLOT: LE AREA,  $M_\infty = 3.35 \cdot 10^{-3}$ . BOTTOM LEFT SUBPLOT:  $c_p$  AT LE AREA OBTAINED WITH LSP,  $M_\infty = 3.35 \cdot 10^{-2}$  &  $3.35 \cdot 10^{-3}$ . TOP RIGHT SUBPLOT: TE AREA,  $M_\infty = 3.35 \cdot 10^{-2}$ . MIDDLE RIGHT SUBPLOT: TE AREA,  $M_\infty = 3.35 \cdot 10^{-3}$ . BOTTOM RIGHT SUBPLOT:  $c_p$  AT TE AREA OBTAINED WITH LSP,  $M_\infty = 3.35 \cdot 10^{-2}$  &  $3.35 \cdot 10^{-3}$ .

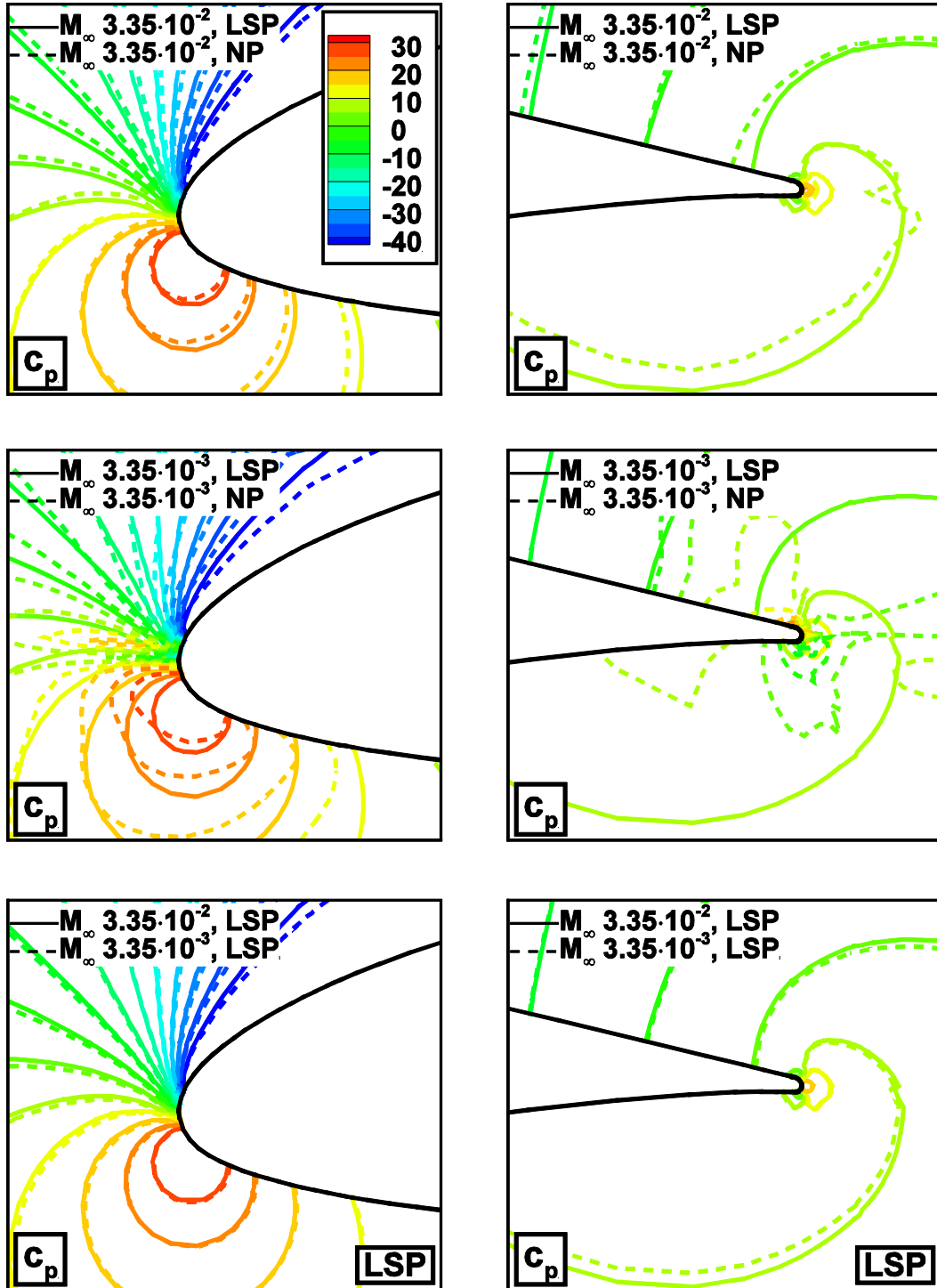


Figure 7.15 COMPARISON OF STATIC PRESSURE COEFFICIENT  $c_p$  CONTOURS OF BLADE SECTION AT 89% RADIUS IN STEADY REGIME AT TWO VALUES OF  $M_\infty$  OBTAINED WITH AND WITHOUT LSP. TOP LEFT SUBPLOT: LE AREA,  $M_\infty = 3.35 \cdot 10^{-2}$ . MIDDLE LEFT SUBPLOT: LE AREA,  $M_\infty = 3.35 \cdot 10^{-3}$ . BOTTOM LEFT SUBPLOT:  $c_p$  AT LE AREA OBTAINED WITH LSP,  $M_\infty = 3.35 \cdot 10^{-2}$  &  $3.35 \cdot 10^{-3}$ . TOP RIGHT SUBPLOT: TE AREA,  $M_\infty = 3.35 \cdot 10^{-2}$ . MIDDLE RIGHT SUBPLOT: TE AREA,  $M_\infty = 3.35 \cdot 10^{-3}$ . BOTTOM RIGHT SUBPLOT:  $c_p$  AT TE AREA OBTAINED WITH LSP,  $M_\infty = 3.35 \cdot 10^{-2}$  &  $3.35 \cdot 10^{-3}$ .

The profile comparisons of the static pressure coefficient  $c_p$  along the aerofoil chord obtained with both NP and LSP solvers for blade sections of 25% and 89% at  $M_\infty = 3.35 \cdot 10^{-2}$  are reported in the top left and right subplots of Figure 7.16 respectively, and the two subplots in the middle present the comparison of results obtained at lower Mach number of  $M_\infty = 3.35 \cdot 10^{-3}$ . The bottom left subplot reports the estimates of static pressure coefficient  $c_p$  obtained with the LSP analysis for two Mach numbers along the aerofoil of 25% blade section, whereas the estimates for blade section of 89% are depicted in the bottom right subplot of Figure 7.16. Inspection of the results presented in the two top subplots corresponding to the real flow condition confirms the necessity of using LSP in the portion of the blade close to the root, where the flow field can be regarded as incompressible and the accuracy of the estimates of  $c_p$  obtained with the compressible NP solver is severely impaired, as highlighted by the significant non-physical oscillations at both leading and trailing edges. However, the flow analysis of the 89% blade section, where a relatively high local Mach number always exists, highlights that only while solving such a high-speed flow problem, the NP calculation can yield the solution of a comparable accuracy with respect to that obtained with the LSP solver. As the free stream Mach number decreases (see two middle subplots of Figure 7.16), the significant non-physical oscillations appearing in the NP-estimate of  $c_p$  profile around the whole aerofoil features a more severely impaired accuracy of the solution computed by the compressible NP solver, even regarding the outer blade section near the tip, whereas the computations with preconditioning have demonstrated a well preserved accuracy of the solution by successfully removing such oscillations and pointed to the necessity of applying the LSP to solve the incompressible flow problems. Through the cross-comparison of the two bottom subplots of Figure 7.16, the only small difference between the two  $c_p$  profiles obtained with LSP for two Mach numbers at 89% section confirms the noticeable compressibility effects highlighted in the previous analyses of the static pressure coefficient contours.

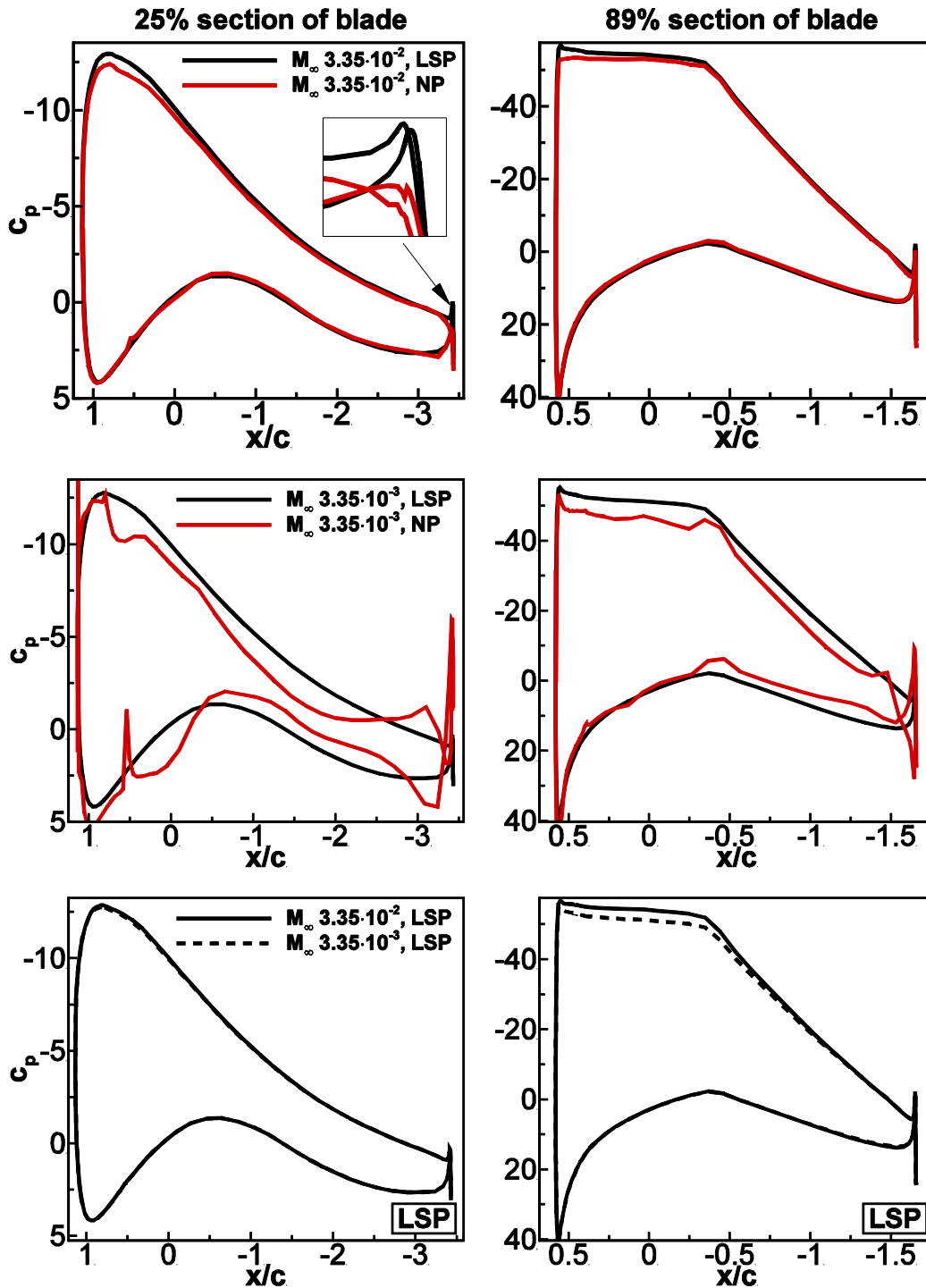


Figure 7.16 COMPARISON OF PRESSURE COEFFICIENT ( $c_p$ ) ALONG THE AEROFOIL OF BLADE SECTION AT 25% AND 89% RADIUS IN STEADY REGIME FOR  $M_\infty = 3.35 \cdot 10^{-2}$  AND  $M_\infty = 3.35 \cdot 10^{-3}$ . TOP LEFT SUBPLOT:  $c_p$  PROFILES AT 25% FROM BOTH SIMULATIONS,  $M_\infty = 3.35 \cdot 10^{-2}$ . MIDDLE LEFT SUBPLOT:  $c_p$  PROFILES AT 25% FROM BOTH SIMULATIONS,  $M_\infty = 3.35 \cdot 10^{-3}$ , BOTTOM LEFT SUBPLOT:  $c_p$  PROFILES AT 25% FROM SIMULATIONS WITH LSP,  $M_\infty = 3.35 \cdot 10^{-2}$  &  $3.35 \cdot 10^{-3}$ . TOP RIGHT SUBPLOT:  $c_p$  AT 89%  $M_\infty = 3.35 \cdot 10^{-2}$ . MIDDLE LEFT SUBPLOT:  $c_p$  AT 89%  $M_\infty = 3.35 \cdot 10^{-3}$ , BOTTOM LEFT SUBPLOT:  $c_p$  AT 89% FROM SIMULATIONS WITH LSP,  $M_\infty = 3.35 \cdot 10^{-2}$  &  $3.35 \cdot 10^{-3}$

$M_\infty$	Shaft Torque ( $N \cdot m$ )	
	<i>LSP</i>	<i>NP</i>
$3.35 \cdot 10^{-2}$	$4.45 \cdot 10^6$	$4.20 \cdot 10^6$
$3.35 \cdot 10^{-3}$	$4.52 \cdot 10^6$	$3.71 \cdot 10^6$

*Table 7.6 COMPARISON OF THE COMPUTED SHAFT TORQUE FOR TWO DIFFERENT  $M_\infty$  WITH AND WITHOUT LSP*

On the basis of the above comparative analyses of the sectional aerodynamic characteristics, the computed shaft torque of the whole rotor is reported in Table 7.6 for two different values of  $M_\infty$ , where the second and third columns represent the results obtained with and without LSP. The noticeable difference between the two computed solutions with respect to the rated wind speed ( $M_\infty = 0.0335$ ) can be accounted for by the incorrect prediction of the NP compressible solver in the inboard blade section close to the hub. To be more specific, in terms of the outer bound of the whole blade, where the relative wind speed perceived by the blade section is relatively high and the compressibility effect is by no means negligible, the NP solver can provide the solutions of comparable accuracy with respect to those computed with the LSP-enhanced solver, same as the case of 89% blade section demonstrated in the previous analysis; however, such small difference will grow dramatically as one moves the considered section towards the root, where the relative local Mach number is fairly small due to the decreased radius in a linear fashion and the flow field becomes incompressible, and the NP-estimate of the solution suffers a severe accuracy issue while solving such low-speed problems as shown in the analysis of 25% blade section, which, as a consequence, makes a major contribution to the difference of the computed solution compared to that of the LSP solver for the whole blade. Although no measured data or reference solution is provided herein to demonstrate the accuracy preserved by the LSP solver, the underestimation of the computed shaft torque without LSP noticed in our research is found to be consistent and proved in the flow analysis of the NREL phase VI wind turbine by Le Pape and Gleize (2006), where a good agreement of the shaft torque is achieved between the experiment data and the results obtained with LSP approach, whereas the computations without LSP underestimate the torque almost in the whole range of the tested wind speeds. The cross

comparison of the data, on the other hand, finds that the difference between the LSP estimates for  $M_\infty = 3.35 \cdot 10^{-2}$  and  $M_\infty = 3.35 \cdot 10^{-3}$  is significantly smaller than that of its NP counterparts, which is again due to the optimisation of the numerical dissipation achieved by the LSP solver.

## 7.3 Vertical axis wind turbine aerodynamics (2D)

Besides the analyses of HAWT applications, a well-developed and universally-applied Navier-Stokes CFD code is also expected to provide a reliable solution to the flow problem in vertical-axis wind turbine analyses. In the recent published work of Balduzzi et al. (2015), a comparative assessment of the predictive capability of COSA and another commercial RANS code FLUENT is presented. The study concerns the flow analysis of a Darrieus turbine, a popular type of VAWT. A very good agreement is achieved between the solutions of two CFD codes and the available experiment data. Therefore we would carry out our low speed preconditioning analysis of this VAWT application on the basis of their work. One important fact to be noted is that the solution of FLUENT simulation to be compared is obtained by a pressure-based solver, which, due to the nature of its formulation, is aimed to solve the low-speed incompressible flow problems (Rhie, 1989, Tamamidis et al., 1996), therefore no LSP is required in the FLUENT simulation for this low Mach test case and taking its solution as the reference correct value is a legitimate choice.

The turbine considered here is a 3-blade H-Darrieus, and its main characteristics are reported in Table 7.7. An operating condition of tip speed ratio (TSR) of 2.637 (corresponding to a revolution speed of 440 rpm and a free stream Mach number  $M_\infty$  0.0265) is chosen for our comparative analysis. The Reynolds number based on the standard density of  $1.22 \text{ kg/m}^3$ , the inlet velocity, the blade chord and the air viscosity at standard temperature 288K is calculated as 52800.

### 7.3 Vertical axis wind turbine aerodynamics (2D)

Blades Number ( $N$ )	3
Blades Shape	Straight
Blades Aerofoil	NACA0021
Radius ( $R$ ) [m]	0.5150
Chord ( $c$ ) [m]	0.0858
$c/R$ ratio	0.166

*Table 7.7 MAIN FEATURES OF THE ANALYSED ROTOR*

Based on the conclusion obtained in the parametric sensitivity analyses (Balduzzi et al., 2015) of computed solutions to various numerical aspects (i.e. the level of mesh refinement, the far field boundary distance specified from the rotor centre, the wall boundary condition and the size of physical time-step), we have decided to apply the same numerical set-up that has been used in the reported COSA analyses of the reference to all simulations presented herein. The grid adopted in the analyses has 729,600 quadrilateral cells and consists of two subdomains: a 522,240-cell circular region with radius 3.5D enclosing all three blades, and another 207,360-cell annular region of inner radius 3.5D and outer radius 120D. It has 448 mesh intervals along the surface of each blade and the distance of the first grid points off the aerofoil surface from the surface itself is about  $10^{-4}$  chords. Figure 7.17 presents the physical domain of the simulation in a schematic view, while local views of the grid around the rotor and the leading edge of the blade are depicted in Figure 7.18 and Figure 7.19 respectively.

### 7.3 Vertical axis wind turbine aerodynamics (2D)

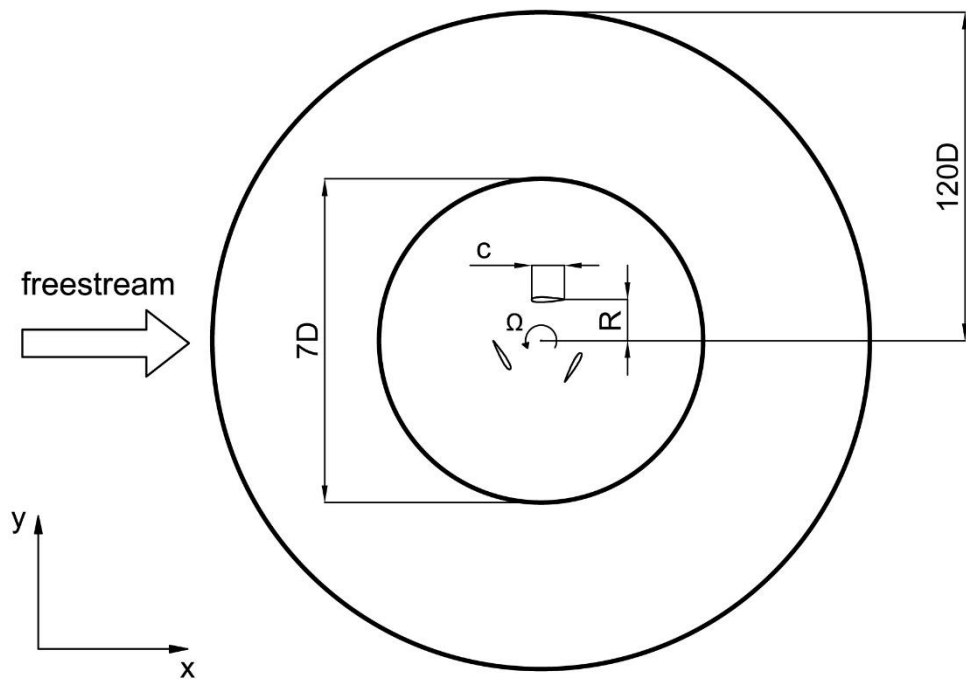
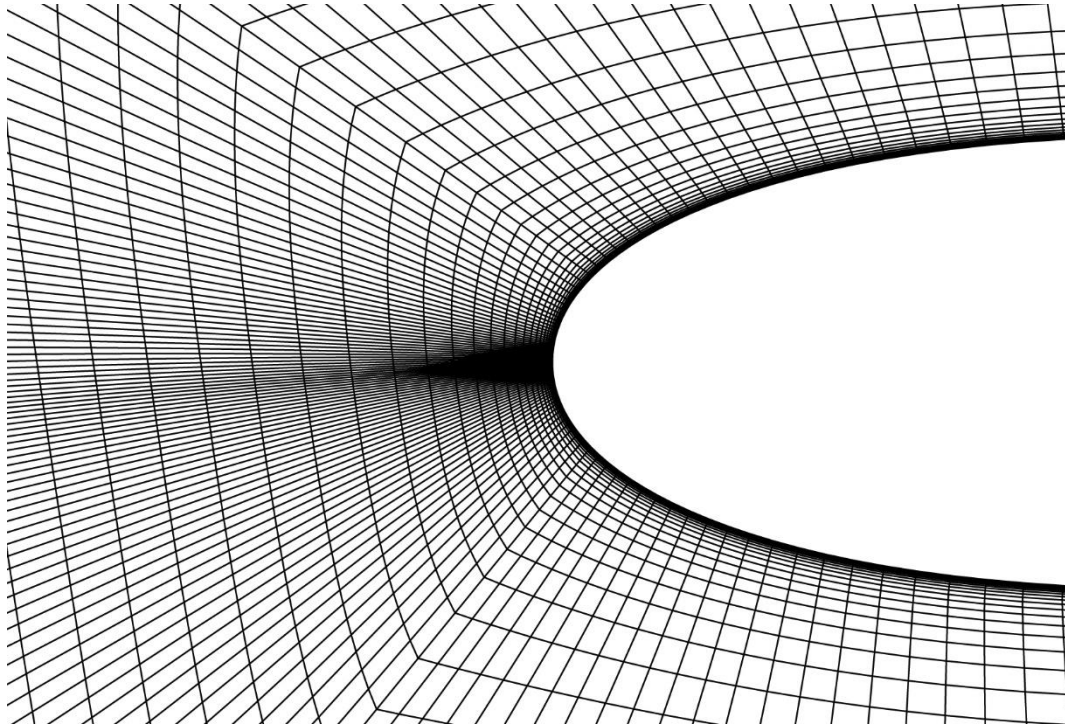


Figure 7.17 PHYSICAL DOMAIN OF COSA SIMULATION (Balduzzi et al., 2015)



Figure 7.18 ADOPTED MESH AROUND THE ROTOR (ONLY EVERY SECOND GRID LINE IN BOTH DIRECTIONS IS PLOTTED FOR CLARITY) (Balduzzi et al., 2015)



*Figure 7.19 ENLARGED VIEW OF GRID IN THE LEADING EDGE AREA (ONLY EVERY SECOND GRID LINE IN BOTH DIRECTIONS IS PLOTTED FOR CLARITY) (Balduzzi et al., 2015)*

The output parameter we aim to analyse in this application is the torque coefficients ( $C_t$ ) defined in Eqn.(7.7), and both the calculations with and without LSP have been performed and compared with the numerical result computed by FLUENT provided by Dr. Balduzzi, Dr. Bianchini and Dr. Ferrari, in order to assess the influence of the implementation of the preconditioning method on the final solutions. In order to obtain the converged solutions to compare, the periodicity error threshold (with the same definition as in previous sections) is set to approximately 1% due to the complexity of the flow problem considered herein, which requires between 30 and 50 revolutions to achieve a periodic state for all simulations.

$$C_t = \frac{T}{\frac{1}{2}\rho_\infty 2R^2 U_\infty^2} \quad (7.7)$$

The comparison of the blade torque coefficients obtained with the above two COSA simulations and FLUENT result is depicted in Figure 7.20. Inspection of the three curves has discovered significant difference between the COSA-NP and the other two simulation results, namely COSA-LSP and FLUENT, occurring when the rotor rotates at the angular position of  $\theta = 135^\circ$ , where the curve of the preconditioned solutions tend to be closer to that of FLUENT with a better and smoother sinusoidal profile. Moreover at the position around  $\theta = 210^\circ$ , the COSA-LSP and FLUENT calculations have displayed undistinguished difference

with respect to each other, and both of them have successfully removed the small abnormal oscillations which appears in the COSA-NP result. Through the above findings of the improved accuracy in the preconditioned simulations, one can confirm that the predictive capability of the VAWT application can be enhanced by using the low speed preconditioning technology, and demonstrate the necessity of using LSP for solving such a particular energy engineering problem in a realistic flow condition.

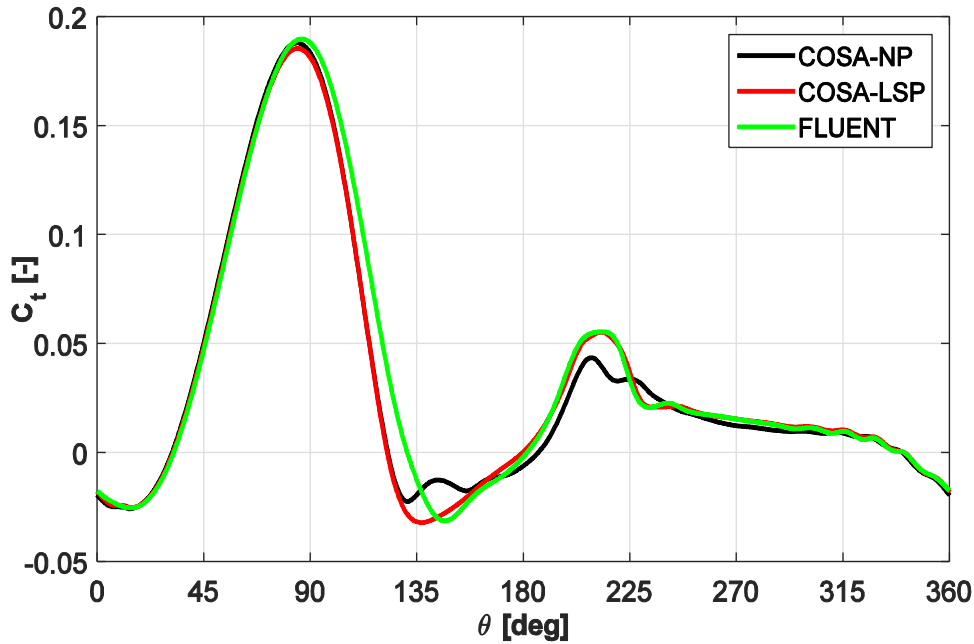


Figure 7.20 BLADE TORQUE COEFFICIENT PREDICTED BY FLUENT, COSA SOLVER WITH AND WITHOUT LSP

Having demonstrated the benefit of improving the solution accuracy by using the LSP solver, the next important objective is to assess the effect of the different implementation forms of low speed preconditioning approach on the calculation, both in terms of the solution accuracy and convergence rate. To this aim, three options have been analysed in this case, namely the one which applies the LSP to both RANS and SST equations and is the default option we have used in all simulations reported in this thesis (denoted as ‘*default*’), one which only applies the LSP to RANS equations and excludes the turbulent kinetic energy in the definition of total energy (labelled as ‘*simplified 1*’) and one which removes the turbulent kinetic energy in the total energy and preconditions the two systems of the equations as well, (‘*simplified 2*’). All the associated matrices and flux dissipation terms regarding these two simplified preconditioning methods are presented in Appendix C.

The convergence properties of the three LSP calculations in one specific time step is presented in Figure 7.21. Its six subplots report the convergence histories of the continuity equation (subplot labelled  $\rho$ ), the  $x$  –component of the momentum equation (subplot labelled  $\rho u$ ), the  $y$  – component of the momentum equation (subplot labelled  $\rho v$ ), the energy equation (subplot labelled  $\rho E$ ), the turbulent kinetic energy equation (subplot labelled  $\rho K$ ), and the specific dissipation rate equation (subplot labelled  $\rho \omega$ ). In all plots, the variable on the  $x$  –axis is the number of multigrid iterations, and the variable  $\Delta l_r$  on the  $y$  –axis is the logarithm in base 10 of the RMS of all cell-residuals for the considered conservation equation.

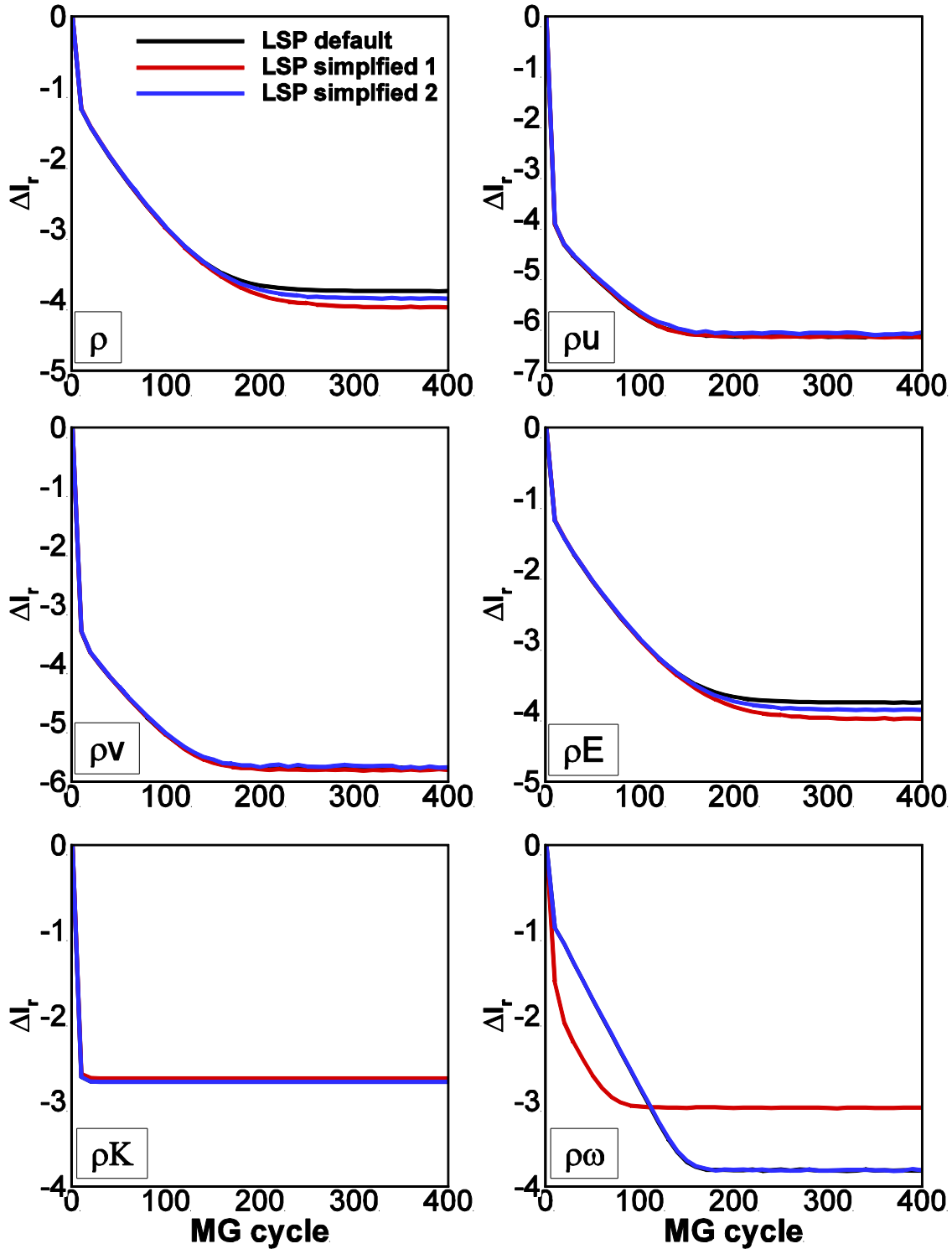


Figure 7.21 CONVERGENCE HISTORIES OF VAWT SIMULATIONS WITH THREE DIFFERENT LSP APPROACHES WITHIN ONE TIME STEP. TOP LEFT SUBPLOT: CONTINUITY EQUATION. TOP RIGHT SUBPLOT: x-COMPONENT OF MOMENTUM EQUATION. MIDDLE LEFT SUBPLOT: y-COMPONENT OF MOMENTUM EQUATION. MIDDLE RIGHT SUBPLOT: ENERGY EQUATION. BOTTOM LEFT SUBPLOT: TURBULENT KINETIC ENERGY EQUATION. BOTTOM RIGHT SUBPLOT: SPECIFIC DISSIPATION RATE EQUATION.

Inspection of the residual histories of the RANS and the  $K$  equations shows that the three LSP approaches yield comparable convergence rates for almost all these flow variables, except that a significant difference is spotted in the residual history of the  $\omega$  equation, where the two methods both applying the preconditioning to the turbulence equations have achieved to drop one more order of magnitude than the one using its non-preconditioned form, pointing to the necessity of applying the LSP to both mean flow and turbulence equations.

The solutions of the torque coefficient predicted by the three different LSP solvers are displayed in Figure 7.22. A better agreement of the computed torque coefficients is noticed between the results of FLUENT and COSA solver with the default LSP approach, whereas the solutions computed with the other two simplified approaches have shown larger discrepancy with respect to the reference solution, which is consistent with their slower convergence rate of certain flow variable (*LSP simplified 1*) discussed above, and may be also due to the ignorance of the turbulent kinetic energy in the total energy and the simplified LSP methods, thus we have demonstrated both the necessity of the full preconditioning approach to both the RANS and turbulence equations, and the essential role of the turbulent kinetic energy while solving such unsteady flow problem.

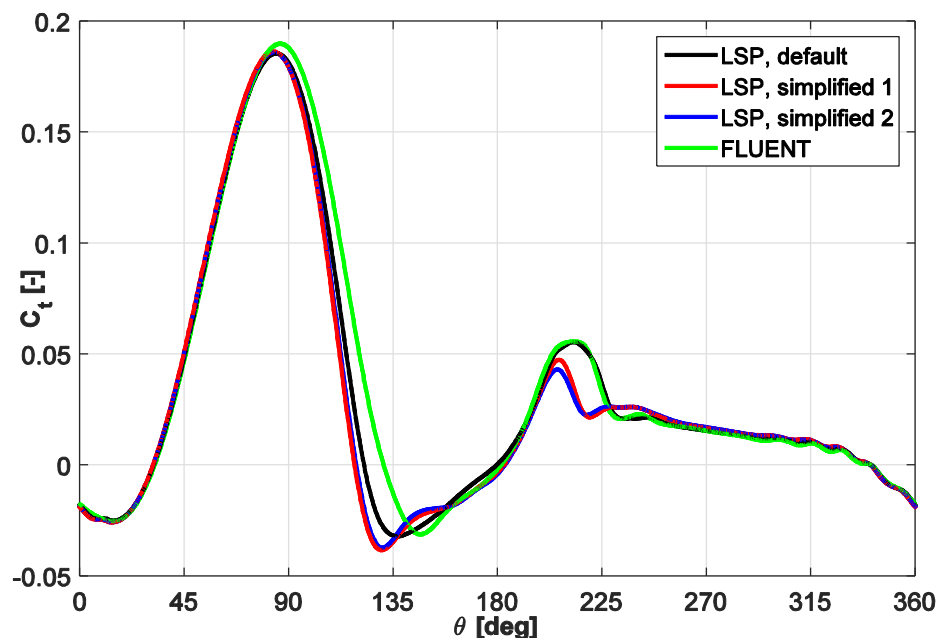
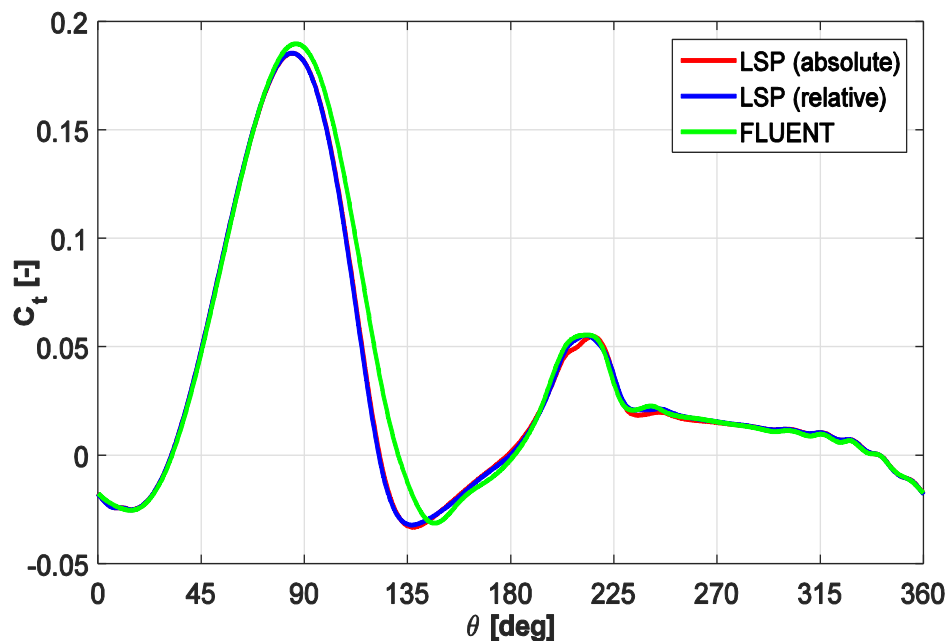


Figure 7.22 BLADE TORQUE COEFFICIENTS PREDICTED BY FLUENT AND COSA LSP-SOLVERS WITH THREE DIFFERENT FORMS OF LSP IMPLEMENTATIONS

The two LSP approaches using the preconditioning parameters based on the absolute and relative velocities (see Section 5.5 for the theoretical analysis) have also been assessed and

analysed in this application. The comparison of the blade torque coefficients obtained with two COSA simulations using different preconditioners and the FLUENT result is depicted in Figure 7.23. Inspection of the three curves has discovered that the two COSA results are almost undistinguishable in the whole period, except only at the position around  $\theta=210^\circ$ , where noticeable difference is found between the two curves, and the one obtained with the preconditioning parameter based on the relative velocity has shown a better agreement with the FLUENT result compared with its counterpart using absolute velocity.

Therefore on the basis of the above findings, we have verified that the predictive capability for low-TSR VAWT flow can be enhanced by using the low speed preconditioning technology and maintaining the turbulent kinetic energy term in the total energy. Moreover the convergence rate can be improved by applying the LSP to the SST turbulence equations, and the preconditioning parameter based on the relative velocity has demonstrated a better suitability for simulating the unsteady moving grid problems with a noticeable improvement of the solution accuracy.



*Figure 7.23 BLADE TORQUE COEFFICIENT PREDICTED BY FLUENT AND COSA LSP SOLVER USING THE PRECONDITIONING PARAMETERS BASED ON ABSOLUTE AND RELATIVE VELOCITY*

## 7.4 Summary

Three different wind turbine application problems have been analysed and solved using the previously validated turbulent preconditioning method. Through comparing the solutions obtained with and without the implementation of LSP for either the whole wind turbine rotor or a specific blade section at different values of  $M_\infty$ , we have seen a great improvement of the solution accuracy achieved by the preconditioning strategy, particular at the blade section close to the hub where the local Mach number is quite small and the compressibility effect can thus become negligible. Moreover, the computational efficiency of the frequency-domain harmonic balance method has also been assessed and compared with that of the conventional time-domain method. Based on our numerical results, a significant reduction of the wall-clock CPU time is achieved with the HB method, meanwhile a comparable accuracy of the solution is also obtained with respect to the time-domain solution when solving the non-linear periodic flow problems.

# Chapter 8

## Conclusion

### 8.1 Summary and concluding remarks

A rigorous novel approach to low-speed preconditioning for the multigrid fully coupled integration of the steady, time-domain and harmonic balance Reynolds-Average Navier-Stokes equations coupled to two-equation shear stress transport turbulence models has been developed, successfully validated and used for the aerodynamics analyses of complex real engineering applications presented herein.

#### 8.1.1 algorithmic conclusions

Thorough analyses of all the developed algorithms are demonstrated in this thesis on both theoretical and numerical aspects. The key features of the fully-coupled turbulent integration approach to low speed preconditioning include:

- the adopted strongly coupled fully preconditioned strategy of the RANS and turbulence equations, which conforms to the fully-coupled integration of the base-line solvers,
- the implementation of the low-speed preconditioned frequency domain method enabling to solve the periodic nonlinear flow problems in a rapid fashion with respect to the classical time-domain counterparts also at low speed regimes,
- the full preconditioning approach applied to both RANS and SST turbulence equations,
- the definition of the total energy taking into account the turbulent kinetic energy,
- the implementation of the preconditioned farfield boundary conditions based on the characteristic variables,

➤ the use of the preconditioning parameter based on relative flow velocity in the unsteady moving-grid problem.

It is unavoidable to apply low-speed preconditioning to the two turbulence equations due to the fact that the numerical dissipation of the RANS equations depends on the gradient of the turbulent kinetic energy also before the LSP is applied, and it is discovered that by preconditioning the turbulence equations, a faster convergence rate can be achieved. The additional coupling through the numerical dissipation of the system resulting from the coupled solution of the fluid and turbulence equations is caused by the presence of the turbulent kinetic energy in the total energy, the importance of which has therefore been verified in the analysis of the VAWT application.

The presented analyses also highlight that a significant reduction of the CPU run-time is obtained by using the frequency-domain harmonic balance solver, whereas negligible influence on the accuracy of the computed solution is noticed compared to that of the time-domain solver for various low-speed flow problems.

It is found that the implementation of the preconditioned farfield boundary conditions plays an essential role in the enhancement of the accuracy of the solution to a low speed problem using the computational mesh of a small size.

An additional algorithmic aspect addressed in this thesis is the impact on the numerical simulation of using the preconditioning parameters based on either the absolute velocity or relative velocity for solving moving-grid problems in terms of the analyses of solution accuracy. Most published literature reveals that former approach is regularly adopted, however a strict motivation of such studies for using either approach is often unfortunately unclear. In the analysis of the vertical axis wind turbine application, it is found that, an improvement of the solution accuracy is obtained in the LSP simulation using the preconditioner based on the relative velocity rather than the absolute velocity, by comparing the results of the above two simulations with the reference solution computed by a state-of-the-art commercial package used by both the industry and the academia worldwide.

## 8.1.2 fluid dynamics conclusions

The main computational results of this research consist of the analyses of two horizontal axis wind turbine applications and one vertical axis wind turbine application. The first one is thorough comparative analyses of steady and unsteady aerodynamics of both 30% and 93.5% blade sections of a VESTAS multi-megawatt HAWT working in various regimes. The main motivation for analysing this problem has been to highlight:

- the predictive capabilities and the numerical robustness of the developed LSP-enhanced turbulent steady, time-domain and frequency domain flow solvers for realistic complex and even more challenging engineering problems, and
- to quantify the effects of flow compressibility on the steady and yawed wind-induced unsteady aerodynamics of the tip region of a 82-m HAWT blade close to rated operating conditions, and
- to assess the computational benefits achieved by using the harmonic balance method of the RANS and SST equations rather than the conventional time-domain method.

The comparative steady aerodynamics analysis reveals that compressibility effects result in the actual (compressible) lift coefficients being about 4% higher than its incompressible counterpart. Increments of the same order of magnitude due to flow compressibility effects are also observed for the axial and circumferential force coefficients of the considered tip section. The differences between the compressible and the incompressible load predictions decrease with the rotor radius. Hence, relatively small differences between overall load characteristics and annual energy production (AEP) predicted using either the compressible or the incompressible NS equations are expected. However, the reported differences correspond to variations of the blade surface static pressure that may significantly affect the aeroacoustic analysis of HAWTs.

Regarding the numerical analyses of the lower blade section where the compressibility effect is fairly insignificant, the comparison of the run-time associated with the COSA LSP time-domain and harmonic balance solvers highlights that

➤ using the latter approach reduces by at least one order of magnitude the run-time required to achieve the periodic flow solution with respect to the run-time required by the time-domain analysis.

The second application is the comparative aerodynamics analysis of a three-dimensional NREL multi-megawatt HAWT working in the inviscid steady flow condition. The main motivation of carrying out this analysis is to demonstrate the accurate solution achieved by using LSP in analysing the entire wind turbine application. Detailed comparisons of the COSA LSP- and NP- steady solutions have confirmed the reliable flow predictive capabilities possessed by COSA solver with LSP technology for solving a three-dimensional low speed engineering problems.

The last application is the time-domain turbulent flow analysis of a VAWT, where simulations with and without LSP technology have been performed and their results are compared with the numerical solution of FLUENT to the aim of demonstrating the necessity of applying the LSP approach to accurately predict the low-TSR VAWT flows with large separation regions, the importance of preconditioning both RANS and turbulence equations and maintaining the turbulent kinetic energy in the definition of total energy in terms of the implementation aspect of the LSP method, and also to highlight a proper implementation of the preconditioning parameter in solving an unsteady moving grid problem. Through the comparative analysis of the solutions obtained by different solvers, it has been found that

- the solution accuracy is greatly improved by using the LSP technology;
- a better convergence rate is achieved by means of preconditioning the turbulence equations;
- the turbulent kinetic energy in the total energy has shown a large positive impact on the solution accuracy and thus cannot be neglected.
- the use of preconditioner based on the relative velocity results in an enhancement of the solution accuracy with respect to the case using the absolute velocity.

## 8.2 Future work

On the numerical side, with the three-dimensional inviscid flow predictive capability demonstrated in the analysis of the NREL horizontal axis wind turbine, future extensions of this work include the development of three-dimensional turbulent flow capability with the implementation of the LSP technology and the harmonic balance method.

On the application side, the forthcoming applications of the harmonic balance LSP solver is the solution to the unsteady periodic turbulent flow problems of a three-dimensional horizontal axis wind turbine working in a realistic operating condition, a gas turbine compressor or the helicopter rotors.

# Appendices

## A Space discretisation (standard form)

In this section, the matrices and all other related terms associated with the space discretisation, particularly the convective fluxes and numerical dissipation, will be provided herein in details.

As highlighted by Eqn. (3.4), the numerical dissipation  $\delta\Phi$  is proportional to  $K_U$ , and this term can also be written as:

$$K_U = \begin{pmatrix} 0 & n_x & n_y & 0 & 0 & 0 \\ \psi q^2 n_x / 2 - u U_n & U_n - \phi n_x u & n_y u - \psi n_x \psi v & \psi n_x & -\psi n_x & 0 \\ \psi q^2 n_y - v U_n & n_x v - \psi n_y u & U_n - \phi n_y v & \psi n_y & -\psi n_y & 0 \\ \psi q^2 U_n - U_n H & n_x H - \psi u U_n & n_y H - \psi v U_n & \gamma U_n & -\psi U_n & 0 \\ -U_n K & n_x K & n_y K & 0 & U_n & 0 \\ -U_n \omega & n_x \omega & n_y \omega & 0 & 0 & U_n \end{pmatrix}$$

where  $q^2 = u^2 + v^2$ ,  $\psi = \gamma - 1$ ,  $\phi = \gamma - 2$ , and  $U_n$  denote the component of the flow velocity along the outwards face normal vector  $\hat{n}$  defined by:

$$U_n = u n_x + v n_y \quad (\text{A.1})$$

The convective terms expressed with respect to the variables  $V$  are:

$$\tilde{A} \frac{\partial V}{\partial x} + \tilde{B} \frac{\partial V}{\partial y} \quad (\text{A.2})$$

with

$$\tilde{A} = \begin{pmatrix} u & \rho & 0 & 0 & 0 & 0 \\ 0 & u & 0 & 1/\rho & 0 & 0 \\ 0 & 0 & u & 0 & 0 & 0 \\ 0 & \rho c^2 & 0 & u & 0 & 0 \\ 0 & 0 & 0 & 0 & u & 0 \\ 0 & 0 & 0 & 0 & 0 & u \end{pmatrix}, \quad \tilde{B} = \begin{pmatrix} v & 0 & \rho & 0 & 0 & 0 \\ 0 & v & 0 & 0 & 0 & 0 \\ 0 & 0 & v & 1/\rho & 0 & 0 \\ 0 & 0 & \rho c^2 & v & 0 & 0 \\ 0 & 0 & 0 & 0 & v & 0 \\ 0 & 0 & 0 & 0 & 0 & v \end{pmatrix} \quad (\text{A.3})$$

where  $c^2$  denotes the square of the sound speed, which is related to the static temperature through the equation  $c^2 = T$ . The process of constructing the required numerical dissipation can be simplified by considering the Jacobian  $K_V = \tilde{A} n_x + \tilde{B} n_y$ , given by

A. Space discretisation (standard form)

$$K_V = \begin{pmatrix} U_n & \rho n_x & \rho n_y & 0 & 0 & 0 \\ 0 & U_n & 0 & n_x/\rho & 0 & 0 \\ 0 & 0 & U_n & n_y/\rho & 0 & 0 \\ 0 & \rho c^2 n_x & \rho c^2 n_y & U_n & 0 & 0 \\ 0 & 0 & 0 & 0 & U_n & 0 \\ 0 & 0 & 0 & 0 & 0 & U_n \end{pmatrix} \quad (\text{A.4})$$

It can be shown that  $K_U = MK_V M^{-1}$ , with

$$M = \frac{\partial U}{\partial V} = \begin{pmatrix} 1 & 0 & 0 & 0 & 0 & 0 \\ u & \rho & 0 & 0 & 0 & 0 \\ v & 0 & \rho & 0 & 0 & 0 \\ \frac{q^2}{2} + K & \rho u & \rho v & \frac{1}{\gamma-1} & \rho & 0 \\ K & 0 & 0 & 0 & \rho & 0 \\ \omega & 0 & 0 & 0 & 0 & \rho \end{pmatrix} \quad (\text{A.5})$$

$$M^{-1} = \frac{\partial V}{\partial U} = \begin{pmatrix} 1 & 0 & 0 & 0 & 0 & 0 \\ -\frac{u}{\rho} & \frac{1}{\rho} & 0 & 0 & 0 & 0 \\ -\frac{v}{\rho} & 0 & \frac{1}{\rho} & 0 & 0 & 0 \\ \frac{(\gamma-1)q^2}{2} & -u(\gamma-1) & -v(\gamma-1) & \gamma-1 & -(\gamma-1) & 0 \\ -\frac{K}{\rho} & 0 & 0 & 0 & \frac{1}{\rho} & 0 \\ -\frac{\omega}{\rho} & 0 & 0 & 0 & 0 & \frac{1}{\rho} \end{pmatrix} \quad (\text{A.6})$$

The eigenvalues of  $K_U$  and  $K_V$  are:

$$\begin{aligned} \lambda_1 = \lambda_2 = \lambda_5 = \lambda_6 &= U_n \\ \lambda_3 &= U_n + c \\ \lambda_4 &= U_n - c \end{aligned} \quad (\text{A.7})$$

The matrix of left eigenvectors of  $K_V$  can be determined as,

$$L^{-1} = \begin{pmatrix} 1 & 0 & 0 & -\frac{1}{c^2} & 0 & 0 \\ 0 & \rho n_y & \rho n_x & 0 & 0 & 0 \\ 0 & \frac{\rho n_x}{2c} & \frac{\rho n_y}{2c} & \frac{1}{2c^2} & 0 & 0 \\ 0 & -\frac{\rho n_x}{2c} & -\frac{\rho n_y}{2c} & \frac{1}{2c^2} & 0 & 0 \\ 0 & 0 & 0 & 0 & \rho & 0 \\ 0 & 0 & 0 & 0 & 0 & \rho \end{pmatrix} \quad (\text{A.8})$$

and its inverse, the matrix of right eigenvectors:

A. Space discretisation (standard form)

$$L = \begin{pmatrix} 1 & 0 & 1 & 1 & 0 & 0 \\ 0 & \frac{n_y}{\rho} & \frac{n_x c}{\rho} & -\frac{n_x c}{\rho} & 0 & 0 \\ 0 & -\frac{n_x}{\rho} & \frac{n_y c}{\rho} & -\frac{n_y c}{\rho} & 0 & 0 \\ 0 & 0 & c^2 & c^2 & 0 & 0 \\ 0 & 0 & 0 & 0 & \frac{1}{\rho} & 0 \\ 0 & 0 & 0 & 0 & 0 & \frac{1}{\rho} \end{pmatrix} \quad (\text{A.9})$$

The matrix  $P$  with the right eigenvectors of  $K_U$  is computed by Eqn. (3.9) shown as,

$$P = ML = \begin{pmatrix} 1 & 0 & 1 & 1 & 0 & 0 \\ u & n_y & u + cn_x & u - cn_x & 0 & 0 \\ v & -n_x & v + cn_y & v - cn_y & 0 & 0 \\ \frac{q^2}{2} + K & U_t & H + U_n c & H - U_n c & 1 & 0 \\ K & 0 & K & K & 1 & 0 \\ \omega & 0 & \omega & \omega & 0 & 1 \end{pmatrix} \quad (\text{A.10})$$

where  $U_t = un_y - vn_x$ . The characteristic variables can be computed by means of Eqn. (3.10). Their expressions are:

$$\begin{aligned} \delta W_1 &= \delta\rho - \frac{1}{c^2} \delta p \\ \delta W_2 &= \rho n_y \delta u - \rho n_x \delta v = \rho U_t \\ \delta W_3 &= \frac{\rho n_x}{2c} \delta u + \frac{\rho n_y}{2c} \delta v + \frac{\delta p}{2c^2} = \frac{\delta p}{2c^2} + \frac{\rho \delta U_n}{2c} \\ \delta W_4 &= -\frac{\rho n_x}{2c} \delta u - \frac{\rho n_y}{2c} \delta v + \frac{\delta p}{2c^2} = \frac{\delta p}{2c^2} - \frac{\rho \delta U_n}{2c} \\ \delta W_5 &= \rho \delta K \\ \delta W_6 &= \rho \delta \omega \end{aligned} \quad (\text{A.11})$$

The sought flux differences computed by Eqn. (3.12) can be expanded as,

$$\begin{aligned} \delta \Phi &= |\lambda_1| \delta W_1 \begin{pmatrix} 1 \\ u \\ v \\ \frac{q^2}{2} + K \\ K \\ \omega \end{pmatrix} + |\lambda_2| \delta W_2 \begin{pmatrix} 0 \\ n_y \\ -n_x \\ U_t \\ 0 \\ 0 \end{pmatrix} + |\lambda_3| \delta W_3 \begin{pmatrix} 1 \\ u + cn_x \\ v + cn_y \\ H + U_n c \\ K \\ \omega \end{pmatrix} \\ &+ |\lambda_4| \delta W_4 \begin{pmatrix} 1 \\ u - cn_x \\ v + cn_y \\ H - U_n c \\ K \\ \omega \end{pmatrix} + |\lambda_5| \delta W_5 \begin{pmatrix} 0 \\ 0 \\ 0 \\ 1 \\ 1 \\ 0 \end{pmatrix} + |\lambda_6| \delta W_6 \begin{pmatrix} 0 \\ 0 \\ 0 \\ 0 \\ 0 \\ 1 \end{pmatrix} \end{aligned} \quad (\text{A.12})$$

## B. Space discretisation (preconditioned form)

In order to maximise the computational efficiency of the numerical implementation, the flux differences provided by Eqn. (A.12) are computed as described below. First, one computes a set of intermediate variables defined as

$$\begin{aligned}
 \alpha_1 &= |\lambda_1| \left( \delta\rho - \frac{1}{c^2} \delta p \right) \\
 \alpha_2 &= |\lambda_2| \rho \\
 \alpha_3 &= |\lambda_3| \left( \frac{\delta p}{c^2} + \frac{\rho \delta U_n}{c} \right) / 2 \\
 \alpha_4 &= |\lambda_4| \left( \frac{\delta p}{c^2} - \frac{\rho \delta U_n}{c} \right) / 2
 \end{aligned} \tag{A.13}$$

The component of  $\delta\Phi$  are then computed by means of the expressions:

$$\begin{aligned}
 \delta\Phi_1 &= \alpha_1 + \alpha_3 + \alpha_4 \\
 \delta\Phi_2 &= \alpha_1 u + \alpha_2 \delta U_t n_y + \alpha_3 (u + cn_x) + \alpha_4 (u - cn_x) \\
 \delta\Phi_3 &= \alpha_1 v - \alpha_2 \delta U_t n_x + \alpha_3 (v + cn_y) + \alpha_4 (v - cn_y) \\
 \delta\Phi_4 &= \alpha_1 \left( \frac{q^2}{2} + K \right) + \alpha_2 U_t \delta U_t + \alpha_3 (H + cU_n) + \alpha_4 (H - cU_n) + \alpha_2 \delta K \\
 \delta\Phi_5 &= \alpha_1 K + \alpha_3 K + \alpha_4 K + \alpha_2 \delta K \\
 \delta\Phi_6 &= \alpha_1 \omega + \alpha_3 \omega + \alpha_4 \omega + \alpha_2 \delta \omega
 \end{aligned} \tag{A.14}$$

## B Space discretisation (preconditioned form)

The preconditioning matrix  $P_c$  is the preconditioner which appears in the flow equations written with respect to the conservative variables. Denote by  $M_p$  the local Mach number parameter on which the low-speed preconditioning strategy is based, the structure of  $P_c$  is reported as below,

$$P_c = \begin{pmatrix} P_{c11} & P_{c12} & P_{c13} & P_{c14} & P_{c15} & 0 \\ P_{c21} & P_{c22} & P_{c23} & P_{c24} & P_{c25} & 0 \\ P_{c31} & P_{c32} & P_{c33} & P_{c34} & P_{c35} & 0 \\ P_{c41} & P_{c42} & P_{c43} & P_{c44} & P_{c45} & 0 \\ P_{c51} & P_{c52} & P_{c53} & P_{c54} & P_{c55} & 0 \\ P_{c61} & P_{c62} & P_{c63} & P_{c64} & P_{c65} & 1 \end{pmatrix} \tag{B.1}$$

with the individual entries shown as

B. Space discretisation (preconditioned form)

$$\begin{aligned}
P_{c11} &= 1 + \frac{(\gamma - 1)(M_p^2 - 1)(u^2 + v^2)}{2a^2} \\
P_{c12} &= -\frac{(\gamma - 1)(M_p^2 - 1)u}{a^2} \\
P_{c13} &= -\frac{(\gamma - 1)(M_p^2 - 1)v}{a^2} \\
P_{c14} &= \frac{(\gamma - 1)(M_p^2 - 1)}{a^2} \\
P_{c15} &= -\frac{(\gamma - 1)(M_p^2 - 1)}{a^2} \\
P_{c21} &= \frac{(\gamma - 1)(M_p^2 - 1)(u^2 + v^2)u}{2a^2} \\
P_{c22} &= 1 - \frac{(\gamma - 1)(M_p^2 - 1)u^2}{a^2} \\
P_{c23} &= -\frac{(\gamma - 1)(M_p^2 - 1)uv}{a^2} \\
P_{c24} &= \frac{(\gamma - 1)(M_p^2 - 1)u}{a^2} \\
P_{c25} &= -\frac{(\gamma - 1)(M_p^2 - 1)u}{a^2} \\
P_{c31} &= \frac{(\gamma - 1)(M_p^2 - 1)(u^2 + v^2)v}{2a^2} \\
P_{c32} &= -\frac{(\gamma - 1)(M_p^2 - 1)uv}{a^2} \\
P_{c33} &= 1 - \frac{(\gamma - 1)(M_p^2 - 1)v^2}{a^2} \\
P_{c34} &= \frac{(\gamma - 1)(M_p^2 - 1)v}{a^2} \\
P_{c35} &= -\frac{(\gamma - 1)(M_p^2 - 1)v}{a^2} \\
P_{c41} &= \frac{(\gamma - 1)(M_p^2 - 1)(u^2 + v^2)H}{2a^2} \\
P_{c42} &= -\frac{(\gamma - 1)(M_p^2 - 1)uH}{a^2} \\
P_{c43} &= -\frac{(\gamma - 1)(M_p^2 - 1)vH}{a^2} \\
P_{c44} &= 1 + \frac{(\gamma - 1)(M_p^2 - 1)H}{a^2} \\
P_{c45} &= -\frac{(\gamma - 1)(M_p^2 - 1)H}{a^2} \\
P_{c51} &= \frac{(\gamma - 1)(M_p^2 - 1)(u^2 + v^2)K}{2a^2} \\
P_{c52} &= -\frac{(\gamma - 1)(M_p^2 - 1)uK}{a^2} \\
P_{c53} &= -\frac{(\gamma - 1)(M_p^2 - 1)vK}{a^2}
\end{aligned} \tag{B.2}$$

## B. Space discretisation (preconditioned form)

$$\begin{aligned}
 P_{c54} &= \frac{(\gamma - 1)(M_p^2 - 1)K}{a^2} \\
 P_{c55} &= 1 - \frac{(\gamma - 1)(M_p^2 - 1)K}{a^2} \\
 P_{c61} &= \frac{(\gamma - 1)(M_p^2 - 1)(u^2 + v^2)\omega}{2a^2} \\
 P_{c62} &= -\frac{(\gamma - 1)(M_p^2 - 1)u\omega}{a^2} \\
 P_{c63} &= -\frac{(\gamma - 1)(M_p^2 - 1)v\omega}{a^2} \\
 P_{c64} &= \frac{(\gamma - 1)(M_p^2 - 1)\omega}{a^2} \\
 P_{c65} &= -\frac{(\gamma - 1)(M_p^2 - 1)\omega}{a^2}
 \end{aligned}$$

where  $H$  represents the total enthalpy,  $H = \frac{u^2 + v^2}{2} + \frac{a^2}{\gamma - 1} + K$ .

Denoting by  $P_c^i$  the inverse of  $P_c$ , and taking the structure of such an inverse as that reported below

$$P_c^i = \begin{pmatrix} P_{c11}^i & P_{c12}^i & P_{c13}^i & P_{c14}^i & P_{c15}^i & 0 \\ P_{c21}^i & P_{c22}^i & P_{c23}^i & P_{c24}^i & P_{c25}^i & 0 \\ P_{c31}^i & P_{c32}^i & P_{c33}^i & P_{c34}^i & P_{c35}^i & 0 \\ P_{c41}^i & P_{c42}^i & P_{c43}^i & P_{c44}^i & P_{c45}^i & 0 \\ P_{c51}^i & P_{c52}^i & P_{c53}^i & P_{c54}^i & P_{c55}^i & 0 \\ P_{c61}^i & P_{c62}^i & P_{c63}^i & P_{c64}^i & P_{c65}^i & 1 \end{pmatrix} \quad (\text{B.3})$$

and the sought entries are:

$$\begin{aligned}
 P_{c11}^i &= 1 - \frac{(\gamma - 1)(M_p^2 - 1)(u^2 + v^2)}{2a^2 M_p^2} \\
 P_{c12}^i &= \frac{(\gamma - 1)(M_p^2 - 1)u}{a^2 M_p^2} \\
 P_{c13}^i &= \frac{(\gamma - 1)(M_p^2 - 1)v}{a^2 M_p^2} \\
 P_{c14}^i &= -\frac{(\gamma - 1)(M_p^2 - 1)}{a^2 M_p^2} \\
 P_{c15}^i &= \frac{(\gamma - 1)(M_p^2 - 1)}{a^2 M_p^2} \\
 P_{c21}^i &= -\frac{(\gamma - 1)(M_p^2 - 1)(u^2 + v^2)u}{2a^2 M_p^2} \\
 P_{c22}^i &= 1 + \frac{(\gamma - 1)(M_p^2 - 1)u^2}{a^2 M_p^2}
 \end{aligned} \quad (\text{B.4})$$

## B. Space discretisation (preconditioned form)

$$\begin{aligned}
 P_{c23}^i &= \frac{(\gamma - 1)(M_p^2 - 1)uv}{a^2 M_p^2} \\
 P_{c24}^i &= -\frac{(\gamma - 1)(M_p^2 - 1)u}{a^2 M_p^2} \\
 P_{c25}^i &= \frac{(\gamma - 1)(M_p^2 - 1)u}{a^2 M_p^2} \\
 P_{c31}^i &= -\frac{(\gamma - 1)(M_p^2 - 1)(u^2 + v^2)v}{2a^2 M_p^2} \\
 P_{c32}^i &= \frac{(\gamma - 1)(M_p^2 - 1)uv}{a^2 M_p^2} \\
 P_{c33}^i &= 1 + \frac{(\gamma - 1)(M_p^2 - 1)v^2}{a^2 M_p^2} \\
 P_{c34}^i &= -\frac{(\gamma - 1)(M_p^2 - 1)v}{a^2 M_p^2} \\
 P_{c35}^i &= \frac{(\gamma - 1)(M_p^2 - 1)v}{a^2 M_p^2} \\
 P_{c41}^i &= -\frac{(\gamma - 1)(M_p^2 - 1)(u^2 + v^2)H}{2a^2 M_p^2} \\
 P_{c42}^i &= \frac{(\gamma - 1)(M_p^2 - 1)uH}{a^2 M_p^2} \\
 P_{c43}^i &= \frac{(\gamma - 1)(M_p^2 - 1)vH}{a^2 M_p^2} \\
 P_{c44}^i &= 1 - \frac{(\gamma - 1)(M_p^2 - 1)H}{a^2 M_p^2} \\
 P_{c45}^i &= \frac{(\gamma - 1)(M_p^2 - 1)H}{a^2 M_p^2} \\
 P_{c51}^i &= -\frac{(\gamma - 1)(M_p^2 - 1)(u^2 + v^2)K}{2a^2 M_p^2} \\
 P_{c52}^i &= \frac{(\gamma - 1)(M_p^2 - 1)uK}{a^2 M_p^2} \\
 P_{c53}^i &= \frac{(\gamma - 1)(M_p^2 - 1)vK}{a^2 M_p^2} \\
 P_{c54}^i &= -\frac{(\gamma - 1)(M_p^2 - 1)K}{a^2 M_p^2} \\
 P_{c55}^i &= 1 + \frac{(\gamma - 1)(M_p^2 - 1)K}{a^2 M_p^2} \\
 P_{c61}^i &= -\frac{(\gamma - 1)(M_p^2 - 1)(u^2 + v^2)\omega}{2a^2 M_p^2} \\
 P_{c62}^i &= \frac{(\gamma - 1)(M_p^2 - 1)u\omega}{a^2 M_p^2}
 \end{aligned}$$

## B. Space discretisation (preconditioned form)

$$P_{c63}^i = \frac{(\gamma - 1)(M_p^2 - 1)v\omega}{a^2 M_p^2}$$

$$P_{c64}^i = -\frac{(\gamma - 1)(M_p^2 - 1)\omega}{a^2 M_p^2}$$

$$P_{c65}^i = \frac{(\gamma - 1)(M_p^2 - 1)\omega}{a^2 M_p^2}$$

The preconditioning matrix  $\Gamma_p$  is written with respect to the primitive variables  $V_p$

$$\Gamma_p = \begin{pmatrix} \Gamma_{p11} & \Gamma_{p12} & \Gamma_{p13} & \Gamma_{p14} & \Gamma_{p15} & 0 \\ -\frac{u}{\rho} & \frac{1}{\rho} & 0 & 0 & 0 & 0 \\ -\frac{v}{\rho} & 0 & \frac{1}{\rho} & 0 & 0 & 0 \\ \Gamma_{p41} & \Gamma_{p42} & \Gamma_{p43} & \Gamma_{p44} & \Gamma_{p45} & 0 \\ -\frac{K}{\rho} & 0 & 0 & 0 & \frac{1}{\rho} & 0 \\ -\frac{\omega}{\rho} & 0 & 0 & 0 & 0 & 1 \end{pmatrix} \quad (\text{B.5})$$

with

$$\Gamma_{p11} = \frac{1}{2}\gamma(\gamma - 1)M_p^2(u^2 + v^2)$$

$$\Gamma_{p12} = -\gamma(\gamma - 1)M_p^2 u$$

$$\Gamma_{p13} = -\gamma(\gamma - 1)M_p^2 v$$

$$\Gamma_{p14} = \gamma(\gamma - 1)M_p^2$$

$$\Gamma_{p15} = -\gamma(\gamma - 1)M_p^2$$

$$\Gamma_{p41} = \frac{-2a^2 + (\gamma - 1)(1 + (\gamma - 1)M_p^2)(u^2 + v^2)}{2\rho} \quad (\text{B.6})$$

$$\Gamma_{p42} = -\frac{(\gamma - 1)(1 + (\gamma - 1)M_p^2)u}{\rho}$$

$$\Gamma_{p43} = -\frac{(\gamma - 1)(1 + (\gamma - 1)M_p^2)v}{\rho}$$

$$\Gamma_{p44} = \frac{(\gamma - 1)(1 + (\gamma - 1)M_p^2)}{\rho}$$

$$\Gamma_{p45} = -\frac{(\gamma - 1)(1 + (\gamma - 1)M_p^2)}{\rho}$$

The inverse of  $\Gamma_p^i$  is,

## B. Space discretisation (preconditioned form)

$$\Gamma_p^i = \begin{pmatrix} \Gamma_{p11}^i & 0 & 0 & -\frac{\rho}{a^2} & 0 & 0 \\ \Gamma_{p21}^i & \rho & 0 & -\frac{\rho u}{a^2} & 0 & 0 \\ \Gamma_{p31}^i & 0 & \rho & -\frac{\rho v}{a^2} & 0 & 0 \\ \Gamma_{p41}^i & \rho u & \rho v & -\frac{\rho}{a^2} \left( \frac{u^2+v^2}{2} + K \right) & \rho & 0 \\ \Gamma_{p51}^i & 0 & 0 & -\frac{\rho K}{a^2} & \rho & 0 \\ \Gamma_{p61}^i & 0 & 0 & -\frac{\rho \omega}{a^2} & 0 & \rho \end{pmatrix} \quad (\text{B.7})$$

with

$$\begin{aligned} \Gamma_{p11}^i &= \frac{1 + (\gamma - 1)M_p^2}{a^2 \gamma M_p^2} \\ \Gamma_{p21}^i &= \frac{(1 + (\gamma - 1)M_p^2)u}{a^2 \gamma M_p^2} \\ \Gamma_{p31}^i &= \frac{(1 + (\gamma - 1)M_p^2)v}{a^2 \gamma M_p^2} \\ \Gamma_{p41}^i &= \frac{2a^2 + (\gamma - 1)(1 + (\gamma - 1)M_p^2)(u^2 + v^2 + 2K)}{2a^2 \gamma (\gamma - 1)M_p^2} \\ \Gamma_{p51}^i &= \frac{(1 + (\gamma - 1)M_p^2)K}{a^2 \gamma M_p^2} \\ \Gamma_{p61}^i &= \frac{(1 + (\gamma - 1)M_p^2)\omega}{a^2 \gamma M_p^2} \end{aligned} \quad (\text{B.8})$$

The eigenvalues of matrix (5.17) are:

$$\begin{aligned} \lambda_1 &= \lambda_2 = \lambda_5 = \lambda_6 = U_n \\ \lambda_3 &= \frac{1}{2} \left[ U_n(1 + M_p^2) + \sqrt{4a^2 M_p^2 + (M_p^2 - 1)^2 U_n^2} \right] \\ \lambda_4 &= \frac{1}{2} \left[ U_n(1 + M_p^2) - \sqrt{4a^2 M_p^2 + (M_p^2 - 1)^2 U_n^2} \right] \end{aligned} \quad (\text{B.9})$$

where  $U_n$  is the velocity component normal to the face being considered and is given by

$$U_n = uk_x + vk_y, \text{ and } a^2 = (\gamma - 1) \left[ H - \frac{u^2+v^2}{2} - K \right].$$

The matrix of right eigenvectors  $\hat{R}$  is

## B. Space discretisation (preconditioned form)

$$\hat{R} = \begin{vmatrix} 0 & 0 & \gamma a(\lambda_3 - U_n) & -\gamma a(\lambda_4 - U_n) & 0 & 0 \\ 0 & \frac{k_y}{\rho} & \frac{ak_x}{\rho} & -\frac{ak_x}{\rho} & 0 & 0 \\ 0 & -\frac{k_x}{\rho} & \frac{ak_y}{\rho} & -\frac{ak_y}{\rho} & 0 & 0 \\ -\frac{a^2}{\rho} & 0 & \frac{a(\gamma-1)(\lambda_3-U_n)}{\rho} & -\frac{a(\gamma-1)(\lambda_4-U_n)}{\rho} & 0 & 0 \\ 0 & 0 & 0 & 0 & \frac{1}{\rho} & 0 \\ 0 & 0 & 0 & 0 & 0 & \frac{1}{\rho} \end{vmatrix} \quad (\text{B.10})$$

whereas its inverse  $\hat{R}^{-1}$  is

$$\hat{R}^{-1} = \begin{vmatrix} \frac{\gamma-1}{a^2\gamma} & 0 & 0 & -\frac{\rho}{a^2} & 0 & 0 \\ 0 & \rho k_y & -\rho k_x & 0 & 0 & 0 \\ \frac{1}{a\gamma(\lambda_3-\lambda_4)} & \frac{-\rho k_x(\lambda_4-U_n)}{a(\lambda_3-\lambda_4)} & \frac{-\rho k_y(\lambda_4-U_n)}{a(\lambda_3-\lambda_4)} & 0 & 0 & 0 \\ \frac{1}{a\gamma(\lambda_3-\lambda_4)} & \frac{-\rho k_x(\lambda_3-U_n)}{a(\lambda_3-\lambda_4)} & \frac{-\rho k_y(\lambda_3-U_n)}{a(\lambda_3-\lambda_4)} & 0 & 0 & 0 \\ 0 & 0 & 0 & 0 & \rho & 0 \\ 0 & 0 & 0 & 0 & 0 & \rho \end{vmatrix} \quad (\text{B.11})$$

The matrix  $\mathcal{R}$ :

$$\mathcal{R} = \begin{vmatrix} 1 & 0 & \frac{\lambda_3-U_n}{aM_p^2} & -\frac{\lambda_4-U_n}{aM_p^2} & 0 & 0 \\ u & k_y & \mathcal{R}_{23} & \mathcal{R}_{24} & 0 & 0 \\ v & -k_x & \mathcal{R}_{33} & \mathcal{R}_{34} & 0 & 0 \\ \frac{1}{2}(u^2 + v^2) + K & uk_y - vk_x & \mathcal{R}_{43} & \mathcal{R}_{44} & 1 & 0 \\ K & 0 & K \frac{\lambda_3-U_n}{aM_p^2} & -K \frac{\lambda_4-U_n}{aM_p^2} & 1 & 0 \\ \omega & 0 & \omega \frac{\lambda_3-U_n}{aM_p^2} & -\omega \frac{\lambda_4-U_n}{aM_p^2} & 0 & 1 \end{vmatrix} \quad (\text{B.12})$$

with

$$\begin{aligned} \mathcal{R}_{23} &= ak_x + \frac{u(\lambda_3 - U_n)}{aM_p^2} \\ \mathcal{R}_{24} &= -ak_x - \frac{u(\lambda_4 - U_n)}{aM_p^2} \\ \mathcal{R}_{33} &= ak_y + \frac{v(\lambda_3 - U_n)}{aM_p^2} \\ \mathcal{R}_{34} &= -ak_y - \frac{v(\lambda_4 - U_n)}{aM_p^2} \\ \mathcal{R}_{43} &= aU_n + \frac{(\lambda_3 - U_n)H}{aM_p^2} \\ \mathcal{R}_{44} &= -aU_n + \frac{(\lambda_4 - U_n)H}{aM_p^2} \end{aligned} \quad (\text{B.13})$$

The matrix  $\mathcal{L}^{-1} = \mathcal{L}^i$  is

## B. Space discretisation (preconditioned form)

$$\mathcal{L}^i = \begin{pmatrix} 1 - \frac{(\gamma-1)(u^2+v^2)}{2a^2} & \frac{(\gamma-1)u}{a^2} & \frac{(\gamma-1)v}{a^2} & -\frac{(\gamma-1)}{a^2} & \frac{(\gamma-1)}{a^2} & 0 \\ -uk_y + vk_x & k_y & -k_x & 0 & 0 & 0 \\ \mathcal{L}_{31}^i & \mathcal{L}_{32}^i & \mathcal{L}_{33}^i & \mathcal{L}_{34}^i & \mathcal{L}_{35}^i & 0 \\ \mathcal{L}_{41}^i & \mathcal{L}_{42}^i & \mathcal{L}_{43}^i & \mathcal{L}_{44}^i & \mathcal{L}_{45}^i & 0 \\ -K & 0 & 0 & 0 & 1 & 0 \\ -\omega & 0 & 0 & 0 & 0 & 1 \end{pmatrix} \quad (\text{B.14})$$

with

$$\begin{aligned} \mathcal{L}_{31}^i &= \frac{2(uk_x + vk_y)(\lambda_4 - U_n) + (\gamma - 1)(u^2 + v^2)}{2a(\lambda_3 - \lambda_4)} \\ \mathcal{L}_{32}^i &= -\frac{(\lambda_4 - U_n)k_x + (\gamma - 1)u}{a(\lambda_3 - \lambda_4)} \\ \mathcal{L}_{33}^i &= -\frac{(\lambda_4 - U_n)k_x + (\gamma - 1)v}{a(\lambda_3 - \lambda_4)} \\ \mathcal{L}_{34}^i &= \frac{\gamma - 1}{a(\lambda_3 - \lambda_4)} \\ \mathcal{L}_{35}^i &= -\frac{\gamma - 1}{a(\lambda_3 - \lambda_4)} \\ \mathcal{L}_{41}^i &= \frac{2(uk_x + vk_y)(\lambda_3 - U_n) + (\gamma - 1)(u^2 + v^2)}{2a(\lambda_3 - \lambda_4)} \\ \mathcal{L}_{42}^i &= -\frac{(\lambda_3 - U_n)k_x + (\gamma - 1)u}{a(\lambda_3 - \lambda_4)} \\ \mathcal{L}_{43}^i &= -\frac{(\lambda_3 - U_n)k_x + (\gamma - 1)v}{a(\lambda_3 - \lambda_4)} \\ \mathcal{L}_{44}^i &= \frac{\gamma - 1}{a(\lambda_3 - \lambda_4)} \\ \mathcal{L}_{45}^i &= -\frac{\gamma - 1}{a(\lambda_3 - \lambda_4)} \end{aligned} \quad (\text{B.15})$$

The matrix  $L_\star^{-1}$  is given by:

$$L_\star^{-1} = \begin{pmatrix} 1 & 0 & 0 & -\frac{1}{a^2} & 0 & 0 \\ 0 & \rho k_y & -\rho k_x & 0 & 0 & 0 \\ 0 & -\frac{\rho k_x(\lambda_4 - U_n)}{a(\lambda_3 - \lambda_4)} & -\frac{\rho k_y(\lambda_4 - U_n)}{a(\lambda_3 - \lambda_4)} & \frac{1}{a(\lambda_3 - \lambda_4)} & 0 & 0 \\ 0 & -\frac{\rho k_x(\lambda_3 - U_n)}{a(\lambda_3 - \lambda_4)} & -\frac{\rho k_y(\lambda_3 - U_n)}{a(\lambda_3 - \lambda_4)} & \frac{1}{a(\lambda_3 - \lambda_4)} & 0 & 0 \\ 0 & 0 & 0 & 0 & \rho & 0 \\ 0 & 0 & 0 & 0 & 0 & \rho \end{pmatrix} \quad (\text{B.16})$$

The preconditioned characteristic variables defined by  $\alpha_j = \delta W = (L_\star^{-1})_j \delta V$  are,

## B. Space discretisation (preconditioned form)

$$\begin{aligned}
\alpha_1 &= \delta\rho - \frac{\delta p}{a^2} \\
\alpha_2 &= \rho(\delta u k_y - \delta v k_x) \\
\alpha_3 &= \frac{\delta p - \rho(\delta u k_x + \delta v k_y)(\lambda_4 - U_n)}{a(\lambda_3 - \lambda_4)} \\
\alpha_4 &= \frac{\delta p - \rho(\delta u k_x + \delta v k_y)(\lambda_3 - U_n)}{a(\lambda_3 - \lambda_4)} \\
\alpha_5 &= \rho\delta K \\
\alpha_6 &= \rho\delta\omega
\end{aligned} \tag{B.17}$$

The flux differences are

$$\begin{aligned}
\delta f_1 &= \alpha_1\lambda_1 + \frac{\alpha_3\lambda_3(\lambda_3 - U_n) - \alpha_4\lambda_4(\lambda_4 - U_n)}{aM_p^2} \\
\delta f_2 &= \alpha_1\lambda_1u + \alpha_2\lambda_2k_y + ak_x(\alpha_3\lambda_3 - \alpha_4\lambda_4) \\
&\quad + \frac{(\alpha_3\lambda_3(\lambda_3 - U_n) - \alpha_4\lambda_4(\lambda_4 - U_n))u}{aM_p^2} \\
\delta f_3 &= \alpha_1\lambda_1v - \alpha_2\lambda_2k_x + ak_y(\alpha_3\lambda_3 - \alpha_4\lambda_4) \\
&\quad + \frac{(\alpha_3\lambda_3(\lambda_3 - U_n) - \alpha_4\lambda_4(\lambda_4 - U_n))v}{aM_p^2} \\
\delta f_4 &= \alpha_1\lambda_1\left(\frac{1}{2}(u^2 + v^2) + K\right) + \alpha_2\lambda_2(uk_y - vk_x) \\
&\quad + \left(\frac{\lambda_3 - U_n}{aM_p^2}H + aU_n\right)\alpha_3\lambda_3 - \left(\frac{\lambda_4 - U_n}{aM_p^2}H + aU_n\right)\alpha_4\lambda_4 + \alpha_5\lambda_5 \\
\delta f_5 &= \alpha_1\lambda_1K + \frac{\alpha_3\lambda_3(\lambda_3 - U_n) - \alpha_4\lambda_4(\lambda_4 - U_n)}{aM_p^2}K + \alpha_5\lambda_5 \\
\delta f_6 &= \alpha_1\lambda_1\omega + \frac{\alpha_3\lambda_3(\lambda_3 - U_n) - \alpha_4\lambda_4(\lambda_4 - U_n)}{aM_p^2}\omega + \alpha_6\lambda_6
\end{aligned} \tag{B.18}$$

The Jacobian matrix  $\bar{\Gamma}_p = \frac{\partial v_p}{\partial U}$  with  $U = [\rho, \rho u, \rho v, \rho E, \rho K, \rho\omega]^T$  and  $V_p = [\gamma p, u, v, T, K, \omega]^T$  is,

## B. Space discretisation (preconditioned form)

$$\bar{\Gamma}_p = \begin{pmatrix} \bar{\Gamma}_{p_{11}} & \bar{\Gamma}_{p_{12}} & \bar{\Gamma}_{p_{13}} & \bar{\Gamma}_{p_{14}} & \bar{\Gamma}_{p_{15}} & 0 \\ -\frac{u}{\rho} & \frac{1}{\rho} & 0 & 0 & 0 & 0 \\ -\frac{v}{\rho} & 0 & \frac{1}{\rho} & 0 & 0 & 0 \\ \bar{\Gamma}_{p_{41}} & \bar{\Gamma}_{p_{42}} & \bar{\Gamma}_{p_{43}} & \bar{\Gamma}_{p_{44}} & \bar{\Gamma}_{p_{45}} & 0 \\ -\frac{K}{\rho} & 0 & 0 & 0 & \frac{1}{\rho} & 0 \\ -\frac{\omega}{\rho} & 0 & 0 & 0 & 0 & 1 \end{pmatrix} \quad (\text{B.19})$$

with

$$\begin{aligned} \bar{\Gamma}_{p_{11}} &= \frac{1}{2}\gamma(\gamma-1)(u^2+v^2) \\ \bar{\Gamma}_{p_{12}} &= -\gamma(\gamma-1)u \\ \bar{\Gamma}_{p_{13}} &= -\gamma(\gamma-1)v \\ \bar{\Gamma}_{p_{14}} &= \gamma(\gamma-1) \\ \bar{\Gamma}_{p_{15}} &= -\gamma(\gamma-1) \\ \bar{\Gamma}_{p_{41}} &= \frac{-2a^2 + \gamma(\gamma-1)(u^2+v^2)}{2\rho} \\ \bar{\Gamma}_{p_{42}} &= -\frac{\gamma(\gamma-1)u}{\rho} \\ \bar{\Gamma}_{p_{43}} &= -\frac{\gamma(\gamma-1)v}{\rho} \\ \bar{\Gamma}_{p_{44}} &= \frac{(\gamma-1)(1+(\gamma-1)M_p^2)}{\rho} \\ \bar{\Gamma}_{p_{45}} &= -\frac{\gamma(\gamma-1)}{\rho} \end{aligned} \quad (\text{B.20})$$

The inverse of  $\bar{\Gamma}_p$  is,

$$\bar{\Gamma}_p^{-1} = \begin{pmatrix} \frac{1}{a^2} & 0 & 0 & -\frac{\rho}{a^2} & 0 & 0 \\ \frac{u}{a^2} & \rho & 0 & -\frac{\rho u}{a^2} & 0 & 0 \\ \frac{v}{a^2} & 0 & \rho & -\frac{\rho v}{a^2} & 0 & 0 \\ \frac{1}{\gamma(\gamma-1)} + \left(\frac{u^2+v^2}{2} + K\right)/a^2 & \rho u & \rho v & -\frac{\rho}{a^2}\left(\frac{u^2+v^2}{2} + K\right) & \rho & 0 \\ \frac{K}{a^2} & 0 & 0 & -\frac{\rho K}{a^2} & \rho & 0 \\ \frac{\omega}{a^2} & 0 & 0 & -\frac{\rho\omega}{a^2} & 0 & \rho \end{pmatrix} \quad (\text{B.21})$$

## C Space discretisation (simplified preconditioned form)

In the section, two simplified preconditioned forms are provided herein. The governing equations that they are based on are the same as those presented in Chapter 2, while the only difference lies in the definition of total energy and total enthalpy which have both excluded the turbulent kinetic energy.

### (C.1) simplified form No. 1

The first choice being tested in the research is developed by enforcing no preconditioning to be applied in the SST equations, through a less strict mathematical derivation process. All the matrices and flux dissipation terms related to this preconditioned system are shown as below.

$$P_c = \begin{pmatrix} P_{c11} & P_{c12} & P_{c13} & P_{c14} & 0 & 0 \\ P_{c21} & P_{c22} & P_{c23} & P_{c24} & 0 & 0 \\ P_{c31} & P_{c32} & P_{c33} & P_{c34} & 0 & 0 \\ P_{c41} & P_{c42} & P_{c43} & P_{c44} & 0 & 0 \\ 0 & 0 & 0 & 0 & 1 & 0 \\ 0 & 0 & 0 & 0 & 0 & 1 \end{pmatrix} \quad (\text{C.1})$$

with the individual entries shown as

$$\begin{aligned} P_{c11} &= 1 + \frac{(\gamma - 1)(M_p^2 - 1)(u^2 + v^2)}{2a^2} \\ P_{c12} &= -\frac{(\gamma - 1)(M_p^2 - 1)u}{a^2} \\ P_{c13} &= -\frac{(\gamma - 1)(M_p^2 - 1)v}{a^2} \\ P_{c14} &= \frac{(\gamma - 1)(M_p^2 - 1)}{a^2} \\ P_{c21} &= \frac{(\gamma - 1)(M_p^2 - 1)(u^2 + v^2)u}{2a^2} \\ P_{c22} &= 1 - \frac{(\gamma - 1)(M_p^2 - 1)u^2}{a^2} \\ P_{c23} &= -\frac{(\gamma - 1)(M_p^2 - 1)uv}{a^2} \\ P_{c24} &= \frac{(\gamma - 1)(M_p^2 - 1)u}{a^2} \end{aligned} \quad (\text{C.2})$$

C. Space discretisation (simplified preconditioned form)

$$\begin{aligned}
 P_{c31} &= \frac{(\gamma - 1)(M_p^2 - 1)(u^2 + v^2)v}{2a^2} \\
 P_{c32} &= -\frac{(\gamma - 1)(M_p^2 - 1)uv}{a^2} \\
 P_{c33} &= 1 - \frac{(\gamma - 1)(M_p^2 - 1)v^2}{a^2} \\
 P_{c34} &= \frac{(\gamma - 1)(M_p^2 - 1)v}{a^2} \\
 P_{c41} &= \frac{(\gamma - 1)(M_p^2 - 1)(u^2 + v^2)H}{2a^2} \\
 P_{c42} &= -\frac{(\gamma - 1)(M_p^2 - 1)uH}{a^2} \\
 P_{c43} &= -\frac{(\gamma - 1)(M_p^2 - 1)vH}{a^2} \\
 P_{c44} &= 1 + \frac{(\gamma - 1)(M_p^2 - 1)H}{a^2}
 \end{aligned}$$

where  $H$  represents the total enthalpy  $H = \frac{u^2+v^2}{2} + \frac{a^2}{\gamma-1}$ .

The eigenvalues of preconditioned system are:

$$\begin{aligned}
 \lambda_1 &= \lambda_2 = \lambda_5 = \lambda_6 = U_n \\
 \lambda_3 &= \frac{1}{2} \left[ U_n(1 + M_p^2) + \sqrt{4a^2M_p^2 + (M_p^2 - 1)^2 U_n^2} \right] \\
 \lambda_4 &= \frac{1}{2} \left[ U_n(1 + M_p^2) - \sqrt{4a^2M_p^2 + (M_p^2 - 1)^2 U_n^2} \right]
 \end{aligned} \tag{C.3}$$

where  $U_n$  is the velocity component normal to the face being considered and is given by

$$U_n = uk_x + vk_y, \text{ and } a^2 = (\gamma - 1) \left[ H - \frac{u^2+v^2}{2} \right].$$

The preconditioned characteristic variables defined by  $\alpha_j = \delta W = (L_\star^{-1})_j \delta V$  are,

$$\begin{aligned}
 \alpha_1 &= \delta\rho - \frac{\delta p}{a^2} \\
 \alpha_2 &= \rho(\delta uk_y - \delta vk_x) \\
 \alpha_3 &= \frac{\delta p - \rho(\delta uk_x + \delta vk_y)(\lambda_4 - U_n)}{a(\lambda_3 - \lambda_4)} \\
 \alpha_4 &= \frac{\delta p - \rho(\delta uk_x + \delta vk_y)(\lambda_3 - U_n)}{a(\lambda_3 - \lambda_4)} \\
 \alpha_5 &= \rho\delta K \\
 \alpha_6 &= \rho\delta\omega
 \end{aligned} \tag{C.4}$$

The flux differences are

C. Space discretisation (simplified preconditioned form)

$$\begin{aligned}
\delta f_1 &= \alpha_1 \lambda_1 + \frac{\alpha_3 \lambda_3 (\lambda_3 - U_n) - \alpha_4 \lambda_4 (\lambda_4 - U_n)}{a M_p^2} \\
\delta f_2 &= \alpha_1 \lambda_1 u + \alpha_2 \lambda_2 k_y + a k_x (\alpha_3 \lambda_3 - \alpha_4 \lambda_4) \\
&\quad + \frac{(\alpha_3 \lambda_3 (\lambda_3 - U_n) - \alpha_4 \lambda_4 (\lambda_4 - U_n)) u}{a M_p^2} \\
\delta f_3 &= \alpha_1 \lambda_1 v - \alpha_2 \lambda_2 k_x + a k_y (\alpha_3 \lambda_3 - \alpha_4 \lambda_4) \\
&\quad + \frac{(\alpha_3 \lambda_3 (\lambda_3 - U_n) - \alpha_4 \lambda_4 (\lambda_4 - U_n)) v}{a M_p^2} \\
\delta f_4 &= \alpha_1 \lambda_1 \left( \frac{1}{2} (u^2 + v^2) \right) + \alpha_2 \lambda_2 (u k_y - v k_x) \\
&\quad + \left( \frac{\lambda_3 - U_n}{a M_p^2} H + a U_n \right) \alpha_3 \lambda_3 - \left( \frac{\lambda_4 - U_n}{a M_p^2} H + a U_n \right) \alpha_4 \lambda_4 \\
\delta f_5 &= \alpha_1 \lambda_1 K + \frac{|U_n + c| \left( \frac{\delta p}{c^2} + \frac{\rho \delta U_n}{c} \right)}{2} K + \frac{|U_n - c| \left( \frac{\delta p}{c^2} - \frac{\rho \delta U_n}{c} \right)}{2} K + \alpha_5 \lambda_5 \\
\delta f_6 &= \alpha_1 \lambda_1 \omega + \frac{|U_n + c| \left( \frac{\delta p}{c^2} + \frac{\rho \delta U_n}{c} \right)}{2} \omega + \frac{|U_n - c| \left( \frac{\delta p}{c^2} - \frac{\rho \delta U_n}{c} \right)}{2} \omega + \alpha_6 \lambda_6
\end{aligned} \tag{C.5}$$

## (C.2) simplified form No. 2

The second choice being tested in the research is derived through a rigorous mathematical process as what is shown in the full preconditioned algorithm. All the matrices and flux dissipation terms related to this preconditioned system are shown as below.

$$P_c = \begin{pmatrix} P_{c11} & P_{c12} & P_{c13} & P_{c14} & 0 & 0 \\ P_{c21} & P_{c22} & P_{c23} & P_{c24} & 0 & 0 \\ P_{c31} & P_{c32} & P_{c33} & P_{c34} & 0 & 0 \\ P_{c41} & P_{c42} & P_{c43} & P_{c44} & 0 & 0 \\ P_{c51} & P_{c52} & P_{c53} & P_{c54} & 1 & 0 \\ P_{c61} & P_{c62} & P_{c63} & P_{c64} & 0 & 1 \end{pmatrix} \tag{C.6}$$

with the individual entries shown as

$$\begin{aligned}
P_{c11} &= 1 + \frac{(\gamma - 1)(M_p^2 - 1)(u^2 + v^2)}{2a^2} \\
P_{c12} &= -\frac{(\gamma - 1)(M_p^2 - 1)u}{a^2} \\
P_{c13} &= -\frac{(\gamma - 1)(M_p^2 - 1)v}{a^2}
\end{aligned} \tag{C.7}$$

C. Space discretisation (simplified preconditioned form)

$$\begin{aligned}
P_{c14} &= \frac{(\gamma - 1)(M_p^2 - 1)}{a^2} \\
P_{c21} &= \frac{(\gamma - 1)(M_p^2 - 1)(u^2 + v^2)u}{2a^2} \\
P_{c22} &= 1 - \frac{(\gamma - 1)(M_p^2 - 1)u^2}{a^2} \\
P_{c23} &= -\frac{(\gamma - 1)(M_p^2 - 1)uv}{a^2} \\
P_{c24} &= \frac{(\gamma - 1)(M_p^2 - 1)u}{a^2} \\
P_{c31} &= \frac{(\gamma - 1)(M_p^2 - 1)(u^2 + v^2)v}{2a^2} \\
P_{c32} &= -\frac{(\gamma - 1)(M_p^2 - 1)uv}{a^2} \\
P_{c33} &= 1 - \frac{(\gamma - 1)(M_p^2 - 1)v^2}{a^2} \\
P_{c34} &= \frac{(\gamma - 1)(M_p^2 - 1)v}{a^2} \\
P_{c41} &= \frac{(\gamma - 1)(M_p^2 - 1)(u^2 + v^2)H}{2a^2} \\
P_{c42} &= -\frac{(\gamma - 1)(M_p^2 - 1)uH}{a^2} \\
P_{c43} &= -\frac{(\gamma - 1)(M_p^2 - 1)vH}{a^2} \\
P_{c44} &= 1 + \frac{(\gamma - 1)(M_p^2 - 1)H}{a^2} \\
P_{c51} &= \frac{(\gamma - 1)(M_p^2 - 1)(u^2 + v^2)K}{2a^2} \\
P_{c52} &= -\frac{(\gamma - 1)(M_p^2 - 1)uK}{a^2} \\
P_{c53} &= -\frac{(\gamma - 1)(M_p^2 - 1)vK}{a^2} \\
P_{c54} &= \frac{(\gamma - 1)(M_p^2 - 1)K}{a^2} \\
P_{c61} &= \frac{(\gamma - 1)(M_p^2 - 1)(u^2 + v^2)\omega}{2a^2} \\
P_{c62} &= -\frac{(\gamma - 1)(M_p^2 - 1)u\omega}{a^2} \\
P_{c63} &= -\frac{(\gamma - 1)(M_p^2 - 1)v\omega}{a^2} \\
P_{c64} &= \frac{(\gamma - 1)(M_p^2 - 1)\omega}{a^2}
\end{aligned}$$

where  $H$  represents the total enthalpy  $H = \frac{u^2 + v^2}{2} + \frac{a^2}{\gamma - 1}$ .

The eigenvalues of preconditioned system are:

C. Space discretisation (simplified preconditioned form)

$$\begin{aligned}\lambda_1 &= \lambda_2 = \lambda_5 = \lambda_6 = U_n \\ \lambda_3 &= \frac{1}{2} \left[ U_n(1 + M_p^2) + \sqrt{4a^2 M_p^2 + (M_p^2 - 1)^2 U_n^2} \right] \\ \lambda_4 &= \frac{1}{2} \left[ U_n(1 + M_p^2) - \sqrt{4a^2 M_p^2 + (M_p^2 - 1)^2 U_n^2} \right]\end{aligned}\tag{C.8}$$

where  $U_n$  is the velocity component normal to the face being considered and is given by  $U_n = uk_x + vk_y$ , and  $a^2 = (\gamma - 1) \left[ H - \frac{u^2 + v^2}{2} \right]$

The preconditioned characteristic variables defined by  $\alpha_j = \delta W = (L_\star^{-1})_j \delta V$  are,

$$\begin{aligned}\alpha_1 &= \delta\rho - \frac{\delta p}{a^2} \\ \alpha_2 &= \rho(\delta uk_y - \delta vk_x) \\ \alpha_3 &= \frac{\delta p - \rho(\delta uk_x + \delta vk_y)(\lambda_4 - U_n)}{a(\lambda_3 - \lambda_4)} \\ \alpha_4 &= \frac{\delta p - \rho(\delta uk_x + \delta vk_y)(\lambda_3 - U_n)}{a(\lambda_3 - \lambda_4)} \\ \alpha_5 &= \rho\delta K \\ \alpha_6 &= \rho\delta\omega\end{aligned}\tag{C.9}$$

The flux differences are

$$\begin{aligned}\delta f_1 &= \alpha_1 \lambda_1 + \frac{\alpha_3 \lambda_3 (\lambda_3 - U_n) - \alpha_4 \lambda_4 (\lambda_4 - U_n)}{a M_p^2} \\ \delta f_2 &= \alpha_1 \lambda_1 u + \alpha_2 \lambda_2 k_y + a k_x (\alpha_3 \lambda_3 - \alpha_4 \lambda_4) \\ &\quad + \frac{(\alpha_3 \lambda_3 (\lambda_3 - U_n) - \alpha_4 \lambda_4 (\lambda_4 - U_n)) u}{a M_p^2} \\ \delta f_3 &= \alpha_1 \lambda_1 v - \alpha_2 \lambda_2 k_x + a k_y (\alpha_3 \lambda_3 - \alpha_4 \lambda_4) \\ &\quad + \frac{(\alpha_3 \lambda_3 (\lambda_3 - U_n) - \alpha_4 \lambda_4 (\lambda_4 - U_n)) v}{a M_p^2} \\ \delta f_4 &= \alpha_1 \lambda_1 \left( \frac{1}{2} (u^2 + v^2) \right) + \alpha_2 \lambda_2 (uk_y - vk_x) \\ &\quad + \left( \frac{\lambda_3 - U_n}{a M_p^2} H + a U_n \right) \alpha_3 \lambda_3 - \left( \frac{\lambda_4 - U_n}{a M_p^2} H + a U_n \right) \alpha_4 \lambda_4 \\ \delta f_5 &= \alpha_1 \lambda_1 K + \frac{\alpha_3 \lambda_3 (\lambda_3 - U_n) - \alpha_4 \lambda_4 (\lambda_4 - U_n)}{a M_p^2} K + \alpha_5 \lambda_5\end{aligned}\tag{C.10}$$

$$\delta f_6 = \alpha_1 \lambda_1 \omega + \frac{\alpha_3 \lambda_3 (\lambda_3 - U_n) - \alpha_4 \lambda_4 (\lambda_4 - U_n)}{a M_p^2} \omega + \alpha_6 \lambda_6$$

## D Similarity transformation

Suppose that the square matrix  $A_1$  has the eigenvalue decomposition  $A_1 = V_1^{-1} \Lambda_1 V_1$ , and  $A_2$  is similar to  $A_1$  through  $X$ ,  $A_2 = X^{-1} A_1 X$ , then  $A_2 = X^{-1} V_1^{-1} \Lambda_1 V_1 X = V_2^{-1} \Lambda_2 V_2$ .

Since  $A_1$  and  $A_2$  have the same eigenvalues, the relationship between their eigenvectors is

$$V_2 = V_1 X \quad (\text{D.1})$$

Now if we consider the similarity transformation case of Eqn. (5.14) to (5.15), on one hand one has,

$$\left| (\bar{\Gamma}_p)^{-1} \Gamma_p \left( \frac{\partial F}{\partial V_p} \bar{\Gamma}_p \right) \right| = V_1^{-1} |\Lambda_1| V_1 \quad (\text{D.2})$$

and on the other hand,

$$\left| \Gamma_p \frac{\partial F}{\partial V_p} \right| = V_2^{-1} |\Lambda_2| V_2 \quad (\text{D.3})$$

The two matrices above have the same eigenvalues  $\Lambda_1 = \Lambda_2$  because they are similar. The equality of Eqns. (5.14) and (5.15) is true if and only if

$$V_2 \bar{\Gamma}_p = V_1 \quad (\text{D.4})$$

This is true because  $\bar{\Gamma}_p$  is the similarity transformation that links the matrices in the LHS of Eqn. (D.2) and (D.3).

## E Non-dimensionalisation

Before the implementation in the CFD solver, the governing equations are nondimensionalised. By doing so, the order of magnitude of the variables appearing in the URANS equations become of order 1, and this occurrence contributes to the reduction of round-off errors. However, even by using the nondimensionalised equations, it is not possible to achieve comparable order of magnitudes of all flow variables for flows with very low

Mach number. Additionally, for all flow regimens, the variable  $\omega$  is several orders of magnitude larger than all other variables.

The adopted basis of reference variables is:

$$[a_\infty, \rho_\infty, T_\infty, \mu_\infty, l] \quad (\text{E.1})$$

where  $a_\infty$  is the freestream sound speed,  $\rho_\infty$  is the freestream density,  $T_\infty$  is the freestream temperature,  $l$  is a reference length, and  $\mu_\infty$  is the freestream molecular viscosity. All dimensional variables appearing in the (dimensional) governing equations are then expressed as the product of a reference dimensional quantity and the nondimensionalised variables.

The reference dimensional variables resulting from the choice of basis (E.1) are:

$$\rho_{ref} = \rho_\infty, \quad u_{ref} = a_\infty, \quad l_{ref} = l, \quad Re_{ref} = \frac{\rho_\infty a_\infty l}{\mu_\infty} \quad (\text{E.2})$$

$$p_{ref} = \rho_\infty a_\infty^2 = \gamma p_\infty, \quad t_{ref} = \frac{l}{a_\infty}, \quad \tau_{ref} = \mu_\infty \frac{a_\infty}{l} \quad (\text{E.3})$$

$$x_{ref} = l, \quad k_{ref} = a_\infty^2, \quad \omega_{ref} = \frac{a_\infty}{l}, \quad \mu_{ref} = \mu_\infty \quad (\text{E.4})$$

Based on the Mach number defined at infinity  $M_\infty = \frac{u_\infty}{a_\infty}$ , the nondimensionalised Reynolds number can be written as

$$Re_{ref} = \frac{Re}{M_\infty} \quad (\text{E.5})$$

where  $Re$  is the Reynolds number based on the freestream velocity.

Using the reference variables (E.1) to perform the nondimensionalisation of the dimensional URANS equations provided by Eqn. (2.8), (2.9) and (2.10) yields the following nondimensional equations:

$$\frac{\partial \rho}{\partial t} + \frac{\partial}{\partial x_j} (\rho u_j) = 0 \quad (\text{E.6})$$

$$\frac{\partial}{\partial t}(\rho u_i) + \frac{\partial}{\partial x_j}(\rho u_j u_i) = -\frac{\partial p}{\partial x_i} + \frac{M_\infty}{Re_\infty} \frac{\partial \hat{\tau}_{ji}}{\partial x_j} \quad (\text{E.7})$$

$$\frac{\partial}{\partial t}(\rho E) + \frac{\partial}{\partial x_j}(\rho u_j H) = \frac{M_\infty}{Re_\infty} \frac{\partial}{\partial x_j} \left[ u_i \hat{\tau}_{ij} + (\mu + \sigma_K \mu_T) \frac{\partial K}{\partial x_j} - \hat{q}_j \right] \quad (\text{E.8})$$

The nondimensionalised Reynolds stress tensor is:

$$\tau_{ij}^R = 2\mu_T \left[ S_{ij} - \frac{1}{3} \frac{\partial u_k}{\partial x_k} \delta_{ij} \right] - \frac{Re_\infty}{M_\infty} \frac{2}{3} \rho k \delta_{ij} \quad (\text{E.9})$$

and the nondimensionalised stress tensor  $\hat{\tau}_{ij}$ , which is the sum of the molecular  $\tau_{ij}$  and the Reynolds stress tensor  $\tau_{ij}^R$ , is:

$$\hat{\tau}_{ij} = (\mu + \mu_T) \left[ \left( \frac{\partial u_i}{\partial x_j} + \frac{\partial u_j}{\partial x_i} \right) - \frac{2}{3} \frac{\partial u_k}{\partial x_k} \delta_{ij} \right] - \frac{Re_\infty}{M_\infty} \frac{2}{3} \rho k \delta_{ij} \quad (\text{E.10})$$

Where the nondimensionalised eddy viscosity is

$$\mu_T = \frac{Re_\infty}{M_\infty} \frac{\alpha_1 \rho K}{\max(\alpha_1 \omega, \Omega F_2)} \quad (\text{E.11})$$

$$F_2 = \tanh(\arg_2^2) \quad (\text{E.12})$$

$$\arg_2 = \max \left( \frac{2\sqrt{K}}{\beta^* \omega d}, \frac{500 \mu}{\rho \omega d^2} \frac{M_\infty}{Re_\infty} \right) \quad (\text{E.13})$$

and the nondimensionalised molecular viscosity  $\mu$  is computed with the nondimensionalised Sutherland's law:

$$\mu = T^{3/2} \frac{1 + S/T_{ref}}{T + S/T_{ref}} \quad (\text{E.14})$$

The nondimensionalised  $j^{th}$  component of the heat flux vector is:

$$\hat{q}_j = -\frac{1}{\gamma - 1} \left[ \frac{\mu}{Pr} + \frac{\mu_T}{Pr_T} \right] \frac{\partial T}{\partial x_j} \quad (\text{E.15})$$

Given that the nondimensionalised equation of state is  $\gamma p = \rho T$ , the nondimensionalised total energy per unit mass is:

$$E = \frac{T}{\gamma(\gamma - 1)} + \frac{u_i u_i}{2} + K = \frac{p}{\rho(\gamma - 1)} + \frac{u_i u_i}{2} + K \quad (\text{E.16})$$

and the total enthalpy per unit mass is:

$$H = \frac{T}{(\gamma - 1)} + \frac{u_i u_i}{2} + K = \frac{\gamma p}{\rho(\gamma - 1)} + \frac{u_i u_i}{2} + K \quad (\text{E.17})$$

Having assumed a perfect gas, the definitions above leads to:

$$p = (\gamma - 1) \left[ \rho E - \frac{1}{2} \rho (u_i u_i) - \rho K \right] \quad (\text{E.18})$$

And this equation is formally identical to its dimensional counterpart.

The nondimensionalised equations of the  $K - \omega$  SST turbulence model are:

$$\frac{\partial}{\partial t} (\rho K) + \frac{\partial}{\partial x_j} (\rho u_j K) = \frac{M_\infty}{Re_\infty} \tau_{ij}^R \frac{\partial u_i}{\partial x_j} - \beta^* \rho \omega K + \frac{M_\infty}{Re_\infty} \frac{\partial}{\partial x_j} \left[ (\mu + \sigma_K \mu_T) \frac{\partial k}{\partial x_j} \right] \quad (\text{E.19})$$

$$\begin{aligned} \frac{\partial}{\partial t} (\rho \omega) + \frac{\partial}{\partial x_j} (\rho u_j \omega) \\ = \frac{\gamma}{\nu_t} \tau_{ij}^R \frac{\partial u_i}{\partial x_j} - \beta \rho \omega^2 + \frac{M_\infty}{Re_\infty} \frac{\partial}{\partial x_j} \left[ (\mu + \sigma_\omega \mu_T) \frac{\partial k}{\partial x_j} \right] + CD_{term} \end{aligned} \quad (\text{E.20})$$

## F Compact differential form of the URANS and SST equations

The nondimensionalised URANS equations (E.6), (E.7) and (E.8), and the  $K - \omega$  SST equations (E.19) and (E.20) can be written in a compact vector form as follows:

$$\frac{\partial \mathbf{U}}{\partial t} + \frac{\partial (\mathbf{E}_c - \mathbf{E}_d)}{\partial x} + \frac{\partial (\mathbf{F}_c - \mathbf{F}_d)}{\partial y} = \mathbf{S} \quad (\text{F.1})$$

where the array  $\mathbf{U}$  collects the conservative flow variables of all transport equations, the arrays  $\mathbf{E}_c$  and  $\mathbf{F}_c$  collect respectively the  $x$ - and  $y$ - components of the convective fluxes of all equations, the arrays  $\mathbf{E}_d$  and  $\mathbf{F}_d$  collect respectively the  $x$ - and  $y$ - components of the diffusive fluxes of all equations, and the array  $\mathbf{S}$  contains the source terms of the  $SST$  equations. The definitions of the arrays  $\mathbf{U}$ ,  $\mathbf{E}_c$  and  $\mathbf{F}_c$  are respectively:

## F. Compact differential form of the URANS and SST equations

$$\mathbf{U} = \begin{bmatrix} \rho \\ \rho u \\ \rho v \\ \rho E \\ \rho K \\ \rho \omega \end{bmatrix}, \quad \mathbf{E}_c = \begin{bmatrix} \rho u \\ \rho u^2 + p \\ \rho uv \\ \rho uE \\ \rho uK \\ \rho u\omega \end{bmatrix}, \quad \mathbf{F}_c = \begin{bmatrix} \rho v \\ \rho vu \\ \rho v^2 + p \\ \rho vE \\ \rho vK \\ \rho v\omega \end{bmatrix} \quad (\text{F.2})$$

where the total energy  $E$  per unit mass and the total enthalpy  $H$  per unit mass are defined by Eqn. (E.16) and (E.17). The definitions of the diffusive flux vectors  $\mathbf{E}_d$  and  $\mathbf{F}_d$  are respectively:

$$\mathbf{E}_d = \frac{M_\infty}{Re_\infty} \begin{bmatrix} 0 \\ \tau_{xx} \\ \tau_{xy} \\ u\tau_{xx} + v\tau_{xy} + (\mu + \sigma_K \mu_T) \frac{\partial K}{\partial x} - q_x \\ (\mu + \sigma_K \mu_T) \frac{\partial K}{\partial x} \\ (\mu + \sigma_\omega \mu_T) \frac{\partial \omega}{\partial x} \end{bmatrix} \quad (\text{F.3})$$

$$\mathbf{F}_d = \frac{M_\infty}{Re_\infty} \begin{bmatrix} 0 \\ \tau_{xy} \\ \tau_{yy} \\ u\tau_{xy} + v\tau_{yy} + (\mu + \sigma_K \mu_T) \frac{\partial K}{\partial y} - q_y \\ (\mu + \sigma_K \mu_T) \frac{\partial K}{\partial y} \\ (\mu + \sigma_\omega \mu_T) \frac{\partial \omega}{\partial y} \end{bmatrix} \quad (\text{F.4})$$

The definition of the array  $\mathbf{S}$  is:

$$\mathbf{S} = \begin{bmatrix} 0 \\ 0 \\ 0 \\ 0 \\ P_K - D_K \\ P_\omega - D_\omega + CD_{term} \end{bmatrix} \quad (\text{F.5})$$

where

$$P_K = \frac{M_\infty}{Re_\infty} \tau_{ij}^R \frac{\partial u_i}{\partial x_j} \quad (\text{F.6})$$

$$D_K = \beta^* \rho \omega K \quad (\text{F.7})$$

F. Compact differential form of the URANS and SST equations

$$P_\omega = \frac{\gamma\rho}{\mu_T} \tau_{ij}^R \frac{\partial u_i}{\partial x_j} \quad (\text{F.8})$$

$$D_K = \beta\rho\omega^2 \quad (\text{F.9})$$

$$CD_{term} = 2\rho(1 - F_1)\sigma_{\omega^2} \frac{1}{\omega} \frac{\partial K}{\partial x_j} \frac{\partial \omega}{\partial x_j} \quad (\text{F.10})$$

# Bibliography

AHMED, H. & CHACKO, S. Computational Optimization of Vehicle Aerodynamics. Annals of DAAAM for 2012 & Proceedings of the 23rd International DAAAM Symposium, 2012. Vienna, Austria. DAAAM International, 313-318.

ARAKAWA, C., FLEIG, O., IIDA, M. & SHIMOOKA, M. 2005. Numerical approach for noise reduction of wind turbine blade tip with earth simulator. *Journal of the Earth Simulator*, 2(3), 11-33.

BALDUZZI, F., BIANCHINI, A., GIGANTE, F. A., FERRARA, G., CAMPOBASSO, M. S. & FERRARI, L. PARAMETRIC AND COMPARATIVE ASSESSMENT OF NAVIER-STOKES CFD METHODOLOGIES FOR DARRIEUS WIND TURBINE PERFORMANCE ANALYSIS. ASME Turbo Expo 2015: Turbine Technical Conference and Exposition, June 15-19, 2015. Montreal, Canada. American Society of Mechanical Engineers.

BALDWIN, B. S. & LOMAX, H. Thin layer approximation and algebraic model for separated turbulent flows. 16th AIAA Aerospace Sciences Meeting, January 16-18, 1978. Huntsville, Alabama, USA. American Institute of Aeronautics and Astronautics.

BECHMANN, A. & SORENSEN, N. 2010. Hybrid RANS/LES method for wind flow over complex terrain. *Wind Energy*, 13(1), 36-50.

BECHMANN, A., SØRENSEN, N. & ZAHLE, F. 2011. CFD Simulations of the MEXICO Rotor. *Wind Energy*, 14(5), 677-689.

BELOV, A., MARTINELLI, L. & JAMESON, A. A new implicit algorithm with multigrid for unsteady incompressible flow calculations. 33rd AIAA Aerospace Sciences Meeting and Exhibit, January 9-12, 1995. Reno, NV, USA. American Institute of Aeronautics and Astronautics, 0049.

BLAZEK, J. 2005. *Computational Fluid Dynamics: Principles and Applications*, Elsevier.

BLAZEK, J., KROLL, N., RADESPIEL, R. & ROSSOW, C. Upwind implicit residual smoothing method for multi-stage schemes. 10th AIAA Computational Fluid Dynamics Conference, 1991. Honolulu, HI, USA. American Institute of Aeronautics and Astronautics.

BLAZEK, J., ROSSOW, C. C., KROLL, N. & SWANSON, R. C. 1993. A comparison of several implicit residual smoothing methods in combination with multigrid. In: NAPOLITANO, M. & SABETTA, F. (eds.) *Thirteenth International Conference on Numerical Methods in Fluid Dynamics*. Springer Berlin Heidelberg.

BRIAN, S. 1994. A near wall model for the k- $\epsilon$  two equation turbulence model. Fluid Dynamics Conference. American Institute of Aeronautics and Astronautics.

BRIGGS, W. L. & MCCORMICK, S. F. 2000. *A multigrid tutorial*, Siam.

BRILEY, W., MCDONALD, H. & SHAMROTH, S. 1983. A low Mach number Euler formulation and application to time-iterative LBI schemes. *AIAA Journal*, 21(10), 1467-1469.

BRILEY, W., TAYLOR, L. & WHITFIELD, D. 2003. High-resolution viscous flow simulations at arbitrary Mach number. *Journal of Computational Physics*, 184(1), 79-105.

BUELOW, P. E., SCHWER, D. A., FENG, J., MERKLE, C. L. & CHOI, D. A preconditioned dual-time, diagonalized ADI scheme for unsteady computations. 13th AIAA Computational Fluid Dynamics

Conference, June 29 - July 2, 1997. Snowmass Village, CO, U.S.A. American Institute of Aeronautics and Astronautics, 2101.

BUELOW, P. E. O. 1995. Convergence enhancement of Euler and Navier-Stokes algorithms. Doctor of Philosophy Ph.D.Thesis, The Pennsylvania State University.

BUELOW, P. E. O. 2014. RE: Personal Communiation.

BUELOW, P. E. O., VENKATESWARAN, S. & MERKLE, C. L. 1994. Effect of grid aspect ratio on convergence. *AIAA Journal*, 32(12), 2401-2408.

CAMPOBASSO, M., YAN, M., DROFELNIK, J., PISKOPAKIS, A. & CABONI, M. Compressible Reynolds-Averaged Navier-Stokes analysis of wind turbine turbulent flows using a Fully-Coupled Low-Speed preconditioned multigrid solver. ASME Turbo Expo 2014: Turbine Technical Conference and Exposition, June 16–20, 2014a. Düsseldorf, Germany. American Society of Mechanical Engineers.

CAMPOBASSO, M. S. & BABA-AHMADI, M. H. 2011. Ad-hoc boundary conditions for CFD analyses of turbomachinery problems with strong flow gradients at Farfield boundaries. *Journal of Turbomachinery*, 133(4), 587-599.

CAMPOBASSO, M. S. & BABA-AHMADI, M. H. 2012. Analysis of Unsteady Flows Past Horizontal Axis Wind Turbine Airfoils Based on Harmonic Balance Compressible Navier-Stokes Equations With Low-Speed Preconditioning. *Journal of Turbomachinery*, 134(6), 061020.

CAMPOBASSO, M. S. & DROFELNIK, J. 2012. Compressible Navier–Stokes analysis of an oscillating wing in a power-extraction regime using efficient low-speed preconditioning. *Computers & Fluids*, 67, 26-40.

CAMPOBASSO, M. S., GIGANTE, F. & DROFELNIK, J. Turbulent unsteady flow analysis of horizontal axis wind turbine airfoil aerodynamics based on the harmonic balance Reynolds-Averaged Navier-Stokes equations. ASME Turbo Expo 2014: Turbine Technical Conference and Exposition, June 16–20, 2014b. Düsseldorf, Germany. American Society of Mechanical Engineers.

CAMPOBASSO, M. S., PISKOPAKIS, A., DROFELNIK, J. & JACKSON, A. 2013. Turbulent Navier–Stokes analysis of an oscillating wing in a power-extraction regime using the shear stress transport turbulence model. *Computers & Fluids*, 88, 136-155.

CATHY, J., MARK, W. & GEORGE, B. Optimising Aspects of a BERP-like Rotor Using Frequency-Domain Methods. 51st AIAA Aerospace Sciences Meeting including the New Horizons Forum and Aerospace Exposition, January 7-10, 2013. Grapevine, Texas, USA. American Institute of Aeronautics and Astronautics.

CHADERJIAN, N. M., PANDYA, S. A., AHMAD, J. & MURMAN, S. Progress toward generation of a Navier-Stokes database for a Harrier in ground effect. 2002 Biennial International Powered Lift Conference and Exhibit, November 5-7, 2002. Williamsburg, Virginia, USA. 2002.

CHOI, Y. 1989. Computation of low Mach number flow. Doctor of Philosophy Ph.D.Thesis, The Pennsylvania State University.

CHOI, Y. H. & MERKLE, C. L. 1993. The Application of Preconditioning in Viscous Flows. *Journal of Computational Physics*, 105(2), 207-223.

CHORIN, A. J. 1967. A Numerical Method for Solving Incompressible Viscous Flow. *Journal of Computational Physics*, 2(1), 12-26.

- COLES, D. & WADCOCK, A. J. 1979. Flying-hot-wire study of flow past an NACA 4412 airfoil at maximum lift. *AIAA Journal*, 17(4), 321-329.
- COLIN, Y., DENIAU, H. & BOUSSUGE, J. F. 2011. A robust low speed preconditioning formulation for viscous flow computations. *Computers & Fluids*, 47(1), 1-15.
- COOK, A. W. & RILEY, J. J. 1996. Direct numerical simulation of a turbulent reactive plume on a parallel computer. *Journal of Computational Physics*, 129(2), 263-283.
- COUTIER-DELGOSHA, O., FORTES-PATELLA, R., REBOUD, J. L., HAKIMI, N. & HIRSCH, C. 2005. Stability of preconditioned Navier–Stokes equations associated with a cavitation model. *Computers & Fluids*, 34(3), 319-349.
- DA RONCH, A., MCCRACKEN, A., BADCOCK, K., WIDHALM, M. & CAMPOBASSO, M. 2013. Linear frequency domain and harmonic balance predictions of dynamic derivatives. *Journal of Aircraft*, 50(3), 694-707.
- DARMOFAL, D. & SIU, K. 1999. A robust multigrid algorithm for the Euler equations with local preconditioning and semi-coarsening. *Journal of Computational Physics*, 151(2), 728-756.
- DOUGLAS, C. C. 1996. Multigrid methods in science and engineering. *Computing in Science and Engineering*, 3(4), 55-68.
- DREEBEN, T. D. & POPE, S. B. 1997. Probability density function and Reynolds - stress modeling of near - wall turbulent flows. *Physics of Fluids (1994-present)*, 9(1), 154-163.
- DRELA, M. 1989. XFOIL: An Analysis and Design System for Low Reynolds Number Airfoils. In: MUELLER, T. (ed.) *Low Reynolds Number Aerodynamics*. Springer Berlin Heidelberg.
- DRIVER, D. M. & SEEGMILLER, H. L. 1985. Features of a reattaching turbulent shear layer in divergent channel flow. *AIAA Journal*, 23(2), 163-171.
- EÇA, L. & HOEKSTRA, M. Testing uncertainty estimation and validation procedures in the flow around a backward facing step. *Proceedings of the 3rd Workshop on CFD Uncertainty Analysis*, October, 2008. Lisbon, Portugal.
- EKATERINARIS, J. A. & MENTER, F. R. 1994. Computation of oscillating airfoil flows with one- and two-equation turbulence models. *AIAA Journal*, 32(12), 2359-2365.
- FERZIGER, J. H. & PERIĆ, M. 2002. *Computational methods for fluid dynamics*, Springer Science & Business Media, Berlin.
- FITERMAN, A., TÜRKEI, E. & VATSA, V. PRESSURE UPDATING METHODS FOR THE STEADY-STATE FLUID EQUATIONS. 12th AIAA Computational Fluid Dynamics Conference, June 1995. San Diego, CA, U.S.A. American Institute of Aeronautics and Astronautics.
- GLEIZE, V. & COSTES, M. 2003. Low-Mach-number preconditioning applied to turbulent helicopter fuselage flowfield computation. *AIAA Journal*, 41(4), 653-662.
- GLEIZE, V. & LE PAPE, A. Low Mach number preconditioning for unsteady flow in general ALE formulation. 44th AIAA Aerospace Sciences Meeting and Exhibit, January 9-12, 2006. Reno, Nevada, USA. American Institute of Aeronautics and Astronautics, 1.
- GÓMEZ-IRADI, S., STEIJL, R. & BARAKOS, G. 2009. Development and Validation of a CFD Technique for the Aerodynamic Analysis of HAWT. *Journal of Solar Energy Engineering*, 131(3), 031009.

- GREENBLATT, D., PASCHAL, K. B., YAO, C.-S., HARRIS, J., SCHAEFFLER, N. W. & WASHBURN, A. E. A separation control CFD validation test case, Part 1: baseline and steady suction. 2nd AIAA Flow Control Conference, 28 June - 1 July, 2004. Portland, Oregon, USA. American Institute of Aeronautics and Astronautics.
- HAKIMI, N. 1997. PRECONDITIONING METHODS FOR TIME DEPENDENT NAVIER-STOKES EQUATIONS - Application to Environmental and Low Speed Flows. Doctor of Philosophy Ph.D.Thesis, Vrije Universiteit Brussel.
- HALL, K. C., THOMAS, J. P. & CLARK, W. S. 2002. Computation of unsteady nonlinear flows in cascades using a harmonic balance technique. *AIAA Journal*, 40(5), 879-886.
- HANSEN, M. O. L., SORENSEN, J. N., VOUTSINAS, S., SØRENSEN, N. & MADSEN, H. A. 2006. State of the art in wind turbine aerodynamics and aeroelasticity. *Progress in aerospace sciences*, 42(4), 285-330.
- HEINRICH, M. & SCHWARZE, R. All-Mach Number Density Based Flow Solver for OpenFOAM. ASME Turbo Expo 2014: Turbine Technical Conference and Exposition, June 16–20, 2014. Düsseldorf, Germany. American Society of Mechanical Engineers.
- HEJRAFAR, K. & KAMALI-MOGHADAM, R. 2012. Assessment of three preconditioning schemes for solution of the two-dimensional Euler equations at low Mach number flows. *International Journal for Numerical Methods in Engineering*, 89(1), 20-52.
- HIRSCH, C. 2007. Numerical Computation of Internal and External Flows: The Fundamentals of Computational Fluid Dynamics: The Fundamentals of Computational Fluid Dynamics, Butterworth-Heinemann.
- HOSSEINI, K. & ALONSO, J. J. Practical implementation and improvement of preconditioning methods for explicit multistage flow solvers. 42nd AIAA Aerospace Sciences Meeting and Exhibit, January 5-8, 2004. Reno, Nevada, USA. American Institute of Aeronautics and Astronautics.
- IM, H.-S. & ZHA, G.-C. Delayed detached eddy simulation of a stall flow over NACA0012 airfoil using high order schemes. 49th AIAA Aerospace Sciences Meeting including the New Horizons Forum and Aerospace Exposition, January 4-7, 2011. Orlando, Florida, USA. American Institute of Aeronautics and Astronautics.
- JACKSON, A. & CAMPOBASSO, M. S. 2011. Shared-memory, distributed-memory, and mixed-mode parallelisation of a CFD simulation code. *Computer Science-Research and Development*, 26(3-4), 187-195.
- JAMESON, A. 1983. Solution of the Euler equations for two dimensional transonic flow by a multigrid method. *Applied mathematics and computation*, 13(3), 327-355.
- JAMESON, A. Time dependent calculations using multigrid, with applications to unsteady flows past airfoils and wings. 10th AIAA Computational Fluid Dynamics Conference, June 24-26, 1991. Honolulu, HI, USA. American Institute of Aeronautics and Astronautics.
- JAMESON, A., SCHMIDT, W. & TURKEL, E. Numerical solutions of the Euler equations by finite volume methods using Runge-Kutta time-stepping schemes. 14th AIAA Fluid and Plasma Dynamics Conference, June 23 - 25, 1981. Palo Alto, CA, USA. American Institute of Aeronautics and Astronautics.

- JESPERSEN, D., PULLIAM, T., BUNING, P., JESPERSEN, D., PULLIAM, T. & BUNING, P. Recent enhancements to OVERFLOW. 35th AIAA Aerospace Sciences Meeting and Exhibit, January 6-9, 1997. Reno, NV, USA. American Institute of Aeronautics and Astronautics.
- JOHANSEN, J., SORENSEN, N., MICHELSEN, J. & SCHRECK, S. Detached-eddy simulation of flow around the NREL phase-VI blade. ASME 2002 Wind Energy Symposium, January 14–17, 2002. Reno, Nevada, USA. American Society of Mechanical Engineers, 106-114.
- JONES, W. & LAUNDER, B. 1973. The calculation of low-Reynolds-number phenomena with a two-equation model of turbulence. *International Journal of Heat and Mass Transfer*, 16(6), 1119-1130.
- KOUBOGIANNIS, D. G., ATHANASIADIS, A. N. & GIANNAKOGLU, K. C. 2003. One- and two-equation turbulence models for the prediction of complex cascade flows using unstructured grids. *Computers & Fluids*, 32(3), 403-430.
- KRIST, S. L., BIEDRON, R. T. & RUMSEY, C. L. 1998. CFL3D user's manual (version 5.0), National Aeronautics and Space Administration, Langley Research Center., Citeseer.
- KUNDU, P. & COHEN, I. 2008. *Fluid mechanics*, Elsevier Academic Press, San Diego.
- LANGLEY, N. 2015. FUN3D - fully unstructured Navier-Stokes [Online]. Available: <http://fun3d.larc.nasa.gov/>.
- LAUNDER, B., REECE, G. J. & RODI, W. 1975. Progress in the development of a Reynolds-stress turbulence closure. *Journal of fluid mechanics*, 68(3), 537-566.
- LE PAPE, A. & GLEIZE, V. Improved Navier-Stokes Computations of a Stall-Regulated Wind Turbine Using Low Mach Number Preconditioning. 44th AIAA Aerospace Sciences Meeting and Exhibit, January 9-12, 2006. Reno, Nevada, USA. American Institute of Aeronautics and Astronautics, 1.
- LE PAPE, A. & LECANU, J. 2004. 3D Navier-Stokes computations of a stall-regulated wind turbine. *Wind Energy*, 7(4), 309-324.
- LEE, D. 1996. Local preconditioning of the Euler and Navier-Stokes Equations. Doctor of Philosophy Ph.D.Thesis, The University of Michigan.
- LEE, D. 1998. The design of local Navier–Stokes preconditioning for compressible flow. *Journal of Computational Physics*, 144(2), 460-483.
- LEE, D., VAN LEER, B. & LYNN, J. A local Navier-Stokes preconditioner for all Mach and cell Reynolds numbers. 13th AIAA Computational Fluid Dynamics Conference, June 29 - July 2, 1997. Snowmass Village, CO, U.S.A. American Institute of Aeronautics and Astronautics.
- LERAT, A., SIDÈS, J. & DARU, V. 1982. An implicit finite-volume method for solving the Euler equations. In: KRAUSE, E. (ed.) *Eighth International Conference on Numerical Methods in Fluid Dynamics*. Springer Berlin Heidelberg.
- LI, X., GU, C. & XU, J. 2009. Development of Roe-type scheme for all-speed flows based on preconditioning method. *Computers & Fluids*, 38(4), 810-817.
- LIN, F. & SOTIROPOULOS, F. 1997. Strongly-coupled multigrid method for 3-D incompressible flows using near-wall turbulence closures. *Journal of fluids engineering*, 119(2), 314-324.
- LIOU, M.-S., ARNONE, A. & POVINELLI, L. Multi-grid Time-accurate Integration of Navier-Stokes Equations. 11th AIAA Computational Fluid Dynamics Conference, July 6-9, 1993. Orlando, Florida, USA. American Institute of Aeronautics and Astronautics.

- LIU, C., ZHENG, X. & SUNG, C. 1998. Preconditioned multigrid methods for unsteady incompressible flows. *Journal of Computational Physics*, 139(1), 35-57.
- LIU, F. & ZHENG, X. 1994. Staggered finite volume scheme for solving cascade flow with a k- $\omega$  turbulence model. *AIAA Journal*, 32(8), 1589-1597.
- LIU, F. & ZHENG, X. 1996. A Strongly Coupled Time-Marching Method for Solving the Navier–Stokes and k- $\omega$  Turbulence Model Equations with Multigrid. *Journal of Computational Physics*, 128(2), 289-300.
- MAVRIPLIS, D. & MARTINELLI, L. 1994. Multigrid solution of compressible turbulent flow on unstructured meshes using a two - equation model. *International journal for numerical methods in fluids*, 18(10), 887-914.
- MELSON, N. D., ATKINS, H. L. & SANETRIK, M. D. Time-accurate Navier-Stokes Calculations with Multigrid acceleration. 11th AIAA Computational Fluid Dynamics Conference, July 6-9, 1993. Orlando, Florida, USA. American Institute of Aeronautics and Astronautics, 1041-1042.
- MENTER, F. R. 1994. Two-equation eddy-viscosity turbulence models for engineering applications. *AIAA Journal*, 32(8), 1598-1605.
- MERKLE, C. L. & CHOI, Y.-H. 1988. COMPUTATION OF LOW-SPEED COMPRESSIBLE FLOWS WITH TIME-MARCHING PROCEDURES. *INTERNATIONAL JOURNAL FOR NUMERICAL METHODS IN ENGINEERING*, 25(2), 293-311.
- MO, J.-O., CHOUDHRY, A., ARJOMANDI, M. & LEE, Y.-H. 2013. Large eddy simulation of the wind turbine wake characteristics in the numerical wind tunnel model. *Journal of Wind Engineering and Industrial Aerodynamics*, 112, 11-24.
- MOINIER, P. & GILES, M. B. 2002. Stability Analysis of Preconditioned Approximations of the Euler Equations on Unstructured Meshes. *Journal of Computational Physics*, 178(2), 498-519.
- MORRIS, P. J., LONG, L. N. & BRENTNER, K. S. An aeroacoustic analysis of wind turbines. 42nd AIAA Aerospace Sciences Meeting and Exhibit, January 5-8, 2004. Reno, Nevada, USA. American Institute of Aeronautics and Astronautics, 2004.
- MORYOSSEF, Y. & LEVY, Y. 2006. Unconditionally positive implicit procedure for two-equation turbulence models: Application to k- $\omega$  turbulence models. *Journal of Computational Physics*, 220(1), 88-108.
- NAKAYAMA, A. 1985. Characteristics of the flow around conventional and supercritical airfoils. *Journal of Fluid Mechanics*, 160, 155-179.
- NASA. 2004. CFD Validation of Synthetic Jets and Turbulent Separation Control [Online]. Available: <http://cfdval2004.larc.nasa.gov/case3.html>.
- NIELSEN, E. J. & ANDERSON, W. K. 1999. Aerodynamic design optimization on unstructured meshes using the Navier-Stokes equations. *AIAA Journal*, 37(11), 1411-1419.
- NIKITIN, N., NICOUD, F., WASISTHO, B., SQUIRES, K. & SPALART, P. 2000. An approach to wall modeling in large-eddy simulations. *Physics of Fluids (1994-present)*, 12(7), 1629-1632.
- OWENS, J. D., HOUSTON, M., LUEBKE, D., GREEN, S., STONE, J. E. & PHILLIPS, J. C. 2008. GPU Computing. *Proceedings of the IEEE*, 96(5), 879-899.

- PANDYA, S. A., VENKATESWARAN, S. & PULLIAM, T. H. Implementation of preconditioned dual-time procedures in overflow. 41st AIAA Aerospace Sciences Meeting and Exhibit, January 6-9, 2003. Reno, Nevada, USA. American Institute of Aeronautics and Astronautics.
- PIOMELLI, U. Large-Eddy Simulation: Present state and future perspectives. 36th AIAA Aerospace Sciences Meeting and Exhibit, January 12-15, 1998. Reno, NV, U.S.A.: American Institute of Aeronautics and Astronautics.
- PIOMELLI, U., BALARAS, E., PASINATO, H., SQUIRES, K. D. & SPALART, P. R. 2003. The inner–outer layer interface in large-eddy simulations with wall-layer models. *International Journal of heat and fluid flow*, 24(4), 538-550.
- PULLIAM, T. H. & CHAUSSEE, D. 1981. A diagonal form of an implicit approximate-factorization algorithm. *Journal of Computational Physics*, 39(2), 347-363.
- RAI, M. M. 1993. Navier-Stokes Simulations of Blade-Vortex Interaction Using High-Order-Accurate Upwind Schemes. *Computational Aeroacoustics*. Springer New York,.
- RANFT, K., AMERI, A. A., ALEXANDER, J. I. D. & ENVIA, E. Acoustic Analysis of the NREL Phase VI Wind Turbine ASME Turbo Expo 2010: Power for Land, Sea, and Air, June 14-18, 2010. Glasgow, UK. American Society of Mechanical Engineers, 911-922.
- RHIE, C. M. 1989. Pressure-based Navier-Stokes solver using the multigrid method. *AIAA Journal*, 27(8), 1017-1018.
- RUMSEY, C. 2013. CFL3D Version 6.6 [Online]. Available: <http://cfl3d.larc.nasa.gov/>.
- SHENG, C. 2011. A Preconditioned Method for Rotating Flows at Arbitrary Mach Number. *Modelling and Simulation in Engineering*, 2011, 1-17.
- SHUEN, J.-S., CHEN, K.-H. & CHOI, Y. A time-accurate algorithm for chemical non-equilibrium viscous flows at all speeds. 28th AIAA Joint Propulsion Conference and Exhibit, July 6 - 8, 1992. Nashville, TN, U.S.A. American Institute of Aeronautics and Astronautics.
- SICOT, F., PUIGT, G. & MONTAGNAC, M. 2008. Block-Jacobi implicit algorithms for the time spectral method. *AIAA Journal*, 46(12), 3080-3089.
- SMITS, A., YOUNG, S. & BRADSHAW, P. 1979. The effect of short regions of high surface curvature on turbulent boundary layers. *Journal of Fluid Mechanics*, 94(2), 209-242.
- SØRENSEN, N. N., BECHMANN, A. & ZAHLE, F. 2011. 3D CFD computations of transitional flows using DES and a correlation based transition model. *Wind Energy*, 14(1), 77-90.
- SØRENSEN, N. N., MICHELSEN, J. & SCHRECK, S. 2002. Navier–Stokes predictions of the NREL phase VI rotor in the NASA Ames 80 ft× 120 ft wind tunnel. *Wind Energy*, 5(2-3), 151-169.
- SPALART, P., JOU, W., STRELETS, M. & ALLMARAS, S. 1997. Comments on the feasibility of LES for wings, and on a hybrid RANS/LES approach. *Advances in DNS/LES*, 1, 4-8.
- SPALART, P. R. 2000. Strategies for turbulence modelling and simulations. *International Journal of Heat and Fluid Flow*, 21(3), 252-263.
- SPALART, P. R. & ALLMARAS, S. R. 1994. A one-equation turbulence model for aerodynamic flows. *Recherche aérospatiale*, 1, 5-21.

- SPALART, P. R., DECK, S., SHUR, M., SQUIRES, K., STRELETS, M. K. & TRAVIN, A. 2006. A new version of detached-eddy simulation, resistant to ambiguous grid densities. *Theoretical and computational fluid dynamics*, 20(3), 181-195.
- SU, X. & YUAN, X. 2010. Implicit solution of time spectral method for periodic unsteady flows. *International journal for numerical methods in fluids*, 63(7), 860-876.
- SWANSON, R. & ROSSOW, C. An efficient flow solver with a transport equation for modeling turbulence. 19th AIAA Computational Fluid Dynamics, June 22-25, 2009. San-Antonio, Texas, USA. American Institute of Aeronautics and Astronautics.
- TAMAMIDIS, P., ZHANG, G. & ASSANIS, D. N. 1996. Comparison of pressure-based and artificial compressibility methods for solving 3D steady incompressible viscous flows. *Journal of computational Physics*, 124(1), 1-13.
- TURKEL, E. 1987. Preconditioned Methods for Solving the Incompressible and Low Speed Compressible Equations. *Journal of Computational Physics*, 72(2), 277-298.
- TURKEL, E. 1999. Preconditioning techniques in computational fluid dynamics. *Annual Review of Fluid Mechanics*, 31(1), 385-416.
- TURKEL, E. Robust low speed preconditioning for viscous high lift flows. 40th AIAA Aerospace Sciences Meeting & Exhibit, January 14-17, 2002. Reno, Nevada, USA. American Institute of Aeronautics and Astronautics.
- TURKEL, E., FITERMAN, A. & LEER, B. V. 1993. PRECONDITIONING AND THE LIMIT TO THE INCOMPRESSIBLE FLOW EQUATIONS. No. ICASE-93-42. Institute for Computer Applications in Science and Engineering.
- TURKEL, E., RADESPIEL, R. & KROLL, N. 1997. Assessment of preconditioning methods for multidimensional aerodynamics. *Computers & Fluids*, 26(6), 613-634.
- TURKEL, E. & VATSA, V. N. Choice of variables and preconditioning for time dependent problems. 16th AIAA Computational Fluid Dynamics Conference, June 23-26, 2003. Orlando, Florida, USA. American Institute of Aeronautics and Astronautics, 2003.
- TURKEL, E. & VATSA, V. N. 2005. Local preconditioners for steady and unsteady flow applications. *ESAIM: Mathematical Modelling and Numerical Analysis*, 39(3), 515-535.
- UNRAU, D., ZINGG, D., UNRAU, D. & ZINGG, D. Viscous airfoil computations using local preconditioning. 13th AIAA Computational Fluid Dynamics Conference, June 29 - July 2, 1997. Snowmass Village, CO, U.S.A. American Institute of Aeronautics and Astronautics.
- VAN DER WEIDE, E., GOPINATH, A. & JAMESON, A. Turbomachinery applications with the time spectral method. 35th AIAA Fluid Dynamics Conference and Exhibit, June 6-9, 2005. Toronto, Ontario, Canada. American Institute of Aeronautics and Astronautics, 2005.
- VAN LEER, B. 1977. Towards the ultimate conservative difference scheme. IV. A new approach to numerical convection. *Journal of computational physics*, 23(3), 276-299.
- VAN LEER, B. 1982. Flux-vector splitting for the Euler equations. In: KRAUSE, E. (ed.) Eighth International Conference on Numerical Methods in Fluid Dynamics. Springer Berlin Heidelberg.

- VAN LEER, B., LEE, W.-T. & ROE, P. L. Characteristic time-stepping or local preconditioning of the Euler equations. 10th AIAA Computational Fluid Dynamics Conference, June 24-27, 1991. Honolulu, HI, USA. American Institute of Aeronautics and Astronautics, 260-282.
- VAN LEER, B., LEE, W.-T., ROE, P. L., POWELL, K. G. & TAI, C.-H. 1992. Design of optimally smoothing multistage schemes for the euler equations. *Communications in Applied Numerical Methods*, 8(10), 761-769.
- VATSA, V. N. & TURKEL, E. Assessment of local preconditioners for steady state and time dependent flows. 34th AIAA Fluid Dynamics Conference and Exhibit, June 28 - July 1, 2004. Portland, Oregon, USA. American Institute of Aeronautics and Astronautics.
- VENKATESWARAN, S., LI, D. & MERKLE, C. Influence of Stagnation Regions on Preconditioned Solutions at Low Speeds. 41st AIAA Aerospace Sciences Meeting and Exhibit, January 6-9, 2003. Reno, Nevada, USA. American Institute of Aeronautics and Astronautics.
- VENKATESWARAN, S. & MERKLE, C. Dual time-stepping and preconditioning for unsteady computations. 33rd AIAA Aerospace Sciences Meeting and Exhibit, January 9-12, 1995. Reno, Nevada, USA. American Institute of Aeronautics and Astronautics.
- VENKATESWARAN, S. & MERKLE, C. Efficiency and accuracy issues in contemporary CFD algorithms. Fluids 2000 Conference and Exhibit, June 19-22, 2000. Denver, CO, USA. American Institute of Aeronautics and Astronautics.
- VENKATESWARAN, S. & MERKLE, L. 1999. Analysis of preconditioning methods for the Euler and Navier-Stokes equations. 30th Lecture series-van Karemman Institute for fluid dynamics, 3, B1-B155.
- WALTHER, B. & NADARAJAH, S. 2012. Constrained Adjoint-Based Aerodynamic Shape Optimization of a Single-Stage Transonic Compressor. *Journal of Turbomachinery*, 135(2), 021017.
- WANG, X., SHENG, C. & CHEN, J. Numerical Study of Preconditioned Algorithm for Rotational Flows. 17th AIAA Computational Fluid Dynamics Conference, June 6-9, 2005. Toronto, Ontario, Canada. American Institute of Aeronautics and Astronautics, 6-9.
- WEISS, J. M., MARUSZEWSKI, J. P. & SMITH, W. A. 1999. Implicit solution of preconditioned Navier-Stokes equations using algebraic multigrid. *AIAA Journal*, 37(1), 29-36.
- WEISS, J. M. & SMITH, W. A. 1995. Preconditioning Applied to Variable and Constant Density Flows. *AIAA Journal*, 33(11), 2050-2057.
- WESSELING, P. 1995. Introduction To Multigrid Methods. No. ICASE-95-11. INSTITUTE FOR COMPUTER APPLICATIONS IN SCIENCE AND ENGINEERING, HAMPTON, VA.
- WILCOX, D. C. 1988. Reassessment of the scale-determining equation for advanced turbulence models. *AIAA Journal*, 26(11), 1299-1310.
- WILCOX, D. C. 1993. Comparison of two-equation turbulence models for boundary layers with pressure gradient. *AIAA Journal*, 31(8), 1414-1421.
- WILCOX, D. C. 1994. Turbulence modeling for CFD, DCW industries, Inc. La Canada, CA.
- WILCOX, D. C. 2008. Formulation of the k-w Turbulence Model Revisited. *AIAA Journal*, 46(11), 2823-2838.

- WILLIAMS, J. F. & HAWKINGS, D. L. 1969. Sound generation by turbulence and surfaces in arbitrary motion. *Philosophical Transactions of the Royal Society of London A: Mathematical, Physical and Engineering Sciences*, 264(1151), 321-342.
- XIAO, T., ANG, H. & YU, S. 2007. A preconditioned dual time-stepping procedure coupled with matrix-free LU-SGS scheme for unsteady low speed viscous flows with moving objects. *International Journal of Computational Fluid Dynamics*, 21(3-4), 165-173.
- XIAO, Y. X., ZENG, C. J., ZHANG, J., YAN, Z. G. & WANG, Z. W. 2013. Numerical analysis of the bucket surface roughness effects in Pelton turbine. *IOP Conference Series: Materials Science and Engineering*, 52(5), 052032.
- YAO, J., JAMESON, A., ALONSO, J. J. & LIU, F. 2001. Development and Validation of a Massively Parallel Flow Solver for Turbomachinery Flows. *Journal of Propulsion and Power*, 17(3), 659-668.
- ZAHLE, F., BAK, C., GUNTUR, S., SORENSEN, N. & TROLDBORG, N. Comprehensive aerodynamic analysis of a 10 mw wind turbine rotor using 3d CFD. 32nd ASME Wind Energy Symposium, January 13-17, 2014. National Harbor, Maryland, USA. American Institute of Aeronautics and Astronautics.
- ZHENG, X., LIAO, C., LIU, C., SUNG, C. & HUANG, T. 1997. Multigrid computation of incompressible flows using two-equation turbulence models: Part I—Numerical method. *Journal of fluids engineering*, 119(4), 893-899.